

[REDACTED]

Form Approved
GME No- 0704 0188

1. The following information was obtained from the records of the Department of the Interior, Bureau of Land Management, regarding the status of the proposed project:

DTIC
ELECTE
FEB 04 1994

27008 94-03919

94 2 03 131

**Best
Available
Copy**

JAMES A. LOTT

Candidate

ELECTRICAL AND COMPUTER ENGINEERING

Department

This dissertation is approved, and it is acceptable in quality
and form for publication on microfilm:

Approved by the Dissertation Committee:

L. J. Malley

, Chairperson

J. C. Chang

S. D. Hame

R. P. Chinnery

Accepted:

Dean, Graduate School

Date

VISIBLE VERTICAL CAVITY SURFACE EMITTING LASERS

BY

JAMES ANTHONY LOTT

B.S., University of California at Berkeley, 1983

M.S., Air Force Institute of Technology, 1987

DISSERTATION

Submitted in Partial Fulfillment of the
Requirements for the Degree of

Doctor of Philosophy in Electrical Engineering

The University of New Mexico
Albuquerque, New Mexico

December 1993

Accession For		
NTIS	CRA&I	<input checked="" type="checkbox"/>
DTIC	TAB	<input type="checkbox"/>
Unannounced		<input type="checkbox"/>
Justification		
By		
Distribution /		
Availability Codes		
Dist	Avail and/or Special	
A-1		

DTIC QUALITY INSPECTED 5

**Copyright © 1993 by James A. Lott
All Rights Reserved**

Dedicated to my Parents
Byron David Lott and Vivian Margretta (Mitchell) Lott

Acknowledgments

The research in this dissertation was performed at Sandia National Laboratories, Albuquerque, New Mexico, and sponsored by the United States Department of Energy under Contract Number DE-AC04-76DP00789. All of my educational costs, along with a generous salary, were paid by the Air Force Institute of Technology, Wright-Patterson Air Force Base, Ohio.

I thank my dissertation adviser, Professor Kevin J. Malloy, for his expert guidance, ceaseless encouragement, and rejuvenating perspectives on the work. I also gratefully acknowledge the other members of my dissertation committee from the University of New Mexico, Professor Julian Cheng and Professor Steve D. Hersee, for reviewing the dissertation manuscript, and for providing valuable, thought provoking comments and suggestions.

This dissertation would not have been possible without the close collaboration between myself and Sandia's premier crystal grower, Dr. Richard P. Schneider, Jr. Thanks for easing the doldrums, and most importantly, for never giving up.

My sincere thanks also goes to Jeffrey J. Figiel, for expert technical growth support and for many extra hours of conscientious work.

Rather than graduate students, my co-workers were Sandia technical staff with wide and distinguished backgrounds. To William C. Banyai, Robert P. Bryan, Richard F. Carson, Scott A. Chalmers, Kent D. Choquette, John P. Hohimer, Eric D. Jones, Sean P. Kilcoyne, Kevin L. Lear, Randy J. Shul, G. Allen Vawter, Mial E. Warren, and John C. Zolper, my praise and thanks.

I have benefited immensely from the many collaborations/associations I have had with Sandians over the years. I especially thank Olga Blum-Spahn, Thomas M. Brennan, L. Ralph Dawson, Timothy J. Drummond, Ian J. Fritz, Paul L. Gourley, B. Gene Hammons, Dale L. Hetherington, Vincent M. Hietala, Harold P. Hjalmarson, Arnold J. Howard, John F. Klem, David R. Myers, Jeffrey S. Nelson, Chris P. Tigges, Harry T. Weaver, and Joel R. Wendt.

Sincere appreciation also goes to the managers of the Microelectronics and Photonics Research Center at Sandia. This includes Dr. Thomas E. Zipperian, Manager of the Compound Semiconductor Research Laboratory, Dr. Adelbert Owyong, Manager of Photonics Research Programs, Dr. Jeffrey Y. Tsao, Manager of Semiconductor Materials Research, and Dr. Paul S. Peercy, Director of the Center. Thank you for creating and maintaining a world class research environment, and for supporting my work.

I also thank the following individuals for expert technical support: Kevin C. Baucom, Robert B. Caldwell, Ric F. Corless, Dave Craft, Sharon Craft, JoAnn Escobedo, Beth A. Fuchs, Pat Glarborg, Geraldine Lopez, John A. Nevers, Jay B. Snelling, Thomas A. Plut, Dennis J. Rieger, Sally Samora, Jeanne M. Sergeant, M. Burt Snipes, Denise B. Webb-Montoya, and Robert J. Winkelman (the "Labmaster").

The administrative support at Sandia was excellent. For their extra efforts and cheer I thank Diane L. Gaylord, Dede L. Sanchez, and Becky R. Wilcox.

I also thank Joan Lillie, Administrative Director of the Graduate Electrical Engineering Office, for her assistance in scheduling exams and presentations, and in meeting deadlines.

Finally, I acknowledge the support of my family in California (and Japan), my new family in New Mexico, and most importantly, the dedication and many sacrifices of Julie Ann Radoslovich and Zachariah Casimir Radoslovich-Lott, my points of light.

VISIBLE VERTICAL CAVITY SURFACE EMITTING LASERS

JAMES ANTHONY LOTT

B.S. Electrical Engineering, University of California at Berkeley, 1983

M.S. Electrical Engineering, Air Force Institute of Technology, 1987

Ph.D. Electrical Engineering, University of New Mexico at Albuquerque, 1993

This dissertation explores the design, fabrication, and characterization of visible (620 to 690 nm) vertical cavity surface emitting lasers (VCSELs), consisting of an $(\text{Al}_y\text{Ga}_{1-y})_x\text{In}_{1-x}\text{P}$ strained quantum well optical cavity active region, surrounded by $\text{AlAs}/\text{Al}_x\text{Ga}_{1-x}\text{As}$ and $\text{Al}_{0.5}\text{In}_{0.5}\text{P}/(\text{Al}_y\text{Ga}_{1-y})_{0.5}\text{In}_{0.5}\text{P}$ distributed Bragg reflectors (DBRs). The lattice-matched device structures are grown on GaAs substrates by metalorganic vapor phase epitaxy (MOVPE). The key design and fabrication issues are reviewed and contrasted with conventional $\text{Ga}_{1-y}\text{In}_y\text{As}/\text{Al}_x\text{Ga}_{1-x}\text{As}$ near infrared (IR) VCSELs. Design trade-offs and quantum well gain characteristics are examined by studying optically pumped structures. Device fabrication techniques are developed, and the first electrically injected visible AlGaInP VCSELs are demonstrated. Prototype devices operate with pulsed current excitation at room temperature with a maximum output power of 3.38 mW at a lasing emission wavelength of 650 nm with threshold current densities of about 4.2 kA/cm² and threshold voltages of about 2.7 V. Due to cavity losses and unoptimized gain layer design, lasing is only achieved with significant gain contributions from the second ($n=2$) quantized quantum well state. With several

design improvements, pulsed room temperature (23 °C) lasing is achieved over the very broad range 629.6 to 691.4 nm, where the lasing emission above 650 nm is due primarily to gain contributions from the first ($n=1$) quantized quantum well state. For conventional top-emitting ion implanted devices, efficient room temperature continuous wave operation is demonstrated over the range 656.6 to 684.9 nm, with threshold currents below 2 mA (with threshold current densities of about 2 kA/cm²), threshold voltages of about 2 to 3 V, and output powers exceeding 0.5 mW.

Table of Contents

Acknowledgments	v
Abstract	vii
Table of Contents	x
List of Tables	xiii
List of Figures	xiv
List of Symbols	xxi
1 Introduction	1
2 Physics of Visible Resonant Cavity Photonic Devices	10
2.1 Introduction	10
2.2 Visible VCSEL Overview	11
2.3 AlGaInP Optical Cavity Active Regions	17
2.4 Distributed Bragg Reflectors	23
2.4.1 Reflectance Measurement Set-Up	26
2.4.2 AlGaAs DBRs for Visible Photonics	26
2.4.3 AlGaInP DBRs for Visible Photonics	33
2.4.4 Dielectric DBRs	39
2.5 Multilayer Fabry-Perot Etalons	42
2.6 Design Considerations for Visible VCSELs	52
2.6.1 DBR Resistance	54
2.6.2 Gain, Loss, and Temperature Effects	63
2.6.3 Comparison of Visible and Infrared VCSELs	75
2.7 Conclusions	83

3	Optically Pumped Visible Vertical Cavity Surface Emitting Lasers	89
3.1	Introduction	89
3.2	Experimental Set-Up	91
3.3	Theoretical Quantum Well Carrier Density at Threshold	93
3.4	Hybrid AlGaInP/AlGaAs Optically Pumped Visible VCSEL	95
3.5	All-AlGaInP Optically Pumped Visible VCSEL	103
3.6	Analysis of Results	113
3.7	Conclusions	117
4	Resonant Cavity Light Emitting Diodes	120
4.1	Introduction	120
4.2	Device Fabrication	122
4.3	Classical Wave Interference Model	126
4.4	Infrared RCLEDs/Hybrid VCSELs	135
4.5	Hybrid AlGaInP/AlGaAs Visible RCLEDs	140
4.6	All-AlGaInP Visible RCLEDs	146
4.7	Conclusions	150
5	Electrically Injected Visible Vertical Cavity Surface Emitting Lasers	156
5.1	Introduction	156
5.2	Device Fabrication	159
5.3	Operation with Gain Contributions from the $n=2$ Quantum Well State	163
5.4	Operation with Gain Contributions Primarily from the $n=1$ Quantum Well State	183
5.5	Continuous Wave Operation	191
5.6	Conclusions.	198
6	Conclusions	204
6.1	Summary	204
6.2	Suggestions for Future Work	207

Appendices

A	Material Parameters	211
B	Metalorganic Vapor Phase Epitaxy System	227
C	Matrix Calculations	232
D	Quantum Well Gain Calculations	238

List of Tables

Table	page
2.1 MOVPE Growth List for AlGaAs DBR Sample XC1019C	32
2.2 MOVPE Growth List for AlGaInP DBR Sample XC0930A	39
2.3 Reflectance Comparison for Selected Quarter Wave Stacks	41
2.4 Estimated Mobility and Conductivity of Selected Epitaxial Layers	58
2.5 Summary of the DBR Voltage Drop Analysis	66
2.6 Summary of Example Gain Calculations	71
2.7 Experimental Temperature Dependence of Example All Semiconductor Fabry-Perot Etalons	75
3.1 MOVPE Growth List for Hybrid Visible VCSEL Sample XC0915C	98
3.2 MOVPE Growth List for All-Phosphide Visible VCSEL Sample XC1104C. .	107
3.3 Comparison of Optically Pumped Hybrid Visible VCSELs	118
5.1 MOVPE Growth List for Hybrid Visible VCSEL Sample XD0222B	165
5.2 Comparison of Hybrid Visible VCSEL Diodes.	188
A.1 Equations for Energy Bandgap and Lattice Constant	212
A.2 Binary Material Parameters	214
A.3 Ternary and Quaternary Material Parameters	217
B.1 Summary of Precursors for the Aixtron MOVPE System	229

List of Figures

Figure	page
1.1 Comparison of visible edge-emitting and vertical cavity surface emitting lasers	3
1.2 Relative response of the human eye to visible wavelengths	6
2.1 Schematic diagram of an all semiconductor visible VCSEL.	12
2.2 Illustration of the longitudinal confinement factor for an example multiple quantum well VCSEL	16
2.3 Calculated peak transition wavelengths against quantum well thickness	19
2.4 Photoluminescence spectra of three example step-graded barrier separate confinement heterostructure, optical cavity active regions	21
2.5 Critical layer thickness and the corresponding compressive strain against $\text{Ga}_{1-x}\text{In}_x\text{P}$ composition referenced to GaAs	22
2.6 Schematic diagram of a quarter-wave distributed Bragg reflector	24
2.7 Schematic diagram of the reflectance and electroluminescence measurement set-up	27
2.8 Calculated reflectance spectra for $\text{AlAs}/\text{Al}_{0.5}\text{Ga}_{0.5}\text{As}$ DBR structures on a GaAs substrate, with variable number of DBR periods.	29
2.9 Reflectance versus number of periods for $\text{AlAs}/\text{Al}_{0.5}\text{Ga}_{0.5}\text{As}$ DBR structures	30
2.10 Measured and calculated reflectance of a 20 period $\text{AlAs}/\text{Al}_{0.5}\text{Ga}_{0.5}\text{As}$ DBR on a GaAs substrate, and calculated reflectivity phase	31
2.11 Three-dimensional reflectance spectra versus number of DBR periods for an $\text{Al}_{0.5}\text{In}_{0.5}\text{P}/(\text{Al}_{0.2}\text{Ga}_{0.8})_{0.5}\text{In}_{0.5}\text{P}$ DBR structure grown on a GaAs substrate.	34
2.12 Calculated <i>in situ</i> reflectance monitoring data	36
2.13 Comparison of $\text{Al}_{0.5}\text{In}_{0.5}\text{P}/(\text{Al}_y\text{Ga}_{1-y})_{0.5}\text{In}_{0.5}\text{P}$ distributed Bragg reflectors grown on GaAs substrates	37
2.14 Reflectance versus number of periods for $\text{Al}_{0.5}\text{In}_{0.5}\text{P}/(\text{Al}_{0.2}\text{Ga}_{0.8})_{0.5}\text{In}_{0.5}\text{P}$ DBR structures	38

Figure	page
2.15 Measured and calculated reflectance of a 25 period $\text{Al}_{0.5}\text{In}_{0.5}\text{P}/(\text{Al}_{0.2}\text{Ga}_{0.8})_{0.5}\text{In}_{0.5}\text{P}$ DBR on a GaAs substrate, and calculated reflectivity phase	40
2.16 Calculated transmittance of two example all-dielectric DBRs	43
2.17 Schematic diagram of a multilayer, all-semiconductor, Fabry-Perot etalon	44
2.18 Calculated reflectance spectra for an example Fabry-Perot etalon with uniform thickness variation in each layer	47
2.19 Calculated reflectance spectra for example Fabry-Perot etalons with varying optical cavity thickness	50
2.20 Calculated standing wave and refractive index profile for the 20λ thick example Fabry-Perot etalon structure near the center of the optical cavity active region at 670 nm and 681 nm	51
2.21 Calculated standing wave and refractive index profile for the 20λ thick example Fabry-Perot etalon structure near the interface between the optical cavity active region and the bottom DBR at 670 nm and 681 nm	53
2.22 Real space energy band diagrams for example $\text{AlAs}/\text{Al}_x\text{Ga}_{1-x}\text{As}$ DBRs	57
2.23 Conduction band diagrams for example $(n)\text{AlAs}/(n)\text{Al}_x\text{Ga}_{1-x}\text{As}$ DBRs	59
2.24 Valence band diagrams for example $(p)\text{AlAs}/(p)\text{Al}_x\text{Ga}_{1-x}\text{As}$ DBRs	60
2.25 Real space energy band diagrams for example $\text{Al}_{0.5}\text{In}_{0.5}\text{P}/(\text{Al}_y\text{Ga}_{1-y})_{0.5}\text{In}_{0.5}\text{P}$ DBRs	62
2.26 Conduction band diagrams for example $(n)\text{Al}_{0.5}\text{In}_{0.5}\text{P}/(n)\text{Al}_y\text{Ga}_{1-y})_{0.5}\text{In}_{0.5}\text{P}$ DBRs	64
2.27 Valence band diagrams for example $(p)\text{Al}_{0.5}\text{In}_{0.5}\text{P}/(p)(\text{Al}_y\text{Ga}_{1-y})_{0.5}\text{In}_{0.5}\text{P}$ DBRs	65
2.28 Calculated electric field intensity for three example visible VCSELs	68
2.29 Reflectance of hybrid $\text{AlGaAs}/\text{AlGaInP}$ and all- AlGaInP Fabry-Perot etalons as a function of temperature	73
2.30 Shift in the Fabry-Perot mode and the quantum well spectral gain peak as functions of temperature for an example visible VCSEL	74
2.31 Example real space, charge neutral, energy band diagrams comparing a conventional $\text{GaInAs}/\text{AlGaAs}$ IR VCSEL to an AlGaInP visible VCSEL	76

Figure	page
2.32	Calculated electric field intensity for the example IR and visible VCSELs shown in Fig. 2.31 79
2.33	Calculated gain as a function of carrier density for single 8 nm thick quantum wells composed of $\text{Ga}_{0.8}\text{In}_{0.2}\text{As}/\text{GaAs}$, and $\text{Ga}_{0.44}\text{In}_{0.56}\text{P}/(\text{Al}_{0.4}\text{Ga}_{0.6})_{0.5}\text{In}_{0.5}\text{P}$ with $Q_c = 0.6$ 81
2.34	Calculated gain as a function of carrier density for single 8 nm thick quantum wells composed of $\text{Ga}_{0.44}\text{In}_{0.56}\text{P}/(\text{Al}_{0.4}\text{Ga}_{0.6})_{0.5}\text{In}_{0.5}\text{P}$ and $\text{Ga}_{0.44}\text{In}_{0.56}\text{P}/(\text{Al}_{0.7}\text{Ga}_{0.3})_{0.5}\text{In}_{0.5}\text{P}$ with $Q_c = 0.4$ 82
3.1	Schematic diagram of the system for optical pumping of visible VCSELs . . . 92
3.2	The electric field intensity on resonance and refractive index against distance for the hybrid visible VCSEL 96
3.3	Photoluminescence of an AlGaInP quantum well optical cavity active region calibration sample at 300, 200, and 100K, just prior to the growth of the hybrid visible VCSEL 97
3.4	Measured reflectance spectra at five approximately equally spaced points across the hybrid visible VCSEL wafer 99
3.5	Optically pumped lasing spectrum at $\lambda_0 = 669$ nm for the hybrid visible VCSEL 100
3.6	Measured average incident power onto the surface of the hybrid visible VCSEL against lasing wavelength 102
3.7	Schematic diagram of the all-phosphide visible VCSEL for optical pumping experiments 104
3.8	The electric field intensity on resonance and refractive index against distance for the all-AlGaInP visible VCSEL 105
3.9	Photoluminescence of an AlGaInP quantum well optical cavity active region calibration sample at 300K, just prior to the growth of the all-AlGaInP visible VCSEL 106
3.10	Measured reflectance and photoluminescence from the all-AlGaInP visible VCSEL at the short end of the wafer, with ~half of the top DBR periods removed, and corresponding calculated reflectance and spontaneous emission spectrum 108
3.11	Measured reflectance spectra at five approximately equally spaced points across the all-AlGaInP visible VCSEL wafer 110

Figure	page
3.12	Optically pumped lasing spectrum at $\lambda_0 = 676.8$ nm for the all-AlGaInP visible VCSEL 111
3.13	Measured incident power at threshold against lasing wavelength and L-L characteristic of the all-phosphide optically pumped visible VCSEL 112
3.14	Calculated central standing wave and real refractive index profile at resonance wavelengths from 660 to 680 nm, and corresponding reflectance and threshold gain versus resonance wavelength both for the optically pumped hybrid visible VCSEL 114
3.15	Qualitative analysis of the gain versus lasing wavelength results for the optically pumped hybrid AlGaInP/AlGaAs visible VCSEL 116
4.1	Schematic diagram of a fabricated IR RCLED and the top contact pad 124
4.2	Schematic cross section diagram of the all-AlGaInP visible RCLED 125
4.3	Schematic diagram of a multilayer Fabry-Perot etalon for use with the Classical Wave Interference Model 127
4.4	Example calculation using the Classical Wave Interference Model 134
4.5	Reflectance spectra at six approximately equally spaced points on the as-grown IR RCLED structure 137
4.6	Electroluminescence of the IR RCLED at three points on a fabricated sample 138
4.7	L-I characteristics for an IR RCLED and the same IR RCLED with a five period dielectric stack added to the top DBR 139
4.8	Measured electroluminescence and reflectance at several points across the centerline of a hybrid AlGaInP/AlGaAs visible RCLED unrotated wafer . . . 142
4.9	Calculated spontaneous emission spectra for the hybrid visible RCLED at Fabry-Perot resonances of 620, 640, and 660 nm 143
4.10	Measured reflectance and electroluminescence for an example hybrid visible RCLED with five top coupling DBR periods 144
4.11	Measured electroluminescence at several points across an unrotated wafer and L-I characteristics at $\lambda_0 = 661$ nm, for hybrid visible RCLEDs 145
4.12	Measured and calculated reflectance spectra, normal to the surface for the as-grown all-AlGaInP visible RCLED at room temperature 147

Figure	page
4.13 Electroluminescence spectra of the all-AlGaInP visible RCLED measured, and calculated	149
4.14 Calculated linewidth versus number of top coupling $\text{Al}_{0.5}\text{In}_{0.5}\text{P}/(\text{Al}_{0.2}\text{Ga}_{0.8})_{0.5}\text{In}_{0.5}\text{P}$ DBR periods for an all-AlGaInP visible RCLED with three different optical cavity thicknesses	151
5.1 Quick visible VCSELs	160
5.2 Schematic diagram of an ion implanted visible VCSEL	162
5.3 Calculated reflectance and reflectivity phase for the hybrid visible VCSEL in Table 5.1	167
5.4 Calculated reflectance and reflectivity phase in and around the primary Fabry-Perot mode, secondary Fabry-Perot mode, and natural mode, for the hybrid visible VCSEL in Table 5.1	168
5.5 Photoluminescence spectra at several points on an unrotated strained quantum well, optical cavity active region calibration wafer	170
5.6 Schematic plot of the variation in Fabry-Perot resonance wavelength and peak quantum well transition wavelengths across unrotated wafer number XD0222B	172
5.7 Measured reflectance at $\lambda_0 \approx 650$ and 670 nm for the hybrid visible VCSEL structure, and reflectance and electroluminescence for a fabricated Quick visible VCSEL prior to the mesa etch step	173
5.8 Electroluminescence spectra for fabricated Quick visible VCSELs prior to the mesa etch step, at several equally spaced points across the hybrid visible VCSEL wafer	175
5.9 Electroluminescence spectra corresponding to the Fabry-Perot resonances at several equally spaced points across the hybrid visible VCSEL wafer	176
5.10 Visible VCSEL lasing spectra below, at, and just above threshold at room temperature	177
5.11 Light-current characteristic at room temperature of a Quick visible VCSEL diode	179
5.12 Electroluminescence sampled from the top of a $50\text{ }\mu\text{m} \times 250\text{ }\mu\text{m}$ broad area stripe geometry, AlGaInP visible edge-emitting laser	181

Figure	page
5.13 Threshold current versus lasing wavelength for Quick visible VCSEL fabricated across sample XD0222B, and the same data overlaid with semi-quantitative quantum well gain spectra	182
5.14 Measured reflectance spectra near wafer center for sample XD0624B, and sample XD0701C	186
5.15 Threshold current versus lasing wavelength for Quick visible VCSEL samples XD0623E and XD0624B, and samples XD0630C and XD0701C	187
5.16 Threshold current versus lasing wavelength for Quick visible VCSEL sample XD0701C, superimposed with a normalized calculated quantum well gain spectrum	190
5.17 Room temperature continuous wave L-I-V curves for a Quick visible VCSEL (wafer XD0701C).	192
5.18 Low temperature continuous wave L-I-V curves for a Quick visible VCSEL (wafer XD0701C).	193
5.19 L-I-V characteristic at 20°C for ion implanted visible VCSELs with a 10 μm optical aperture and a 10 μm implant aperture, and a 15 μm optical aperture and a 20 μm implant aperture	195
5.20 L-I-V characteristics for an ion implanted visible VCSEL with a 10 μm optical aperture and a 10 μm implant aperture as a function of heatsink temperature from 20 to 45 °C.	196
5.21 Continuous wave threshold current versus lasing wavelength for ion implanted visible VCSELs across sample XD0701C.	197
A.1 Bandgap energy and photon wavelength, both versus lattice constant for AlGaAs and AlGaInP III-V compound semiconductors	211
A.2 Real refractive index dispersion data for AlGaInP lattice-matched to GaAs	213
A.3 Real refractive index dispersion data for AlGaAs below the energy bandgap	215
A.4 Complex refractive index dispersion data for GaAs and Al _{0.5} Ga _{0.5} As from photon wavelengths of 550 to 850 nm	216
A.5 Unit cell of ordered Ga _{0.5} In _{0.5} P, and schematic diagram of a Ga _{1-x} In _x P ordered crystal grown on (001) oriented GaAs	218
A.6 Low temperature photoluminescence peak emission energy of Ga _{0.5} In _{0.5} P epitaxial layers	219

Figure		page
A.7	Low temperature photoluminescence of disordered (Al _y Ga _{1-y}) _{0.5} In _{0.5} P epitaxial layers.	221
A.8	Low temperature photoluminescence spectra of ordered and disordered strained and unstrained, AlGaInP quantum well heterostructures	222
A.9	Compositional dependence of band offsets for Al _x Ga _{1-x} As and (Al _y Ga _{1-y}) _{0.5} In _{0.5} P heterostructures	224
B.1	Simplified schematic diagram of the Aixtron MOVPE system	228
C.1	A multilayer VCSEL structure used to model the electric field intensity on resonance	234

List of Symbols

Symbol	Description	units
α	loss coefficient	cm^{-1}
Γ	confinement factor	unitless
Γ_r	relative confinement factor	unitless
δ	Kronecker (delta) function	unitless
δ_{oc}	optical cavity phase factor	radians
$\Delta\nu$	spectral half width frequency	s^{-1}
ΔE_c	conduction band offset	eV
ΔE_v	valence band offset	eV
$\Delta\lambda_{BW}$	reflectance bandwidth	nm
$\Delta\lambda_{1/2}$	linewidth (full width at half maximum)	nm
Δ_0	split-off band energy	eV
$\Delta\tau$	pulse width	seconds
ε	lattice strain	unitless or %
ζ	phenomenological loss = $1 - e^{\zeta}$, with $\zeta = -\alpha L_{eff}$	unitless
η	differential quantum efficiency	unitless or %
θ	reflectivity phase	radians or degrees
κ	extinction coefficient, imaginary part of the refractive index	unitless
λ	$\lambda = \lambda_0/n$, wavelength in a medium with refractive index n	nm

Symbol	Description	units
λ_0	free space wavelength	nm
μ_n	electron mobility	cm ² /V-s
μ_p	hole mobility	cm ² /V-s
ν	frequency	s ⁻¹
ρ	resistivity	Ω -cm
ρ	reflectivity coefficient (complex)	unitless
σ	conductivity	S/cm
τ	transmittivity coefficient (complex)	unitless
τ_c	coherence time	seconds
τ_c	intraband scattering time	seconds
φ	reflectivity phase	radians
Φ_B	energy barrier due to an energy band offset	eV
ω	radian frequency, $\omega = 2\pi\nu$	s ⁻¹
Ω	resistance	Ohms (Ω)
a_0	lattice constant	\AA
A	absorptance	unitless
A	area	cm ²
A^*	effective Richardson constant	A/cm ² K ²
A_{qw}	fraction of the incident pump energy that is absorbed in the quantum well(s)	unitless
c	$c = c_0/n$ speed of light in a medium with index n	cm/s

Symbol	Description	units
c_0	speed of light in a vacuum	cm/s
C	constant in the semi-quantitative gain model	cm^{-1}
C_{11}	elastic stiffness coefficient	dyn/cm^2
C_{12}	elastic stiffness coefficient	dyn/cm^2
d	total length of the quantum wells in the active region	nm
D_ℓ	2x2 dynamical matrix for layer ℓ	unitless
$ E(\omega) ^2$	quantum well emission spectra without DBRs	arbitrary units
$ E_{R1}(\omega) ^2$	spontaneous emission spectrum of an RCLED emitted from DBR1	arbitrary units
E_g^Γ	gamma point or band, energy bandgap	eV
E_g^X	X-point or band, energy bandgap	eV
E_o^+	complex amplitude of the incident electric field plane waves	V/cm
E_o^-	complex amplitude of the reflected electric field plane waves	V/cm
E	electric field amplitude (complex)	V/cm
E	energy	eV or J
E_c	conduction band energy	eV
E_f, E_F	Fermi energy level	eV
E_g	energy bandgap	eV
E_v	valence band energy	eV
f	focal length of a lens	mm
$f_{c, v}$	Fermi-Dirac distribution function	unitless
\mathcal{F}	finesse	unitless
FSR	free spectral range	nm

Symbol	Description	units
$g(E)$	gain of a quantum well	cm^{-1}
g_{th}	threshold gain	cm^{-1}
$G(\hbar\omega)$	convolved quantum well gain	cm^{-1}
h	Planck's constant	J-s
\hbar	reduced Planck's constant = $h/2\pi$	J-s
H	Heavyside function	unitless
i	$\sqrt{-T}$	unitless
I	current	A
I	optical intensity	W/m^2
I_{th}	threshold current	A
J	current density	A/cm^2
J_{rad}	radiative current density	$\text{kA}/\mu\text{m-cm}^2$
J_{th}	threshold current density	kA/cm^2
k	wavevector	cm^{-1}
k_B	Boltzmann's constant	J/K
ℓ_p	phase penetration length (into a DBR)	μm
l_c	coherence length	μm
L	length	cm
L	light (input or output power)	mW
L_{eff}	effective length of the optical cavity	μm
$L(E)$	Lorentzian lineshape function	unitless
L_z	quantum well thickness	nm

Symbol	Description	units
m_0	electron rest mass	kg
m_e^*	electron effective mass	kg
m_{hh}^*	heavy-hole effective mass	kg
m_{lh}^*	light-hole effective mass	kg
m_r	reduced mass	kg
M	2x2 transfer matrix (complex)	unitless
$ M ^2$	transition matrix element (QW gain model)	kg-J
n	real part of the refractive index	unitless
n	density of free electrons	cm ⁻³
n_{cav}	average real refractive index of the optical cavity	unitless
\mathcal{N}	carrier density in an optically pumped quantum well	cm ⁻³
N	integer	unitless
N	complex refractive index $N(\omega) = n(\omega) - i\kappa(\omega)$	unitless
N_e	density of free electrons	cm ⁻³
N_p	integer number of DBR periods	unitless
N_{QW}	density of carriers in a quantum well	cm ⁻³
p	density of free holes	cm ⁻³
P_ℓ	2x2 propagation matrix for layer ℓ	unitless
P	power	mW
P_h	density of free holes	cm ⁻³
q	electronic charge per electron	Coul
Q	cavity quality factor	unitless
Q_c	$Q_c = \Delta E_c / \Delta E_g$	unitless

Symbol	Description	units
R	reflectance	unitless
R(E)	rate of spontaneous emission	$1/(\text{J}\cdot\text{cm}^2\cdot\text{s})$
t	time	seconds
T	transmittance	unitless
T	temperature	$^{\circ}\text{C}$ or K
u	integer	unitless
V	voltage	Volts (V)
V_{th}	threshold voltage	Volts (V)
x	alloy mole fraction, as in $\text{Al}_x\text{Ga}_{1-x}\text{As}$	unitless
y	alloy mole fraction, as in $(\text{Al}_y\text{Ga}_{1-y})_{0.5}\text{In}_{0.5}\text{P}$	unitless

Chapter 1 Introduction

Semiconductor laser diodes were first demonstrated in 1962, within two years of the first ruby laser [Siegman 1986]. During the 1970s, GaAs/AlGaAs laser diodes emitting in the near infrared (IR), 0.8 to 0.9 μm , were developed as sources for fiber optic communication systems [Casey and Panish 1978]. Subsequent research focused on GaInAsP/InP laser diodes for emission at 1.3 and 1.55 μm , where silica fibers have their lowest dispersion and loss [Agrawal and Dutta 1986]. Laser diode performance drastically improved during the 1980s, due largely to advances in molecular beam epitaxy (MBE) and metalorganic vapor phase epitaxy (MOVPE). These techniques are used for the growth (with monolayer precision) of quantum well lasers, and for a plethora of other "Bandgap Engineered" microstructures. Today, double heterostructure and quantum well GaAs/AlGaAs edge-emitting lasers are mass produced, inexpensive, and the workhorses of the photonics industry [Hecht 1993b]. Such lasers, emitting a few milliwatts at 780 nm in a single transverse mode, are the "styli" of audio compact disc players.

The study of diode lasers remains one of the most active areas in semiconductor device research. Much of the recent work has centered on new III-V and II-VI compound semiconductor materials for shorter wavelength, *visible lasers* [Hecht 1993a]. Visible lasers are composed of GaInP/AlGaInP for emission at ~560 to 690 nm (green to red), or ZnCdSe/ZnMgSSe for emission at ~450 to 510 nm (blue to blue-green). The first practical red lasers (continuous wave operation at room temperature) were demonstrated in 1985. The first (prototype) blue-green laser diodes were demonstrated in 1991 [Haase *et al.* 1991, Gunshor *et al.* 1993].

Compared to gas and solid-state lasers, semiconductor lasers have the advantage of smaller size and higher efficiency (typically 30 to 50%, compared to 1% or less), and they can be manufactured in large quantities by using microcircuit fabrication techniques. While several laser diode device geometries have been studied over the past three decades, the majority of manufactured devices are individual *edge-emitting lasers*. A new type of laser diode, the *vertical cavity surface emitting laser* (VCSEL), promises to do for photonics what integrated circuits did for electronics

Figure 1.1 compares a visible edge-emitting laser to a visible VCSEL. The primary differences are the physical size of the resonant cavity, the construction of the mirrors, the geometry of the emission aperture, and the direction and properties of the light emission. For the VCSEL, the resonant cavity is typically 1 to 2λ thick ($\lambda = \lambda_0/n$, where λ_0 is the free space emission wavelength and n is the refractive index), the mirrors are distributed Bragg reflectors (DBRs) (otherwise used in optics as high reflectance coatings), the aperture is lithographically defined on the surface as a circular opening, and the round emission beam is straight-up, perpendicular to the wafer surface. For the edge-emitting laser, the resonant cavity is ~ 1.5 to $5k\lambda$ thick, the mirrors are cleaved facets (along {110} planes), the aperture is intrinsic to the device geometry, and the oval (astigmatic) emission beam is sideways, parallel to the wafer surface. VCSELs have several key advantages over the edge-emitting lasers including: 1) surface normal output, 2) a circular symmetric output beam with Gaussian intensity profile, 3) a low beam divergence ($\leq 7^\circ$ full angle), 4) single wavelength emission (linewidth $< 1 \text{ \AA}$), and 5) ease of manufacture.

One of the major attractions of surface normal emission is the ability to fabricate monolithic two-dimensional (2D) arrays of microlasers, where each laser can be modulated independently. With conventional fabrication technology, vast numbers (hundreds of thousands) of microscopic "points of light" can be defined on a single 2 inch

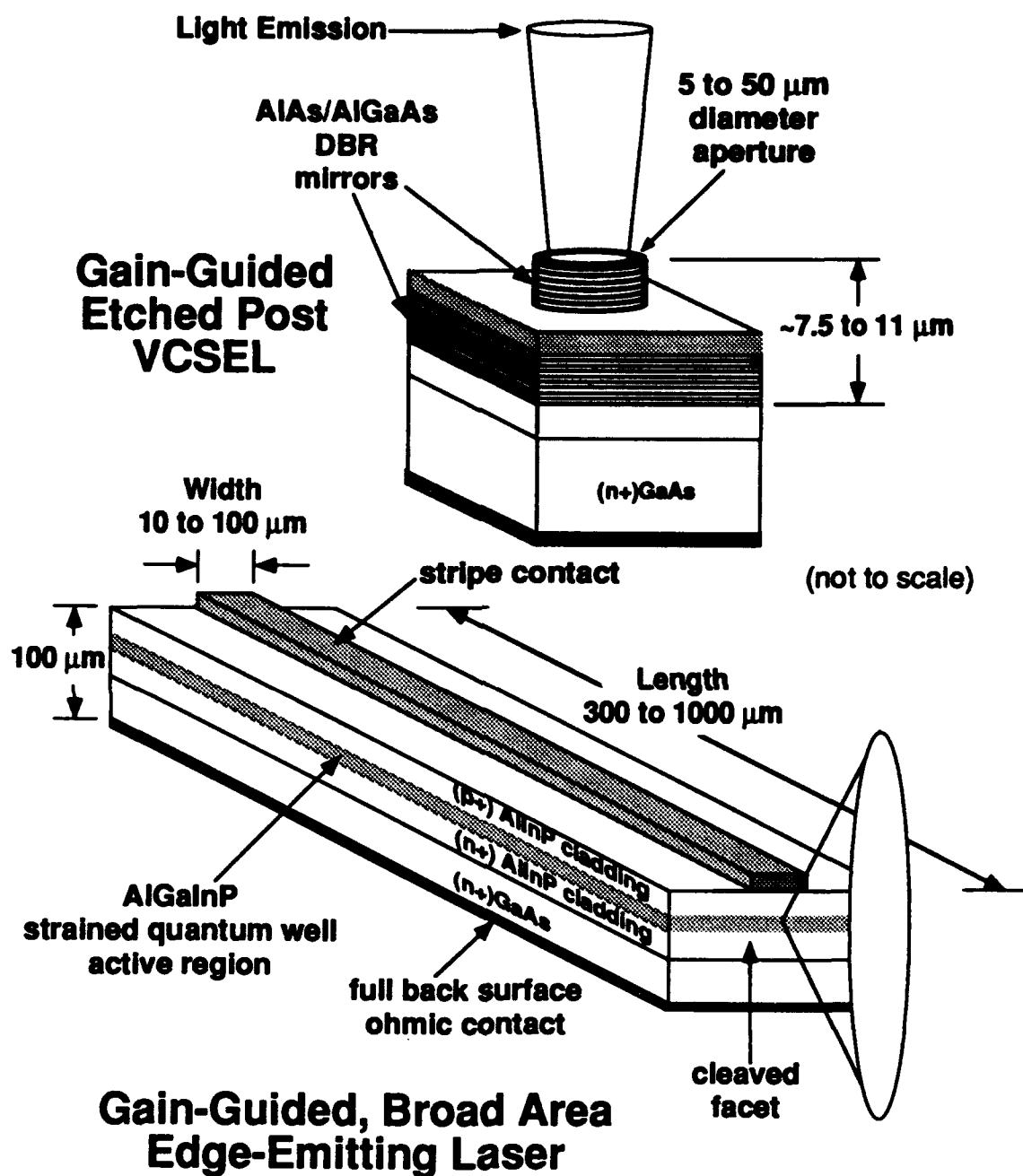


Fig. 1.1 Comparison of visible edge-emitting and vertical cavity surface emitting lasers.

diameter GaAs wafer. The circular output beams are easily coupled into optical fibers, or focused or collimated with microlenslets. The VCSELs can be tested individually at the wafer level, greatly reducing manufacturing costs. Additionally, the as-grown VCSEL is complete and does not require elaborate post fabrication steps. Although the VCSEL structure is more complicated than that of the edge-emitting laser, the critical epitaxial layer compositions and thicknesses are accomplished during growth, whereas only micron sized feature definition is required during device fabrication. The disadvantages of VCSELs, compared to edge-emitting lasers include lower output power, higher temperature sensitivity, and a limited range (~ 0.8 to $1.3\ \mu\text{m}$) of emission wavelengths.

The vertical Fabry-Perot cavity surface emitting laser, later called a VCSEL, was pioneered by a research group at the Tokyo Institute of Technology [Soda *et al.* 1979, Iga *et al.* 1988]. The first device was composed of GaInAsP/InP, with an $\sim 90\ \mu\text{m}$ thick optical cavity and metallic mirrors (the top metal film was semi-transparent). As the structure evolved, quantum well active regions and DBR mirrors were added. This complexity necessitated the use of the more mature GaAs/AlGaAs material system. The first practical GaAs IR VCSELs, emitting at $\lambda_0 \sim 870\ \text{nm}$, were demonstrated in 1988 [Koyama *et al.* 1989]. Recent advances in strained quantum well GaInAs/AlGaAs IR VCSELs emitting at $\lambda_0 \sim 980\ \text{nm}$ include submilliamp threshold current [Geels *et al.* 1990], low threshold voltage (1.49 V) [Lear *et al.* 1993], and high (100 mW) output power [Peters *et al.* 1993]. Additionally, the first practical GaInAsP/InP VCSELs emitting at $1.3\ \mu\text{m}$ were recently demonstrated [Baba *et al.* 1993].

Prior to 1991, published research on shorter wavelength ($\lambda_0 < 800\ \text{nm}$) VCSELs was limited to all-AlGaAs structures, where the active regions were composed of GaAs/AlAs multiple quantum wells or short period superlattices [Gourley and Drummond 1987, Lee *et al.* 1991]. However, the efficiency of an all-AlGaAs active region greatly diminishes for emission below $\sim 770\ \text{nm}$ due to nonradiative

recombination and poor carrier confinement. A more efficient choice for visible (red) emission is AlGaInP active regions. Shorter wavelengths are desirable, for example, because the storage density of optical discs increase as the measurement wavelength decreases. Shorter wavelengths are also important for visual applications. As shown in Fig. 1.2, the human eye is increasingly sensitive to shorter red wavelengths. The eye sensitivity to emission at 640 nm is 10 times that at 680 nm, and the sensitivity at 630 nm is ~70 times that at 700 nm. For applications such as barcode readers or projection displays, much lower output powers can be used with lasing emission at the shorter wavelengths, while maintaining equal receptor response. Other potential applications for visible (620 to 690 nm) AlGaInP VCSELs include low cost plastic fiber communications, optical interconnections and computing, distance measurements, holographic memories, medical diagnostics, and high resolution printing.

The focus of this dissertation is the design, fabrication, and characterization of visible (620 to 690 nm) VCSELs, composed of AlGaInP quantum well optical cavity active regions, and surrounded by AlGaAs and AlGaInP DBRs. The development of AlGaInP visible VCSELs is very materials and growth intensive. The proper design of visible VCSELs requires a full understanding of the optical, electrical, and thermal properties of the constituent materials. Whereas the properties and optimal growth conditions of AlGaAs have been extensively studied, the epitaxial growth and properties of AlGaInP materials and devices remains a very active and relatively new area of semiconductor materials research. The epitaxial structures described in this dissertation, unless noted, were grown by metalorganic vapor phase epitaxy (MOVPE) at Sandia National Laboratories under the direction of R. P. Schneider, Jr. Highlights of the initial ground breaking studies on the growth and properties of AlGaInP bulk and quantum well

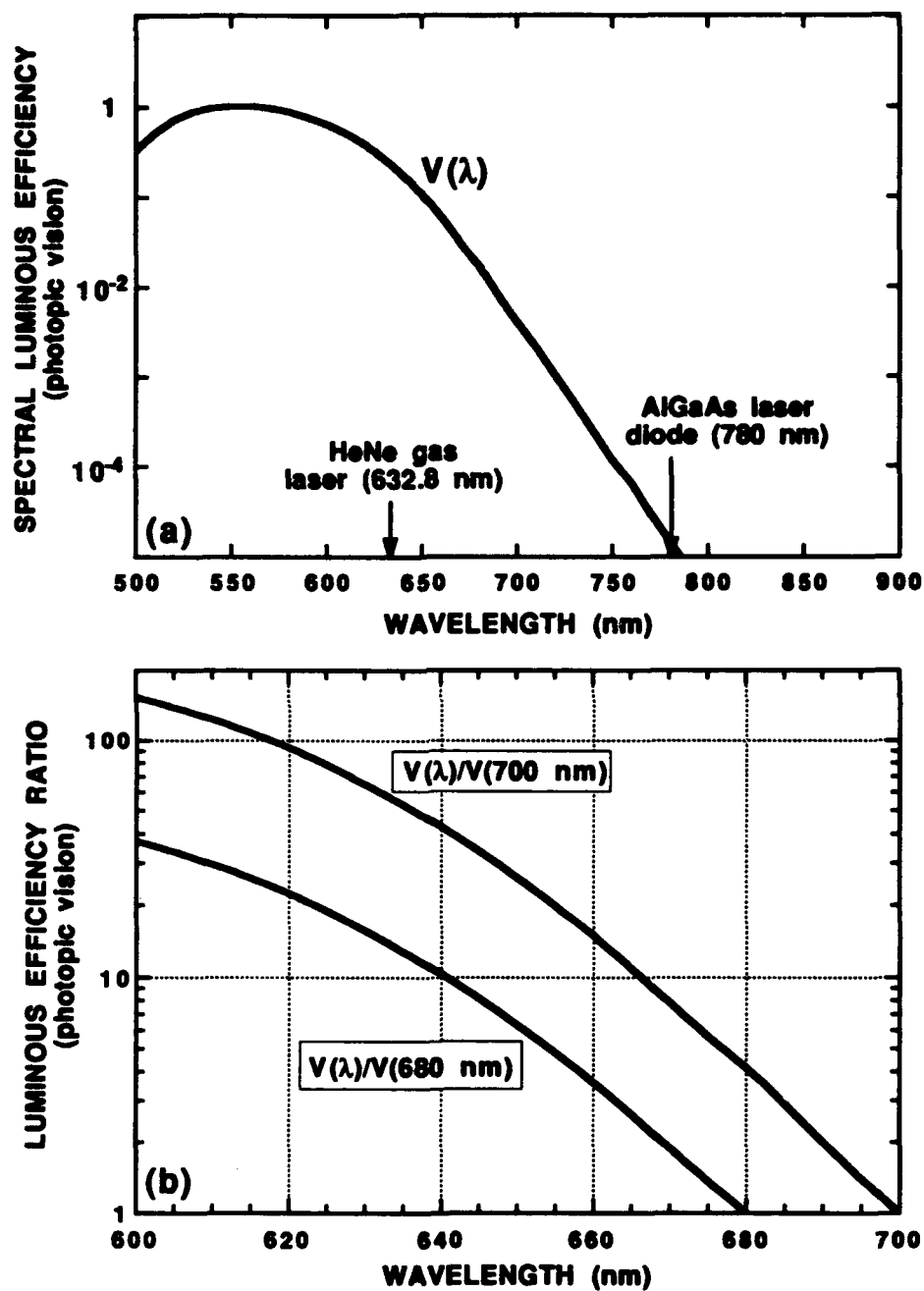


Fig. 1.2 (a) Relative response of the human eye to visible wavelengths, and (b) relative eye response, divided by the eye response at 680 and 700 nm. For the "red" portion of the spectrum (~610 to 780 nm), the eye is increasingly sensitive to shorter wavelengths. Data from Wyszecki and Stiles [1982].

structures, and on AlGaInP and AlGaAs DBRs for visible photonic applications, appear in some of the figures in Chapter 2 and Appendix A.

The dissertation is organized as follows. Chapter 2 overviews the device physics and design of AlGaInP visible VCSELs and related structures. Chapter 3 presents data on undoped, optically pumped visible VCSELs with both AlGaAs and AlGaInP DBRs. The design and spectral characteristics of a new type of microcavity device, the resonant cavity light emitting diode (RCLED), are presented in Chapter 4. Chapter 5 contains the characteristics of the electrically injected visible VCSEL diodes. Finally, a summary of the research results and suggestions for future work are given in Chapter 6.

References for Chapter 1

Agrawal, G. P., and N. K. Dutta, *Long-Wavelength Semiconductor Lasers*, (Van Nostrand Reinhold:New York, 1986).

Baba, T., Y. Yogo, K. Suzuki, F. Koyama, and K. Iga, "Near Room Temperature Continuous Wave Lasing Characteristics of GaInAsP/InP Surface Emitting Laser", *Electronics Letters*, 29(10), p. 913-914 (13 May 1993).

Casey, Jr., H. C., and M. B. Panish, *Heterostructure Lasers*, (Academic Press:San Diego, 1978).

Geels, R. S., S. W. Corzine, J. W. Scott, D. B. Young, and L. A. Coldren, "Low Threshold Planarized Vertical-Cavity Surface-Emitting Lasers", *IEEE Photonics Technology Letters*, 2(4), p. 234-236 (April 1990).

Gourley, P. L., and T. J. Drummond, "Visible, Room-Temperature, Surface-Emitting Laser Using an Epitaxial Fabry-Perot Resonator With AlGaAs/AlAs Quarter-Wave High Reflectors and AlGaAs/GaAs Multiple Quantum Wells", *Applied Physics Letters* 50(18), p. 1225-1227 (4 May 1987).

Gunshor, R. L., N. Otsuka, and A. V. Nurmikko, "Blue Lasers on the Horizon", *IEEE Spectrum*, p. 28-33 (May 1993).

Haase, M. A., J. Qiu, J. M. DePuydt, and H. Cheng, "Blue-Green Laser Diodes", *Applied Physics Letters*, 59(11), p. 1272-1274 (9 September 1991).

Hecht, J., "Semiconductor Diode Lasers Span the Rainbow", *Laser Focus World*, p. 199-211 (April 1993a).

Hecht, J., "Gallium Arsenide Lasers Offer an Array of Options", *Laser Focus World*, p. 83-92 (July 1993b).

Iga, K., F. Koyama, and S. Kinoshita, "Surface Emitting Semiconductor Lasers", *IEEE Journal of Quantum Electronics*, 24(9), p. 1845-1855 (September 1988).

Koyama, F., S. Kinoshita, and K. Iga, "Room-Temperature Continuous Wave Lasing Characteristics of a GaAs Vertical Cavity Surface-Emitting Laser", *Applied Physics Letters*, 55(3), p. 221-222 (17 July 1989).

Lear, K. L., S. A. Chalmers, and K. P. Killeen, "Low Threshold Voltage Vertical Cavity Surface Emitting Lasers", *Electronics Letters*, 29, p. 584-586 (1993).

Lee, Y. H., B. Tell, K. F. Brown-Goebeler, R. E. Leibenguth, and V. D. Mittera, "Deep-Red Continuous Wave Top-Surface-Emitting Vertical-Cavity AlGaAs Superlattice Lasers", *IEEE Photonics Technology Letters*, 3(2), p. 108-109 (1991).

Peters, F. H., M. G. Peters, D. B. Young, J. W. Scott, B. J. Thibeault, S. W. Corzine, and L. A. Coldren, "High-Power Vertical-Cavity Surface-Emitting Lasers", *Electronics Letters* 29(2), p. 200-201 (21 January 1993).

Siegman, A. E., *Lasers*, (University Science Books: Mill Valley, California, 1986).

Soda, H., K. Iga, C. Kitahara, and Y. Suematsu, "GaInAsP/InP Surface Emitting Injection Lasers", *Japanese Journal of Applied Physics*, 18(12), p. 2329-2330 (December 1979).

Wyszecki, G., and Stiles, W. S., *Color Science*, 2nd ed., (Wiley:New York, 1982).

Chapter 2 Physics of Visible Resonant Cavity Photonic Devices

2.1 Introduction

This chapter outlines the design of visible (620 to 690 nm) vertical cavity surface emitting lasers (VCSELs) and related resonant cavity photonic devices. For our purposes, visible VCSELs consist of an AlGaInP quantum well optical cavity active region, surrounded by either AlGaAs or AlGaInP distributed Bragg reflectors (DBRs). In contrast, the widely studied (conventional) infrared (IR) VCSELs typically consist of GaInAs or GaAs quantum well active regions, surrounded by AlGaAs DBRs. The useful design equations are drawn from standard references on thin-film optical coatings, and from the last decade of published research on IR VCSELs. Several example structures are analyzed in detail. These structures provide insight into the research methodology and experimental results presented in Chapters 3, 4, and 5. While the basic design principles of IR VCSELs have been treated elsewhere [Iga *et al.* 1988, Jewell *et al.* 1991], this is the first comprehensive design review of visible VCSELs.

The Chapter organization is as follows. Section 2.2 is a general overview, and includes a comparison between visible VCSELs and visible edge emitting lasers. Next in Section 2.3, AlGaInP optical cavity active regions are presented. This is followed by a discussion of distributed Bragg reflectors (DBRs) for visible photonics applications in Section 2.4. Here, some example DBRs, grown by metalorganic vapor phase epitaxy (MOVPE), are analyzed in detail. In Section 2.5, some general properties of multilayer Fabry-Perot etalons are reviewed. This structure, consisting of an optical cavity

surrounded by DBR mirrors, is the *optical basis* for VCSELs. Section 2.6 contains some design considerations for complete visible VCSEL structures including trade-offs between DBR doping, quantum well gain and placement in the optical cavity, cavity losses, and temperature effects. A comparison between conventional IR and visible VCSELs is also included. Finally, the chapter conclusions are given in Section 2.7.

2.2 Visible VCSEL Overview

Figure 2.1 is a schematic diagram of a general visible (620 to 690 nm) VCSEL structure. The structure is grown by MOVPE on a GaAs substrate, and can be divided into three optical blocks: 1) an optical cavity active region; 2) a top DBR mirror, and; 3) a bottom DBR mirror. For VCSEL diodes, the DBRs and the adjacent optical cavity active regions are doped n and p-type. Since GaAs is highly absorbing at the wavelengths of interest, the reflectance of the bottom DBR is made ~100% and emission is through a top coupling DBR. The thickness of the optical cavity is typically ~200 to 400 nm, although some devices use cavities as thick as ~1.5 μm . The thickness of the top (output coupling) DBR is typically ~3 to 4 μm , while the thickness of the bottom DBR (high reflector) is typically ~4 to 6 μm . The VCSEL is essentially a very high finesse (defined later), asymmetric Fabry-Perot (etalon) resonant cavity designed for lasing operation at λ_o , the design wavelength.

An important characteristic of the optical cavity (for normal incidence) is the phase factor δ_{oc} , given by [MacLeod 1989]

$$\delta_{oc} = \frac{2 \pi N d_{oc}}{\lambda_o} \quad (\text{radians}) \quad (2.1)$$

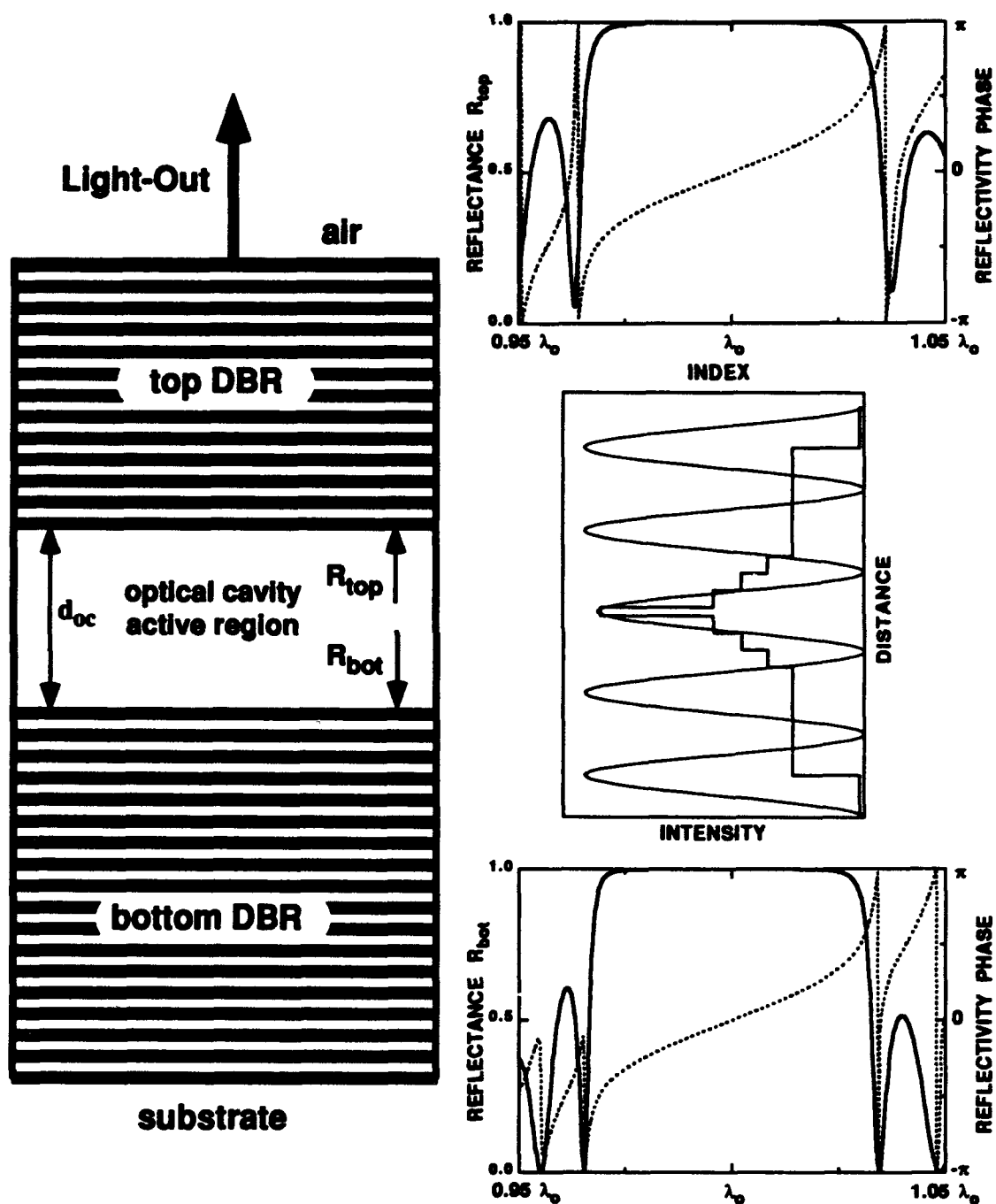


Fig. 2.1 Schematic diagram of an all semiconductor visible VCSEL. Also shown is the DBR reflectance and reflectivity phase, as seen from the optical cavity, and the electric field intensity on resonance and refractive index profile in the optical cavity.

where N is the complex index of refraction, and d_{oc} is the physical thickness. A complex phase factor corresponds to absorption in the medium. Twice the phase factor is the phase shift for a round trip pass in the optical cavity. If $d_{oc} = u\lambda_0/2N$, with $u = 1, 2, 3, \dots$, then $2\delta_{oc} = 2\pi$. This phase plus the DBR mirror phases should be 2π at λ_0 (thus satisfying the modal condition for lasing). Included in Fig. 2.1 is a plot of a standing wave pattern (on resonance) overlapping a single $\text{Ga}_{0.48}\text{In}_{0.52}\text{P}$ quantum well that is centered in the optical cavity. The position of the quantum well(s) relative to the standing wave peaks (antinodes) is a critical design parameter. This is discussed in more detail in Section 2.6. The important characteristics of the DBRs include the reflectances R_{top} and R_{bottom} (as seen from the optical cavity), and the reflectivity phases (ϕ), all of which are functions of wavelength. Included in Fig. 2.1 are example DBR reflectance and reflectivity phase characteristics.

It is useful to examine the gain length, required threshold gain, required reflectance, and the number of modes of VCSELs, as compared to standard edge-emitting lasers. For edge-emitting lasers at threshold, the round trip cavity gain equals the round trip cavity loss, such that [Casey and Panish 1978]

$$\Gamma g_{th} = \alpha_i + \frac{1}{L} \ln[1/R] \quad (\text{cm}^{-1}) \quad (2.2)$$

where Γ is the confinement factor, g_{th} is the gain required at threshold, α_i is the internal cavity loss coefficient, L is the gain length, and $R = \sqrt{R_1 R_2}$ is the reflectance of the two facets. For an AlGaInP stripe geometry gain-guided edge-emitting laser emitting at $\lambda_0 = 650 \text{ nm}$, with uncoated cleaved facets, $R = 0.32$ ($n \sim 3.6$). The gain length is equal to the device length, and is typically $300 \mu\text{m}$ to $1000 \mu\text{m}$. For growth in the z direction, the confinement factor $\Gamma = \Gamma_x \Gamma_y \Gamma_z$, where Γ_y and Γ_z are the transverse (lateral) confinement factors, and Γ_x is the longitudinal confinement factor. For a typical AlGaInP broad area

edge-emitter with a single 10 nm thick $\text{Ga}_{0.5}\text{In}_{0.5}\text{P}$ quantum well, $\Gamma_y \approx 0.04$ [Bour *et al.* 1993], and $\Gamma_x = \Gamma_z \approx 1$. Ignoring cavity loss and using Eq. (2.2) with $L = 500 \mu\text{m}$, $R = 0.32$, and $\Gamma = 0.04$, the gain at threshold is $g_{\text{th}} \approx 570 \text{ cm}^{-1}$, and the modal gain (Γg_{th}) required at threshold is $\sim 23 \text{ cm}^{-1}$. This value can be reduced by using a high reflectance coating on one of the facets. The edge-emitter has several longitudinal modes, separated by $\Delta\lambda = \lambda_0^2/2nL \approx 0.117 \text{ nm}$ [Saleh and Teich 1991]. If the spectral gain width from the active region is 15 nm, then over 125 longitudinal modes may oscillate.

An equation similar to Eq. (2.2) for VCSELs is [after Corzine *et al.* 1989]

$$\Gamma_r g_{\text{th}} d = \alpha_i L + \alpha_m L_m + \alpha_{\text{oc}}(d_{\text{oc}} - L) + \ln[1/R] \quad (\text{unitless}) \quad (2.3)$$

with

$$\alpha_i = \Gamma_z \alpha_a + (1 - \Gamma_z) \alpha_p + \alpha_{\text{scat}} \quad (\text{cm}^{-1}) \quad (2.4)$$

where $0 \leq \Gamma_r \leq 2.0$ is the relative confinement factor, d is the total thickness of the active layer(s), L is the physical thickness of the standing wave that overlaps the quantum well(s), L_m is the penetration length of the mode into the DBR mirrors, α_m is scattering/absorption loss within the DBRs, α_a is the free carrier loss within the quantum wells, α_p is the free carrier loss within the passive layers, and α_{scat} is scattering loss throughout the cavity due to sidewall roughness. The term $\alpha_{\text{oc}}(d_{\text{oc}} - L)$ accounts for the passive absorptive losses in an extended optical cavity (i.e. when the optical cavity thickness $d_{\text{oc}} > \lambda/2$). For VCSELs with diameters $> 5 \mu\text{m}$ and growth direction along the

z-axis, $\Gamma_x = \Gamma_y \approx 1$ (transverse confinement). The longitudinal confinement factor Γ_z is given by [Corzine *et al.* 1989]

$$\Gamma_z = \frac{\int_{\text{active layer}} E^2(z) dz}{\int_L E^2(z) dz} \quad (\text{unitless}) \quad (2.5)$$

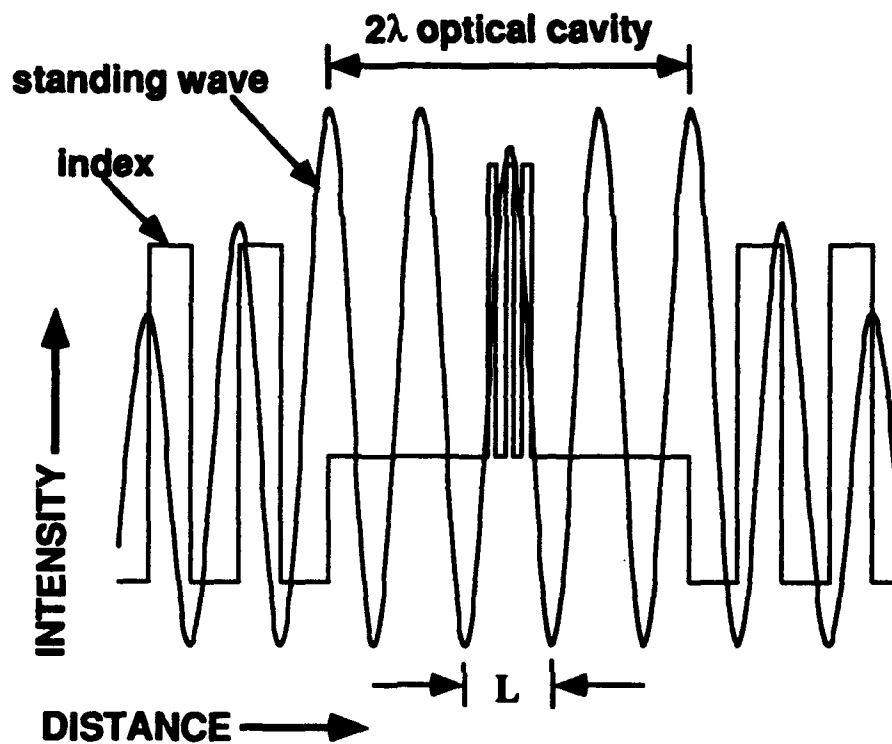
where the relative confinement factor is defined from

$$\Gamma_z \equiv \frac{d}{L} \Gamma_r \quad (\text{unitless}) \quad (2.6)$$

The longitudinal confinement factor is illustrated in Fig. 2.2. For a single $d = 10$ nm thick $\text{Ga}_{0.48}\text{In}_{0.52}\text{P}$ quantum well visible VCSEL structure designed for $\lambda_0 \approx 650$ nm, $\Gamma_z = 0.2145$ and $L = 90$ nm (found numerically, see Appendix C), thus $\Gamma_r = 1.93$. Using these values with $g_{\text{th}} \approx 570 \text{ cm}^{-1}$ in Eq. (2.3) and ignoring loss, a value of $R = 0.9989$ is required to balance the equation. For the VCSEL, $R = \sqrt{R_{\text{top}} R_{\text{bottom}}}$. Since emission is desired out the top DBR, the reflectance of the bottom DBR is made $R_{\text{bottom}} = 0.9999$ (~ 1.0). Thus, the reflectance of the top DBR must be $R_{\text{top}} = 0.9979$ to reach threshold with the given g_{th} . The modal gain ($\Gamma_z g_{\text{th}}$) required to reach threshold in this example calculation is $\sim 122 \text{ cm}^{-1}$.

The separation of Fabry-Perot modes in the VCSEL is given approximately by the effective free spectral range (FSR) [Jewell *et al.* 1988, Yeh 1988, Kishino *et al.* 1991]

$$\text{FSR} \approx \frac{\lambda_0^2}{2 n_{\text{cav}} L_{\text{eff}}} \quad (\text{nm}) \quad (2.7)$$



$$\Gamma_z = \frac{\int_{\text{active layers}} E^2(z) dz}{\int_L E^2(z) dz} = \frac{\text{(quantum well area beneath central standing wave)}}{\text{(area beneath central standing wave)}}$$

The equation shows the confinement factor Γ_z as the ratio of the integral of the electric field squared over the active layers to the integral over the entire cavity length L . To the right, the numerator is visually represented by three thin horizontal bars, labeled "(quantum well area beneath central standing wave)". The denominator is represented by a wide, dark triangular shape, labeled "(area beneath central standing wave)".

Fig. 2.2 Illustration of the longitudinal confinement factor for an example multiple quantum well VCSEL.

where n_{cav} is the average refractive index of the optical cavity, and

$$L_{\text{eff}} = \ell_{\text{ptop}} + \ell_{\text{pbottom}} + d_{\text{oc}} \quad (\text{nm}) \quad (2.8)$$

is the effective cavity length. The effective cavity length is determined by the penetration depths of the standing wave into the two DBRs [Babic and Corzine 1991], and the optical cavity thickness d_{oc} as given in Eq. (2.1). The penetration depth at normal incidence is found from [Jewell *et al.* 1988]

$$\ell_p = \frac{\lambda_o^2}{4 \pi n_{\text{cav}}} \frac{d\phi}{d\lambda_o} \quad (\text{nm}) \quad (2.9)$$

where $d\phi/d\lambda_o$ is the slope of the DBR reflectivity phase at λ_o . As shown in Fig. 2.1, this slope is \sim linear at and around λ_o . For the example VCSEL structure with $d_{\text{oc}} = 2\lambda$ (~ 406 nm) and $\ell_{\text{ptop}} = \ell_{\text{pbottom}} \approx 561$ nm ($d\phi/d\lambda_o = 0.0534$ radian/nm), then $L_{\text{eff}} \approx 1.53$ μm . Then by using Eq. (2.7) with $\lambda_o = 650$ nm and $n_{\text{cav}} = 3.2$, the free spectral range $\text{FSR} \approx 43$ nm. With a quantum well spectral gain width of 15 nm, only one longitudinal mode may oscillate.

2.3 AlGaInP Optical Cavity Active Regions

Optical cavity active regions consist of gain layers, such as quantum wells, surrounded by cladding (larger energy bandgap) spacer layers. The total optical thickness of the layers is designed to be a multiple of a half wavelength $\lambda_o/2$, where λ_o is the wavelength on resonance (i.e. the design wavelength). Thus

$$\sum_{\ell=1}^N n_{\ell} d_{\ell} = \frac{u \lambda_0}{2}, \quad u = 1, 2, 3, \dots \quad (\text{nm}) \quad (2.10)$$

where n_{ℓ} is the (real) index of refraction of layer ℓ at λ_0 , d_{ℓ} is the physical thickness of layer ℓ , u is an integer, and N is the number of layers. Except for the quantum wells, the layers are non or nearly nonabsorbing at λ_0 , by design. For this reason, Eq. (2.10) is useful for estimating the physical thickness required of layers in an optical cavity active region. A full accounting of absorption and other loss mechanisms, for example via the complex indices of refraction (N) for the absorptive layers, is best accomplished by numerical computation (see Appendix C).

The advantages of using strained quantum wells are well known [Yablonovitch and Kane 1986, 1988, Zory 1993, Bour 1993b]. In strained quantum wells, the heavy- and light-hole valence band degeneracy is lifted at $k = 0$ (the Γ point in reciprocal space). For $\text{Ga}_{1-x}\text{In}_x\text{P}$ quantum wells in biaxial compression (i.e. $0.5 < x \leq 1.0$), the energy bandgap increases due to the strain, but it also decreases due to the change in ternary composition, as compared to $\text{Ga}_{0.5}\text{In}_{0.5}\text{P}$ lattice matched material. The net result is a decrease in the energy bandgap. With compressive or no strain, the upper valence band is the heavy-hole band, with a heavy effective mass in the direction perpendicular to the plane of the interfaces (used to calculate the energies of the quantized states), and a lighter effective mass in the direction parallel to the growth interfaces (used to calculate the density of states) [Coleman 1993]. It is the lighter (parallel or in-plane) effective mass that affects optical gain and thus threshold current density. The smaller effective mass results in a smaller density of states (DOS) and thus a smaller transparency carrier density. Also, the peak optical gain is reached at a lower injected carrier density [Lau 1993].

Figure 2.3 is a plot of the calculated peak emission wavelength versus quantum well thickness for single $\text{Ga}_{0.5}\text{In}_{0.5}\text{P}$ (~unstrained) and $\text{Ga}_{0.44}\text{In}_{0.56}\text{P}$ (~0.56% compressive

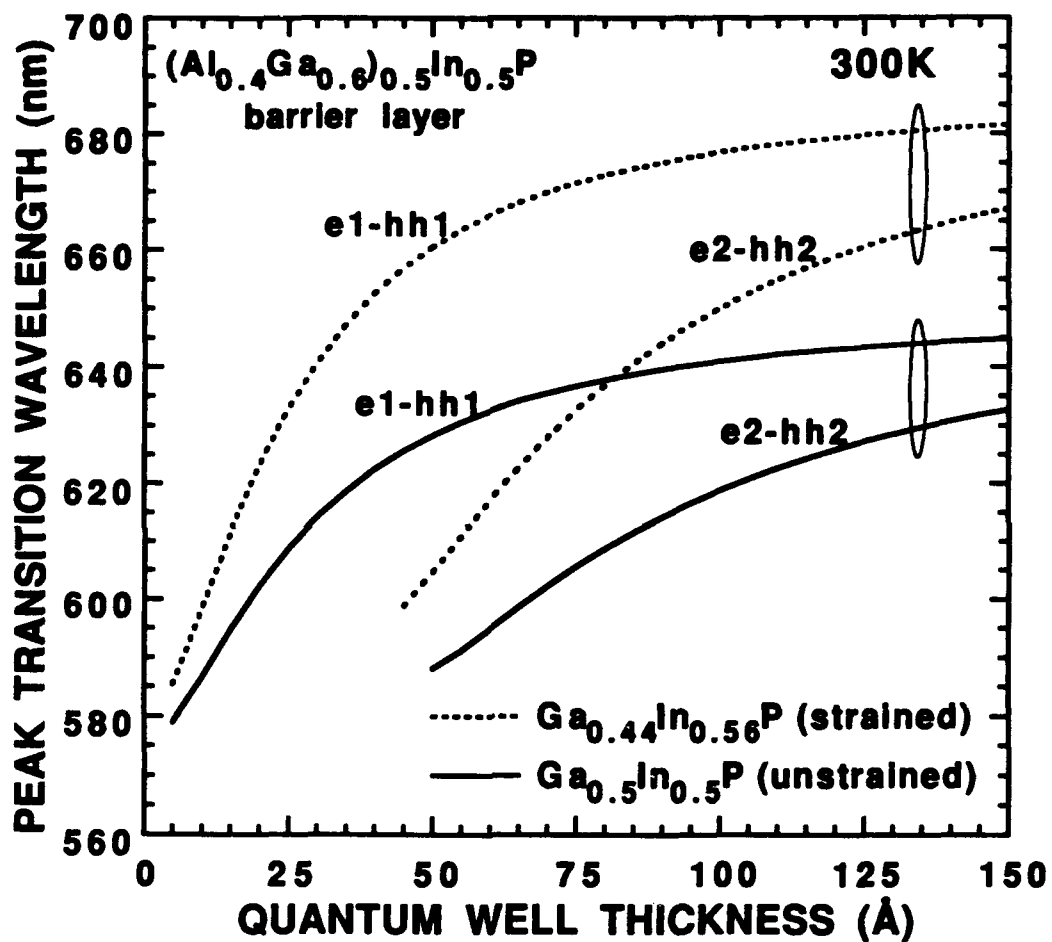


Fig. 2.3 Calculated peak transition wavelengths against quantum well thickness.

strain) quantum wells surrounded by $(\text{Al}_{0.4}\text{Ga}_{0.6})_{0.5}\text{In}_{0.5}\text{P}$ barrier layers. (The data values used for the calculation are given in Appendix A, where $\Delta E_c = 0.6\Delta E_g$). The emission for the unstrained well approaches ~650 nm as the well thickness approaches infinity (bulk value). This plot demonstrates that the ~630 to 680 nm wavelength emission range is readily achieved with 6 to 10 nm thick wells by varying the amount of compressive strain.

Figure 2.4 is room temperature photoluminescence (PL) data from three different strained quantum well optical cavity active regions. In each case, three ~10 nm thick quantum wells are separated by ~10 nm thick $(\text{Al}_{0.4}\text{Ga}_{0.6})_{0.5}\text{In}_{0.5}\text{P}$ barrier layers, and surrounded by $(\text{Al}_y\text{Ga}_{0.5-y})_{0.5}\text{In}_{0.5}\text{P}$ with $y \approx 0.4$, stepped to $y = 0.7$ in 20 nm thick $\Delta y = 0.1$ incremental steps. The triple $\text{Ga}_{1-x}\text{In}_x\text{P}$ quantum well compositions are $x \approx 0.56$, 0.54, and 0.52 with peak PL emission at 675, 664, and 653 nm, respectively. These structures were grown on (100) GaAs substrates, misoriented 6° toward the nearest $\langle 111 \rangle_A$, at ~775 °C (see Appendix A and B).

The strained quantum wells described above must be below a certain critical thickness. This insures that the strain is accommodated by elastic deformation, rather than by the formation of misfit dislocations which degrade optical efficiency. Figure 2.5 shows the calculated critical layer thickness for a single $\text{Ga}_{1-x}\text{In}_x\text{P}$ ($0.50 \leq x \leq 0.58$) epitaxial layer grown on a GaAs substrate, as a function of composition [Ozasa *et al.* 1990]. This plot shows the results from the Matthews & Blakeslee (force-balancing) model for a single strained epitaxial layer grown on an infinite substrate, and for a single quantum well layer surrounded by infinite and semi-infinite lattice-matched layers. Also shown is the result from the People & Bean (energy-balancing) model. This data represents a first-order design criterion. For multiple strained quantum well (MQW) active regions an effective strain can be used, as outlined by Vawter and Myers [1989].

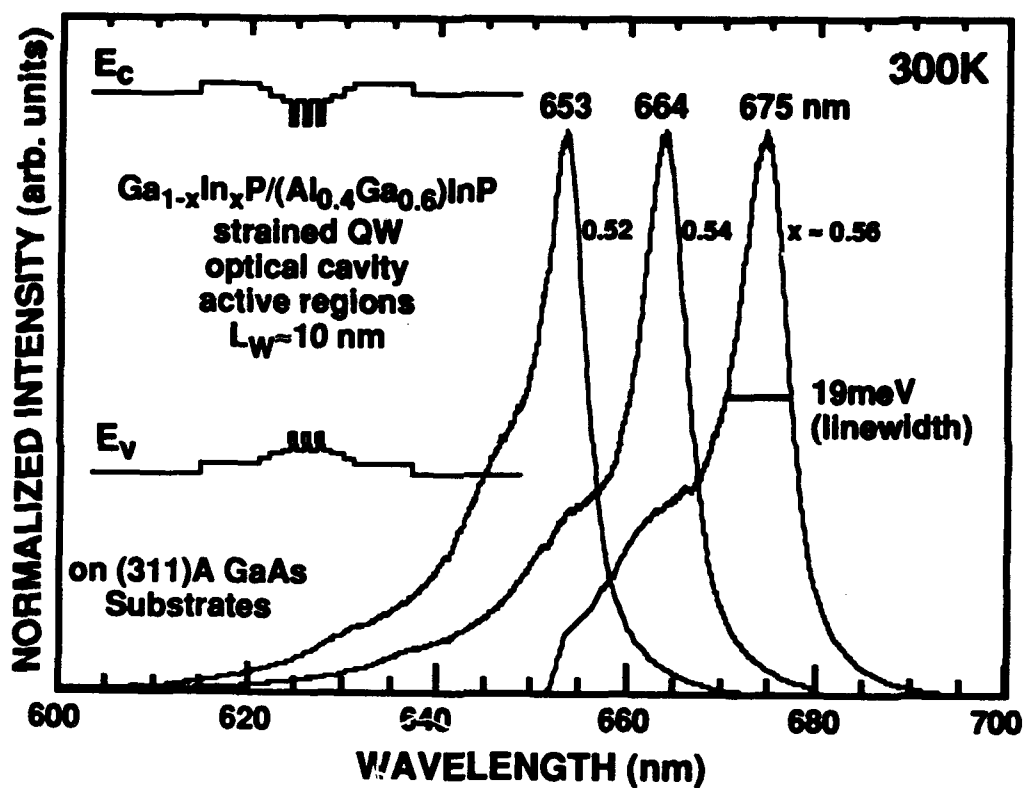


Fig 2.4 Photoluminescence intensity of three example step-graded barrier, separate confinement heterostructure (SCH), optical cavity active regions. The strain in the quantum wells is increased, leading to increased emission wavelength, by increasing x from 0.52, to 0.54, and finally to 0.56. Unpublished data [Schneider 1993].

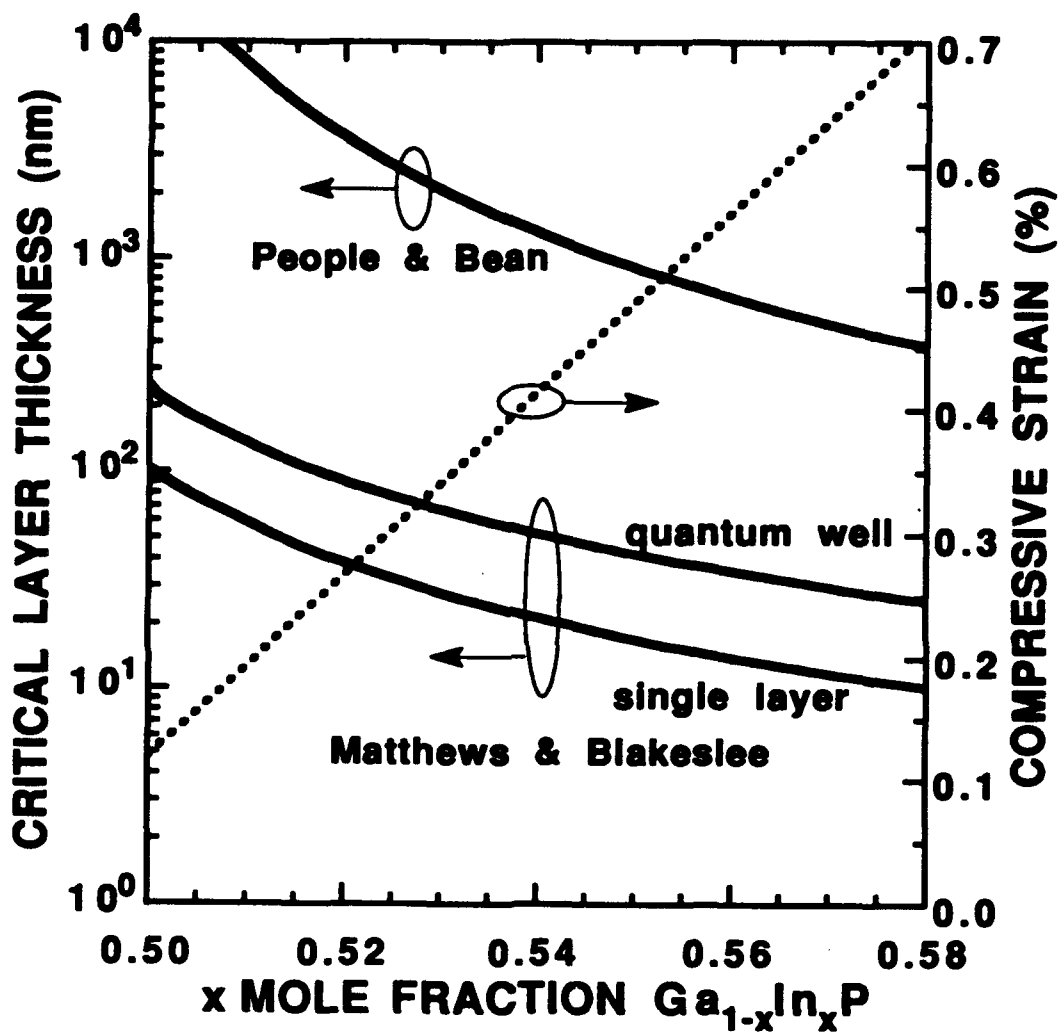


Fig 2.5 Critical layer thickness and the corresponding compressive strain against $\text{Ga}_{1-x}\text{In}_x\text{P}$ composition. The strain is relative to the lattice constant of GaAs.

2.4 Distributed Bragg Reflectors

Distributed Bragg reflectors (DBRs) are periodic layered structures consisting of alternating quarter wave ($\lambda/4$) layers of low (L) and high (H), usually non or nearly nonabsorbing, refractive index material [Yeh 1988, MacLeod 1989]. The physical thickness (d_ℓ) of a $\lambda/4$ layer ℓ is given by

$$d_\ell = \frac{\lambda_0}{4 n_\ell} \quad (\text{nm}) \quad (2.11)$$

where n_ℓ is the real refractive index of layer ℓ . The optical thickness of layer ℓ is $d_\ell n_\ell$. Since n_ℓ is a function of wavelength, the layer ℓ is a quarter-wave thick only at λ_0 . The DBR structures exhibit resonance reflection of electromagnetic waves, in a manner similar to the diffraction of x-rays by crystal planes, hence the name. While thin metallic layers can also act as moderate to high reflectors, the metals absorb a significant portion of the incident light and are thus too lossy for most VCSEL applications. Dielectric DBRs have been used as multilayer optical interference filters for many years. The first semiconductor DBR, composed of GaAs and $\text{Al}_{0.3}\text{Ga}_{0.7}\text{As}$ $\lambda/4$ layers, was grown by molecular beam epitaxy [van der Ziel 1975, 1976]. Since this early demonstration, many groups have reported III-V compound semiconductor and dielectric DBRs for photonic device applications [Gourley *et al.* 1986a, 1986b, Thornton *et al.* 1984, Tai *et al.* 1990, Choa *et al.* 1991, and many others].

Shown in Fig. 2.6 is a schematic of an all semiconductor DBR high reflector. An incident ray and some of the resulting multiple reflections are traced through part of the structure. At each interface within the structure the same fraction of light intensity is reflected. Light reflected in an H layer undergoes a 0 radian phase shift, whereas light reflected in an L layer undergoes a π radian phase shift. At the Bragg design wavelength,

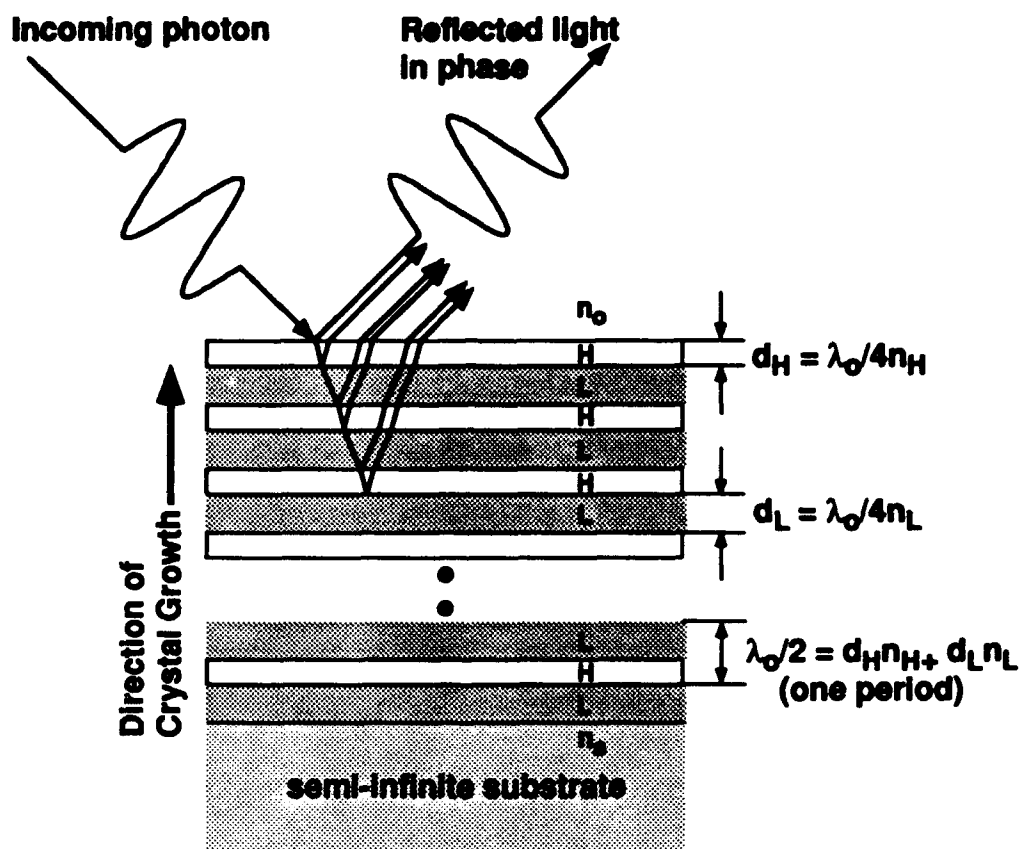


Fig. 2.6 Schematic diagram of a quarter-wave distributed Bragg reflector. An incident wave is shown propagating through the stack, along with some of the primary and higher order reflected waves. High reflectivity is obtained if the resultant reflections are in phase.

the components of light resulting from the multiple reflections recombine constructively (in phase) at the front surface. The sum of the reflected wave magnitudes increases toward the value of the incident wave magnitude as the number of quarter wave layers increases. The reflectance (R) at λ_0 for the structure in Fig. 2.6, neglecting absorption, at normal incidence is [Yeh 1988]

$$R_{2N_p} = \left[\frac{1 - (n_s/n_o)(n_1/n_2)^{2N_p}}{1 + (n_s/n_o)(n_1/n_2)^{2N_p}} \right]^2 \quad (\text{unitless}) \quad (2.12)$$

where N_p is the number of DBR periods, n_1 ($= n_H$) is the top $\lambda/4$ layer, and n_2 is the subsequent $\lambda/4$ layer ($= n_L$), and this HL sequence repeats N_p times. A DBR period is defined as one pair of LH (or HL) $\lambda/4$ layers. Equation (2.12) indicates that the reflectance increases as both the ratio n_1/n_2 and number of periods N_p increases, and is equally valid if the L and H layers are switched. If an extra half DBR period is added to the stack, such that the sequence becomes LHLH. . . LHL or HLHL. . . HLH, then the reflectance is [Born and Wolfe 1975]

$$R_{2N_p+1} = \left[\frac{1 - (n_1/n_o)(n_1/n_s)(n_1/n_2)^{2N_p}}{1 + (n_1/n_o)(n_1/n_s)(n_1/n_2)^{2N_p}} \right]^2 \quad (\text{unitless}) \quad (2.13)$$

where as before, n_1 is the uppermost $\lambda/4$ layer. Note that the number of DBR periods in Eq. (2.13) for a given N_p is actually $N_p + 0.5$.

For common VCSEL diodes, current injection is through doped DBR material layers. The conduction and/or valence energy band offsets at each interface, if too large, significantly add to device series resistance. Various interface grading schemes have been effectively employed to reduce this resistance [Tai *et al.* 1990, Chalmers *et al.* 1993]. Although the DBR reflectance decreases when part of each $\lambda/4$ layer is compositionally

varied, adding additional DBR periods can make up the difference. This aspect of DBR design for VCSELs is discussed in more detail in Section 2.6. For VCSELs, the DBR optical parameters of most interest are the reflectance bandwidth, the reflectivity phase dispersion, the phase penetration length, the losses (absorptive, scatter), and the number of periods required to reach a certain reflectance at λ_0 .

2.4.1 Reflectance Measurement Set-Up

A schematic of the set-up for reflectance measurements of epitaxial DBR and VCSEL structures is shown in Fig. 2.7. A broad band white light source is focused onto the material surface at a zero angle of incidence. The reflected light returns through the focusing lens and is directed into an optical multi-channel spectrum analyzer (i.e. a grating spectrometer with a charge-coupled device detector array). The lens magnification is typically 10x or 5x with a numerical aperture (NA) of 0.21 or 0.18, respectively. Thus, the lens accepts reflected light within a 24° cone, and some minor smearing of the reflectance spectrum is expected. The measured reflectance is normalized to a dielectric mirror standard (>99.9% reflectance at visible wavelengths) to correct for the system response. The resultant reflectance spectrum is semi-quantitative since relative rather than exact values for the reflectance are measured. However, this measurement set-up provides a fast method to characterize DBR and VCSEL structures, returning the essential spectral features such as the Fabry-Perot resonance dip position (discussed below) relative to the mirror center, and the reflectance bandwidth. The system is also used as a probe station to measure the electroluminescence spectra of fabricated devices.

2.4.2 AlGaAs DBRs for Visible Photonics

The refractive index of $\text{Al}_x\text{Ga}_{1-x}\text{As}$ increases with decreasing wavelength, and with decreasing AlAs mole fraction. Thus, the higher the energy bandgap, the lower the

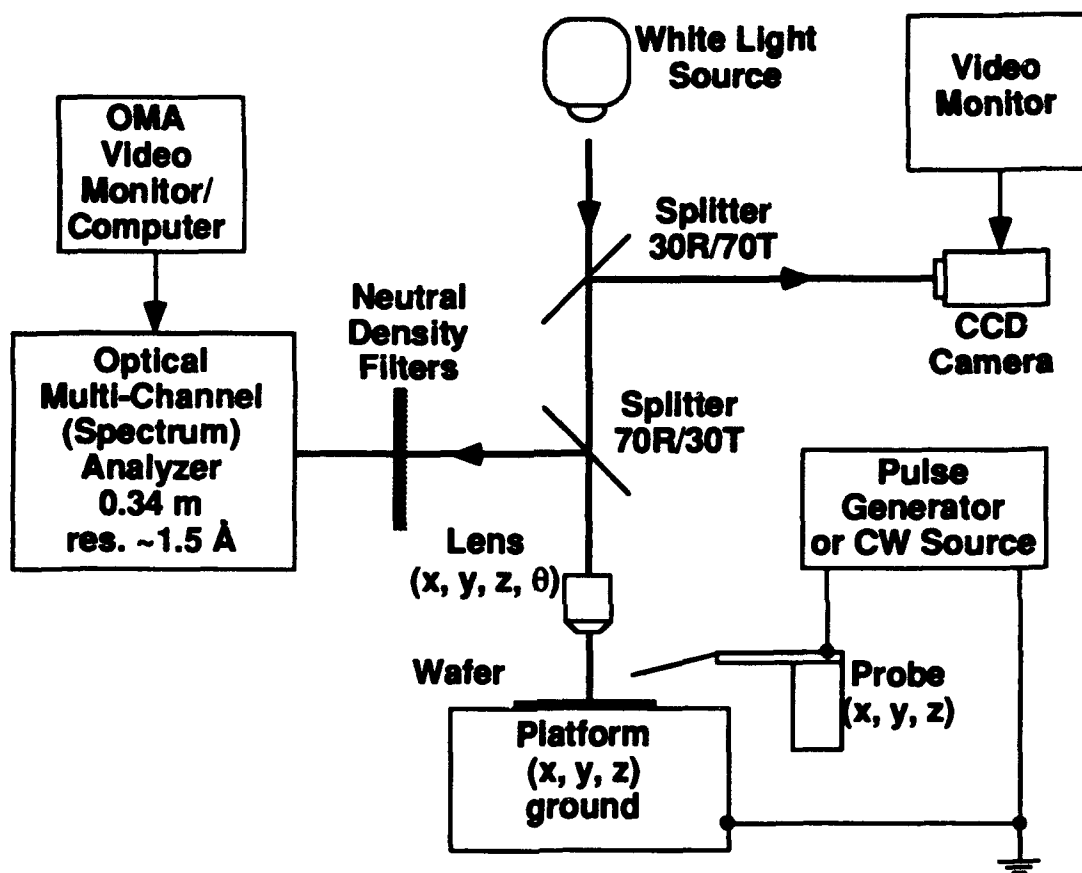


Fig. 2.7 Schematic diagram of the reflectance and electroluminescence measurement set-up.

refractive index. To minimize the absorptive losses in $\text{Al}_x\text{Ga}_{1-x}\text{As}$ DBRs at wavelengths < 700 nm, the AlAs mole fraction x in the high index $\text{Al}_x\text{Ga}_{1-x}\text{As}$ $\lambda/4$ layer is chosen to be ≥ 0.4 . The low index $\lambda/4$ layer is usually AlAs to maximize the differential refractive index $\Delta n = n_H - n_L$, since the reflectance bandwidth ($\Delta\lambda_{BW}$) increases as Δn increases.

Figure 2.8 is the calculated reflectance spectra of an $\text{Al}_{0.5}\text{Ga}_{0.5}\text{As}/\text{AlAs}$ DBR high reflector with $\lambda_0 = 680$ nm, for 5 to 30 periods in 5 period increments. The high reflectance zone is limited in extent. As DBR periods are added, the reflectivity increases, and the number of oscillations outside the reflectance bandwidth increases. With 15 or more periods, $\Delta\lambda_{BW}$ remains essentially constant. The value of $\Delta\lambda_{BW}$ (~ 50 nm in Fig. 2.8) can be estimated by [MacLeod 1989]

$$\frac{\Delta\lambda_{BW}}{\lambda_0} = \frac{\pi}{4} \sin^{-1} \left(\frac{n_H - n_L}{n_H + n_L} \right) \quad (\text{unitless}) \quad (2.14)$$

Figure 2.9 is a plot of the calculated reflectance of $\text{Al}_{0.5}\text{Ga}_{0.5}\text{As}/\text{AlAs}$ DBR structures (with $\lambda_0 = 660$ nm) as a function of the number of periods for two similar structures (a) and (b). The incident material is $\text{Al}_{0.5}\text{In}_{0.5}\text{P}$, which is typically the optical cavity material adjacent to the DBRs in visible VCSELs. The plotted reflectance is that as seen from the optical cavity looking out. Structure (a) can be described by Eq. (2.12), while structure (b) can be described by Eq. (2.13). Over 40 DBR periods are needed to reach $R = 0.9999$ with structure (a), while 29.5 DBR periods are needed to reach $R = 0.999$ with structure (b).

The measured (solid curve) and calculated (dashed curve) reflectance (at normal incidence) of a 20 period AlGaAs DBR grown by MOVPE is shown in Fig. 2.10(a), and the calculated reflectivity phase is shown in Fig. 2.10(b). A growth list for the DBR structure is given in Table 2.1. The reflectance is measured as described in Fig. 2.7. The

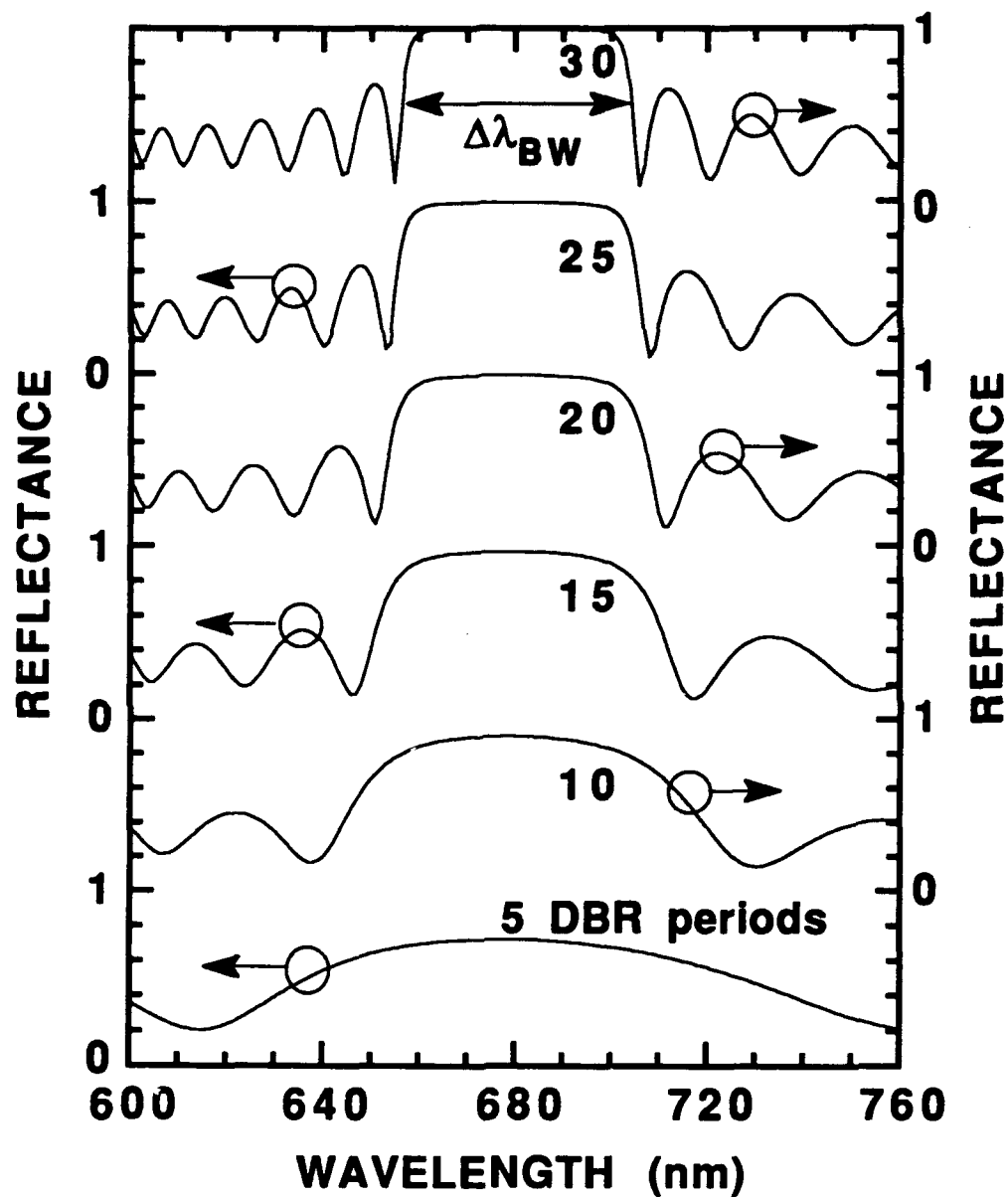


Fig 2.8 Calculated reflectance spectra for AlAs/Al_{0.5}Ga_{0.5}As DBR structures on a GaAs substrate, with variable number of DBR periods. The Bragg wavelength $\lambda_0 = 680$ nm.

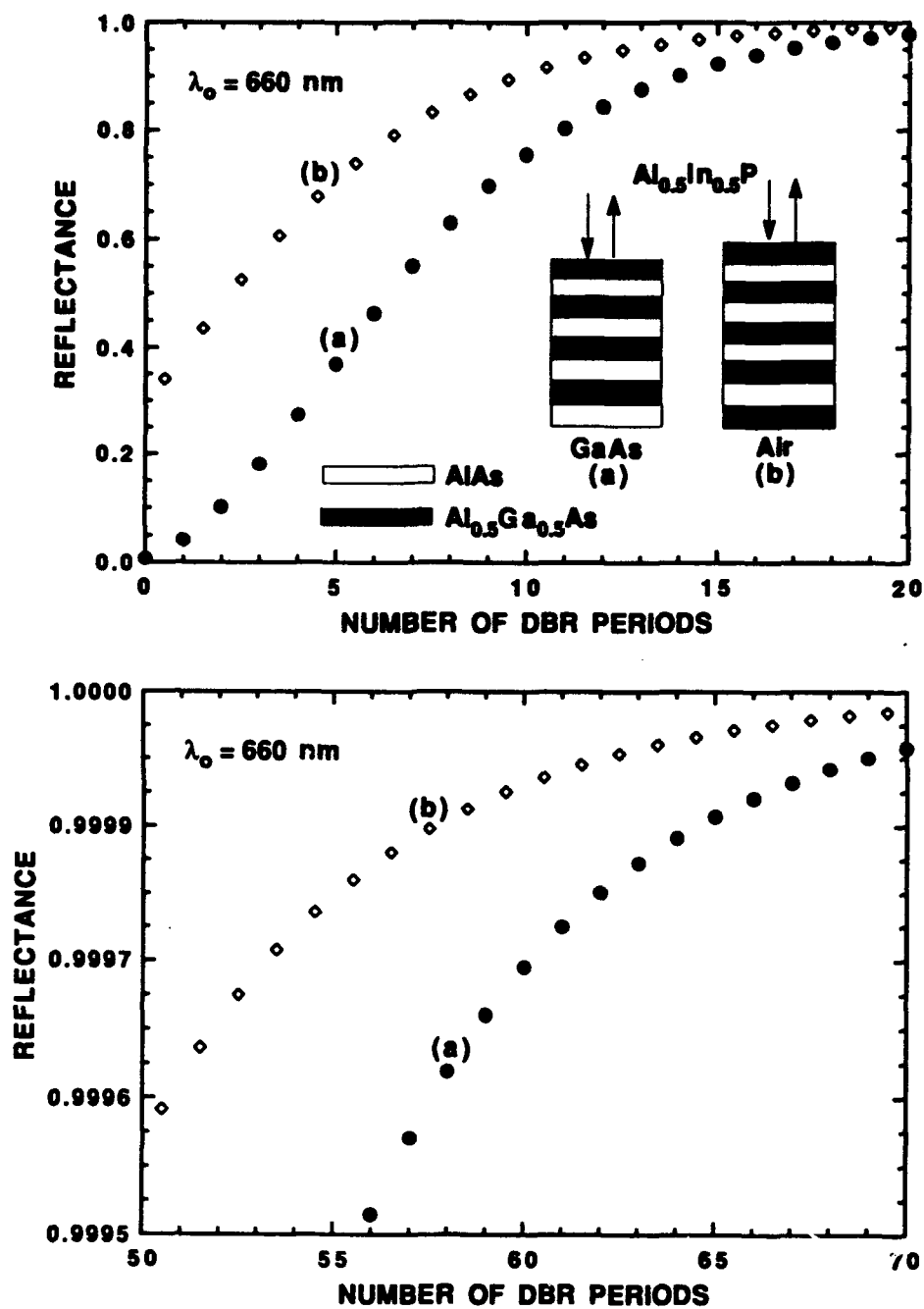


Fig 2.9 Reflectance versus number of periods for AlAs/Al_{0.5}Ga_{0.5}As DBR structures.

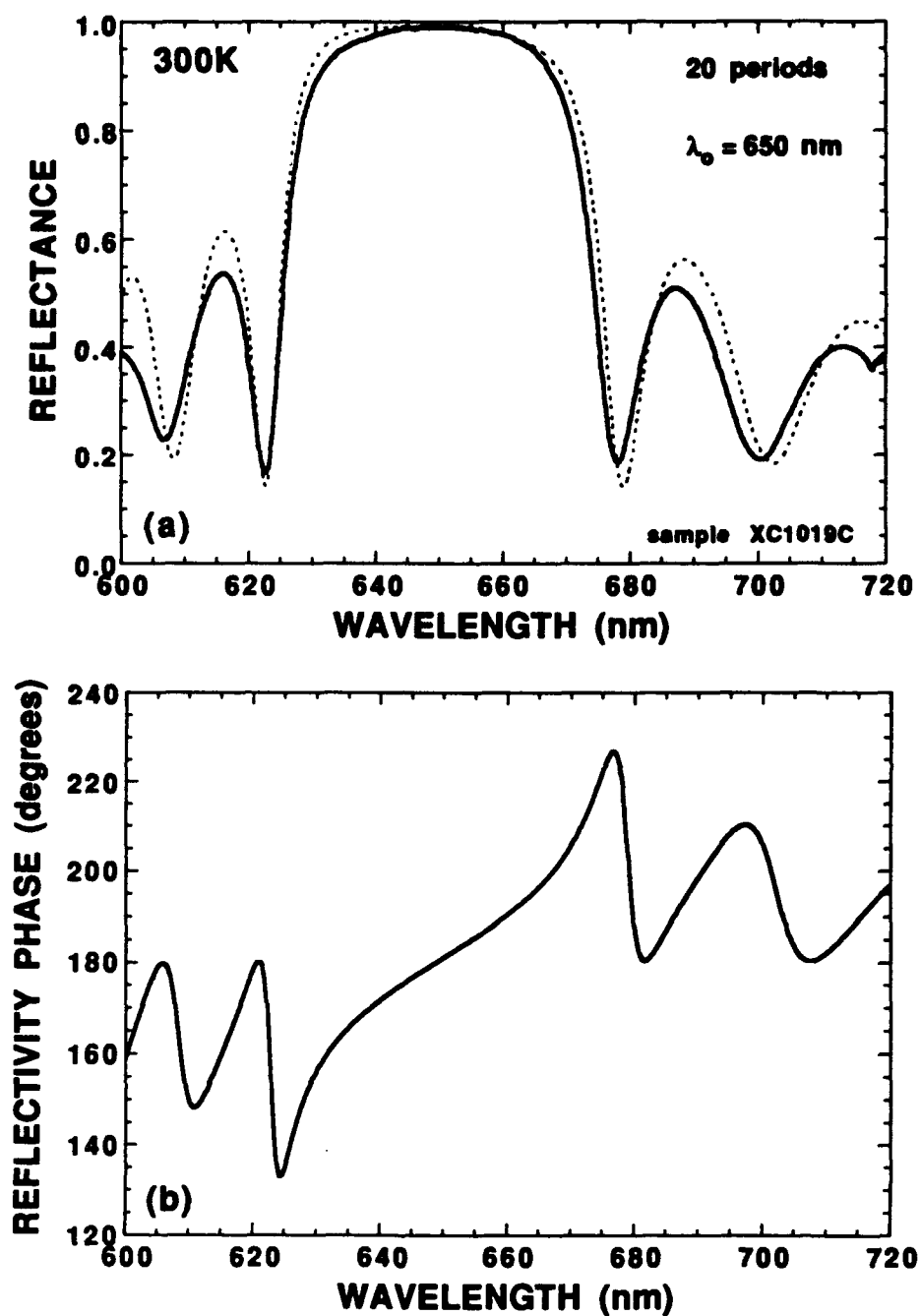


Fig 2.10 (a) Measured (solid line) and calculated (dashed line) reflectance of a 20 period $\text{Al}_{0.5}\text{Ga}_{0.5}\text{As}$ DBR on a GaAs substrate, and (b) calculated reflectivity phase.

high index $\lambda/4$ layer is a composite, composed of $\text{Al}_{0.5}\text{Ga}_{0.5}\text{As}$ layers surrounded by 5 nm thick $\text{Al}_{0.75}\text{Ga}_{0.25}\text{As}$ layers. The low index $\lambda/4$ layer is also a composite, composed of AlAs layers surrounded by 5 nm thick $\text{Al}_{0.75}\text{Ga}_{0.25}\text{As}$ layers. Thus the 10 nm thick $\text{Al}_{0.75}\text{Ga}_{0.25}\text{As}$ barrier reduction interface layers are effectively divided in half, and are part of both the low and high index $\lambda/4$ layers. The thickness requirement for a $\lambda/4$ layer is given by Eq. (2.11). For a composite $\lambda/4$ layer composed of N layers, the sum of the optical thicknesses of the individual layers must total a quarter wave, such that

$$\sum_{\ell=1}^N n_{\ell} d_{\ell} = \frac{\lambda_0}{4} \quad (\text{nm}) \quad (2.15)$$

Table 2.1 MOVPE Growth List for AlGaAs DBR Sample XC1019C

Thickness (Å)	Material	Refractive Index at λ_0
100.0	GaAs	3.83 - i0.194
304.2	$\text{Al}_{0.5}\text{Ga}_{0.5}\text{As}$	3.541
100.0	$\text{Al}_{0.75}\text{Ga}_{0.25}\text{As}$	3.299
(repeat)		
416.3	AlAs	3.111
100.0	$\text{Al}_{0.75}\text{Ga}_{0.25}\text{As}$	3.299
365.7	$\text{Al}_{0.5}\text{Ga}_{0.5}\text{As}$	3.541
100.0	$\text{Al}_{0.75}\text{Ga}_{0.25}\text{As}$	3.299
x19		
416.3	AlAs	3.111
50.0	$\text{Al}_{0.75}\text{Ga}_{0.25}\text{As}$	3.299
substrate	(n+) GaAs (100) 6°	3.83 - i0.194
Bragg wavelength $\lambda_0 = 650 \text{ nm}$		

For the structure in Table 2.1, the $\text{Al}_{0.75}\text{Ga}_{0.25}\text{As}$ layers are chosen to be 10 nm thick. Thus, the thickness of the high index $\text{Al}_{0.5}\text{Ga}_{0.5}\text{As}$ layer $d_H = 365.7 \text{ \AA}$, where $6500/4 - 50(3.299) + 50(3.299) = d_H(3.541)$. Note that the last $\lambda/4$ composite layer includes a 10 nm thick GaAs capping layer. This layer is highly absorbing at 650 nm ($\alpha = 37.5 \times 10^3 \text{ cm}^{-1}$, and thus the 10 nm thick layer absorbs $\sim 3.7\%$ of the propagating energy), but is used to reduce the contact resistance in VCSEL diodes. The reflectance bandwidth of the measured curve in Fig. 2.10(a) is slightly smaller than the calculated bandwidth, suggesting that the composition of the high index $\text{Al}_x\text{Ga}_{1-x}\text{As}$ layer might be slightly off with $0.5 > x > 0.6$.

2.4.3 AlGaInP DBRs for Visible Photonics

The refractive index dispersion for $(\text{Al}_y\text{Ga}_{1-y})_{0.5}\text{In}_{0.5}\text{P}$ alloys lattice-matched to GaAs is shown in Appendix A, Fig. A.2. The construction of AlGaInP "all-phosphide" DBRs is analogous to the construction of AlGaAs DBRs. The low index layer is typically $\text{Al}_{0.5}\text{In}_{0.5}\text{P}$, while the high index material for $\lambda_0 \geq 620 \text{ nm}$ is $(\text{Al}_{0.2}\text{Ga}_{0.8})_{0.5}\text{In}_{0.5}\text{P}$. This insures that the DBR is nonabsorbing within the quantum well optical gain spectrum (except possibly at the short wavelength tail). Figure 2.11 is a 3-D plot of the calculated reflectance spectra of an $(\text{Al}_{0.2}\text{Ga}_{0.8})_{0.5}\text{In}_{0.5}\text{P}/\text{Al}_{0.5}\text{In}_{0.5}\text{P}$ DBR high reflector with $\lambda_0 = 660 \text{ nm}$, for 0 to 30 DBR periods in 2 period increments. As in Fig. 2.8, the high reflectance zone is limited in extent, with oscillations outside the reflectance bandwidth that increase in number, over a given wavelength range, as the number of DBR periods increases.

The actual reflectance at a given wavelength as a function of layer thickness does not follow Fig. 2.11 as plotted, if small incremental amounts of material are added to the structure such as during epitaxial growth. This is because Fig. 2.11 represents the reflectance only for discrete numbers of DBR periods. To illustrate this point, the

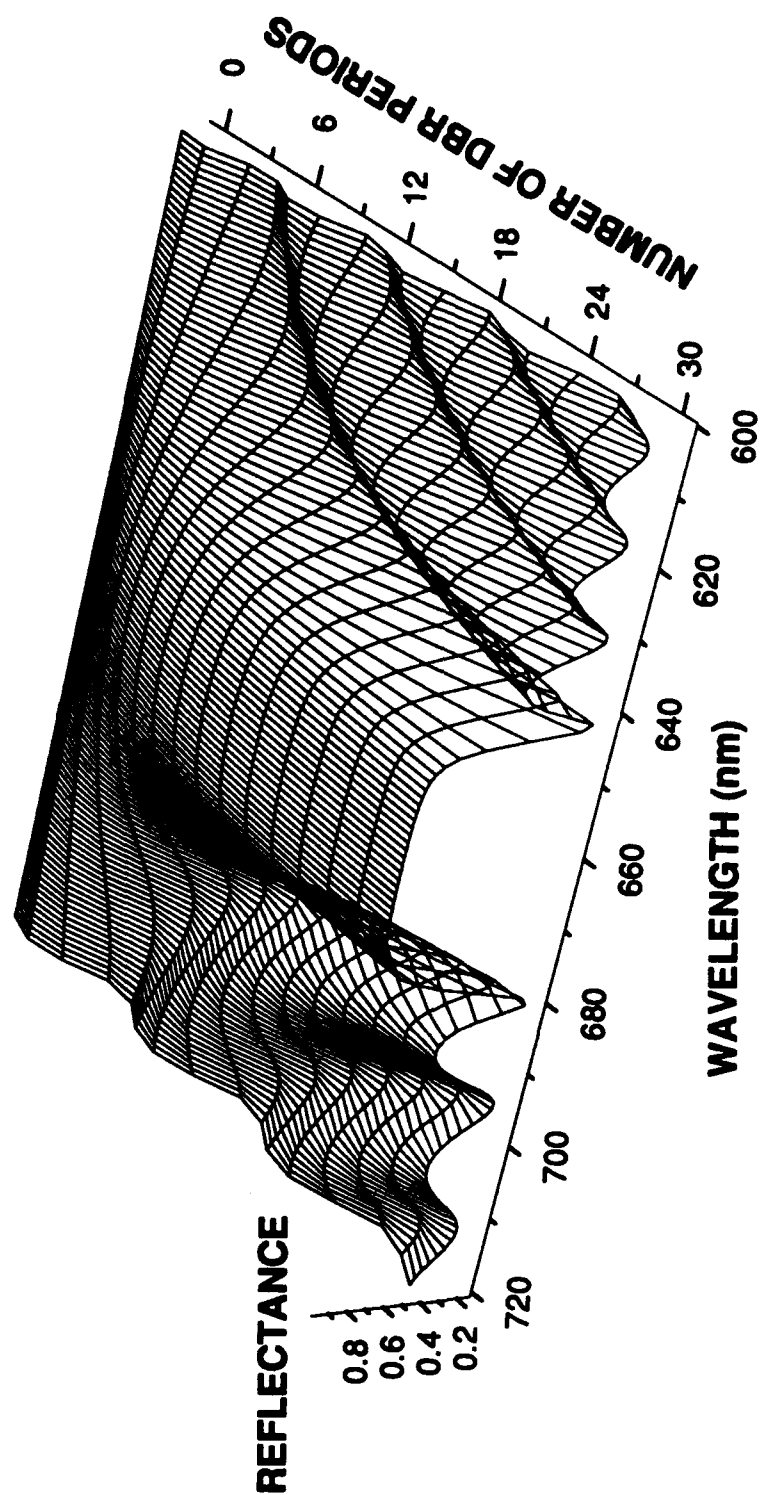


Fig 2.11 Three-dimensional reflectance spectra versus number of DBR periods for an $\text{Al}_{0.5}\text{In}_{0.5}\text{P}/(\text{Al}_{0.2}\text{Ga}_{0.8})_{0.5}\text{In}_{0.5}\text{P}$ DBR grown on a GaAs substrate. The Bragg wavelength is 660 nm

calculated reflectance at 660 nm and normal incidence for the DBR in Fig. 2.11, starting with 30 periods, as a function of etch depth from the surface is shown in Fig. 2.12. The reflectance oscillates as incremental bits of material are removed. The oscillation maxima occur as in Fig. 2.11, when an even number of DBR periods are present, whereas the minima occur when an extra half DBR period (a low index layer in this case) is present at the surface. The oscillation maxima and minima can be calculated with Eqs (2.12) and (2.13), respectively. This behavior is very useful for the accurate plasma etching of DBRs [Vawter *et al.* 1993]. Moreover, *in situ* reflectance monitoring systems are commonly used with dielectric thin-film deposition systems, for example to accurately deposit a high reflector coating composed of $\lambda/4$ layers.

Unlike AlGaAs DBRs which are limited to ~ 600 nm or longer wavelengths (using for example an AlAs/Al_{0.7}Ga_{0.3}As DBR), all-phosphide DBRs with $y = 0.2, 0.35$ and 0.6 for the high index layer can be made for $\lambda_0 = 660, 615$ and 565 nm, respectively [Schneider and Lott 1993]. This is demonstrated in Fig. 2.13, which shows measured reflectance spectra. Also shown is the calculated reflectance (for the given number of DBR periods) and reflector color at λ_0 . The reflectance bandwidth decreases for a given DBR as y increases since the differential refractive index Δn decreases, consistent with Eq. (2.14). Also, the number of DBR periods required to reach a given reflectance increases since the n_H/n_L ratio decreases, consistent with Eq. (2.12).

Figure 2.14 is a plot of the calculated reflectance of (Al_{0.2}Ga_{0.8})_{0.5}In_{0.5}P/Al_{0.5}In_{0.5}P DBR structures (with $\lambda_0 = 660$ nm) as a function of the number of periods for two similar structures (a) and (b). The incident material is taken as Al_{0.5}In_{0.5}P. The plotted reflectance is that as seen from the optical cavity looking out. Structure (a) can be described by Eq. (2.12), while structure (b) can be described by Eq. (2.13). Over 60 DBR periods are needed to reach $R = 0.9999$ with structure (a), while 44.5 DBR periods are needed to reach $R = 0.999$ with structure (b).

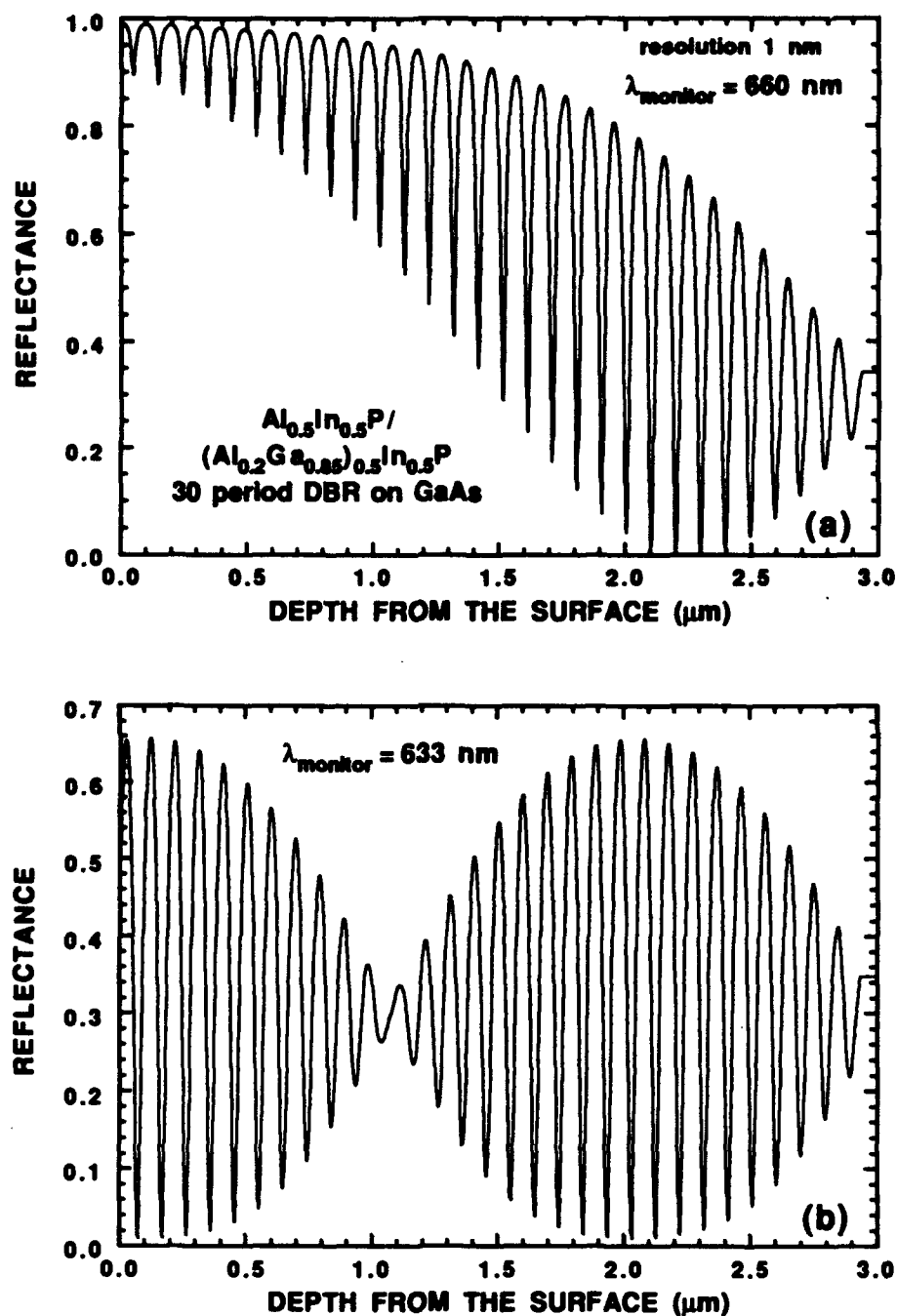


Fig 2.12 Calculated *in situ* reflectance monitoring data. The reflectance at normal incidence is shown for a 30 period AlGaInP DBR as incremental amounts (1 nm sheets) of the epitaxial material is removed. The Bragg design wavelength for the DBR is 660 nm. The laser monitor wavelength is (a) 660 nm, and (b) 633 nm. Calculated using a program developed by G. A. Vawter [1993].

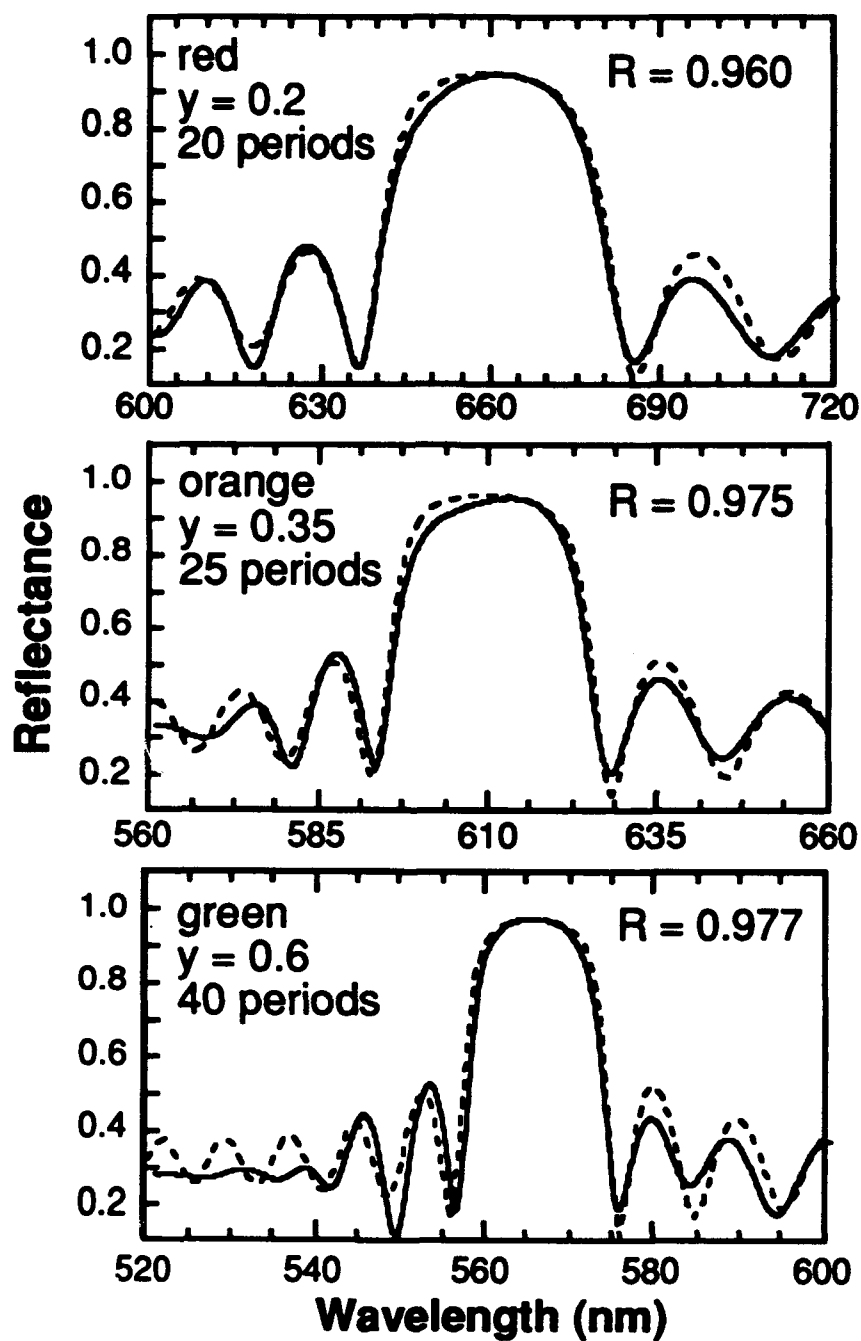


Fig. 2.13 Comparison of $\text{Al}_{0.5}\text{In}_{0.5}\text{P}/(\text{Al}_y\text{Ga}_{1-y})_{0.5}\text{In}_{0.5}\text{P}$ distributed Bragg reflectors grown on GaAs substrates. Measured data (solid lines), calculated data (dashed lines) [Schneider and Lott 1993].

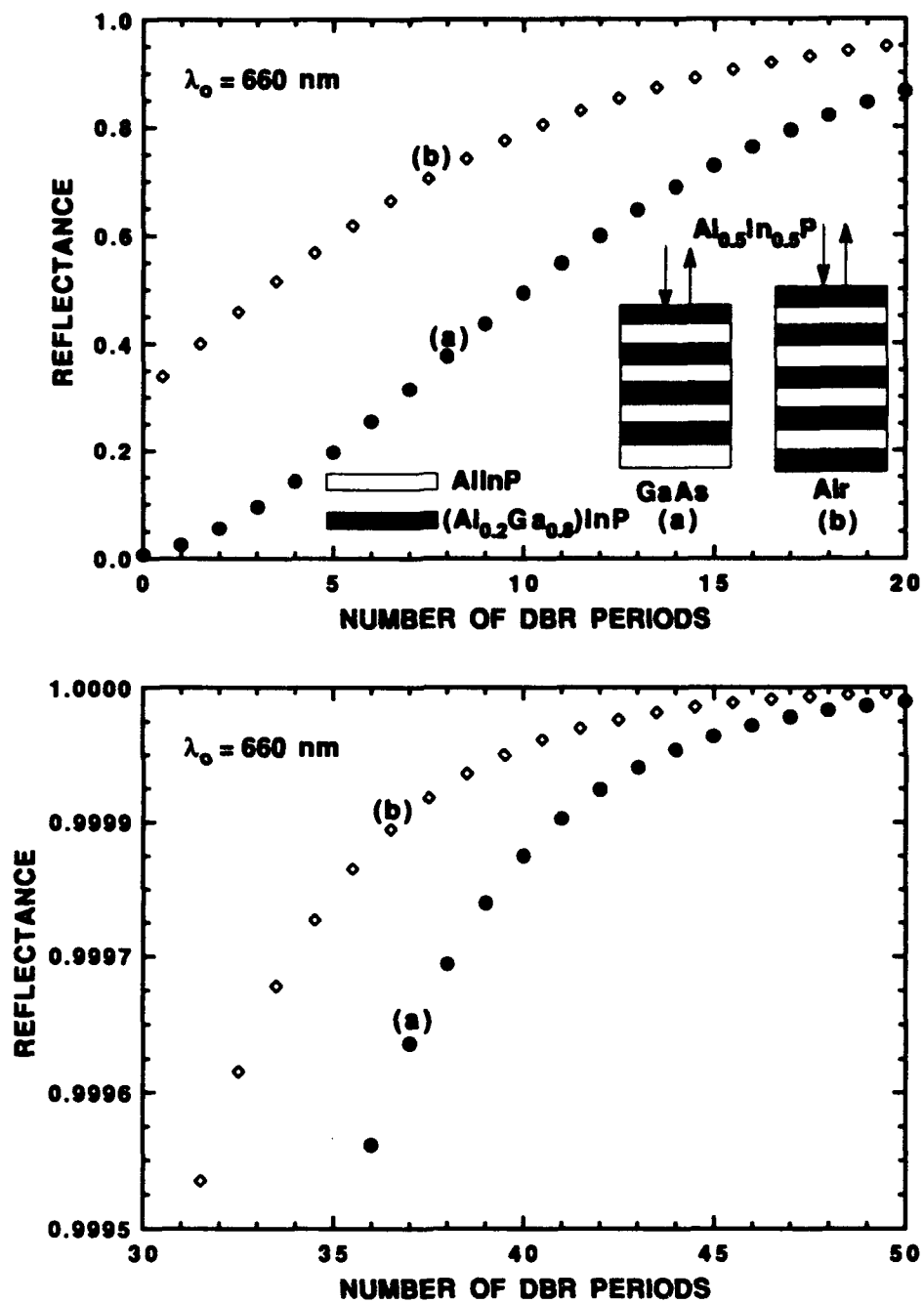


Fig 2.14 Reflectance versus number of periods for $\text{Al}_{0.5}\text{In}_{0.5}\text{P}/(\text{Al}_{0.2}\text{Ga}_{0.8})_{0.5}\text{In}_{0.5}\text{P}$ DBR structures.

The measured (solid curve) and calculated (dashed curve) reflectance (at normal incidence) of a 25 period $(\text{Al}_{0.2}\text{Ga}_{0.8})_{0.5}\text{In}_{0.5}\text{P}/\text{Al}_{0.5}\text{In}_{0.5}\text{P}$ DBR with $\lambda_0 \approx 660$ nm grown by MOVPE on a GaAs substrate is shown in Fig. 2.15(a), and the calculated reflectivity phase is shown in Fig. 2.15(b). A growth list for the DBR structure is given in Table 2.2.

Table 2.2 MOVPE Growth List for AlGaInP DBR Sample XC0930A

Thickness (Å)	Material	Refractive Index at λ_0
(repeat) 470.1	$(\text{Al}_{0.2}\text{Ga}_{0.8})_{0.5}\text{In}_{0.5}\text{P}$	3.510
508.8	$(\text{Al}_{0.5}\text{In}_{0.5}\text{P})$	3.243
x25		
substrate	(n+) GaAs (100) 6°	3.816 - i0.178
Bragg wavelength	$\lambda_0 = 660$ nm	Reflectance Bandwidth $\Delta\lambda_{BW} \approx 33.2$ nm

The measured reflectance accurately fits the calculated reflectance, as in Fig. 2.13. This helps to verify the accuracy of the refractive index dispersion data. The slight deviations at the shorter wavelengths are due most likely to DBR absorptance which is not included in the calculation.

2.4.4 Dielectric DBRs

Many amorphous dielectric materials are transparent (minimally absorbing) to infrared and visible wavelength light, and typically their refractive indices vary slowly with wavelength. Examples and their approximate refractive indices (n) at 620 to 690 nm

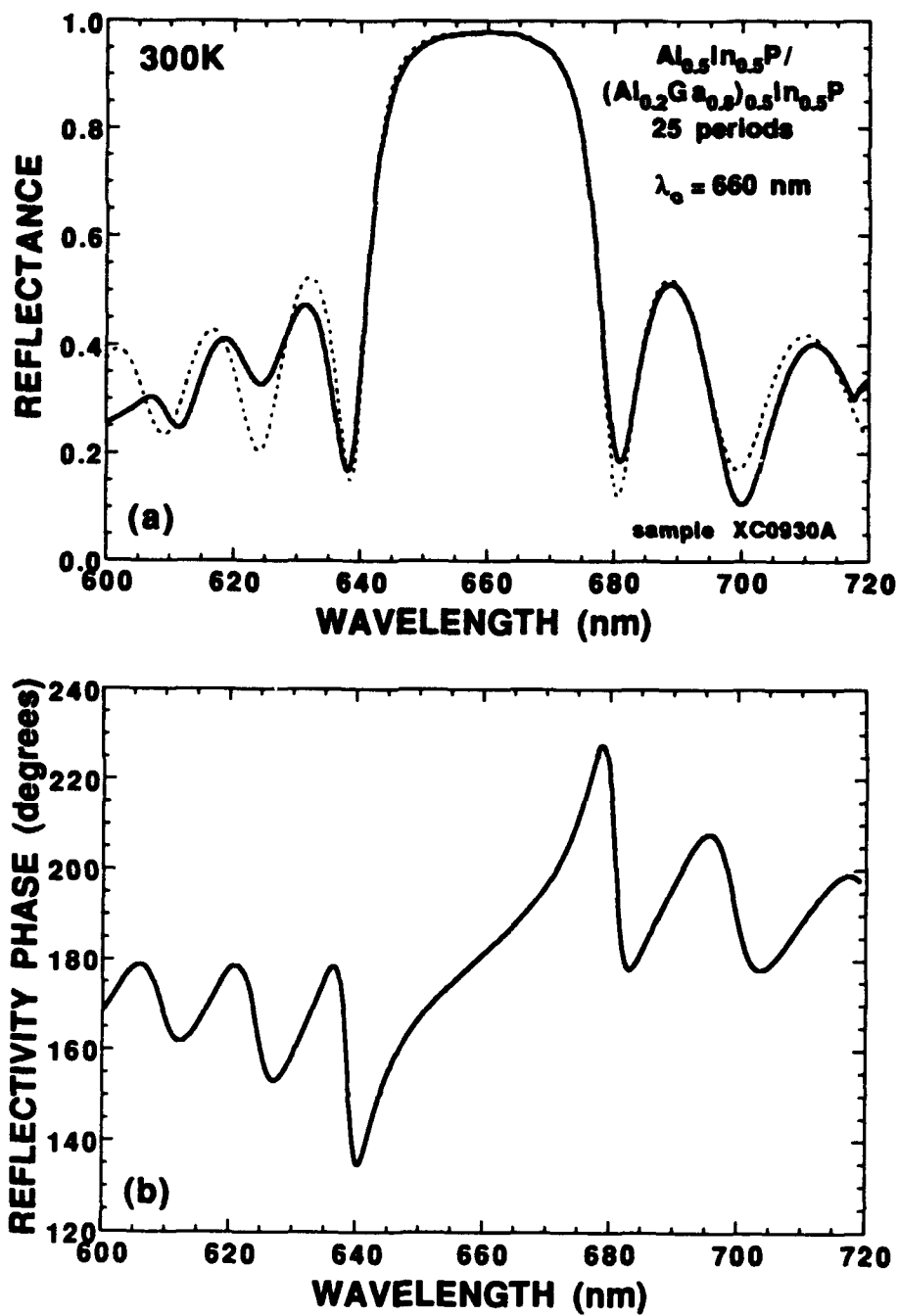


Fig 2.15 (a) Measured (solid line) and calculated (dashed line) reflectance of a 25 period $\text{Al}_{0.5}\text{In}_{0.5}\text{P}/(\text{Al}_{0.2}\text{Ga}_{0.8})_{0.5}\text{In}_{0.5}\text{P}$ DBR on a GaAs substrate, and (b) calculated reflectivity phase.

include SiO_2 (1.45), TiO_2 (2.40), ZrO_2 (1.95), Nb_2O_5 (2.30), Al_2O_3 (1.63), CaF_2 (1.35), ZnSe (2.54). Part or all of VCSEL DBRs may be replaced by dielectric $\lambda/4$ layers as previously demonstrated [Koyama *et al.* 1989, Lei *et al.* 1991, Scherer *et al.* 1992, Baba *et al.* 1993]. This is done to reduce the device series resistance and absorptive losses, and to reduce heating. In long wavelength (1.3 μm) VCSELs composed of GaInPAs/InP DBRs, the differential index is small and many thick semiconductor DBR periods would be required. As shown in Table 2.3, very few dielectric DBR periods are needed to reach $R \geq 0.99$ over the visible wavelength range.

Table 2.3 Reflectance Comparison for Selected Quarter Wave Stacks. The incident medium is $\text{Al}_{0.5}\text{In}_{0.5}\text{P}$ ($n = 3.256$), the substrate is air ($n = 1.0$), and $\lambda_0 = 650 \text{ nm}$.

Number of DBRs	$\text{SiO}_2/\text{Nb}_2\text{O}_5$ ($n = 1.45/2.30$)	CaF_2/ZnSe ($n = 1.35/2.54$)	$\text{AlAs}/\text{Al}_{0.5}\text{Ga}_{0.5}\text{As}$ ($n = 3.111/3.541$)	$\text{Al}_{0.5}\text{In}_{0.5}\text{P}/(\text{Al}_{0.2}\text{Ga}_{0.8})\text{InP}$ ($n = 3.256/3.530$)
0	0.29128	0.29128	0.29128	0.29128
1	0.62031	0.71276	0.39065	0.35338
2	0.82776	0.90897	0.48668	0.41500
3	0.92766	0.97340	0.57497	0.47478
4	0.97060	0.99241	0.65306	0.53167
5	0.98821	0.99785	0.72009	0.58495
6	0.99530	0.99939	0.77628	0.63416
7	0.99813	0.99983	0.82253	0.67907
8	0.99926	0.99995	0.86006	0.71964
9	0.99970	0.99999	0.89017	0.75598
10	0.99988	1.00000	0.91412	0.78829

Figure 2.16 shows the calculated transmittance ($T + R = 1$) and reflectivity phase of example dielectric Fabry-Perot etalon structures (discussed in Section 2.5). Since the differential refractive indices are large, the bandwidth is also large. Note that the transmission resonances at $\lambda_0 = 650$ nm occur at the energy center of the transmittance (or reflectance) bandwidth, rather than at the wavelength center of the bandwidth. The phase penetration lengths for the structure in Fig. 2.16(a) are ~ 190 nm.

2.5 Multilayer Fabry-Perot Etalons

All-dielectric multilayer Fabry-Perot etalons (FPE) consist of an optical cavity surrounded by DBRs. These structures are commonly used as interferometers for the precise measurement of spectral linewidths. One variation of the multilayer FPE that closely resembles typical VCSEL structures is the multilayer Gires-Tournois interferometer. This structure is an asymmetric FPE, such that the reflectance of one DBR mirror is ≈ 1.0 (100%) within the wavelengths of interest, while the other (coupling) DBR is partially reflecting. A schematic diagram of an example all-semiconductor FPE is shown in Fig. 2.17. This structure has a H index optical cavity, although a L index optical cavity is also possible (surrounded by H $\lambda/4$ layers). In VCSELs, the average index of the optical cavity is usually H- ($n_L < n_H- < n_H$), as compared to the L and H index $\lambda/4$ layers.

In Section 2.1, equations (2.7) to (2.9) contained some of the parameters that describe Fabry-Perot resonant cavities such as the free spectral range (FSR), the DBR phase penetration lengths (ℓ_p), and the effective cavity length (L_{eff}). Other important parameters include the cavity quality factor (Q), the cavity finesse (\mathcal{F}), and the (transmission) linewidth ($\Delta\lambda_{1/2}$). The Q is the number of cycles (radian) for the optical field energy in the cavity to decay by a factor of $1/e$, and is given by

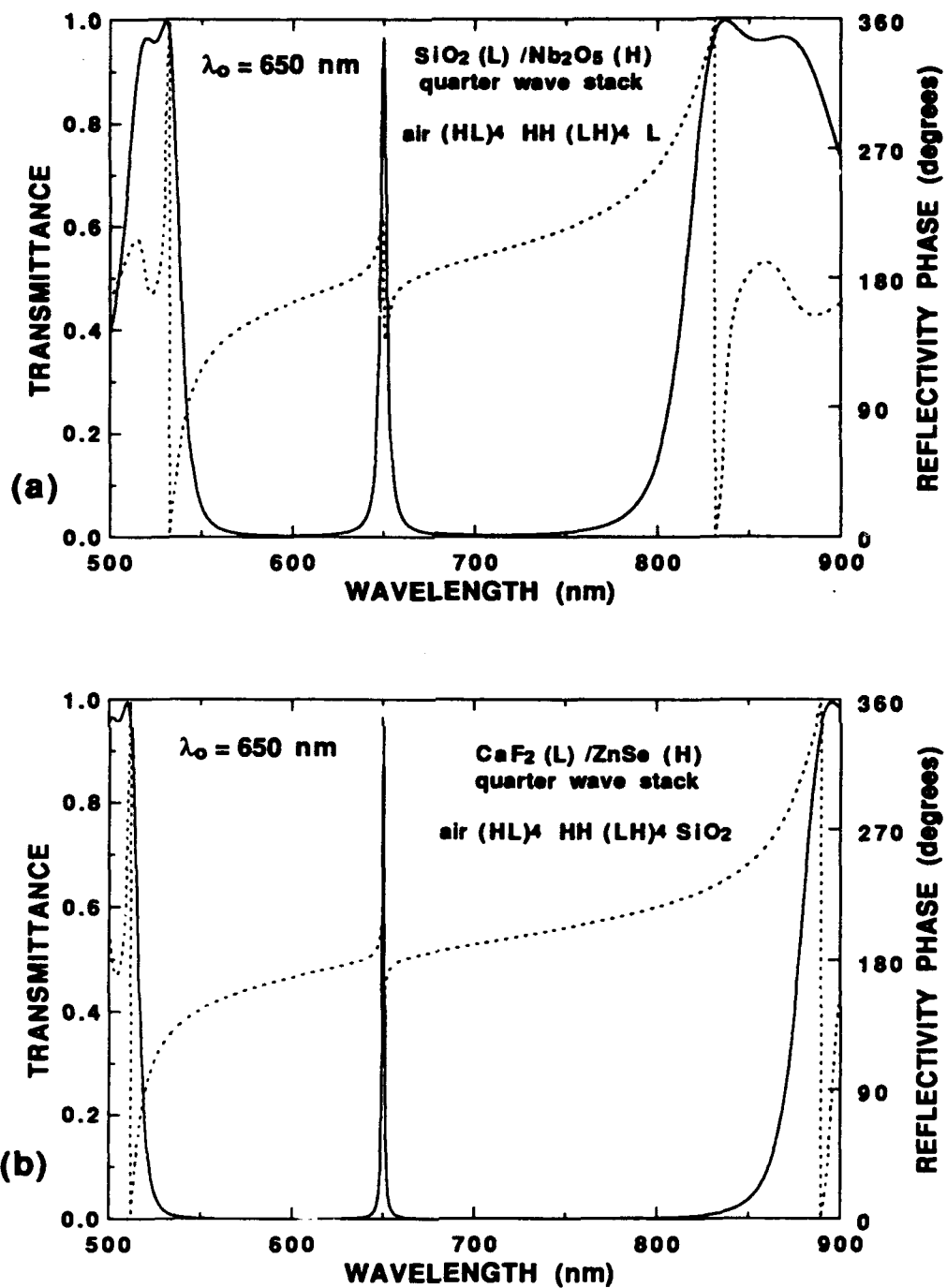


Fig 2.16 Calculated transmittance of two example all-dielectric DBRs.

$$Q = \frac{\lambda_0}{\text{FSR}} \mathcal{F} \quad (\text{unitless}) \quad (2.16)$$

The cavity finesse (\mathcal{F}) is defined as the ratio of the FSR to the linewidth ($\Delta\lambda_{1/2}$), and is given by

$$\mathcal{F} = \frac{\text{FSR}}{\Delta\lambda_{1/2}} = \frac{\pi (R_1 R_2)^{1/4}}{1 - (R_1 R_2)^{1/2}} \quad (\text{unitless}) \quad (2.17)$$

where R_1 and R_2 are the reflectances of the top and bottom DBR as seen from within the optical cavity looking out. The finesse is a measure of the resolving power of the etalon. Finally, the $\Delta\lambda_{1/2}$ is given by

$$\frac{\Delta\lambda_{1/2}}{\lambda_0} = \frac{1}{Q} = \frac{\lambda_0}{2 L_{\text{eff}} n_{\text{cav}} \mathcal{F}} \quad (\text{unitless}) \quad (2.18)$$

More precisely, the linewidth parameter is the full width at half maximum linewidth ($\Delta\lambda_{1/2}$) of light that is transmitted out of a FPE. For VCSELs, this parameter is the expected emission linewidth.

It is shown elsewhere [Yeh 1988, MacLeod 1989] that when "spacer" layers of thickness $d_{\text{oc}} = u\lambda_0/2n$, $u = 1, 2, 3, \dots$ (see Eq. (2.10)) are placed within a stack of $\lambda/4$ layers, they act as absentee layers at λ_0 . This means that the reflectance of the multilayer stack will not change if the spacer layer is removed and the surrounding layers are butted together. When this is done in Fig. 2.17, the two L index $\lambda/4$ layers surrounding the optical cavity spacer layer, subsequently form another absentee spacer layer that is $\lambda/2$ thick. This layer can be removed, and its surrounding H index $\lambda/4$ layers form another absentee layer, and so on. This layer elimination process continues in Fig. 2.17 until the

top DBR is removed. The resulting structure consists of a portion of the bottom DBR with a L index layer upper most next to the incident medium, which is almost always air with $n = 1.0$. The reflectance of the resulting structure at λ_0 can be calculated by using Eq. (2.13). The reflectance spectrum, as measured on the top surface at normal incidence, is similar to the reflectance of a typical DBR except that a Fabry-Perot resonance "dip" occurs at λ_0 with a linewidth equal to $\Delta\lambda_{1/2}$. As shown below, secondary Fabry-Perot resonances can also occur, with a separation equal to the FSR.

As an example FPE structure, consider the all-phosphide DBR structure given in Table 2.2 with $\lambda_0 = 660$ nm, but with 30.5 DBR periods on the bottom and 20 DBR periods on the top, surrounding a $\lambda/2$ -thick ($d_{oc} = 99.099$ nm) optical cavity composed of $(Al_{0.7}Ga_{0.3})_{0.5}In_{0.5}P$ ($n = 3.33$ at $\lambda_0 = 660$ nm). The calculated reflectances and phase penetration lengths for the bottom and top DBRs (as seen from within the optical cavity looking outward) are $R_b = 0.97181$ and $\ell_{pb} = 818.26$ nm, and $R_t = 0.95062$ and $\ell_{pt} = 792.15$ nm, respectively. Thus, $\mathcal{F} = 79.3$, $L_{eff} = 1709.5$ nm, $Q = 1368$, $FSR = 38.26$ nm, and $\Delta\lambda_0 = 0.483$ nm. Also, the reflectance bandwidth $\Delta\lambda_{BW} = 33.2$ nm. A plot of the calculated reflectance is shown in Fig. 2.18 (labeled as 0%). From Eq. (2.13), the reflectance at λ_0 (the bottom of the Fabry-Perot dip) is ≈ 0.08 .

It is informative to consider the variation in reflectance with small variation in layer thickness. Figure 2.18 shows the reflectance spectra for the example FPE structure above, with every layer varying by the same percent relative to the layer thickness at $\lambda_0 = 660$ nm. A 2% deviation in layer thickness roughly corresponds to a rigid 10 nm shift in the reflectance spectrum. The shape of the reflectance remains very nearly identical, despite the thickness variation. However, the optical thickness of a DBR period ($\lambda_0/2 = d_H n_H + d_L n_L = \lambda_0/4 + \lambda_0/4$) does not change by the same percentage as the layer thicknesses d_H and d_L . For example, given $\lambda_0 = 660$ nm, then $n_H = 3.510$ and $n_L = 3.243$, and thus $d_H = 47.01$ nm and $d_L = 50.88$ nm are uniquely determined. For a +6%

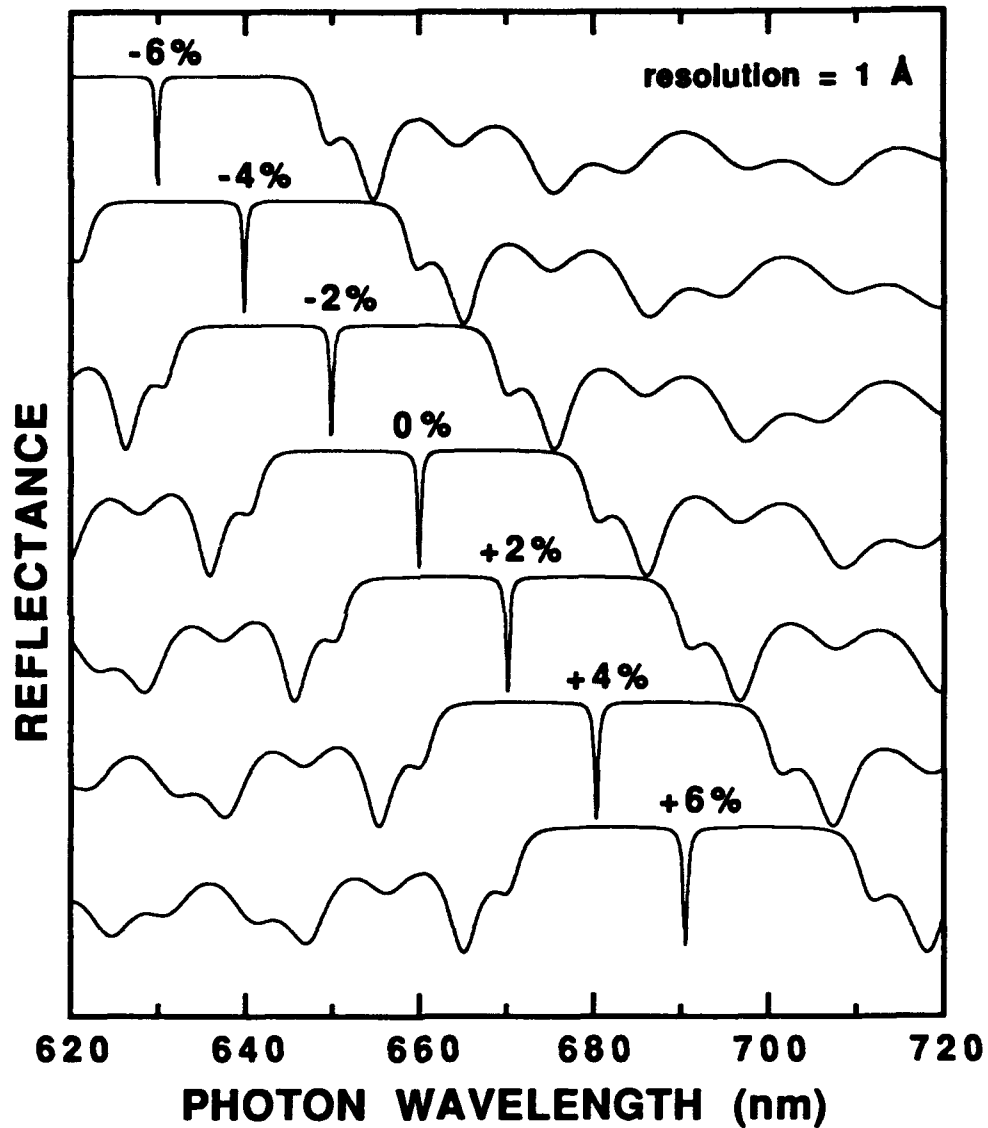


Fig. 2.18 Calculated reflectance spectra for an example Fabry-Perot etalon, with uniform thickness variation in each layer. All layers are referenced to their values at $\lambda_0 = 660$ nm. The top and bottom DBRs are 20 and 30.5 periods of $\text{Al}_{0.5}\text{In}_{0.5}\text{P}/(\text{Al}_{0.2}\text{Ga}_{0.8})_{0.5}\text{In}_{0.5}\text{P}$, respectively. The $\lambda/2$ thick optical cavity is composed of $(\text{Al}_{0.7}\text{Ga}_{0.3})_{0.5}\text{In}_{0.5}\text{P}$.

change in the layer thicknesses, the new optical thickness of a DBR period is $\lambda_o^*/2 = 1.06 [d_H n_H(\lambda_o^*) + d_L n_L(\lambda_o^*)] \neq 1.06 \lambda_o/2$, since n_H and n_L are functions of wavelength. Solving this iteratively results in $\lambda_o^* = 690.36$ nm, which is a +4.6% wavelength increase from $\lambda_o = 660$ nm. Moreover, the optical thickness of the optical cavity changes at a slightly different rate as compared to the DBRs. A +6% change in the optical cavity thickness results in $\lambda_o^* = 690.85$ nm. The calculated Fabry-Perot resonance dip at +6% in Fig. 2.18 occurs at 690.5 nm.

The structures described in this dissertation were grown in an MOVPE system that uses a horizontal reaction chamber. The 2 inch wafers are rotated during growth to achieve layer thickness uniformities within $\pm 1\%$. Alternately, the wafers are not rotated during growth to achieve an approximately linear variation in layer thickness (from front to back) up to several percent, depending on the exact growth conditions. This variation has proven useful for studies of visible VCSELs and resonant cavity light-emitting diodes (RCLEDs), as described in Chapters 3, 4 and 5. The thickness variation, however, is more complex than as given in Fig. 2.18. It is not uniform for layers of different alloy composition, since the growth rates and constituent incorporation efficiencies are different. The degree of nonuniformity is varied most readily by varying the growth pressure. Thus, the relative thickness variation in an AlAs/AlGaAs DBR is different compared to an AlGaInP optical cavity active region since these materials are typically grown at two different pressures (80 and 110 mbar, respectively). This implies that the Fabry-Perot resonance dip will not stay exactly centered in the DBR reflectance bandwidth (energy center of the mirror) at all points on the wafer. Furthermore, the ratio of Ga/In in a $\text{Ga}_{1-y}\text{In}_y\text{P}$ quantum well increases from wafer front to back when rotation is not employed due to a difference in Ga and In incorporation efficiency. Thus, the small variation in emission wavelength (see Figs 2.3 and 5.5) across the wafer is due primarily to slight changes in quantum well composition, rather than well thickness.

Typically, VCSELs are designed to have a short optical cavity thickness ($\lambda/2$ or 1λ) to minimize absorptive losses in the cavity, and to limit the emission to a single longitudinal mode by using a large FSR. The FSR is decreased by increasing the effective optical cavity length, as given by Eq. (2.7). As the FSR decreases, secondary Fabry-Perot modes occur in the reflectance spectra. Each mode represents a 2π phase shift for a wave during a round trip in the optical cavity (DBR mirror phase upon reflection and cavity propagation phase). As an example, Fig. 2.19 shows the calculated (normal incidence) reflectance spectra for an FPE with a 20 and 10 period bottom and top DBR, respectively, and with different size optical cavities where $d_{oc} = 2, 8, 14$, and 20λ . The corresponding thicknesses of the optical cavities are about 0.4, 1.65, 2.89, and 4.14 μm , respectively. The DBRs are composed of $\text{AlAs}/\text{Al}_{0.5}\text{Ga}_{0.5}\text{As}$ with 10 nm $\text{Al}_{0.75}\text{Ga}_{0.25}\text{As}$ barrier reduction layers at each interface, with $\lambda_0 = 670$ nm. The central part of the optical cavity is 2λ -thick $(\text{Al}_{0.7}\text{Ga}_{0.3})_{0.5}\text{In}_{0.5}\text{P}$, and this is surrounded by pairs of cladding $\text{Al}_{0.5}\text{In}_{0.5}\text{P}$ spacer layers, with thicknesses 0, 3, 6, or 9λ .

The FSR in conventional edge-emitting lasers and in VCSELs is the wavelength separation of Fabry-Perot lasing modes. The switching from one mode to another in edge emitters occurs, in part, as a consequence of changes in the peak spectral gain wavelength, resulting for example from changes in injected carrier density or device temperature. In quantum well VCSELs however, strong lasing emission is not possible at every Fabry-Perot mode if multiple modes are present as in Fig. 2.19. For a properly designed VCSEL, the quantum well gain layers are placed together at a peak of the standing wave (i. e. electric field intensity) in the optical cavity. An example is shown in Fig. 2.20(a), which is the calculated electric field intensity on resonance ($\lambda_0 = 670$ nm) for the 20λ thick FPE structure in Fig. 2.19(d). Also shown is the real refractive index profile of the active region. Three 10 nm thick $\text{Ga}_{0.5}\text{In}_{0.5}\text{P}$ quantum wells surrounded by

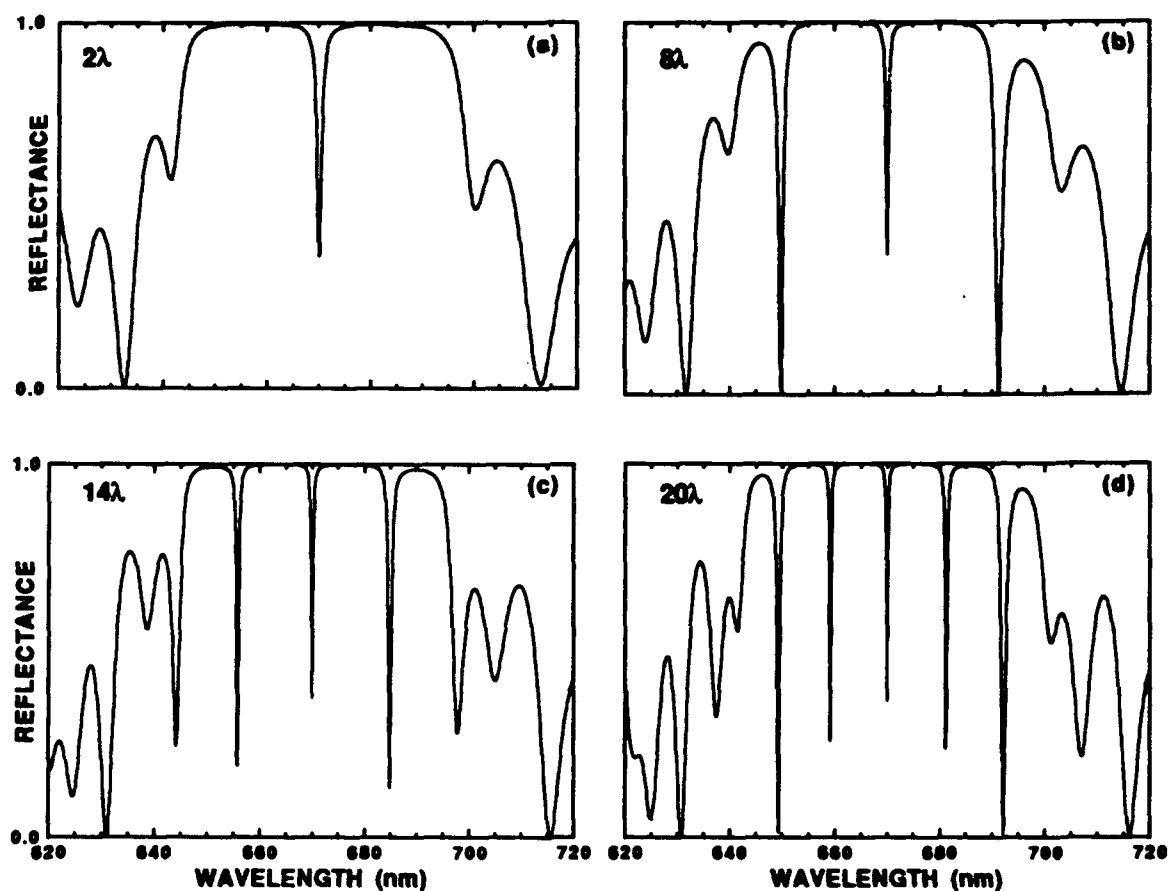


Fig. 2.19 Calculated reflectance spectra for example Fabry-Perot etalons with varying optical cavity thickness. The top and bottom DBRs are 10 and 20 periods of $\text{AlAs}/\text{Al}_{0.5}\text{Ga}_{0.5}\text{As}$, respectively, with 10 nm thick $\text{Al}_{0.75}\text{Ga}_{0.25}\text{As}$ barrier reduction layers at each interface. The central optical cavity is composed of 2λ thick $(\text{Al}_{0.7}\text{Ga}_{0.3})_{0.5}\text{In}_{0.5}\text{P}$, surrounded by $\text{Al}_{0.5}\text{In}_{0.5}\text{P}$ phase matching spacer layers, with thicknesses of 0, 3, 6, or 9λ . The optical cavity thickness is (a) 2λ , (b) 8λ , (c) 14λ , and (d) 20λ .

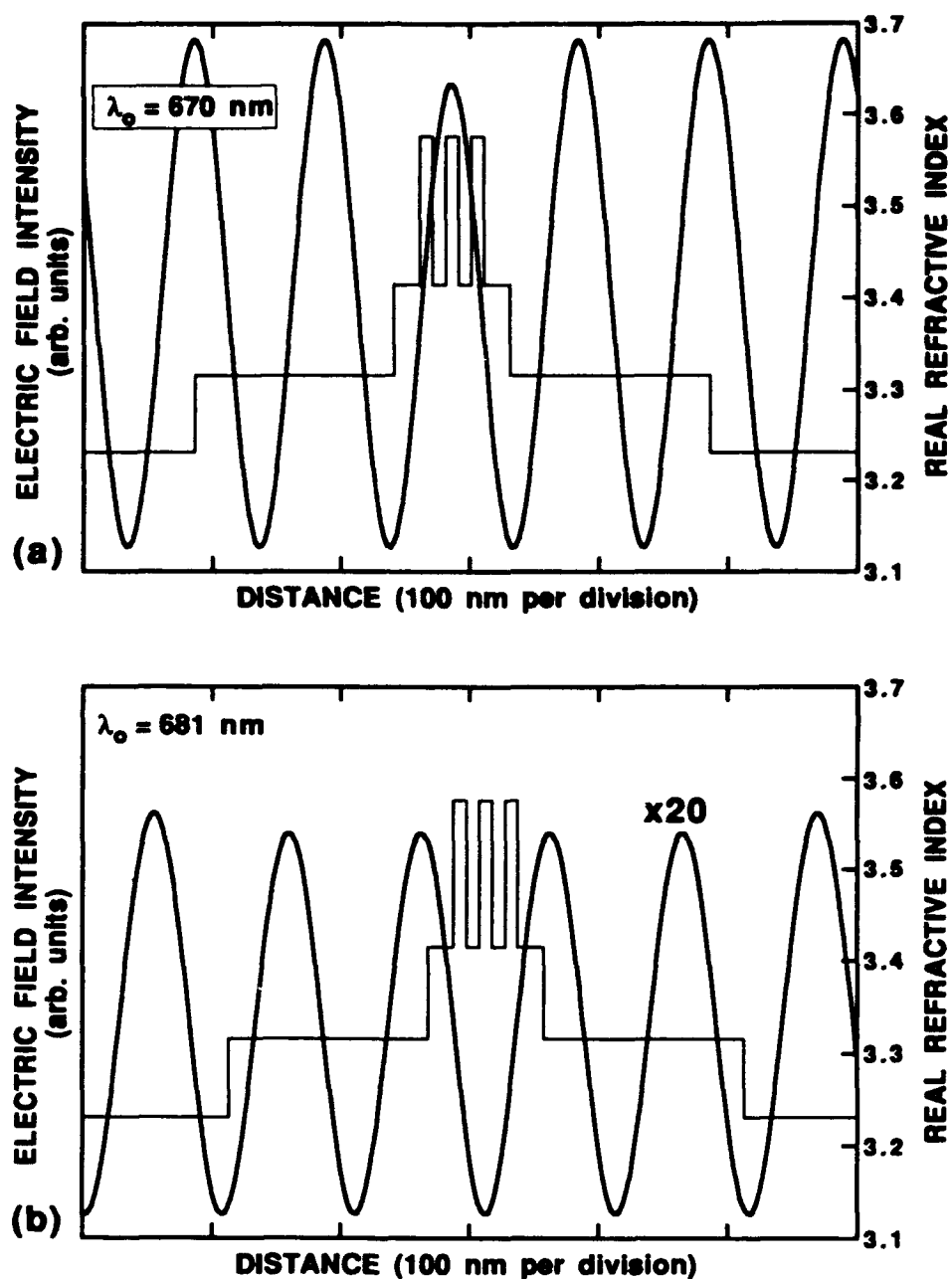


Fig 2.20 Calculated standing wave and refractive index profile for the 20λ thick example Fabry-Perot etalon structure near the center of the optical cavity active region at (a) 670 nm (the primary mode), and (b) 681 nm (a secondary mode).

$(\text{Al}_{0.4}\text{Ga}_{0.6})_{0.5}\text{In}_{0.5}\text{P}$ barrier layers have been added to the structure, centered in the optical cavity. The resonance at $\lambda_0 = 670$ nm corresponds to the primary Fabry-Perot resonance dip in Fig. 2.19(d). In contrast, Fig. 2.20(b) shows the electric field intensity in the optical cavity for the secondary resonance with $\lambda_0 = 681$ nm. This resonance is also seen as a Fabry-Perot dip in Fig. 2.19(d), but the standing wave peak (antinode) is offset from the quantum wells by a full half wavelength. Rather than a gain enhancement, just the opposite is true. The spontaneous emission is inhibited since the gain layers fall at a node of the standing wave.

The same resonant standing waves in Fig. 2.20 are plotted in Fig. 2.21, only this time at the interface of the optical cavity active region and the bottom DBR stack. For the primary Fabry-Perot resonance, the standing wave nodes lie in the center of every other 10 nm thick $\text{Al}_{0.75}\text{Ga}_{0.25}\text{As}$ barrier reduction layer. This is the effective point of the L to H index layer transitions, when moving from the optical cavity, through the DBR, toward the substrate (these points are readily defined for $\lambda/4$ stacks without the heterointerface grading). Similarly, the standing wave nodes lie at the L to H index transitions in the top DBR stack, when moving out from the optical cavity toward the surface. The reflectivity phase of the DBR is 0 radians at $\lambda_0 = 670$ nm. In contrast, the standing wave nodes of the secondary resonance do not line up precisely with the L to H index transitions, and the intensity peaks are reduced by over 20 times compared to the 670 nm resonance. The reflectivity phase of the bottom DBR at $\lambda_0 = 681$ nm is ~ 0.61 radian (35°), and the standing wave node eventually aligns to the L to H index at the far end of the DBR.

2.6 Design Considerations for Visible VCSELs

The optical design of visible VCSELs has been described in Sections 2.2 through 2.5. This Section discusses the design of complete visible VCSEL structures including the trade-offs between optical and electrical characteristics, and those due to the practical

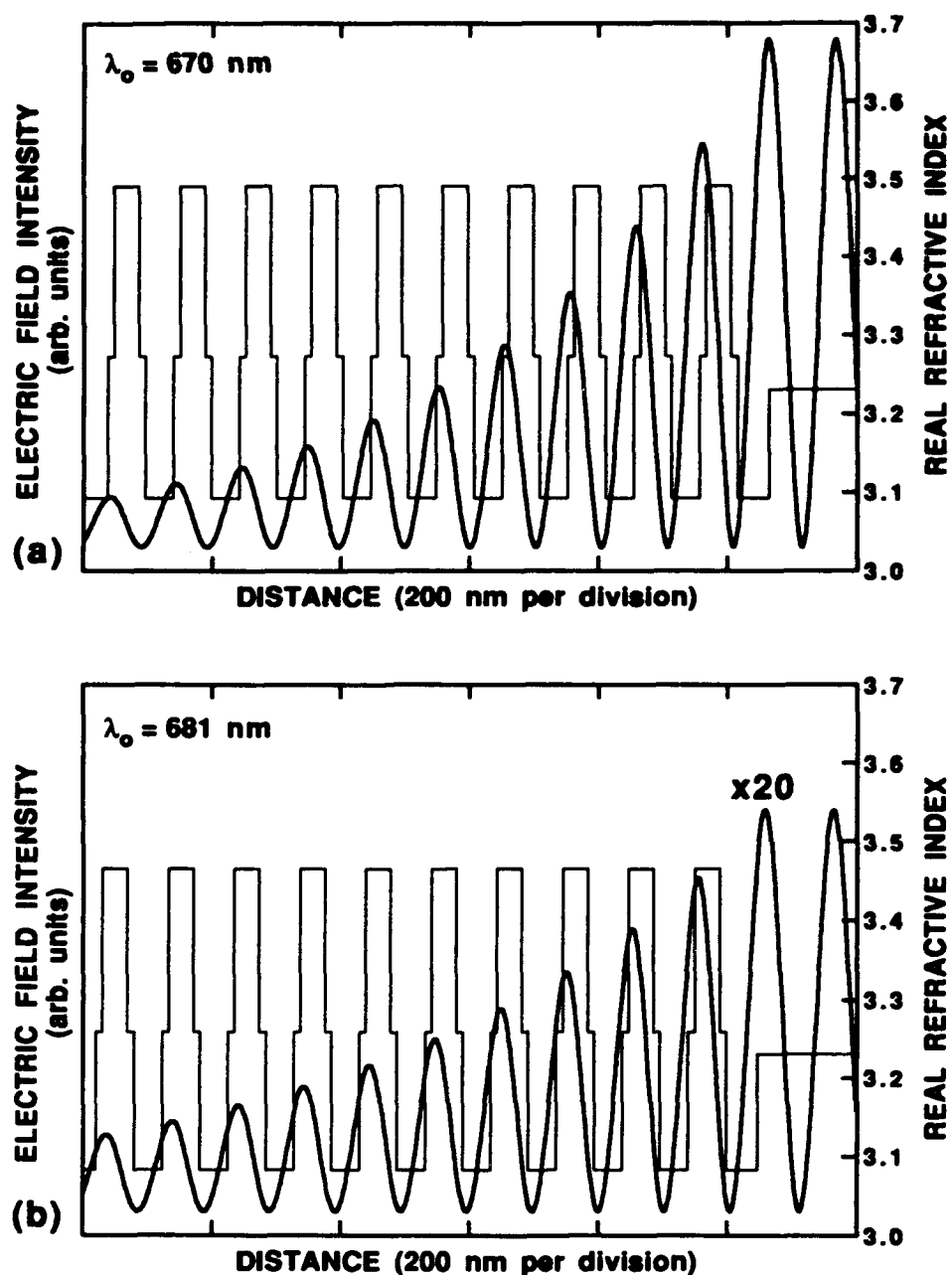


Fig 2.21 Calculated standing wave and refractive index profile for the 20λ thick example Fabry-Perot etalon structure near the interface between the optical cavity active region and the bottom DBR at (a) 670 nm (the primary mode), and (b) 681 nm (a secondary mode).

limitations of the materials and the current epitaxial growth technology. Resistance and temperature effects in visible VCSELs are examined for the first time. Also, quantum well gain and cavity losses are explored by using conventional models. The results are used in Chapters 3 and 5 to help explain the observed characteristics of the optically pumped and electrically injected visible VCSELs. Finally, this Section concludes with a comparison of conventional GaInAs/AlGaAs IR VCSELs and AlGaInP visible VCSELs.

2.6.1 DBR Resistance

As mentioned in Section 2.3, the DBRs are doped p and n-type on either side of the optical cavity. Based on data from IR VCSELs, it is essential that the resistance of the DBRs be as low as possible since large series resistances lead to excessive device heating and thus degraded performance [Tai *et al.* 1990, Yoffe 1991, Chalmers *et al.* 1993]. The DBR resistance is minimized by reducing the barriers at each heterointerface. This is accomplished by compositional grading and by using high doping densities to achieve high bulk conductivities. Current spreading and injection uniformity improves with increased doping, especially for top surface emitting devices [Nakwaski *et al.* 1992]. Unfortunately, increased doping density leads to increased free carrier absorption. This and other cavity loss mechanisms must then be overcome by increasing the optical gain, which is in-turn achieved by increasing the injection current density. Also important is the reduced reflectance at λ_0 of the DBRs when part of each of the L and H $\lambda/4$ layers are graded. As shown elsewhere [Born and Wolf 1975], given a pair of L and H index dielectric materials, the coating with the maximum reflectivity at λ_0 is obtained with a $\lambda/4$ stack configuration, rather than with index grading or chirping schemes. But the resulting conduction and valence energy band offsets between the $\lambda/4$ layers act as barriers to current flow and thus add series resistance. Compositional grading at the heterointerfaces greatly reduces these barriers. The reflectance lost due to the grading can

be regained by adding additional DBR pairs. An analytical method to calculate the DBR reflectance at λ_0 for various grading schemes has been reported by Corzine *et al.* [1991].

A first order analysis of the resistance of DBRs composed of AlAs/Al_{0.5}Ga_{0.5}As and of Al_{0.5}In_{0.5}P/(Al_{0.2}Ga_{0.8})_{0.5}In_{0.5}P is now given. Carrier transport across heterointerfaces has been investigated using both analytical and numerical techniques that include for example thermionic emission, and quantum mechanical tunneling and reflection [Wu and Yang 1979, Batey *et al.* 1985, Horio and Yanai 1990]. Here, carrier transport in the DBRs is modeled using thermionic emission theory. The current density is given by [Sze 1981]

$$J = A^* T^2 \exp\left(\frac{-q\phi_B}{k_B T}\right) \left[\exp\left(\frac{qV}{k_B T}\right) - 1 \right] \quad (\text{A/cm}^2) \quad (2.19)$$

where T is temperature, k_B is Boltzmann's constant, q is the electronic charge per electron, ϕ_B is the energy barrier, and V is the applied voltage. The effective Richardson constant A^* is given by

$$A^* = \frac{4 \pi q k_B^2 m^*}{h^3} \approx 120 \frac{m^*}{m_0} \quad (\text{A/cm}^2 \text{ K}^2) \quad (2.20)$$

where m^*/m_0 is the relative effective mass. For transport in p-doped layers, $m^* = (m_{lh}^* + m_{hh}^*)$, and in n-doped layers, $m^* = m_e^*$. The term ϕ_B is the energy difference between the barrier peak and the Fermi level. In bulk layers, the current is

$$J = \sigma E \quad (\text{A/cm}^2) \quad (2.21)$$

where the conductivity (σ) is related to the resistivity (ρ) and to the electron and hole mobilities (μ_n and μ_p) by

$$\sigma = \frac{1}{\rho} = q (\mu_n n + \mu_p p) \quad (\text{S/cm}) \quad (2.22)$$

The terms n and p are the densities of free electrons and holes, respectively, and the electric field $E = \text{Volts/length}$. The resistance of a bulk layer may also be given as

$$R = \rho \frac{\ell}{A} = \rho \frac{\text{length}}{\text{Area}} \quad (\Omega) \quad (2.23)$$

The space-charge neutral, real space energy band diagrams for 2.5 periods of example $\text{AlAs}/\text{Al}_x\text{Ga}_{1-x}\text{As}$ DBRs are given in Fig. 2.22. The solid line is the conduction band (E_c), and the dashed line is the valence band (E_v). Note that 1800 meV has been removed between E_c and E_v . The Bragg design wavelength is $\lambda_0 = 650 \text{ nm}$. Plot (a) is the case for alternating $\lambda/4$ layers without any grading at the heterointerface, with $d_H \approx 46 \text{ nm}$ and $d_L \approx 52 \text{ nm}$. In plots (b) and (c), a 10 nm thick $\text{Al}_{0.75}\text{Ga}_{0.25}\text{As}$ barrier reduction layer at the heterointerface is employed, as in Table 2.1. Plot (d) has a 10 nm thick grade at the heterointerface where the composition of $\text{Al}_x\text{Ga}_{1-x}\text{As}$ varies linearly from $x = 1.0$ to 0.5, and from 0.5 to 1.0. Plot (e) is similar to plot (d), except that the 10 nm thick grade is a half sinusoid.

Poisson's equation in one-dimension, is solved numerically for the set of example DBR heterostructures by using a computer program developed by C. P. Tigges [1993]. The material parameters are those given in Appendix A. The rigid steady-state solution to Poisson's equation defines the energy band offsets at each heterointerface. These band offsets are then used with the thermionic emission model to estimate the

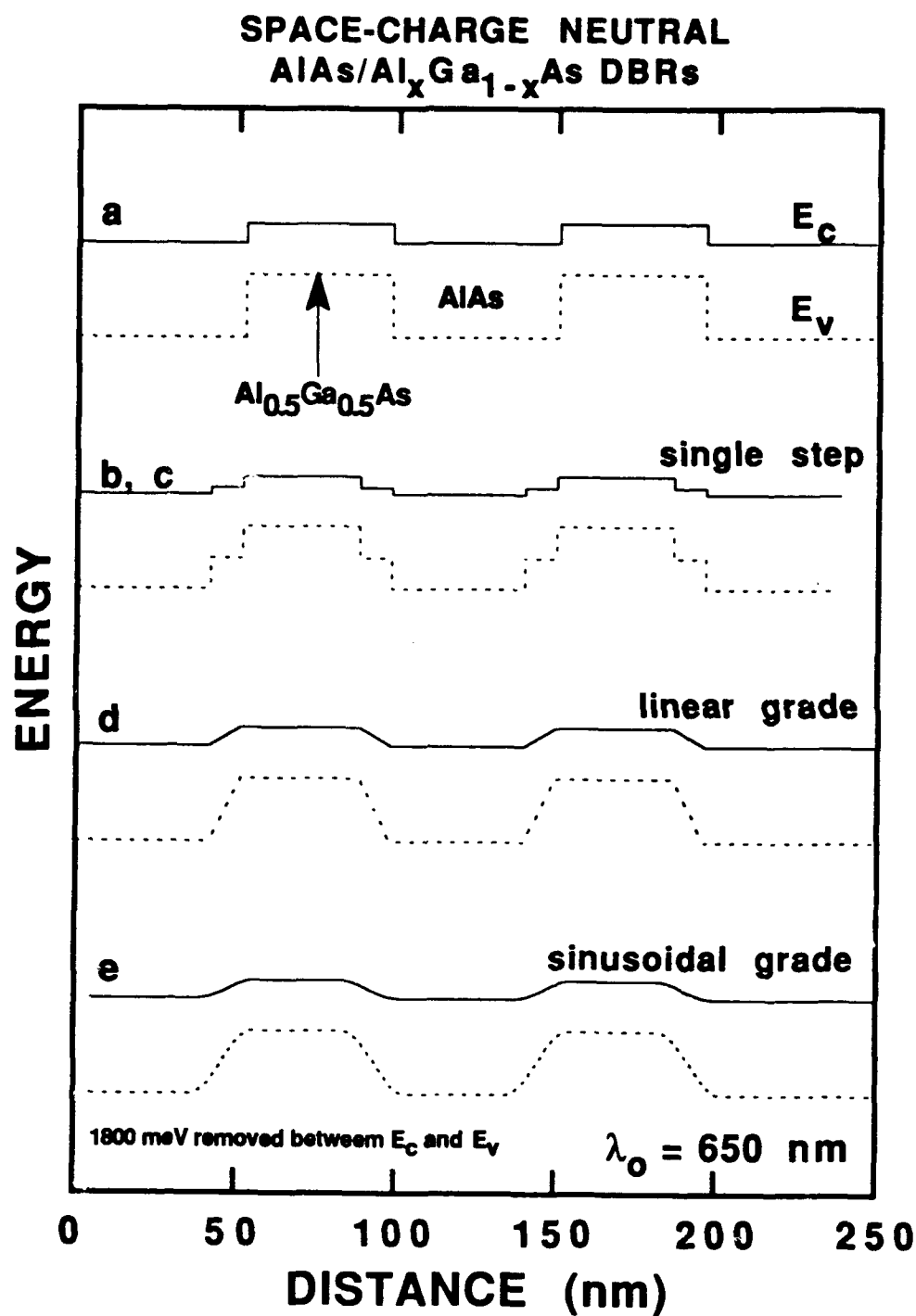


Fig 2.22 Real space energy band diagrams for example AlAs/ $\text{Al}_x\text{Ga}_{1-x}\text{As}$ DBRs. Conduction band (solid line), and valence band (dashed line).

voltage drop at each heterointerface. Figure 2.23 shows the conduction band and Fermi level of n-doped structures. The doping density is $2 \times 10^{18} \text{ cm}^{-3}$, except in plot 2.22(c), where 5 nm thick doping spikes of $1 \times 10^{19} \text{ cm}^{-3}$ have been placed in the AlAs and the $\text{Al}_{0.75}\text{Ga}_{0.25}\text{As}$. This pulse doping, placed at the nodes of the on-resonance standing wave, is thought to be useful for current spreading in laterally injected VCSELs [Scott *et al.* 1993] with minimal added free carrier absorption. Figure 2.24 shows the valence band and Fermi level of the corresponding p-doped structures. Since the layers are very nearly lattice matched, no distinction is made between the light-hole and the heavy hole bands. The p-doping density is $4 \times 10^{18} \text{ cm}^{-3}$ in the AlAs layers, $3 \times 10^{18} \text{ cm}^{-3}$ in the $\text{Al}_x\text{Ga}_{1-x}\text{As}$ layers ($0.5 < x < 1.0$), and $2 \times 10^{18} \text{ cm}^{-3}$ in the $\text{Al}_{0.5}\text{Ga}_{0.5}\text{As}$ layers, except in plot 2.23(c) as above, where additional $5 \times 10^{19} \text{ cm}^{-3}$ doping spikes are used.

The bulk resistance of a given DBR structure is calculated with Eq. (2.23) for a given area by neglecting current spreading. Table 2.4 lists estimated values for the conductivities. Note that the free carrier densities, taken from the solution to the Poisson

Table 2.4 Estimated Mobility and Conductivity of Selected Epitaxial Layers

Material	Dopant	Free Carrier Density ($\times 10^{17} \text{ cm}^{-3}$)	Mobility ($\text{cm}^2/\text{V-s}$)	Conductivity (S/cm)
(p) $\text{Al}_{0.5}\text{Ga}_{0.5}\text{As}$	C	$p \sim 4.0$	80	5.1
(n) $\text{Al}_{0.5}\text{Ga}_{0.5}\text{As}$	Si	$n \sim 7.0$	400	44.9
(p)AlAs	C	$p \sim 4.0$	50	3.2
(n)AlAs	Si	$n \sim 7.0$	150	16.8
(p) $\text{Ga}_{0.5}\text{In}_{0.5}\text{P}$	Mg	$p \sim 4.0$	50	3.2
(n) $\text{Ga}_{0.5}\text{In}_{0.5}\text{P}$	Si	$n \sim 7.0$	700	78.5
(p) $\text{Al}_{0.5}\text{In}_{0.5}\text{P}$	Mg	$p \sim 4.0$	20	1.3
(n) $\text{Al}_{0.5}\text{In}_{0.5}\text{P}$	Si	$n \sim 7.0$	100	11.2

estimated, based on data from [Schneider and Figiel 1993, Bour 1993c]

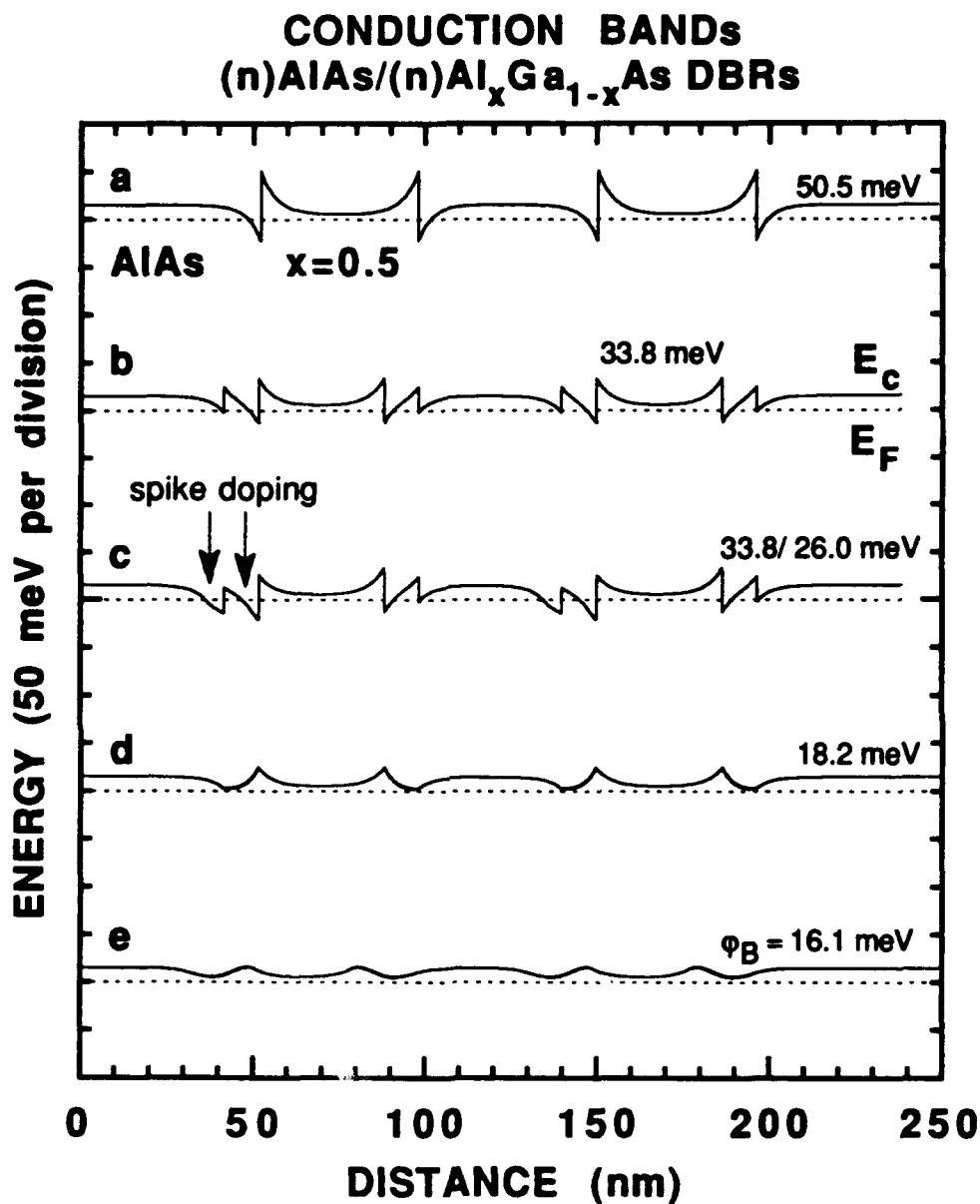


Fig 2.23 Conduction band diagrams for example (n)AlAs/(n)Al_xGa_{1-x}As DBRs. Conduction band (solid line), and Fermi level (dashed line). The doping density is $2 \times 10^{18} \text{ cm}^{-3}$. Calculated data obtained by numerically solving the 1-D Poisson equation.

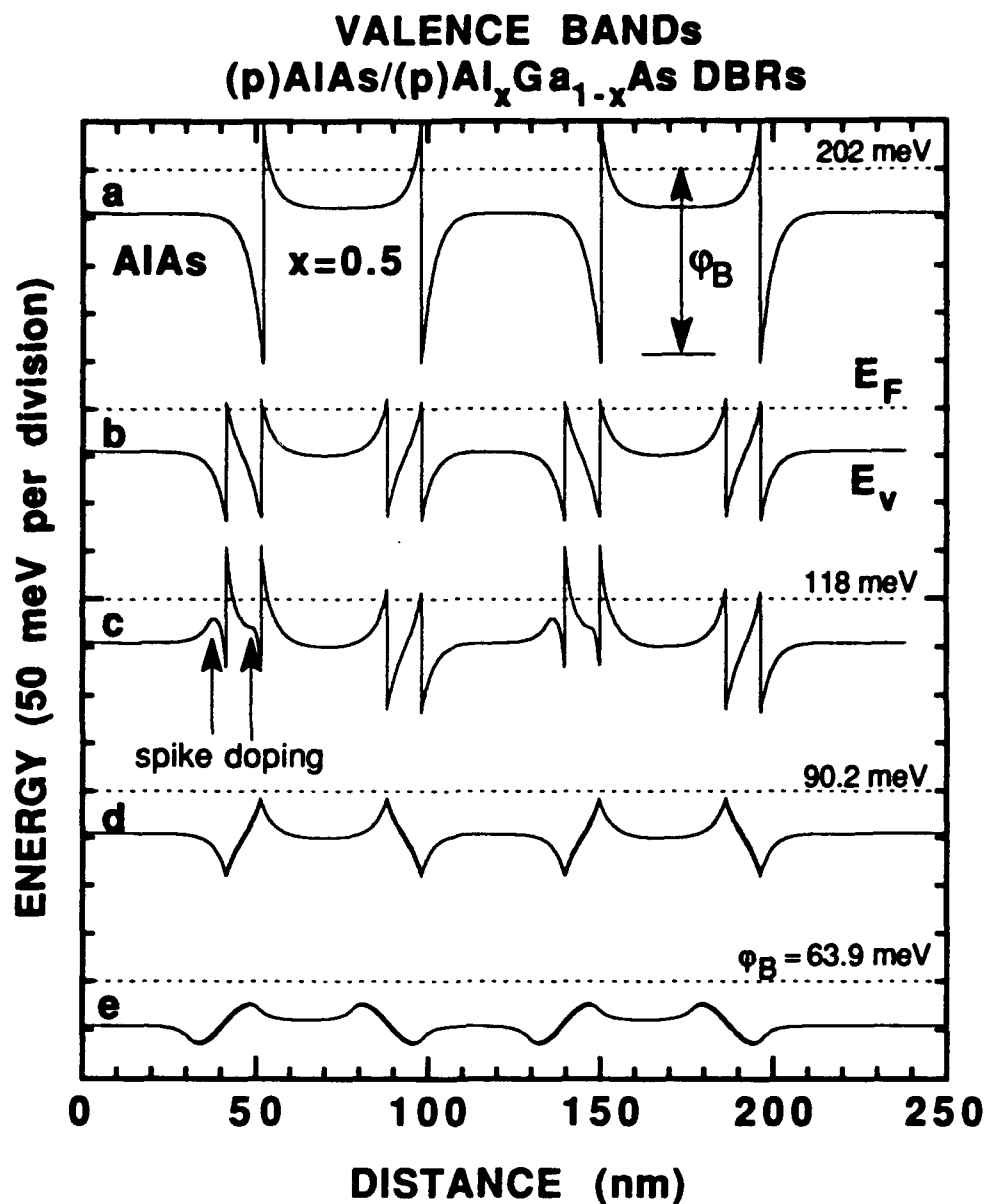


Fig 2.24 Valence band diagrams for example (p)AlAs/(p)Al_xGa_{1-x}As DBRs. Valence (heavy-hole) band (solid line), and Fermi level (dashed line). The doping density is $4 \times 10^{18} \text{ cm}^{-3}$ in the AlAs, $3 \times 10^{18} \text{ cm}^{-3}$ in the Al_xGa_{1-x}As ($0.5 < x < 1.0$), and $2 \times 10^{18} \text{ cm}^{-3}$ in the Al_{0.5}Ga_{0.5}As. Calculated data obtained by numerically solving the 1-D Poisson equation.

equation, are smaller than the doping densities due to partial ionization of the donors and acceptors. From Eq. (2.23), the bulk vertical resistance of the (n)DBR in Fig. 2.23(a) with a 20 μm diameter circular contact is $R \sim 0.131 \Omega/\text{DBR period}$, or $\sim 7.2 \Omega$ for 55 periods. The bulk vertical resistance of the (p) DBR in Fig. 2.24(a) with a 20 μm diameter circular contact is $R \sim 0.80 \Omega/\text{DBR period}$, or $\sim 29 \Omega$ for 36 periods.

The space-charge neutral, real space energy band diagrams for 2.5 periods of example $\text{Al}_{0.5}\text{In}_{0.5}\text{P}/(\text{Al}_{0.2}\text{Ga}_{0.8})_{0.5}\text{In}_{0.5}\text{P}$ DBRs are given in Fig. 2.25. The solid line is the conduction band (E_c), and the dashed line is the valence band (E_v). Note that 2000 meV has been removed between E_c and E_v . The Bragg design wavelength is $\lambda_0 = 650 \text{ nm}$. Plot (a) is the case for alternating $\lambda/4$ layers without any grading at the heterointerface, with $d_H \approx 46 \text{ nm}$ and $d_L \approx 50 \text{ nm}$. In plot (b), a 10 nm thick $(\text{Al}_{0.6}\text{Ga}_{0.8})_{0.5}\text{In}_{0.5}\text{P}$ barrier reduction layer is inserted at the heterointerface. In plot (c), a 10 nm thick $(\text{Al}_{0.35}\text{Ga}_{0.65})_{0.5}\text{In}_{0.5}\text{P}$ barrier reduction layer is inserted at the heterointerface. The single steps in (b) and (c) divide the valence and conduction band offsets in half, respectively. (The stepping compositions were determined from Fig. A.9 in Appendix A. The compositions of the $(\text{Al}_y\text{Ga}_{1-y})_{0.5}\text{In}_{0.5}\text{P}$ layers that divide the valence and conduction bands in half, depend on the band offsets that are used, and are thus estimates in the example calculations). Plot (d) has a 20 nm thick grade at the heterointerface where the composition of $(\text{Al}_y\text{Ga}_{1-y})_{0.5}\text{In}_{0.5}\text{P}$ varies linearly from $y = 0.55$ to 0.2, and from 0.2 to 0.55. (Linear grading from $y = 0.2$ to $y = 1.0$ in AlGaInP DBRs has been previously reported [Schneider *et al.* 1992]). Plots (e) and (f) are similar to plot (d), except that the 20 nm thick grade is a half sinusoid. The grading range for plot (e) is $y = 0.55$ to 0.2 and is designed to result in the lowest possible conduction band barrier. In contrast, the grading range for plot (f) is $y = 1.0$ to 0.2 and is designed to result in the lowest possible valence band barrier.

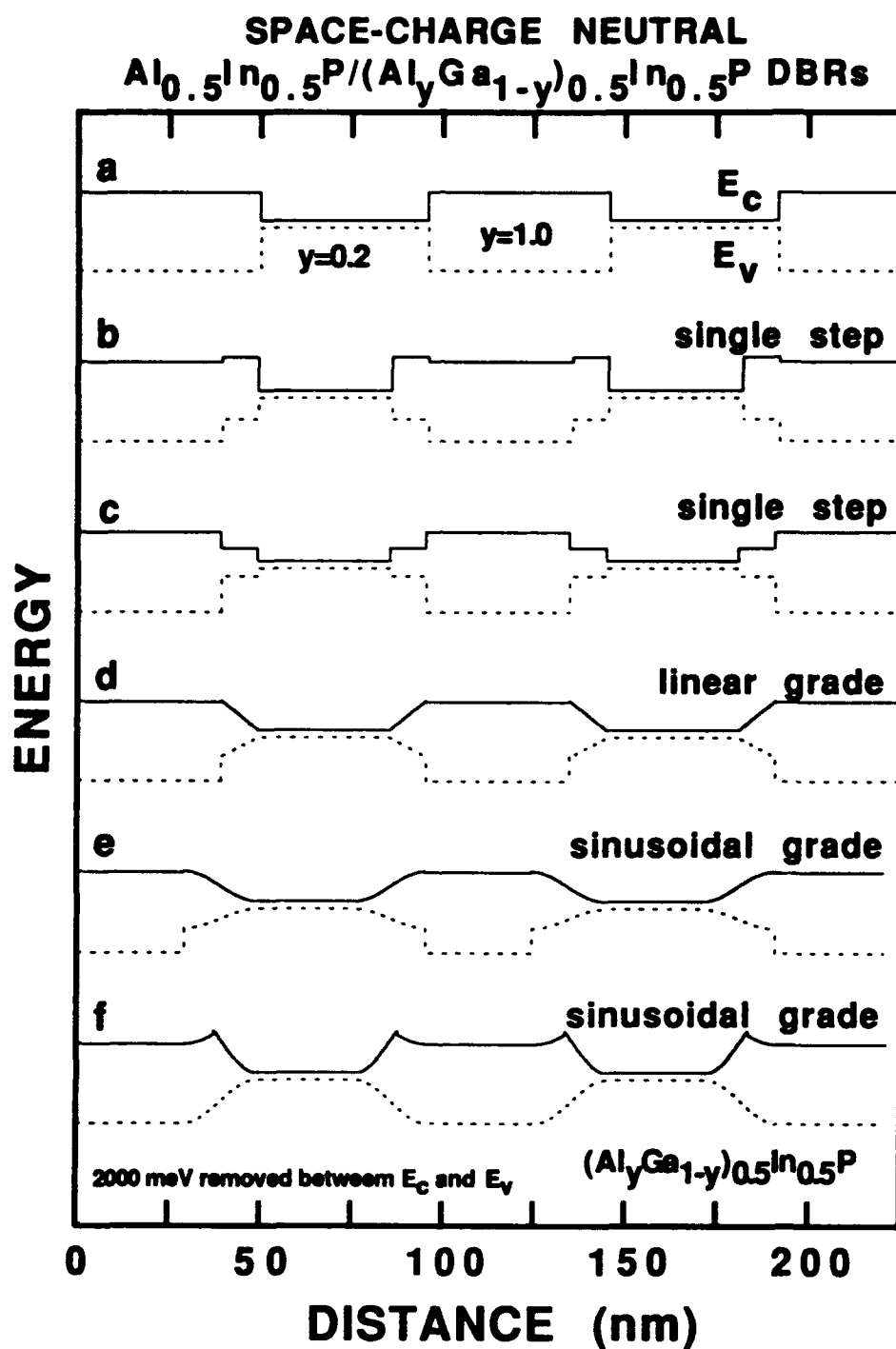


Fig 2.25 Real space energy band diagrams for example $\text{Al}_{0.5}\text{In}_{0.5}\text{P}/(\text{Al}_y\text{Ga}_{1-y})_{0.5}\text{In}_{0.5}\text{P}$ DBRs. Conduction band (solid line), and valence band (dashed line).

Poisson's equation is solved as above. Figure 2.26 shows the conduction band and Fermi level of n-doped structures. The doping density is $2 \times 10^{18} \text{ cm}^{-3}$ in all layers. Figure 2.27 shows the valence band and Fermi level of the corresponding p-doped structures. Since the layers are very nearly lattice matched, no distinction is made between the light-hole and the heavy hole bands. The p-doping density is $1 \times 10^{18} \text{ cm}^{-3}$ in the $(\text{Al}_y\text{Ga}_{1-y})_{0.5}\text{In}_{0.5}\text{P}$ layers when $y \geq 0.7$, and $2 \times 10^{18} \text{ cm}^{-3}$ otherwise. The resulting conductivities, corrected for partial ionization, are given in Table 2.4

Table 2.5 is a summary of the voltage drop analysis for the AlGaAs and AlGaInP DBR structures. The resistance of the (n)AlGaAs DBR is dominated by the bulk resistance. For the (p)AlGaAs DBR, the simple step grade greatly reduces the resistance. The resistance of the (n)AlGaInP DBR is dominated by the bulk resistance, as is the (p)AlGaInP DBR. The bulk resistance is relatively high because it is difficult to p-dope the $\text{Al}_{0.5}\text{In}_{0.5}\text{P}$ above $\sim 1 \times 10^{18} \text{ cm}^{-3}$. The resistance could be reduced by increasing the doping density of the $(\text{Al}_{0.2}\text{Ga}_{0.8})_{0.5}\text{In}_{0.5}\text{P}$ layers above $2 \times 10^{18} \text{ cm}^{-3}$ with either Mg or Zn [Schneider *et al.* 1992].

2.6.2 Gain, Loss, and Temperature Effects

This Section overviews some key aspects of VCSEL design. The ideal VCSEL has a very low current and voltage threshold, high efficiency, and high output power. For the ideal visible VCSEL, the resistance of the DBRs is low, the injection efficiency and internal quantum efficiency are high, (i.e. the differential gain (dg/dJ) is high), the carrier leakage current from the quantum wells is low, absorptive losses are small, and the device temperature stays reasonably constant by extracting heat efficiently. In practical devices, heating causes shifts (at different rates) of both the Fabry-Perot resonance mode and the peak of the spectral gain. Optimum performance occurs when the mode and gain peak are aligned. The mode and gain could be made to align at higher currents to maximize the

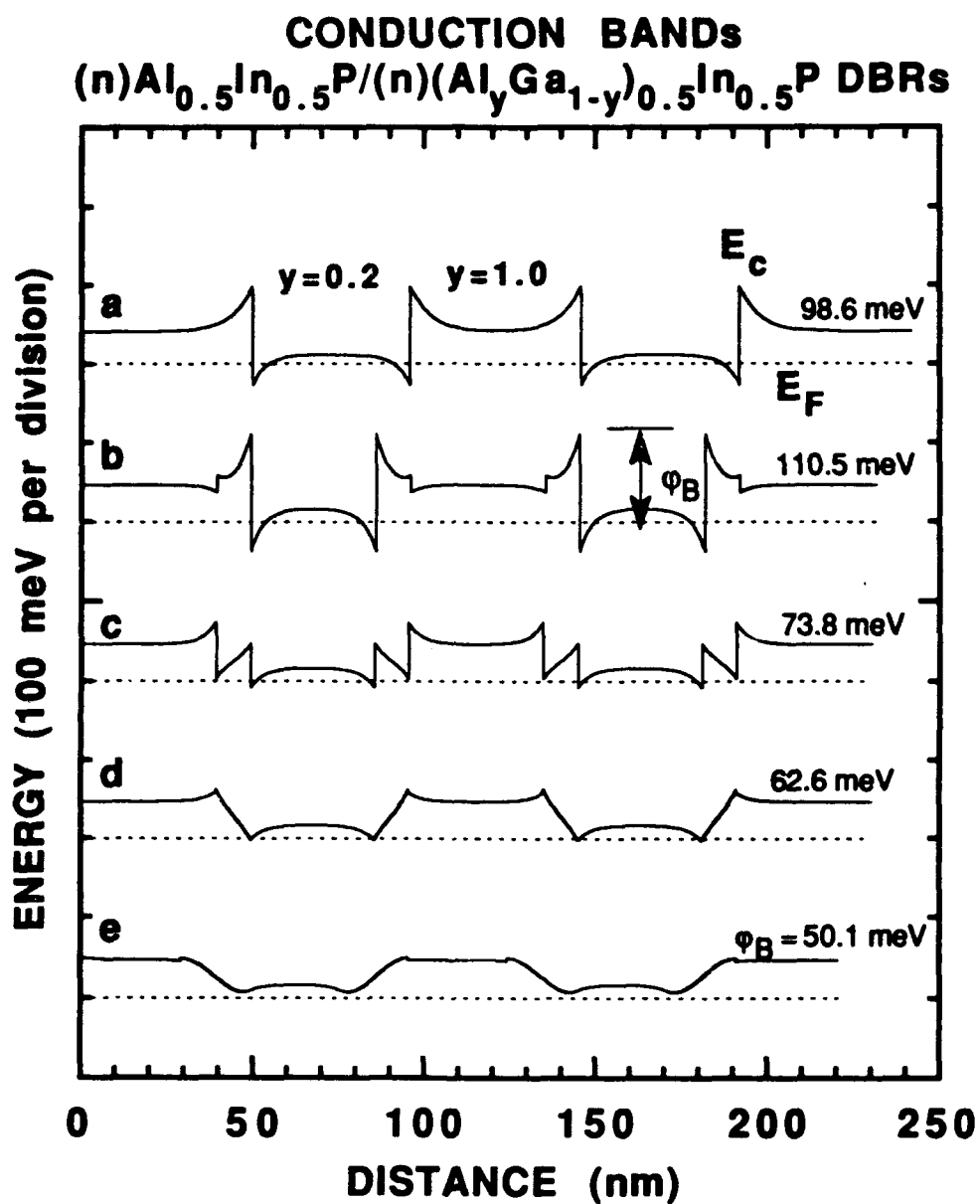


Fig 2.26 Conduction band diagrams for example $(n)\text{Al}_{0.5}\text{In}_{0.5}\text{P}/(n)\text{Al}_y\text{Ga}_{1-y})_{0.5}\text{In}_{0.5}\text{P}$ DBRs. Conduction band (solid line), and Fermi level (dashed line). The doping density is $2 \times 10^{18} \text{ cm}^{-3}$. Calculated data obtained by numerically solving the 1-D Poisson equation.

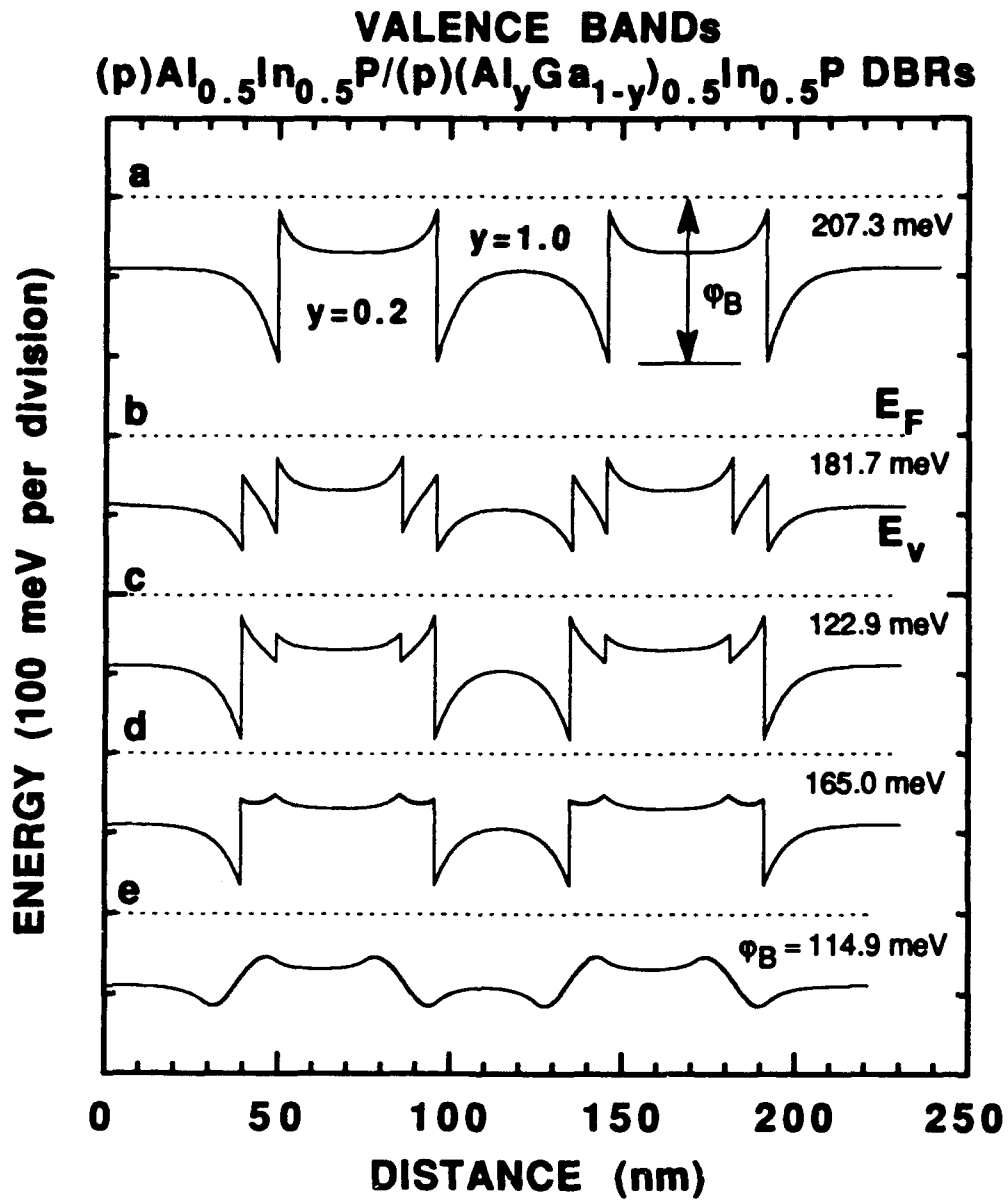


Fig 2.27 Valence band diagrams for example (p)Al_{0.5}In_{0.5}P/(p)(Al_yGa_{1-y})_{0.5}In_{0.5}P DBRs. Valence (heavy-hole) band (solid line), and Fermi level (dashed line). The doping density is $1 \times 10^{18} \text{ cm}^{-3}$ in the layers with $y \geq 0.7$, and $2 \times 10^{18} \text{ cm}^{-3}$ in all other layers. Calculated data obtained by numerically solving the 1-D Poisson equation.

Table 2.5 Summary of the DBR Voltage Drop Analysis
($J = 2 \text{ kA/cm}^2$, and $T = 300\text{K}$)

DBR Structure	Φ_B (meV)	Heterointerface Voltage Drop ($\mu\text{V/DBR period}$)	Total Voltage Drop (mV)
(n) $\text{Al}_x\text{Ga}_{1-x}\text{As}$ (where $m_e^*/m_0 \sim 0.8$, the bulk voltage drop is $\sim 824 \mu\text{V/DBR period}$)			
			(55.5 (n) DBR periods)
a	50.49	42.2	48.1
b	33.81	22.1	47.0
c	33.81/25.97	22.1/16.3	46.8
d	18.17	12.1	46.4
e	16.12	11.2	46.4
(p) $\text{Al}_x\text{Ga}_{1-x}\text{As}$ (where $m_h^*/m_0 \sim 0.52$ and the bulk voltage drop is $\sim 1.81 \text{ mV/DBR period}$)			
			(36 (p) DBR periods)
a	201.67	16,172	647.4
b	118.25	877.1	96.7
c	118.25/70.35	877.1/139.5	83.5
d	90.22	300.0	76.0
e	63.92	108.9	69.0
(n)($\text{Al}_y\text{Ga}_{1-y}$) $_{0.5}\text{In}_{0.5}\text{P}$ (where $m_e^*/m_0 \sim 0.62$, and the bulk voltage drop is $\sim 1.01 \text{ mV/DBR period}$)			
			(60.5 (n) DBR periods)
a	98.55	346.9	82.1
b	110.51	548.8	94.3
c	73.82	133.8	69.2
d	62.61	86.8	66.4
e	50.121	53.6	64.4
(p)($\text{Al}_y\text{Ga}_{1-y}$) $_{0.5}\text{In}_{0.5}\text{P}$ (where $m_h^*/m_0 \sim 0.4$ and the bulk voltage drop is $\sim 10.6 \text{ mV/DBR period}$)			
			(45 (p) DBR periods)
a	207.25	22,658	1,497
b	122.90	1,352	537.8
c	181.73	10,869	966.1
d	164.95	6,242	757.9
f	114.90	999.3	522.0

output power, or to achieve operation over a broad temperature range [Peters *et al.* 1993, Young *et al.* 1993]. Alternately, alignment with minimal heating leads to a low threshold current. The visible VCSELs in this dissertation are prototype devices, and not all of the above factors were directly investigated. However, the following factors were addressed for the initial demonstrations.

The available gain from a given quantum well or wells, is primarily an intrinsic property of the well and barrier material. As discussed in Section 2.3, strained wells are used to reduce the carrier density required for inversion, increase the differential gain at low carrier densities, and as a design parameter to select an emission wavelength. A first order model to calculate the spectral gain from quantum wells is given in Appendix D. This model is useful for relative comparisons between material systems, and for semi-quantitative descriptions of band filling, and gain due to contributions from the first and/or second quantum well states. This is further discussed in Subsection 2.6.3.

As briefly described in Section 2.2, the position of quantum well(s) in an optical cavity is an important design criterion, and results in either enhanced or inhibited spontaneous emission. The equivalent phenomena in VCSELs is usually referred to as resonant periodic gain [Raja *et al.* 1989, Corzine *et al.* 1989]. Figure 2.28 shows the standing wave pattern for an example visible VCSEL structure. The optical cavity active region consists of a single 10 nm thick $\text{Ga}_{0.45}\text{In}_{0.55}\text{P}$ quantum well, positioned in the center of the optical cavity, surrounded by 20 nm thick $(\text{Al}_{0.4}\text{Ga}_{0.6})_{0.5}\text{In}_{0.5}\text{P}$ barrier layers, in-turn surrounded by $(\text{Al}_{0.7}\text{Ga}_{0.3})_{0.5}\text{In}_{0.5}\text{P}$ spacer layers. The DBRs are $\lambda/4$ layers of AlAs and $\text{Al}_{0.5}\text{Ga}_{0.5}\text{As}$ with 20 periods on the top, and 30.5 periods on the bottom. In Fig. 2.28(a), the optical cavity is 2λ thick, and the first DBR layers are AlAs with a L index. The quantum well is positioned at the standing wave antinode for maximum gain. Note that the nodes of the standing wave lie at the L to H index transitions in the DBRs, when moving away from the optical cavity in either direction. In

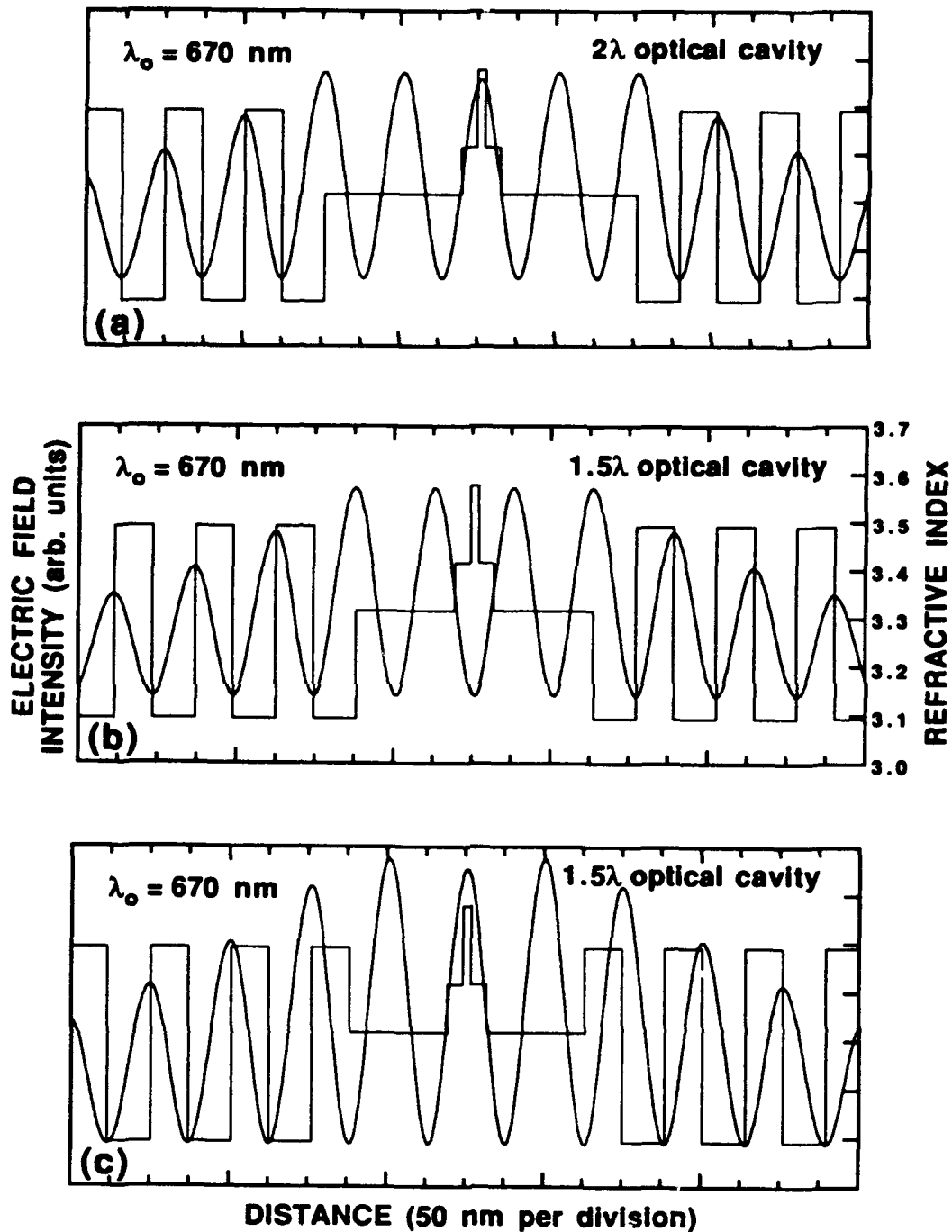


Fig 2.28 Calculated electric field intensity (standing wave) for three example visible VCSELs. The AlGaInP optical cavity active region is surrounded by AlAs/Al_{0.5}Ga_{0.5}As DBRs. The thickness of the optical cavity is (a) 2λ , (b) 1.5λ , and (c) 1.5λ . For VCSEL design, a standing wave antinode should peak at the quantum well(s) gain layer(s), as in (a) and (c).

Fig. 2.28(b), the thickness of the optical cavity is decreased to 1.5λ (by thinning the $(\text{Al}_{0.7}\text{Ga}_{0.3})_{0.5}\text{In}_{0.5}\text{P}$) and the quantum well now falls at a standing wave node, while the standing wave in the DBRs is unchanged. This configuration is undesirable since the optical gain is inhibited. The quantum well could be moved $\lambda/4$ in either direction so that it again lies at an antinode. However, for the epitaxial layer growth, the results are more consistent if the quantum well(s) is placed at the center of the optical cavity. In Fig. 2.28(c), the first set of $L \lambda/4$ layers are removed while retaining the 1.5λ thick optical cavity, and the quantum well again lies at a standing wave antinode. Thus, some flexibility exists in the choice between d_{oc} and the relative index of the first DBR layers.

The relevant equations describing gain and loss in VCSELs (repeated here for convenience, see Eqs (2.3) to (2.6)), are

$$\Gamma_r g_{\text{th}} d = \alpha_i L + \alpha_m L_m + \alpha_{\text{oc}}(d_{\text{oc}} - L) + \ln[1/R] \quad (\text{unitless}) \quad (2.24)$$

with α_i given by

$$\alpha_i = \Gamma_z \alpha_a + (1 - \Gamma_z) \alpha_p + \alpha_{\text{scat}} \quad (\text{cm}^{-1}) \quad (2.25)$$

It is important to consider the relative magnitudes of the loss terms in the above equations. The scattering loss (α_{scat}) due to sidewall roughness is not important for ion implanted devices or for devices with diameters of $5 \mu\text{m}$ or larger. The interface scattering loss contained within α_m is also very small due to the high precision of the epitaxial growth process and can be neglected [Gourley *et al.* 1991]. Absorptive losses within the layers are minimized by using above energy bandgap materials in all layers, except the quantum wells. This leaves free carrier absorptive losses, which are contained within the terms α_a , α_{oc} , and α_m . For GaAs at 300K and for energies near the bandgap,

the free carrier absorption loss coefficient is $\alpha_{fc} \approx 3 \times 10^{-18}n + 7 \times 10^{-18}p$ (cm^{-1}) [Casey and Panish 1978]. A similar relationship is plausible for the AlGaInP and AlGaAs materials used in visible VCSELs. With typical carrier densities of ~ 1 to $7 \times 10^{18} \text{ cm}^{-3}$, $\alpha_{fc} \approx 10$ to 70 cm^{-1} . Consider an example visible VCSEL with three 6 nm thick quantum wells such that $\Gamma_z = 0.347$, $\Gamma_r = 1.779$, $L = 92 \text{ nm}$, $L_m = 900 \text{ nm}$, $d = 18 \text{ nm}$, $\alpha_p = \alpha_{oc} = 20 \text{ cm}^{-1}$, $\alpha_a = \alpha_m = 50 \text{ cm}^{-1}$, and let $R = 0.99925$. From Eq. (2.24), $g_{th} = 1891 \text{ cm}^{-1}$ with the given free carrier losses, and $g_{th} = 234 \text{ cm}^{-1}$ without the given free carrier losses. Minimizing the free carrier losses is accomplished primarily by reducing the doping in the DBRs. This, however, increases the series resistance and leads to device heating and reduced optical gain. The free carrier absorption is higher for p-doped material. Additionally, the resistance of p-doped DBRs is higher than the equivalent n-doped DBRs. An interesting alternative design for VCSELs is to replace all or part of the (p)DBR with a dielectric stack as described in Subsection 2.4.4.

Now consider the number and thickness of the quantum wells, and the thickness of the layers that separate them. Increasing the number of wells increases the available gain and thus higher output powers are possible, but at the expense of increased threshold current density (for a given R). The desired emission wavelength puts limits on the thickness and composition (i.e. percent strain) of the quantum wells. The idea is to maximize the available gain per unit length, for the total length of quantum wells used. Table 2.6 is a summary of gain calculations for visible VCSELs emitting at $\lambda_0 = 650 \text{ nm}$. The thickness of the quantum wells and separation layers are varied, as is the number of wells centered in the optical cavity. A comparison can be made for the structures that have the same total gain length d . For example, five 6 nm wells and three 10 nm wells both give $d = 30 \text{ nm}$. The value of g_{th} is 168.8 cm^{-1} for the five 6 nm wells with 6 nm separation layers, and is 155.9 cm^{-1} and 175.3 cm^{-1} for the 10 nm wells with 6 nm

and 10 nm separation layers, respectively. The lowest g_{th} indicates the best design choice, assuming uniform gain in each well.

Table 2.6 Summary of Example Gain Calculations. The quantum wells are $Ga_{1-x}In_xP$, and the barrier separation layers are $(Al_{0.4}Ga_{0.6})_{0.5}In_{0.5}P$. The Bragg design wavelength is $\lambda_0 = 650$ nm (obtained by varying the amount of strain for a given quantum well thickness). The threshold gain is calculated with $R = 0.99925$, and the absorptive losses are neglected for the calculation of g_{th} .

Number of QWs	QW/Barrier Thickness (nm/nm)	g_{th} (cm^{-1})	Total Gain thickness d (nm)	Longitudinal Confinement Factor Γ_z	Relative Confinement Factor Γ_r
1	6	626.9	6	0.129	1.995
2	6/6	324.3	12	0.247	1.928
3	6/6	234.3	18	0.347	1.779
4	6/6	191.0	24	0.422	1.637
5	6/6	168.8	30	0.473	1.482
1	8	487.6	8	0.171	1.923
2	8/6	249.0	16	0.324	1.883
3	8/6	179.5	24	0.446	1.741
4	8/6	159.5	32	0.523	1.470
5	8/6	147.2	40	0.562	1.274
1	10	391.2	10	0.213	1.918
2	10/6	203.3	20	0.398	1.845
3	10/6	155.9	30	0.529	1.604
4	10/6	136.2	40	0.603	1.377
5	10/6	130.6	50	0.626	1.149
1	10	391.2	10	0.213	1.918
2	10/10	217.5	20	0.383	1.725
3	10/10	175.3	30	0.476	1.427
4	10/10	166.2	40	0.502	1.129

As described previously, the temperature of the VCSEL increases during operation. The rise in temperature causes a decrease in the material refractive indices and thus the DBR reflectance shifts to longer wavelengths [Dudley *et al.* 1992]. The increased temperature also reduces the bandgap of the active region gain layers causing a red shift in the spectral gain. The gain shifts long at a faster rate than does the DBR. Figure 2.29 shows the temperature characteristics of two example FPE structures. Both FPEs have a 2λ thick AlGaInP quantum well optical cavity active region. The hybrid structure is then surrounded by $\lambda/4$ Al_{0.5}In_{0.5}P layers, followed by AlGaAs DBRs as in Table 2.1 with 50 bottom and 5.5 top periods. The all-phosphide structure has DBRs as in Table 2.2, with 60.5 bottom and 5 top periods. The reflectance spectra of the FPEs are monitored at three points as a function of temperature, including the two side reflectance minima, and the Fabry-Perot resonance. The rate of change of the three reflectance points is summarized in Table 2.7. The shifts are due primarily to the changing refractive indices of the DBRs with temperature. The hybrid structure shifts at a faster rate than does the all-phosphide structure, and this indicates that the refractive indices of AlGaAs decrease faster with increasing temperature than do those of AlGaInP.

Figure 2.30 is a plot of the Fabry-Perot resonance and spectral gain peak as functions of temperature for an example hybrid visible VCSEL structure. The spectral gain peak overlaps with the Fabry-Perot resonance at only one temperature (325K). The inset in Fig. 2.30 shows an example reflectance and optical gain spectra. With increasing temperature due to increasing current, the gain peak shifts through and past the Fabry-Perot resonance. As a result, the light intensity-current (L-I) characteristic of VCSELs typically rises sharply and then rolls over as described in [Hasnain *et al.* 1991]. By varying the initial alignment of the Fabry-Perot resonance and the optical gain peak, it is possible to maximize the coupling of the gain to the mode at different device operating temperatures.

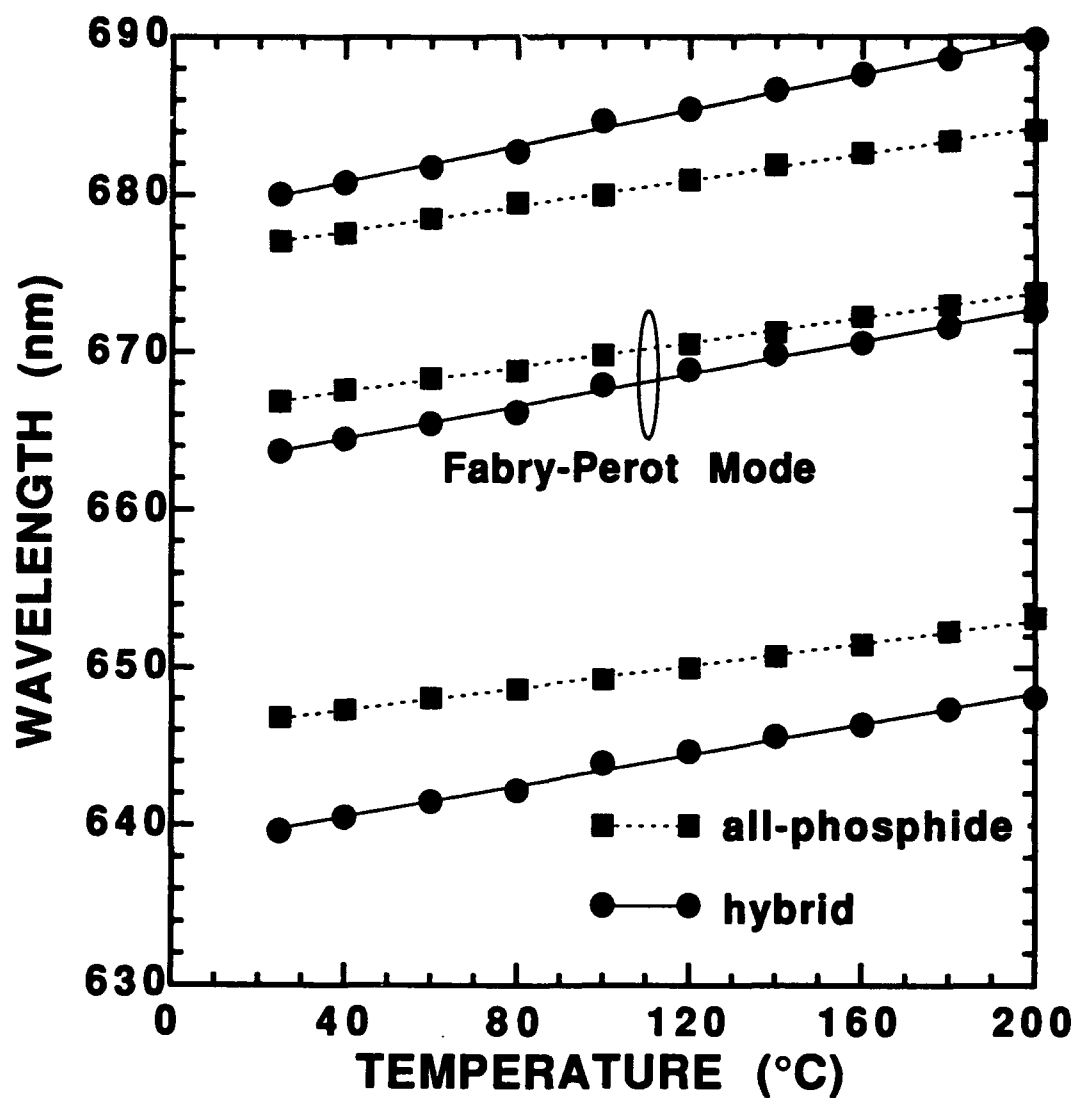


Fig 2.29 Reflectance of hybrid AlGaAs/AlGaInP and all-AlGaInP Fabry-Perot etalons as a function of temperature. The three lines for each structure correspond to the Fabry-Perot resonance mode, and the edges of the reflectance bandwidth (see Table 2.7).

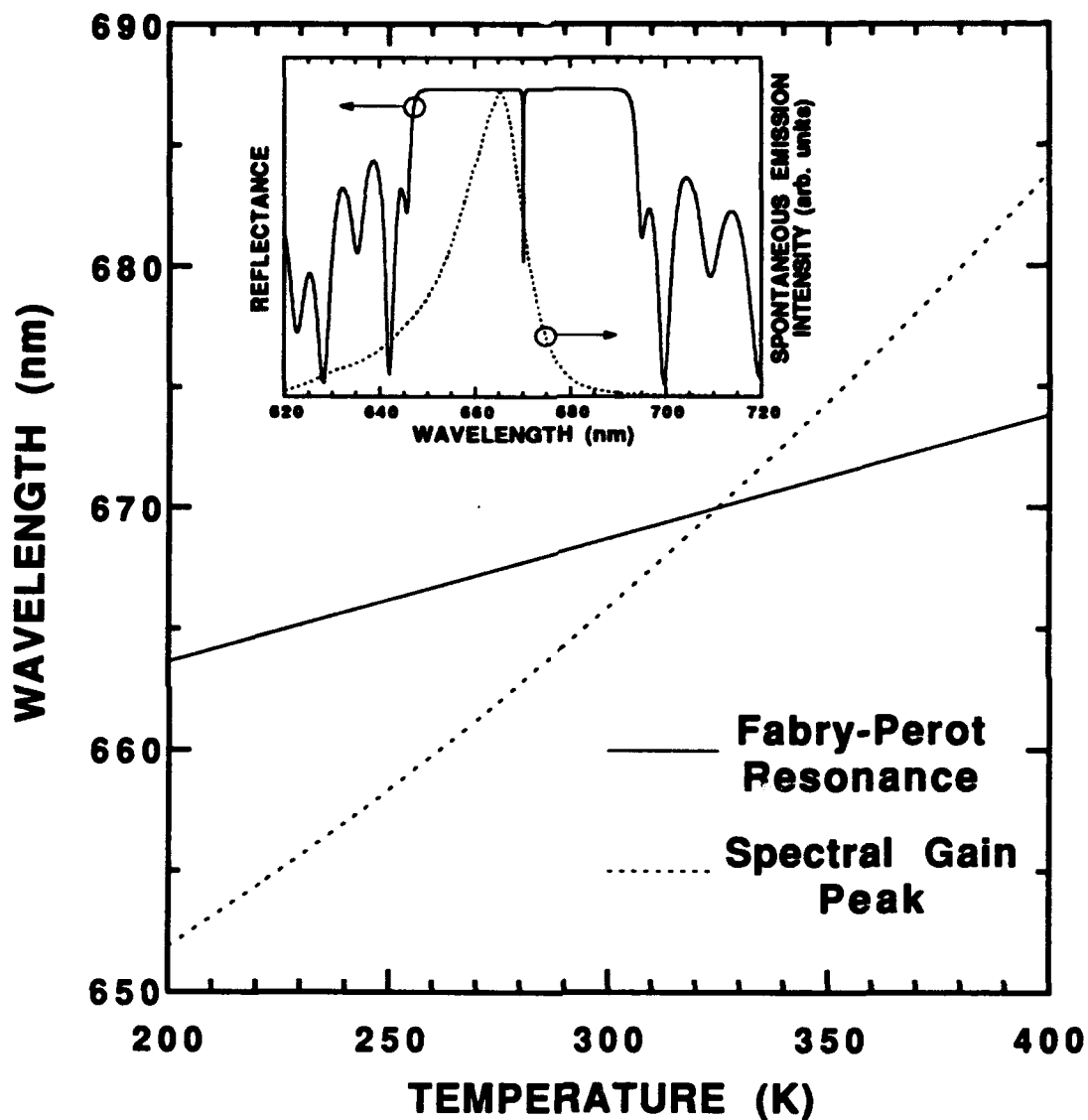


Fig 2.30 Shift in the Fabry-Perot mode and the quantum well spectral gain peak as functions of temperature for an example visible VCSEL. The mode and gain overlap at one specific temperature (325K in this case). This fact can be included in the device design to maximize the output power, or to minimize the threshold current.

Table 2.7 Experimental Temperature Dependence of Example All Semiconductor Fabry-Perot Etalons.

Etalon Structure	Short Edge (nm/°C)	Fabry-Perot Resonance (nm/°C)	Long Edge (nm/°C)
Hybrid	0.0569	0.05106	0.04835
All-Phosphide	0.04147	0.0388	0.03497

2.6.3 Comparison of Visible and Infrared VCSELs

The charge neutral, real space energy band diagrams for an example infrared (IR) ($\lambda_0 = 980$ nm) and visible ($\lambda_0 = 650$ nm) VCSEL are shown in Fig. 2.31. The IR VCSEL [after Geels *et al.* 1991] has three 8 nm thick $\text{Ga}_{0.8}\text{In}_{0.2}\text{As}$ strained quantum wells surrounded by GaAs barrier layers, in-turn surrounded by $\text{Al}_{0.5}\text{Ga}_{0.5}\text{As}$ layers, forming a separate confinement heterostructure (SCH). The optical cavity is 1λ thick. The DBRs are $\lambda/4$ layers of AlAs and GaAs (the heterointerface grading is not included in Fig. 2.31 for simplicity), with 14 periods on the top, and 18.5 periods on the bottom. The top DBR is capped with Au, and emission is out the substrate via the bottom DBR. The energy band offsets are taken from Fig. A.9 in Appendix A for the $\text{Al}_x\text{Ga}_{1-x}\text{As}$, and from the model reported in [Krijn 1991] for the $\text{Ga}_{0.8}\text{In}_{0.2}\text{As}/\text{GaAs}$. The example visible VCSEL has three 8 nm thick $\text{Ga}_{0.44}\text{In}_{0.56}\text{P}$ strained quantum wells surrounded by $(\text{Al}_y\text{Ga}_{1-y})_{0.5}\text{In}_{0.5}\text{P}$ $y = 0.4$ barrier layers, stepped from $y = 0.4$ to 0.7, in 0.1 increments, forming a SCH. For a $\text{Ga}_{0.5}\text{In}_{0.5}\text{P}$ quantum well, the largest conduction band offset is thought to occur with $y = 0.7$ barrier layers. However, recent low temperature magneto-luminescence data on AlGaInP quantum well structures suggests that the value could instead be closer to $y \sim 0.5$ to 0.6 [Jones 1993]. Surrounding the central 2λ SCH are 1λ phase matching spacer layers of $\text{Al}_{0.5}\text{In}_{0.5}\text{P}$. Thus the total thickness of the optical cavity is 4λ . The DBRs are AlAs/ $\text{Al}_{0.5}\text{Ga}_{0.5}\text{As}$ on one side, and $\text{Al}_{0.5}\text{In}_{0.5}\text{P}/(\text{Al}_{0.2}\text{Ga}_{0.8})_{0.5}\text{In}_{0.5}\text{P}$ on the other for

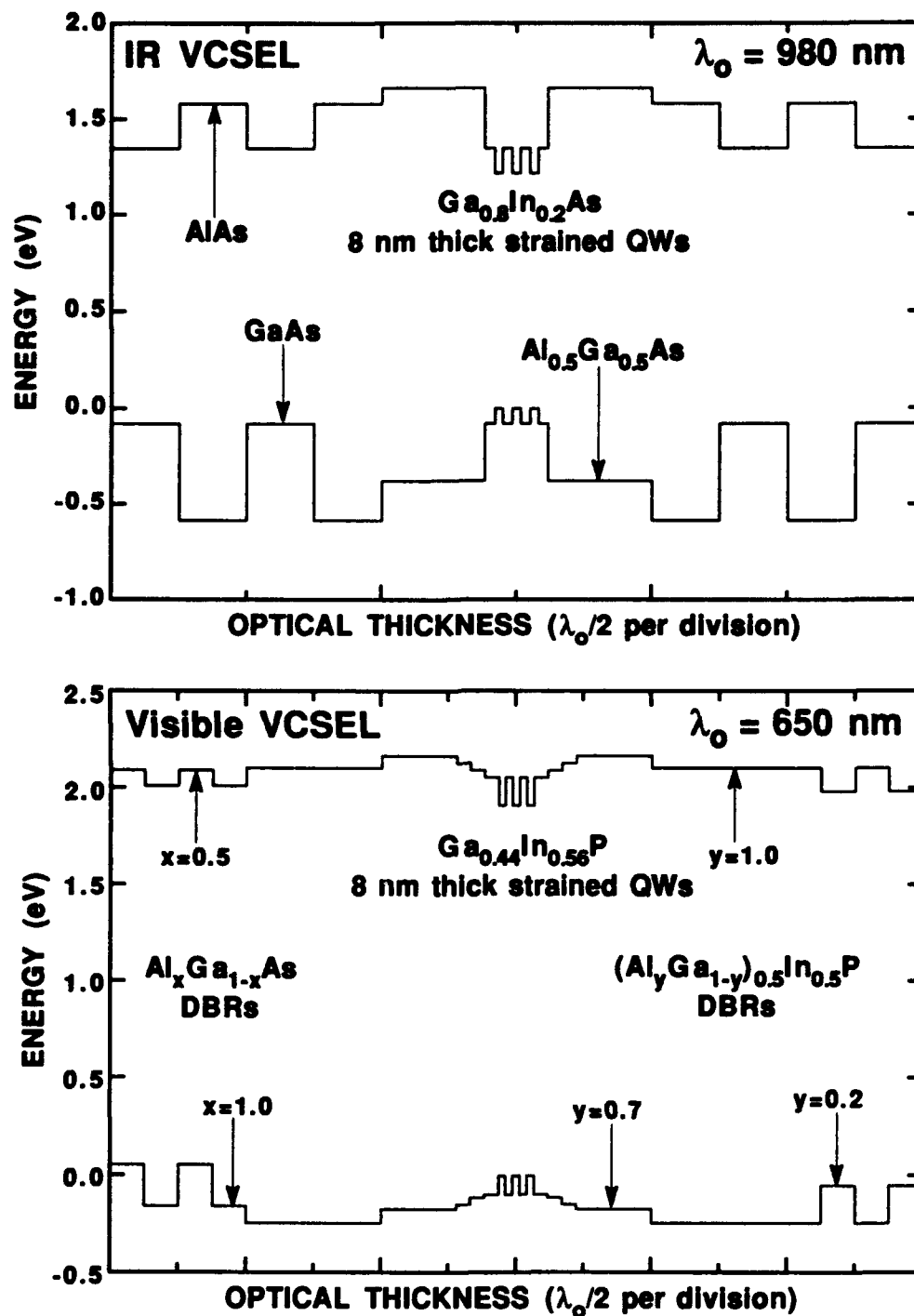


Fig 2.31 Example real space, charge neutral, energy band diagrams comparing a conventional GaInAs/AlGaAs IR VCSEL to an AlGaInP visible VCSEL.

comparison. For a conservative design, the actual structures would have 32 and 55.5 AlGaAs DBR periods and 45 and 60.5 AlGaInP DBR periods, on the top and bottom, respectively. The physical thickness of a DBR period ($\lambda/2$) for the IR VCSEL is ~ 152 nm, and for the visible VCSEL the physical thickness is ~ 102 nm (AlGaAs DBR) or ~ 99.8 nm (AlGaInP DBR).

The energy scales in Fig 2.31(a) and (b) are equally stepped, and it is seen that the quantum well confining potentials between Ga_{0.8}In_{0.2}As/GaAs and Ga_{0.44}In_{0.56}P/(Al_{0.4}Ga_{0.6})_{0.5}In_{0.5}P are roughly equal. However, the overall confinement is much better in the IR VCSEL due to the Al_{0.5}Ga_{0.5}As barriers in the SCH. For the visible VCSEL, the Al_{0.5}In_{0.5}P spacer layers moderately increase the hole confinement. (The confinement for both electrons and holes is further improved when the Al_{0.5}In_{0.5}P layers are doped [Bour 1993a]). The quantum well leakage currents are higher for the visible VCSEL, most notably at increased temperatures (> 300 K). Also, the thermal resistance of AlGaInP is higher than for AlGaAs, thus heat is not dissipated as well in the visible VCSELs (especially for an all-phosphide structure), making continuous wave (CW) operation more difficult. The DBR bandoffsets are larger in the IR VCSEL, especially the valence band offsets. In fact, graded (p)DBR heterointerfaces are a necessity in the IR VCSELs to reduce series resistance. The differential refractive indices are higher for the IR DBRs and thus fewer periods are needed to achieve a given reflectance. Additionally, the phase penetration lengths are smaller leading to reduced effective cavity lengths, and smaller passive absorptive losses in the DBRs. For example, to reach $R > 0.999$, 21 DBR periods are required for the IR VCSEL, while 30 AlAs/Al_{0.5}Ga_{0.5}As, or 47 Al_{0.5}In_{0.5}P/(Al_{0.2}Ga_{0.8})_{0.5}In_{0.5}P DBR periods are required for the visible VCSEL. The total DBR thickness would be roughly equal at ~ 3.19 μ m (IR) and ~ 3.06 μ m (AlGaAs visible), or ~ 4.51 μ m (AlGaInP visible). The phase penetration lengths, from Eq. (2.9), are

~470 nm for the IR VCSEL, while they are ~533 nm (AlGaAs) and ~849 nm (AlGaInP) for the visible VCSEL.

Figure 2.32(a) and (b) shows the electric field intensity on resonance and the real refractive index profile for the IR and visible VCSELs. For the IR VCSEL, the standing wave fully overlaps the three 10 nm thick quantum wells at an intensity that is 77% of the peak value at the antinode, with $\Gamma_z = 0.308$ and $\Gamma_r = 1.84$. In contrast, the equivalent visible VCSEL standing wave intensity at full overlap is only 43%, with $\Gamma_z = 0.476$ and $\Gamma_r = 1.46$. Typically, quantum well gain layers are 6 to 10 nm thick, whether for IR or visible emission. But since visible wavelengths are roughly 2/3 (i. e. 650/980) or 3/4 (i. e. 650/850) as long as IR wavelengths, the increased Γ_z and reduced Γ_r (for equal well thickness) is unavoidable, and the available gain is less efficiently used. It is clear that shorter wavelength VCSELs should have reduced quantum well and/or barrier layer thicknesses to optimize the utilization of the available gain. At $\lambda_0 \sim 600$ nm or shorter, it may become more advantageous to use $\lambda/4$ bulk (double heterostructure) or short period superlattice gain layers, rather than the conventional set of quantum wells.

By using Eq.(2.3) with $\alpha_m = 5 \text{ cm}^{-1}$ and neglecting α_i , the threshold gain for the above IR VCSEL is $g_{th} = 635 \text{ cm}^{-1}$, and for the above visible VCSEL $g_{th} = 241 \text{ cm}^{-1}$. The threshold gain is lower for the visible VCSEL due to the large number of DBR periods ($R_{vis} = 0.99947$, whereas $R_{IR} = 0.99697$). By using 18 periods on the top (plus a Au cap), and 22.5 periods on the bottom, the gain threshold for the IR VCSEL drops to 221 cm^{-1} ($R = 0.99925$).

A judicious active region design is required to make the most of the available gain. Unfortunately, the available gain (g) per unit quantum well length is lower for visible AlGaInP quantum wells, as compared to IR GaInAs or GaAs quantum wells. In fact, the gain ratio $g_{IR}/g_{vis} \sim 1.3$. The calculated gain spectra for single 8 nm thick $\text{Ga}_{0.8}\text{In}_{0.2}\text{As}/\text{GaAs}$ and $\text{Ga}_{0.44}\text{In}_{0.56}\text{P}/(\text{Al}_{0.4}\text{Ga}_{0.6})_{0.5}\text{In}_{0.5}\text{P}$ quantum wells are plotted in

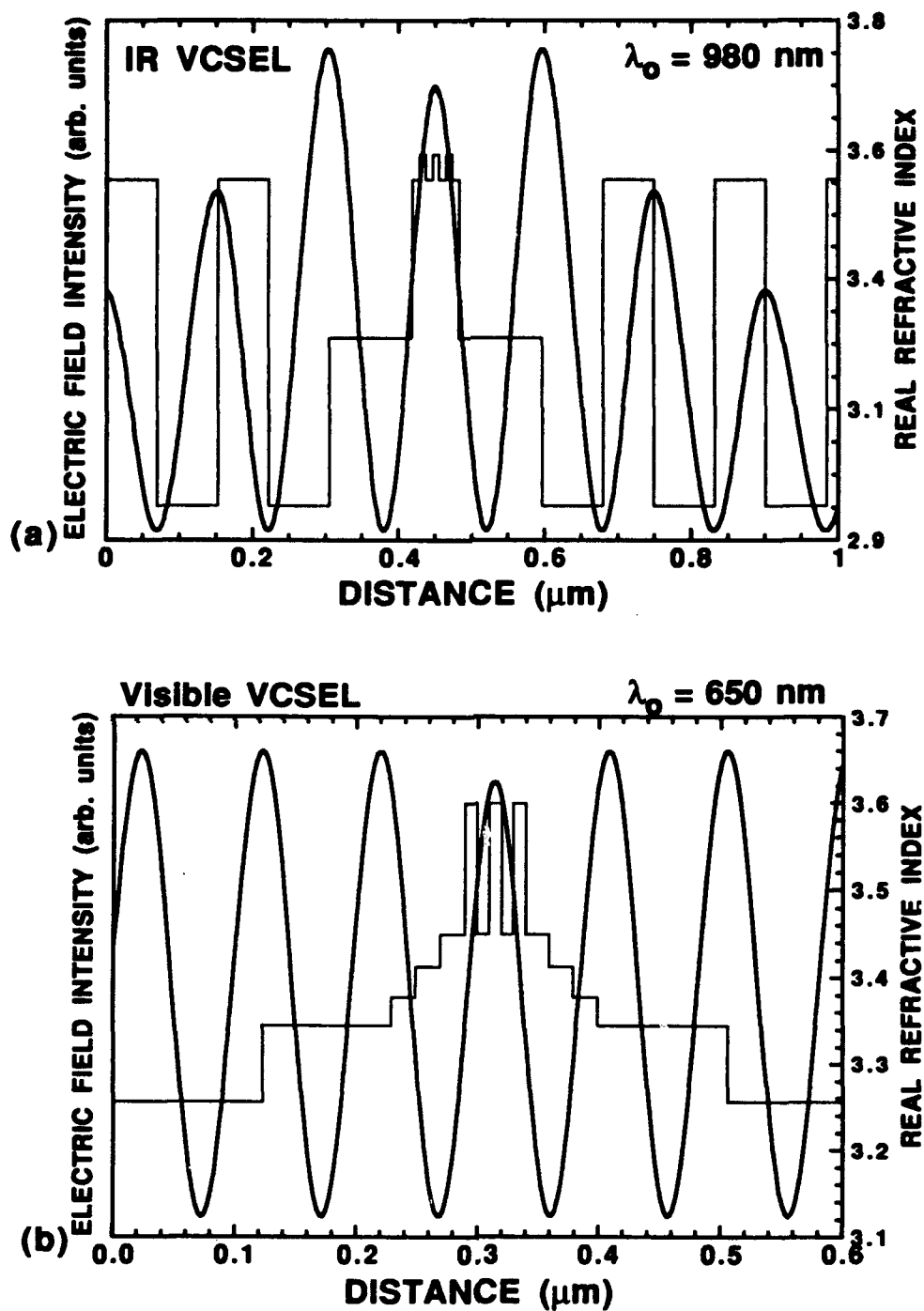


Fig 2.32 Calculated electric field intensity for the example IR and visible VCSELs shown in Fig. 2.31. (Calculation details are given in Appendix C).

Fig. 2.33, for the case of TE (transverse electromagnetic) polarized emission (see Appendix D or [Chinn *et al.* 1988]). For the AlGaInP calculation, $\Delta E_c = 0.6\Delta E_g$. The parametric variable is the density of carriers in the quantum well. The dashed lines are the unconvolved gain, while the solid lines are the convolved gain (a Lorentzian convolving function is used with an intraband scattering time of 0.1 ps). Strain effects are neglected, except for small changes in the energy bandgaps and the energy band offsets using the model by Krijn [1991] and the parameters in Appendix A. Strict \mathbf{k} -selection rules are used, only the two lowest heavy hole, light hole, and electron quantized states are included, and nonradiative recombination and carrier leakage are neglected. It is seen that the peak gain is higher for the IR structure for a given carrier density. Also, the gain contributions from the second ($n=2$) quantized state over take those from the first ($n=1$) quantized state at a lower carrier density in the IR structure. The separation between the $n=1$ and $n=2$ gain peaks is ~ 80 nm in the IR structure, while it is ~ 25 nm in the visible structure. This difference is due primarily to the smaller band offsets and the larger effective masses in the AlGaInP material system.

The difference in the $n=1$ and $n=2$ spectral gain peaks is a sensitive function of the position of the energy of the quantized states relative to the bottom of the conduction and valence bands. These energies, in-turn, depend on the band offsets and the effective masses. As mentioned in Appendix A, these material parameters are not firmly established. Thus, some care must be exercised in interpreting the gain spectrum in Fig. 2.33(b). For comparison, gain spectra for 8 nm thick $\text{Ga}_{0.44}\text{In}_{0.56}\text{P}/(\text{Al}_{0.4}\text{Ga}_{0.6})_{0.5}\text{In}_{0.5}\text{P}$ and $\text{Ga}_{0.44}\text{In}_{0.56}\text{P}/(\text{Al}_{0.7}\text{Ga}_{0.3})_{0.5}\text{In}_{0.5}\text{P}$ quantum wells are plotted in Fig. 2.34, where the bandoffsets were determined by using $Q_c \approx 0.4$ (as given in [Bour 1993c], see Appendix A), with the gamma point conduction band offset $\Delta E_c = Q_c(\Delta E_g)$. With the reduced fractional conduction band offset, the separation between the $n=1$ and $n=2$ gain peaks is reduced to ~ 15 nm in Fig. 2.34(a).

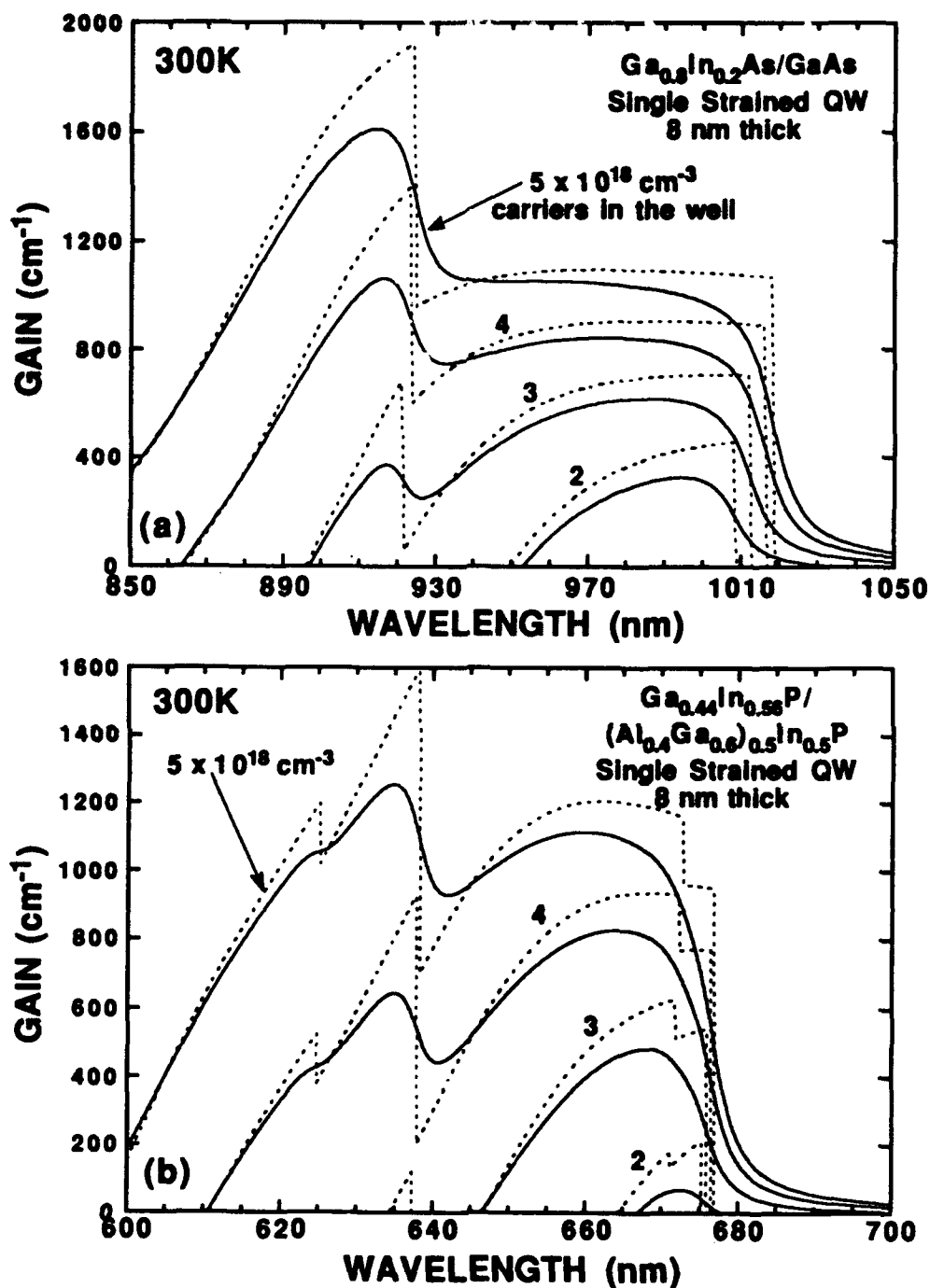


Fig 2.33 Calculated gain as a function of carrier density for single 8 nm thick quantum wells composed of (a) $\text{Ga}_{0.8}\text{In}_{0.2}\text{As}/\text{GaAs}$, and (b) $\text{Ga}_{0.44}\text{In}_{0.56}\text{P}/(\text{Al}_{0.4}\text{Ga}_{0.6})_{0.5}\text{In}_{0.5}\text{P}$. (The calculation uses the material values given in Appendix A, including $\Delta E_c = 0.6\Delta E_g$, and the gain model in Appendix D). The dashed lines are unconvolved gain, whereas the solid lines are convolved gain.

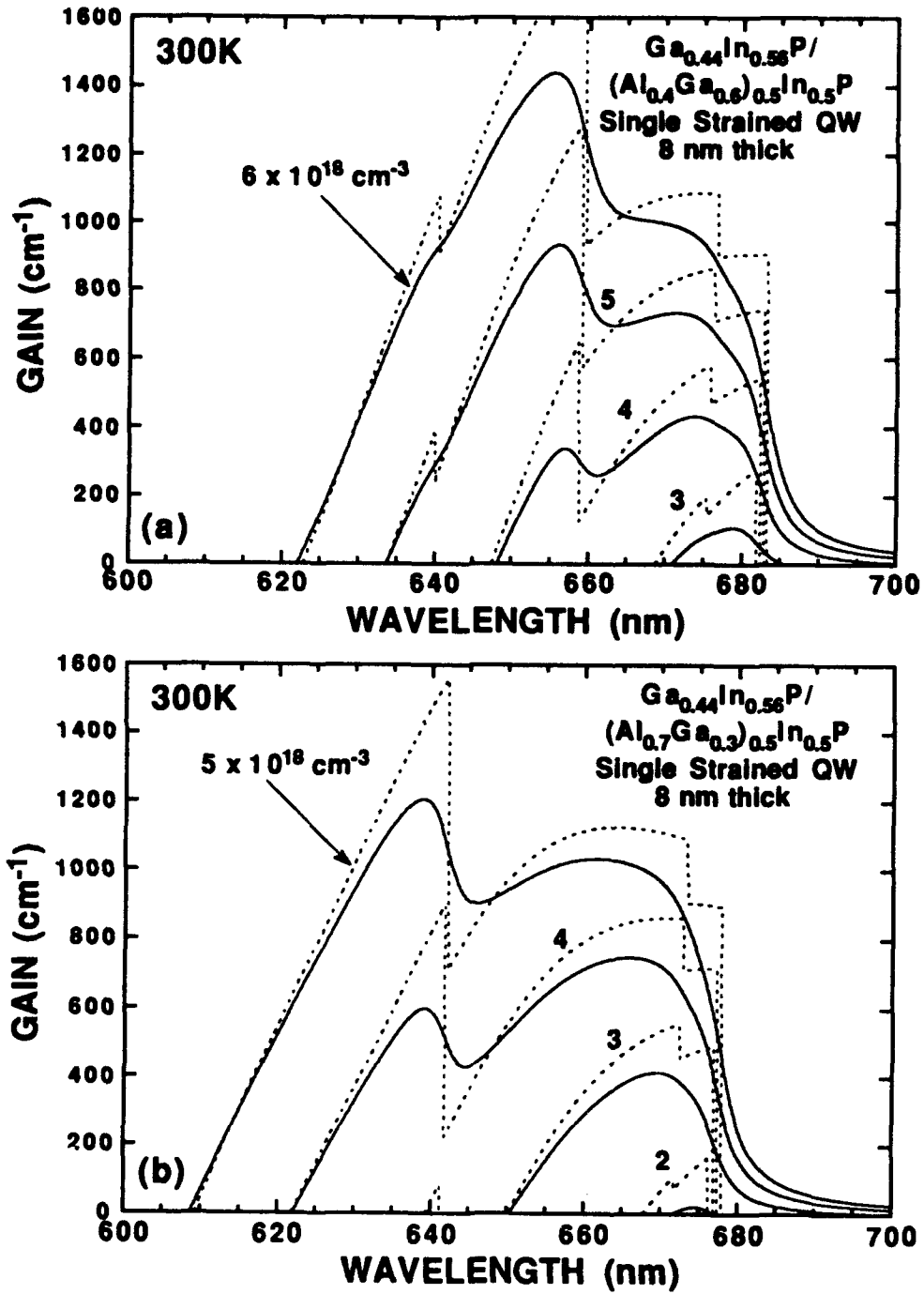


Fig 2.34 Calculated gain as a function of carrier density for single 8 nm thick quantum wells composed of (a) Ga_{0.44}In_{0.56}P/(Al_{0.4}Ga_{0.6})_{0.5}In_{0.5}P and (b) Ga_{0.44}In_{0.56}P/(Al_{0.7}Ga_{0.3})_{0.5}In_{0.5}P. For comparison to Fig. 2.33, this calculation uses $\Delta E_c = 0.4\Delta E_g$. As before, the dashed lines are unconvolved gain, whereas the solid lines are convolved gain.

2.7 Conclusions

In this Chapter, the design of visible (620 to 690 nm) VCSELs composed of AlGaInP quantum well optical cavity active regions, surrounded by AlGaAs and/or AlGaInP DBRs, has been reviewed. Several specific examples were given to illustrate the key points. While the design of infrared VCSELs has been treated elsewhere, this is the first comprehensive design review of visible VCSELs.

Compared to conventional IR devices, visible VCSELs are expected to have lower differential gain and efficiency, and be more sensitive to heating effects. This is due to several intrinsic factors such as less efficient utilization of gain (reduced overlap between the standing wave and the gain layers), and reduced carrier confinement. Because of doping limitations, smaller differential refractive indices, difficulty in fabrication, and the higher thermal resistivity of AlGaInP DBRs, AlGaAs DBRs are the better design choice for visible VCSELs emitting at ≥ 630 nm.

While 3 mW "orange" (615 nm) edge-emitting (CW at room temperature) lasers have been demonstrated[†], reproducing this with VCSELs would be very difficult. In fact, demonstrating 633 nm (CW at room temperature) with an AlGaInP VCSEL would be a major accomplishment. Indeed, it would take at least 50 DBR periods (~ 5 μm thick) of either AlAs/Al_{0.7}Ga_{0.3}As or Al_{0.5}In_{0.5}P/(Al_{0.3}Ga_{0.7})_{0.5}In_{0.5}P to get an $R \geq 0.999$ for the top output coupler. If unstrained, the quantum wells could be ~ 5.0 nm thick. With $\sim 0.56\%$ compressive strain, the well thickness would be ~ 2.5 nm. A short period strained layer superlattice active region, appropriately placed within the central standing wave, would be a promising design choice.

For these reasons, the initial studies of visible VCSEL diodes (Chapter 5) concentrated on the emission wavelength range of 650 to 680 nm.

[†] see page 42, *Photonics Spectra* (September 1992)

References for Chapter 2

Baba, T., K. Suzuki, Y. Yogo, K. Iga, and F. Koyama, "Low Threshold Room Temperature Pulsed and -57°C CW Operations of $1.3\text{ }\mu\text{m}$ GaInP/InP Circular Planar Buried Heterostructure Surface-Emitting Lasers", *IEEE Photonics Technology Letters*, 5(7), p. 744-746 (July 1993).

Babic, D. I., and S. W. Corzine, "Analytic Expressions for the Reflection Delay, Penetration Depth, and Absorptance of Quarter-Wave Dielectric Mirrors", *IEEE Journal of Quantum Electronics*, 28(2), p. 514-524 (February 1992).

Batey, J., S. L. Wright, and D. J. DiMaria, "Energy Band-Gap Discontinuities in GaAs:(Al,Ga)As Heterojunctions", *Journal of Applied Physics*, 57(2), p. 484-487 (15 January 1985).

Born, M., and E. Wolf, *Principles of Optics*, 5th ed. (Pergamon Press:New York, 1975).

Bour, D. P., D. W. Treat, R. L. Thornton, R. S. Geels, and D. F. Welch, "Drift Leakage Current in AlGaInP Quantum Well Lasers", *IEEE Journal of Quantum Electronics*, 29(5), p. 1337-1343 (May 1993a).

Bour, D. P., T. L. Paoli, R. L. Thornton, D. W. Treat, Y. S. Park, and P. S. Zory, "Polarized Electroluminescence Spectra of $\text{Ga}_x\text{In}_{1-x}\text{P}/(\text{Al}_{0.6}\text{Ga}_{0.4})_{0.5}\text{In}_{0.5}\text{P}$ Quantum Wells", *Applied Physics Letters*, p. 3458-3460, 62(26) (28 June 1993b).

Bour, D. P., "AlGaInP Quantum Well Lasers", Ch. 9 in *Quantum Well Lasers*, P. S. Zory, Jr., ed., (Academic Press:San Diego, 1993c).

Casey, Jr., H. C., and M. B. Panish, *Heterostructure Lasers*, (Academic Press:San Diego, 1978).

Chalmers, S. A., K. L. Lear, and K. P. Killeen, "Low Resistance Wavelength-Reproducible p-Type (Al,Ga)As Distributed Bragg Reflectors Grown by Molecular Beam Epitaxy", *Applied Physics Letters*, 62(14), p. 1585-1587 (5 April 1993).

Chinn, S. R., P. S. Zory, and A. R. Reisinger, "A Model for GRIN-SCH-SQW Diode Lasers", *IEEE Journal of Quantum Electronics*, 24(11), p. 2191-2214 (November 1988).

Choa, F. S., K. Tai, W. T. Tsang, and N. G. Chu, "High Reflectivity $1.55\text{ }\mu\text{m}$ InP/InGaAsP Bragg Mirror Grown by Chemical Beam Epitaxy", *Applied Physics Letters*, 59(22), p. 2820-2822 (25 November 1991).

Coleman, J. J., "Strained Layer Quantum Well Heterostructure Lasers", Ch. 8 in *Quantum Well Lasers*, P. S. Zory, Jr., ed., (Academic Press:San Diego, 1993).

Corzine, S. W., R. S. Geels, J. W. Scott, R.-H. Yan, and L. A. Coldren, "Design of Fabry-Perot Surface-Emitting Lasers with a Periodic Gain Structure", *IEEE Journal of Quantum Electronics*, 25(6), p. 1513-1524 (June 1989).

Corzine, S. W., R. H. Yan, and L. A. Coldren, "A Tanh Substitution Technique for the Analysis of Abrupt and Graded Interface Multilayer Dielectric Stacks", *IEEE Journal of Quantum Electronics*, 27(9), p. 2086-2090 (September 1991).

Dudley, J. J., D. L. Crawford, and J. E. Bowers, "Temperature Dependence of the Properties of DBR Mirrors Used in Surface Normal Optoelectronic Devices", *IEEE Photonics Technology Letters*, 4(4), p. 311-314 (April 1992).

Geels, R. S., S. W. Corzine, and L. A. Coldren, "InGaAs Vertical-Cavity Surface-Emitting Lasers", *IEEE Journal of Quantum Electronics*, 27(6), p. 1359-1367 (June 1991).

Gourley, P. L., R. M. Biefeld, and T. E. Zipperian, "Single-Crystal, Optical Interference Filters and Integrated High Reflector/Photodiode using Multilayers of GaP and GaAs_xP_{1-x}", *Applied Physics Letters*, 49(5), p. 242-244 (4 August 1986a).

Gourley, P. L., and T. J. Drummond, "Single-Crystal, Epitaxial Multilayers of AlAs, GaAs, and Al_xGa_{1-x}As for use as Optical Interferometric Elements", *Applied Physics Letters*, 49(9), p. 489-491 (1 September 1986b).

Gourley, P. L., L. R. Dawson, T. M. Brennan, B. E. Hammons, J. C. Stover, C. F. Schaus, and S. Sun, "Optical Scatter in Epitaxial Semiconductor Multilayers", *Applied Physics Letters*, 58(13), p. 1360-1362 (1 April 1991).

Hasnain, G., K. Tai, L. Yang, Y. H. Wang, R. J. Fischer, J. D. Wynn, B. Weir, N. K. Dutta, and A. Y. Cho, "Performance of Gain-Guided Surface Emitting Lasers with Semiconductor Distributed Bragg Reflectors", *IEEE Journal of Quantum Electronics*, 27(6), p. 1377-1385 (June 1991).

Horio, K., and H. Yanai, "Numerical Modeling of Heterojunctions Including the Thermionic Emission Mechanism at the Heterojunction Interface", *IEEE Transactions on Electron Devices*, 37(4), p. 1093-1098 (April 1990).

Iga, K., F. Koyama, and S. Kinoshita, "Surface Emitting Semiconductor Lasers", *IEEE Journal of Quantum Electronics*, 24(9), p. 1845-1855 (September 1988).

Kishino, K., M. S. Ünlü, J.-I. Chyi, J. Reed, L. Arsenault, and H. Morkoç, "Resonant Cavity-Enhanced (RCE) Photodetectors", *IEEE Journal of Quantum Electronics*, 27(8), p. 2025-2034 (August 1991).

Koyama, F., S. Kinoshita, and K. Iga, "Room-Temperature Continuous Wave Lasing Characteristics of a GaAs Vertical Cavity Surface-Emitting Laser", *Applied Physics Letters*, 55(3), p. 221-222 (17 July 1989).

Krijn, M. P. C. M., "Heterojunction Band Offsets and Effective Masses in III-V Quaternary Alloys", *Semiconductor Science Technology*, 6, p. 27-31 (1991).

Jewell, J. L., Y. H. Lee, S. L. McCall, J. P. Harbison, and L. T. Florez, "High-Finesse (Al,Ga)As Interference Filters Grown by Molecular Beam Epitaxy", *Applied Physics Letters*, 53(8), p. 640-642 (22 August 1988).

Jewell, J. L., J. P. Harbison, A. Scherer, Y. H. Lee, and L. T. Florez, "Vertical-Cavity Surface-Emitting Lasers: Design, Growth, Fabrication, Characterization", *IEEE Journal of Quantum Electronics*, 27(6), p. 1332-1346 (June 1991).

Jones, E. D., Distinguished Member of Technical Staff, Sandia National Laboratories, Albuquerque, NM, unpublished (1993).

Lau, K. Y., "Ultralow Threshold Quantum Well Lasers", Ch. 4 in *Quantum Well Lasers*, P. S. Zory, Jr., ed., (Academic Press:San Diego, 1993).

Lei, C., T. J. Rogers, D. G. Deppe, and B. G. Streetman, "ZnSe/CaF₂ Quarter-Wave Bragg Reflector for the Vertical Cavity Surface-Emitting Laser", *Journal of Applied Physics*, 69(11), p. 7430-7434 (1 June 1991).

MacLeod, H. A., *Thin-Film Optical Coatings*, 2nd ed., (McGraw-Hill:New York, 1989).

Nakwaski, W., M. Osinski, and J. Cheng, "Spreading Resistance in Proton-Implanted Vertical-Cavity Surface-Emitting Diode Lasers", *Applied Physics Letters*, 61(26), p. 3101-3103 (28 December 1992).

Ozasa, K., M. Yuri, S. Tanaka, and H. Matsunami, "Effect of Misfit Strain on Physical Properties of InGaP Grown By Metalorganic Molecular-Beam Epitaxy", *Journal of Applied Physics*, 68(1), 107-111 (1 July 1990).

Peters, F. H., M. G. Peters, D. B. Young, J. W. Scott, B. J. Thibeault, S. W. Corzine, and L. A. Coldren, "High-Power Vertical-Cavity Surface-Emitting Lasers", *Electronics Letters* 29(2), p. 200-201 (21 January 1993).

Raja, M. Y. A., S. R. J. Brueck, M. Osinski, C. F. Schaus, J. G. McInerney, T. M. Brennan, and B. E. Hammons, "Resonant Periodic Gain Surface-Emitting Lasers", *IEEE Journal of Quantum Electronics*, 25(6), p. 1500-1512 (June 1989).

Saleh, B. E. A., and M. C. Teich, *Fundamentals of Photonics*, (Wiley:New York, 1991).

Scherer, A., J. L. Jewell, M. Walther, J. P. Harbison, and L. T. Florez, "Fabrication of Low Threshold Voltage Microlasers", *Electronics Letters*, 28(13), p. 1224-1226 (18 June 1992).

Schneider, Jr., R. P., J. A. Lott, and E. D. Jones, "InAlGaP Distributed Bragg Reflectors for Visible Photonic Devices", Digest of the Fall Materials Research Society (MRS) Conference, Boston, MA (30 November to 4 December 1992).

Schneider, Jr., R. P., and J. A. Lott, "InAlP/InAlGaP Distributed Bragg Reflectors for Visible Vertical Cavity Surface Emitting Lasers", *Applied Physics Letters*, 62(22), p. 2748-2750 (31 May 1993).

Schneider, Jr., R. P., and J. J. Figiel, unpublished (1993).

Scott, J. W., R. S. Geels, S. W. Corzine, and L. A. Coldren, "Modeling Temperature Effects and Spatial Hole Burning to Optimize Vertical Cavity Surface Emitting Laser Performance", *IEEE Journal of Quantum Electronics*, 29(5), p. 1295-1308 (May 1993).

- Sze, S. M., *Physics of Semiconductor Devices*, 2nd Ed., (Wiley:New York, 1981).
- Tai, K., L. Yang, Y. H. Wang, J. D. Wynn, and A. Y. Cho, "Drastic Reduction of Series Resistance in Doped Semiconductor Distributed Bragg Reflectors for Surface-Emitting Lasers", *Applied Physics Letters*, 56(25), p. 2496-2498 (18 June 1990).
- Thelen, A., *Design of Optical Interference Coatings*, (McGraw-Hill:New York, 1989).
- Thornton, R. L., R. D. Burnham, and W. Streifer, "High Reflectivity GaAs-AlGaAs Mirrors Fabricated by Metalorganic Chemical Vapor Deposition", *Applied Physics Letters*, 45(10), p. 1028-1030 (15 November 1984).
- Tigges, C. P., Senior Member of Technical Staff, Sandia National Laboratories, Albuquerque, NM, private communication (1993).
- van der Ziel, J. P., and M. Ilegems, "Multilayer GaAs-AlGaAs Dielectric Quarter Wave Stacks Grown By Molecular Beam Epitaxy", *Applied Optics*, 14(11), p. 2627-2630 (November 1975).
- van der Ziel, J. P., and M. Ilegems, "Interference Filters: Single Crystal Multilayer AlAs-GaAs", *Applied Optics*, 15(5), p. 1256-1257 (May 1976).
- Vawter, G. A., and D. R. Myers, "Useful Design Relationships for the Engineering of Thermodynamically Stable Strained-Layer Structures", *Journal of Applied Physics*, 65(12), p. 4769-4773 (15 June 1989).
- Vawter, G. A., J. F. Klem, G. R. Hadley, and S. H. Kravitz, "Highly Accurate Etching of Ridge-Waveguide Directional Couplers Using in situ Reflectance Monitoring and Periodic Multilayers", *Applied Physics Letters*, 62, p. 1-3 (1993).
- Vawter, G. A., Senior Member of Technical Staff, Sandia National Laboratories, Albuquerque, NM, private communication (1993).
- Weisbuch, C., and B. Vinter, *Quantum Semiconductor Structures: Fundamentals and Applications*, (Academic Press:San Diego 1991).
- Wu, C. M., and E. S. Yang, "Carrier Transport Across Heterojunction Interfaces", *Solid-State Electronics*, 22, p. 241-248 (1979).
- Yablonovitch, E., and E. O. Kane, "Band Structure Engineering of Semiconductor Lasers for Optical Communications", *Journal of Lightwave Technology*, 6, p. 504-506 (1986).
- Yablonovitch, E., and E. O. Kane, "Reduction of Lasing Threshold Current Density by the Lowering of Valence Band Effective Mass", *Journal of Lightwave Technology*, 4, p. 1292-1299 (August 1988).
- Yeh, P., *Optical Waves in Layered Media*, (Wiley:New York, 1988).
- Yoffe, G. W., "Rectification in Heavily Doped p-Type GaAs/AlAs Heterojunctions", *Journal of Applied Physics*, 70(2), p. 1081-1083 (15 July 1991).

Young, D. B., J. W. Scott, F. H. Peters, B. J. Thibeault, S. W. Corzine, M. G. Peters, S.-L. Lee, and L. A. Coldren, "High-Power Temperature-Insensitive Gain-Offset InGaAs/GaAs Vertical-Cavity Surface-Emitting Lasers", *IEEE Photonics Technology Letters*, 5(2), p. 129-132 (February 1993).

Zory, P. S., Jr., ed., *Quantum Well Lasers*, (Academic Press:San Diego, 1993).

Chapter 3 Optically Pumped Visible Vertical Cavity Surface Emitting Lasers

3.1 Introduction

The first step in the development of visible vertical cavity surface emitting lasers (VCSELs) is the demonstration of an optically pumped structure. Optically pumped structures contain the essential building-blocks of VCSEL diodes, that is, quantum well optical cavity active regions and distributed Bragg reflectors (DBRs). The layers can be unintentionally doped, however, since carriers accumulate in the quantum well(s) due to absorption of the pump energy, rather than by injection. This simplifies the design of both the optical cavity active region and the DBRs, since carrier injection efficiency and DBR series resistance are insignificant in this case. Nevertheless, the physical thickness of the individual layers must still be precise, within ~2% of the design values. Overall, optically pumped structures serve to prove the feasibility of diodes, and to help characterize some basic design trade-offs. For example, they can help determine the number of quantum wells (gain) needed to achieve lasing for a given number of DBR periods (reflectance) in the coupling mirror, and vice versa.

The first optically pumped "visible" (emission at 740 nm) VCSEL was reported in 1987 [Gourley and Drummond]. This device consisted entirely of $\text{Al}_x\text{Ga}_{1-x}\text{As}$, including an $\text{Al}_{0.4}\text{Ga}_{0.6}\text{As}/\text{GaAs}$ (20 nm/10 nm) 150 period multiple quantum well active region. Efficient emission at wavelengths shorter than ~690 nm is not possible with the $\text{Al}_x\text{Ga}_{1-x}\text{As}$ material system. In contrast, visible red emission (620 to 690 nm) is readily achieved by using an AlGaInP optical cavity active region (see Section 2.3 and

Appendix A). The first optically pumped visible VCSEL composed of an AlGaInP quantum well active region was demonstrated in October 1991 and first published in April 1992 [Schneider *et al.* 1992a]. This device structure used AlAs/Al_{0.5}Ga_{0.5}As DBRs and emitted at 657 nm. Subsequently, several similar structures were investigated and emission was achieved over the range 632 to 661 nm [Schneider *et al.* 1992b]. The first optically pumped "all-phosphide" visible VCSEL, composed of an AlGaInP optical cavity active region and Al_{0.5}In_{0.5}P/ (Al_{0.2}Ga_{0.8})_{0.5}In_{0.5}P DBRs, was demonstrated in November 1992 and first published in May 1993 [Lott *et al.* 1993a, Schneider and Lott 1993]. Lasing in this structure was achieved over the range 668.2 to 676.8 nm. (For a comparison of AlGaAs DBRs to AlGaInP DBRs, see Chapter 2 and Schneider and Lott [1993].)

In this Chapter, optically pumped lasing in AlGaInP quantum well visible VCSELs with both AlGaAs and AlGaInP DBRs is examined in detail for two specific structures. For these structures, it is shown that lasing is achieved due to significant gain contributions from the second ($n=2$) quantized quantum well state. This is in contrast to the first AlGaInP visible VCSEL cited above, where the gain contributed primarily from the first ($n=1$) quantized quantum well state was sufficient to overcome the cavity losses and achieve lasing. The results are significant in that: 1) this is the first demonstration and analysis of optically pumped lasing in VCSELs due to significant gain contributions from the $n=2$ quantum well state; and 2) the results are useful for the analysis of the electrically injected visible VCSELs described in Chapter 5. In fact, the results contributed to an improved quantum well optical cavity active region design. The results, along with improved doping (and grading) in the DBRs and the optical cavity, increased the differential gain, reduced the current threshold, and ultimately resulted in visible VCSELs that operated continuous wave at room temperature.

Section 3.2 below describes the equipment used to perform the optical pumping experiments. Next, Section 3.3 presents a first order model that is used to estimate the density of carriers in the quantum well(s) at threshold for a given VCSEL structure. This is followed by Sections 3.4 and 3.5, which contain the experimental results from the two optically pumped AlGaInP visible VCSELs, one with AlGaAs DBRs, and the other with AlGaInP DBRs. In Section 3.6, the optical pumping results are qualitatively analyzed by employing a conventional quantum well gain model. Finally, Section 3.7 contains the Chapter conclusions.

3.2 Experimental Set-Up

A schematic of the measurement system for optical pumping of visible VCSELs is shown in Fig. 3.1. One of two laser sources is used to pump a tunable (~ 630 to 680 nm) dye laser. The laser sources include a continuous wave (CW) argon laser (emitting at 514.5 nm), or a Nd:YAG mode-locked laser (emitting at 1.06 μm , ~ 4 - 5 ps pulses at ~ 82 - 88 MHz) whose output is sent through a KDP (potassium dihydrogen phosphate) frequency doubling crystal for emission at 530 nm. When the argon laser is used, the dye output is fed through an acousto-optic modulator (AOM) which is controlled by a square wave pulse generator. In either case, the dye emission is focused onto the surface (or subsurface) of the wafer under test, at normal incidence. The reflected dye emission plus the photoluminescence from the wafer are directed through a bandpass or edge filter to eliminate the dye emission, and into both a CCD (charge-coupled device) camera and an OMA (optical multi-channel spectrum analyzer, which includes a CCD detector array). A power meter, which measures average power, is used to measure the power incident onto the wafer.

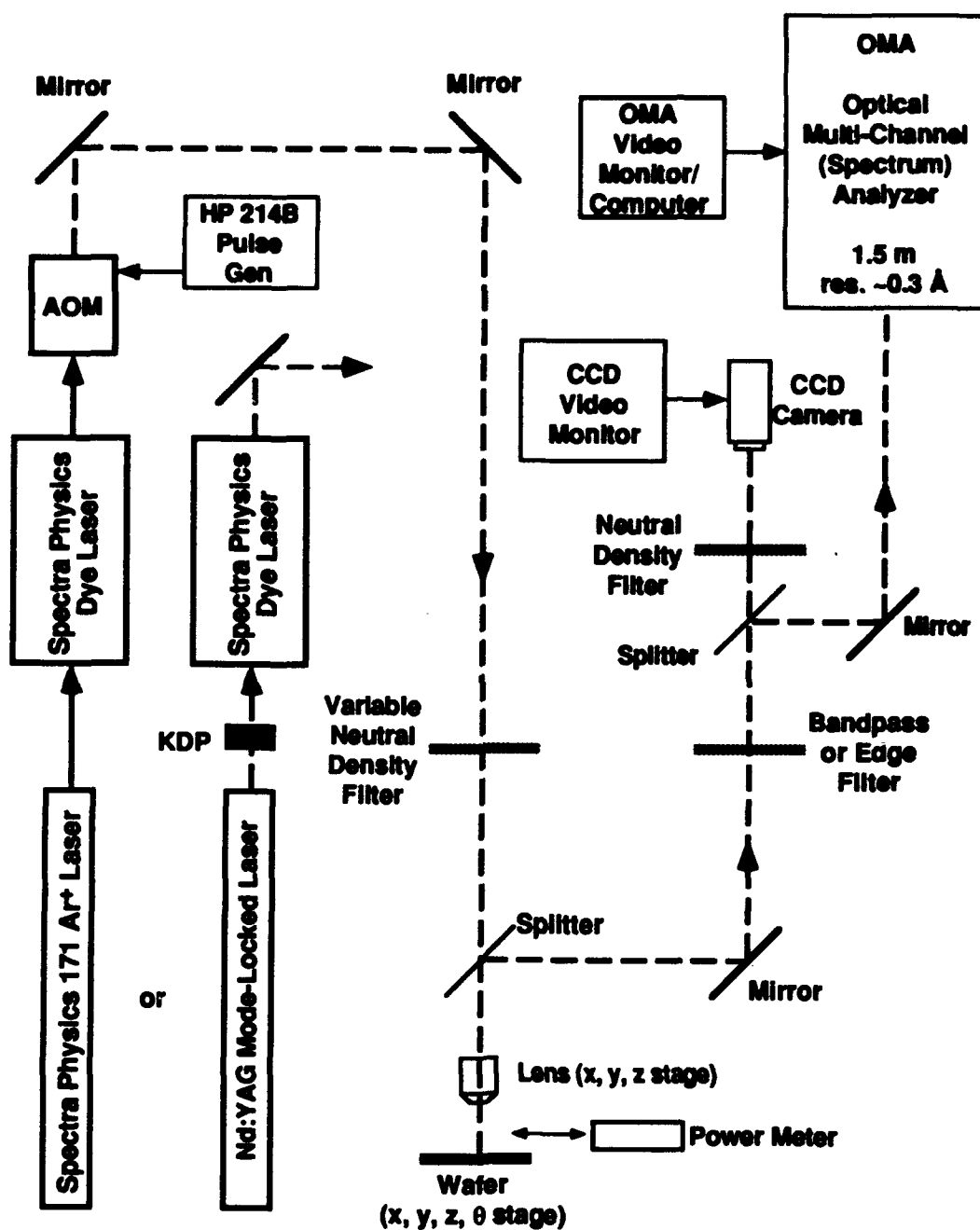


Fig. 3.1 Schematic diagram of the system for optical pumping of visible VCSELs.

3.3 Theoretical Quantum Well Carrier Density at Threshold

This section describes a method to estimate (order of magnitude) the density of carriers in the quantum well(s) at or below threshold for an optically pumped VCSEL. The following assumptions are made:

- 1) The absorption is uniform and can be modeled by Beer's Law (i.e. $I = I_0 e^{-\alpha l}$)
- 2) The steady-state heating effects are negligible
- 3) The excitation pulse width is shorter than the carrier relaxation time
- 4) An ultrafast relaxation of carriers to the lower two quantized quantum well states
- 5) The quantum efficiency is 1.0 (1 electron-hole pair for every absorbed photon)
- 6) The carrier diffusion effects are negligible
- 7) The pumping beam has a Gaussian intensity profile

The average power of the pulsed optical excitation incident on the wafer is given by the mean value theorem

$$P_{ave} = \frac{1}{\tau_p} \int_0^{\tau_p} P dt = \frac{1}{\tau_p} P_{peak} \Delta\tau \quad (W) \quad (3.1)$$

where P_{peak} is the peak power, τ_p is the pulse to pulse spacing, and $\Delta\tau$ is the pulse width.

The energy in each ~square pulse is thus

$$E_{pulse} = P_{ave} \tau_p = P_{peak} \Delta\tau \quad (J) \quad (3.2)$$

The fraction of the incident pump energy that is absorbed in the quantum well(s) at a given pump wavelength (λ_p) is

$$A_{qw}(\lambda_p) = (1 - R) \left[\prod_{\ell=1}^N e^{-\alpha_{\ell} L_{\ell}} \right] (1 - e^{-\alpha_{qw} L_{qw}}) \quad (\text{unitless}) \quad (3.3)$$

where R is the reflectance normal to the surface, α_{ℓ} is the absorption coefficient and L_{ℓ} is the thickness of layer ℓ in the top coupling DBR, respectively, α_{qw} is the absorption coefficient of the GaInP quantum well(s), and L_{qw} is the total thickness of the quantum well layers. Typically for unintentionally doped DBR layers with bandgaps above the emission energy, the bracketed term in Eq. (3.3) is close to unity and can be neglected.

The absorptive volume

$$\text{Volume} = \text{area} \cdot \text{length} = \frac{\pi d_{\text{spot}}^2 L_{qw}}{4} \quad (\text{cm}^3) \quad (3.4)$$

is found from an assumed diffraction limited (focused) spot diameter [Saleh and Teich 1991]

$$d_{\text{spot}} \approx \frac{4 f \lambda_p}{\pi d_{\text{laser}}} \quad (\mu\text{m}) \quad (3.5)$$

where f is the focal length of the focusing lens, and d_{laser} is the beam diameter of the pumping laser. The energy converted from a photon to a charge carrier is

$$E_{\text{conv}} = E_{\text{trans}} \quad (\text{J/electron-hole pair}) \quad (3.6)$$

where E_{trans} is the transition energy between electron and hole quantum well states. (The excess pump energy is lost to the lattice). By using Eqs (3.1) to (3.6), the estimated carrier density (\mathcal{N}) for a measured P_{ave} at or below threshold is

$$\mathcal{N} = \frac{(E_{\text{pulse}})(A_{\text{qw}})}{(E_{\text{conv}})(\text{Volume})} \quad (\text{electrons/cm}^3) \quad (3.7)$$

3.4 Hybrid AlGaInP/AlGaAs Optically Pumped Visible VCSEL

The layer details of a hybrid visible VCSEL structure for optical pumping experiments are given in Table 3.1. Also given are the estimated layer thicknesses corresponding to a Bragg wavelength (λ_0) of 670 nm, which are determined from the refractive index dispersion relationships outlined in Appendix A. The structure consists of a 2λ AlGaInP quantum well optical cavity active region surrounded by AlAs/AlGaAs DBRs, as outlined in Chapter 2. The electric field intensity on resonance (i.e. at λ_0) was calculated (see Appendix C) and is shown in Fig. 3.2. The calculated reflectances of the bottom (45 periods) and top (32.5 periods) DBR stacks, as seen from the optical cavity, are 0.99990 and 0.99931, respectively.

Just prior to VCSEL growth, an active region calibration sample was grown. This sample is identical to the optical pumping sample but without the top and bottom DBRs. The photoluminescence (PL) measurements from this calibration sample, taken at temperatures (T) of 300K, 200K, and 100K, are given in Fig. 3.3. The peak emission can be fit to the equation $\lambda_p \text{ (nm)} = 653 + 0.04T + 0.2 \times 10^{-3}T^2$ (T in K), and at 300K the peak value (e1 to hh1 transition) is ~683 nm.

The VCSEL is grown without rotation, such that the Fabry-Perot resonance wavelength varies ~linearly with position across the two inch wafer, from ~690 nm

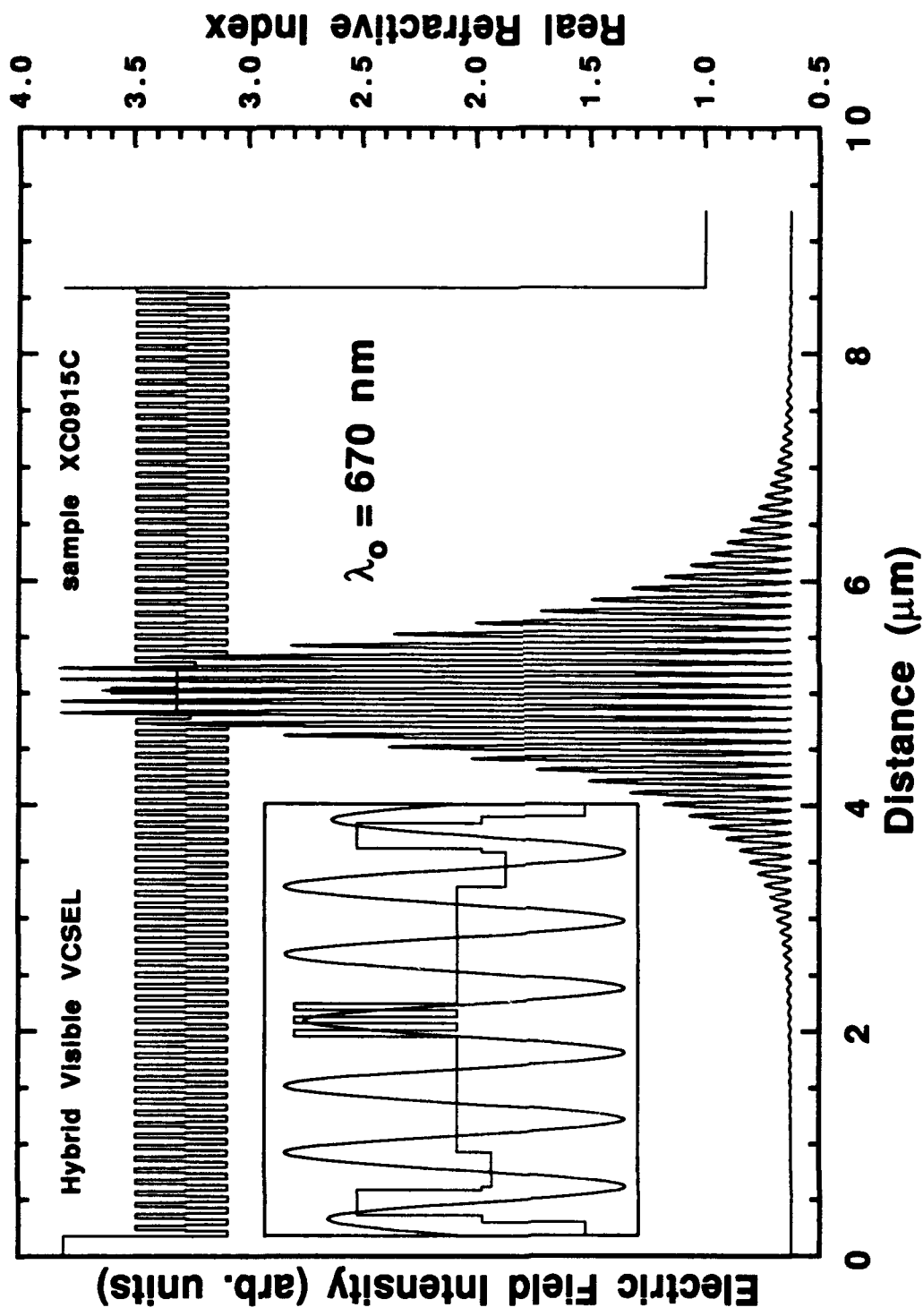


Fig. 3.2 The electric field intensity on resonance and refractive index against distance for the hybrid visible VCSEL.

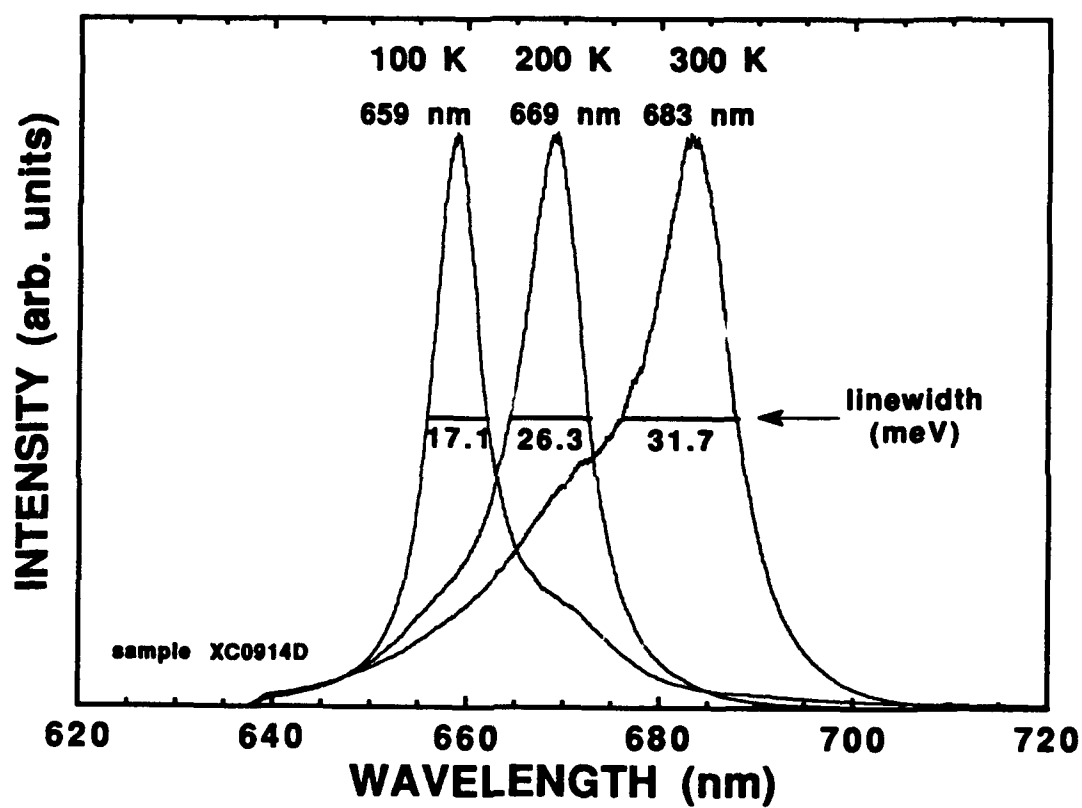


Fig. 3.3 Photoluminescence of an AlGaInP quantum well optical cavity active region calibration sample at 300, 200, and 100K, just prior to the growth of the hybrid visible VCSEL.

Table 3.1 MOVPE Growth List for Hybrid Visible VCSEL Sample XC0915C

Thickness (Å)	Material	Index at λ_0	Thickness (Å)	Material	Index at λ_0
100.0	GaAs	3.81 - i0.16		continued	
332.1	Al _{0.5} Ga _{0.5} As	3.491	1747.5	(Al _{0.7} Ga _{0.3}) _{0.5} In _{0.5} P	3.316
			518.4	Al _{0.5} In _{0.5} P	3.231
(repeat)			50.00	Al _{0.75} Ga _{0.25} As	3.273
100.0	Al _{0.75} Ga _{0.25} As	3.273			
435.7	AlAs	3.093	(repeat)		
100.0	Al _{0.75} Ga _{0.25} As	3.273	386.0	Al _{0.5} Ga _{0.5} As	3.491
386.0	Al _{0.5} Ga _{0.5} As	3.491	100.0	Al _{0.75} Ga _{0.25} As	3.273
x 32			435.7	AlAs	3.093
			100.0	Al _{0.75} Ga _{0.25} As	3.273
50.00	Al _{0.75} Ga _{0.25} As	3.273	x 44		
518.4	Al _{0.5} In _{0.5} P	3.231			
1747.5	(Al _{0.7} Ga _{0.3}) _{0.5} In _{0.5} P	3.316	386.0	Al _{0.5} Ga _{0.5} As	3.491
(repeat)			100.0	Al _{0.75} Ga _{0.25} As	3.273
100.0	Ga _{0.44} In _{0.56} P (SQW)	3.577	435.7	AlAs	3.093
100.0	(Al _{0.7} Ga _{0.3}) _{0.5} In _{0.5} P	3.316	50.00	Al _{0.75} Ga _{0.25} As	3.273
x 2			5000	GaAs	3.81 - i0.16
			substrate	(n+) GaAs (100) 6°	
100.0	Ga _{0.44} In _{0.56} P (SQW)	3.577	Bragg wavelength	$\lambda_0 = 670$ nm	
			all epitaxial layers are unintentionally doped		

to ~640 nm from front (thickest) to back (thinnest). Figure 3.4 shows the measured reflectance spectra. The position of the Fabry-Perot resonances are indicated for each spectrum. The thickness variation is approximately linear except near the edge on the thin side where the layer thickness tapers off (decreases at a higher rate). The range of lasing wavelengths, described below, is within the dashed lines in Fig. 3.4.

Optically pumped lasing is achieved in and around the center of the wafer from 663.8 to 675.0 nm. Fig. 3.5 is a plot of the lasing spectrum at 669 nm (solid curve). Also shown is the attenuated dye laser pump at 643 nm, and the reflectance of the structure (dashed curve) at the same spot on the wafer. Note that the laser emission is shifted

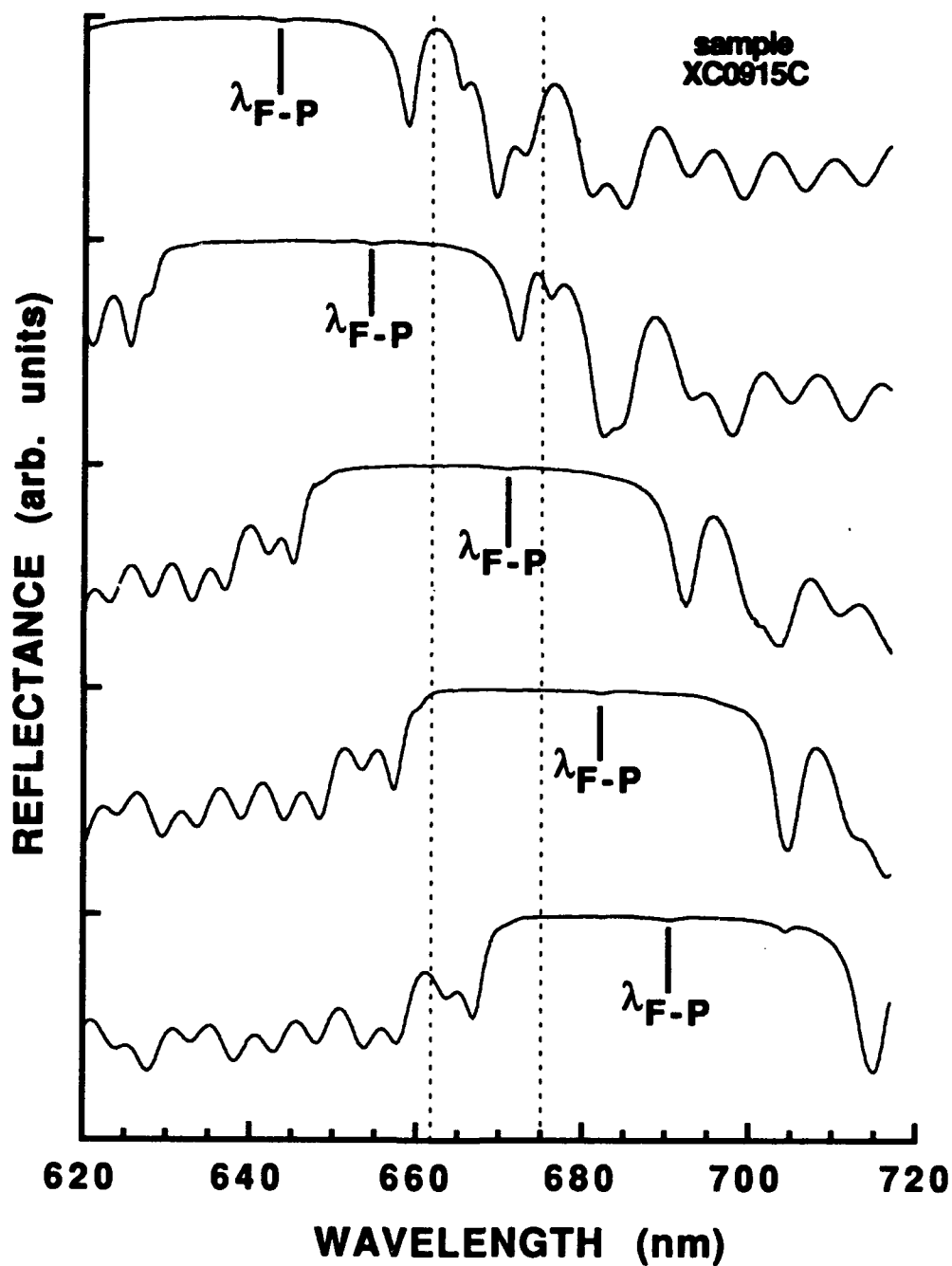


Fig. 3.4 Measured reflectance spectra (at normal incidence) at five approximately equally spaced points across the hybrid visible VCSEL wafer.

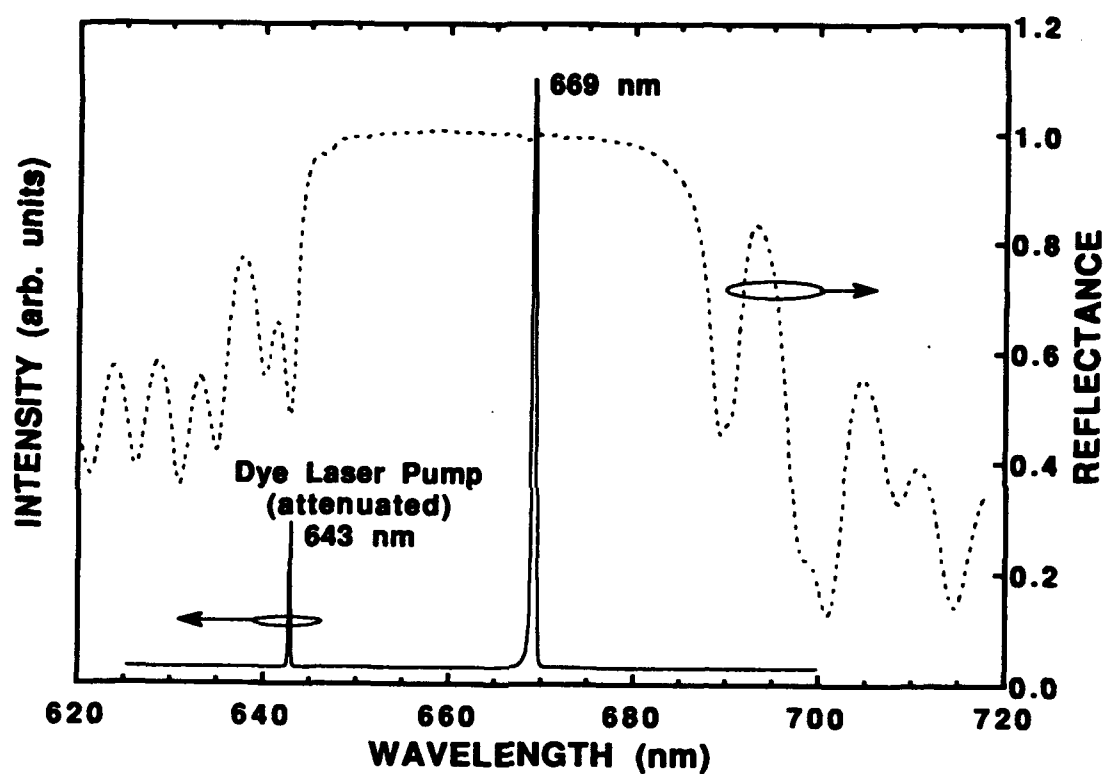


Fig. 3.5 Optically pumped lasing spectrum at $\lambda_0 = 669$ nm for the hybrid visible VCSEL. The attenuated dye laser pump is also shown (at $\lambda_0 = 643$ nm), as is the corresponding reflectance spectrum at normal incidence.

(~1 nm) longer than the Fabry-Perot wavelength from the reflectance measurement due to heating. The shift corresponds to an increase in temperature of ~20 to 25 °C (see Table 2.7). Also note that the pump wavelength is close to a reflectance minima, in order to increase the amount of energy transmitted into the structure.

By using Eqs (3.2) to (3.7), the density of carriers in the quantum wells at threshold can be estimated. For pumping at 643 nm in Fig. 3.5, $R \approx 0.49$, $d_{\text{spot}} \approx 15 \mu\text{m}$, $\alpha_{\text{GaAs}} \approx 40.2 \times 10^3 \text{ cm}^{-1}$, $\alpha_{\text{GaInP}} \approx 58.6 \times 10^3 \text{ cm}^{-1}$ (using interpolation between InP and GaP), $\alpha_{\text{AlGaAs}} \approx 25 \text{ cm}^{-1}$ (rough estimate), $P_{\text{ave}} = 23 \text{ mW}$, $\tau_p = 11 \text{ ns}$, $E_{\text{conv}} = 297 \times 10^{-21} \text{ J/electron}$, and thus $A_{\text{QW}} \approx 0.078$ and $\text{Volume} \approx 5.3 \times 10^{-12} \text{ cm}^3$. Note that the top 10 nm thick GaAs layer absorbs ~4% of the incoming energy and that ~40% of the incident light is absorbed in the GaAs substrate. The resultant carrier density is $\mathcal{N} \approx 1 \times 10^{19} \text{ cm}^{-3}$, which is probably an over estimate by ~30 to 50%. Why the overestimate? Because it is difficult to accurately assess all of the mechanisms involved in the optical pumping process. Certainly the number is less because of carrier diffusion and leakage, and a quantum efficiency < 100%. On the other hand, the absorption coefficients for the GaInP quantum wells and for the above bandgap AlGaAs layers are not accurately known, and they should increase when the temperature increases due to bandgap shrinkage. For these reasons, the model serves only as a rough estimate of carrier density.

The average pump power at threshold for the structure in Table 3.1 as a function of emission wavelength (or equivalently wafer position) is plotted in Fig. 3.6. The data is for pumping with the mode-locked Nd:YAG/dye lasers with 5 ps pulses at a period of 11 ns. Similar results were obtained for pumping with the Ar⁺/dye lasers with 100 ns pulses at a period of 4 μs . The power at threshold goes through a minimum near 665 nm. This is curious since it is known from Fig. 3.3 that the peak room temperature PL emission occurs near 683 nm. In fact, lasing is achieved from 661.8 to 675.0 nm and not

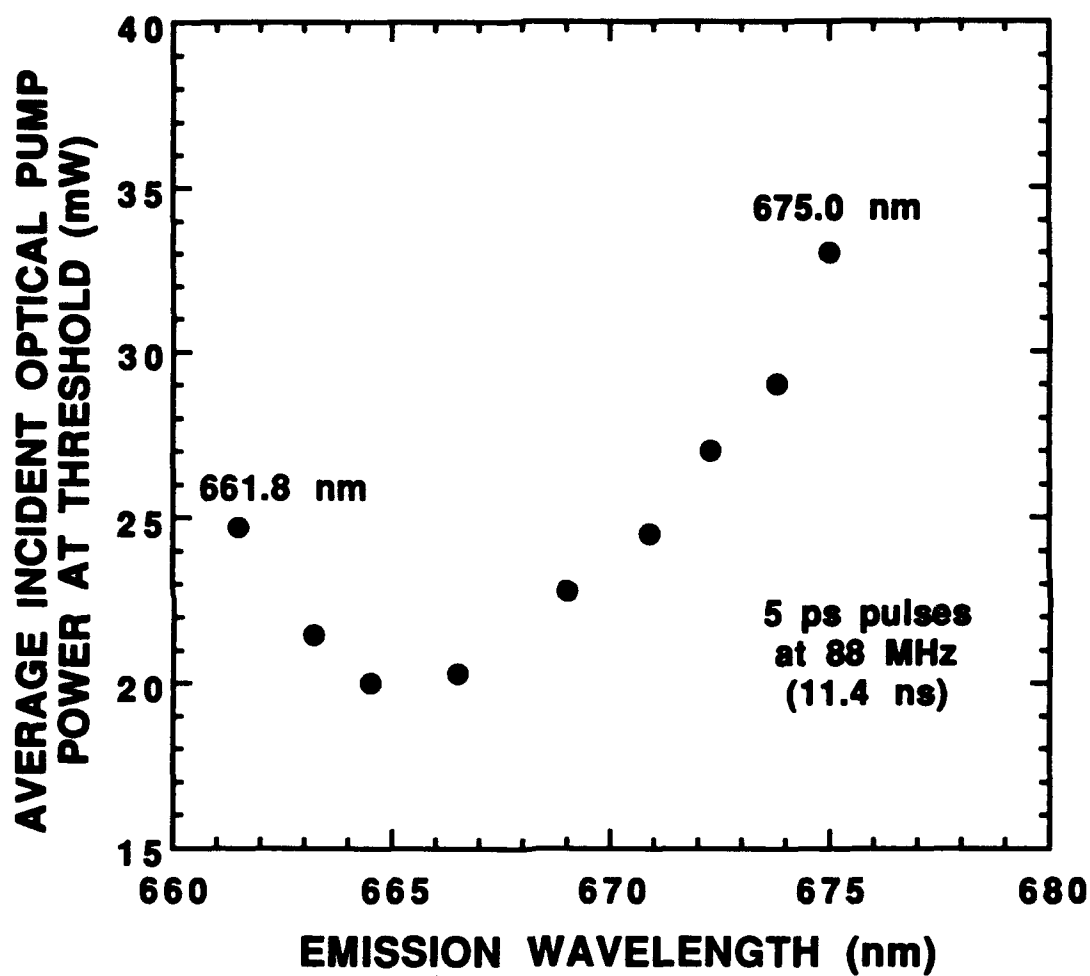


Fig. 3.6 Measured average incident power onto the surface of the hybrid visible VCSEL against lasing wavelength (or equivalently, against position on the wafer).

at ~683 nm. With heating, the threshold minimum would be expected to occur at ~685 nm and not at ~665 nm. The only possible explanation for this phenomena is that gain contributions from the second ($n=2$) quantized quantum well state are required to achieve lasing. This is explained qualitatively in Section 3.6 by employing the quantum well gain model described in Appendix D.

3.5 All-AlGaInP Optically Pumped Visible VCSEL

The layer details of an all-AlGaInP visible VCSEL structure for optically pumping experiments are given in Table 3.2, along with the estimated layer thicknesses corresponding to a Bragg wavelength (λ_0) of 670 nm. These thicknesses are determined from the refractive index dispersion relationships outlined in Appendix A. The structure consists of a 2λ AlGaInP quantum well optical cavity active region surrounded by $\text{Al}_{0.5}\text{In}_{0.5}\text{P}/(\text{Al}_{0.2}\text{Ga}_{0.8})_{0.5}\text{In}_{0.5}\text{P}$ DBRs, as outlined in Chapter 2. The substrate is oriented (311)A to maximize the optical efficiency of the quantum well optical cavity active region. A schematic diagram of the structure, along with the (charge neutral) real space energy band diagram and refractive index profile (at $\lambda_0 = 670$ nm) in and around the optical cavity active region, is shown in Fig. 3.7. The electric field intensity on resonance was calculated (see Appendix C) and is shown in Fig. 3.8. The calculated reflectances of the bottom (60.5 periods) and top (45 periods) DBR stacks, as seen from the optical cavity, are 0.99970 and 0.99887, respectively.

Just prior to VCSEL growth, an active region calibration sample was grown. This sample is identical to the optical pumping sample but without the top and bottom DBRs. The photoluminescence (PL) measurement from this calibration sample, taken at 300K, is given in Fig. 3.9. The peak emission is ~678 nm. As an additional check to verify the peak emission wavelength of the quantum wells (~corresponding to the $n=1$ transition), a small piece of the actual visible VCSEL wafer, near the short thickness end with

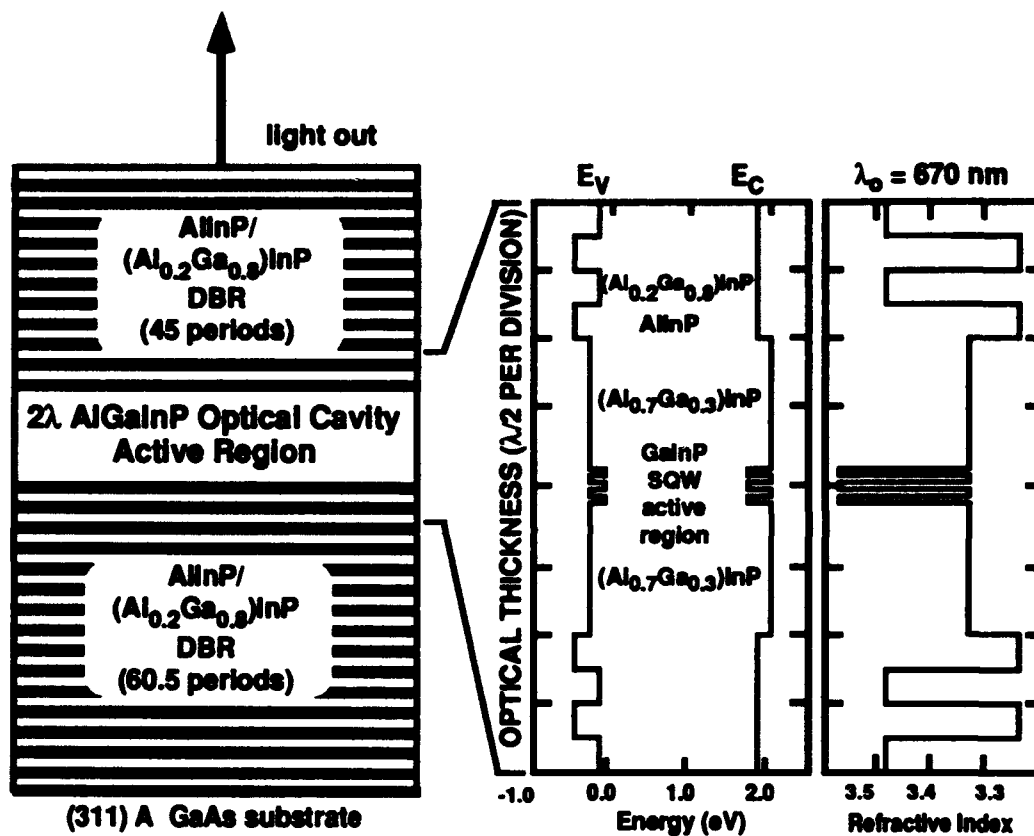


Fig. 3.7 Schematic diagram of the all-phosphide visible VCSEL for optical pumping experiments. Also shown is the real space, charge neutral energy band diagram and real refractive index profile for the optical cavity active region and two periods of the surrounding DBRs.

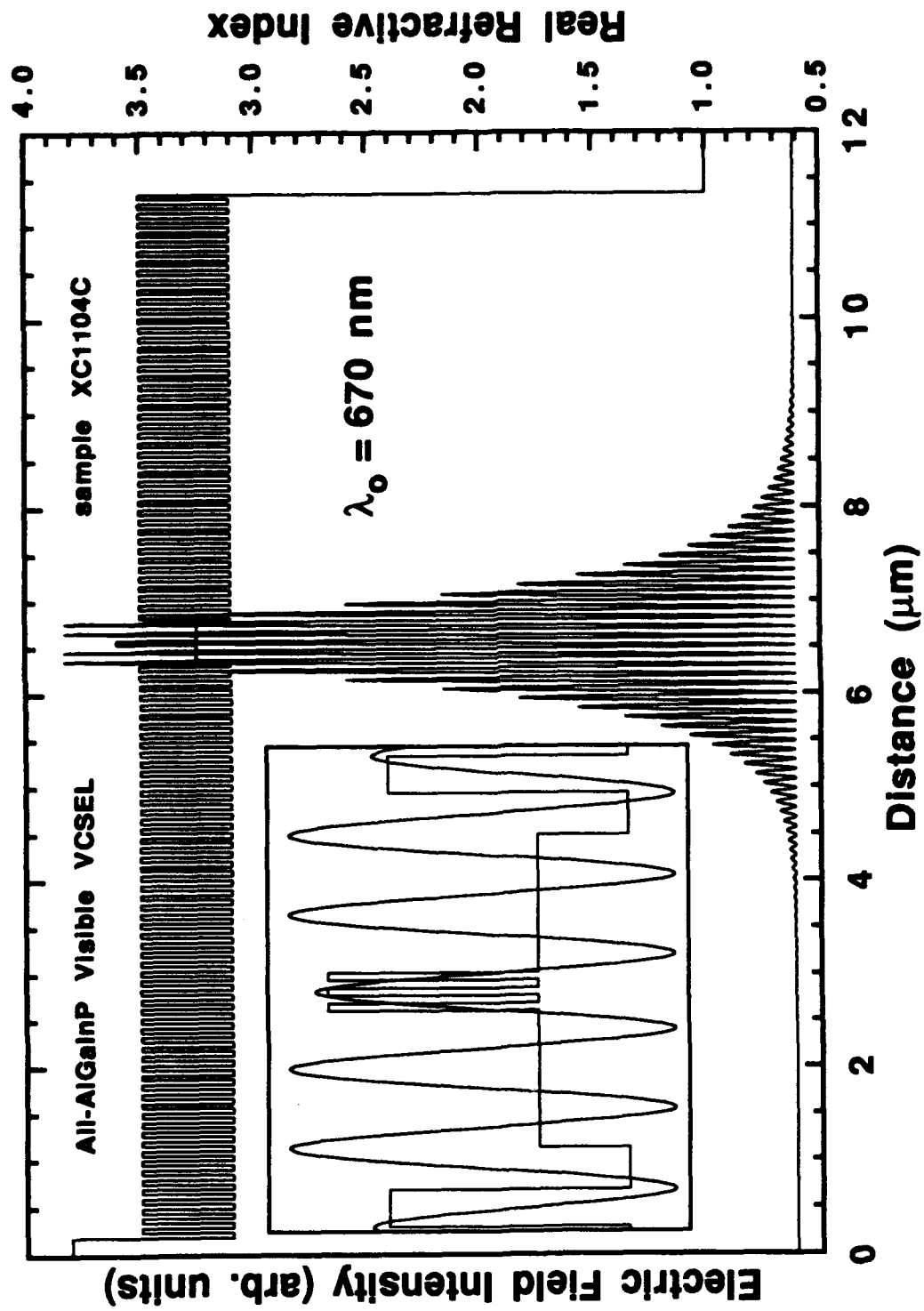


Fig. 3.8 The electric field intensity on resonance and refractive index against distance for the all-AlGaInP visible VCSEL.

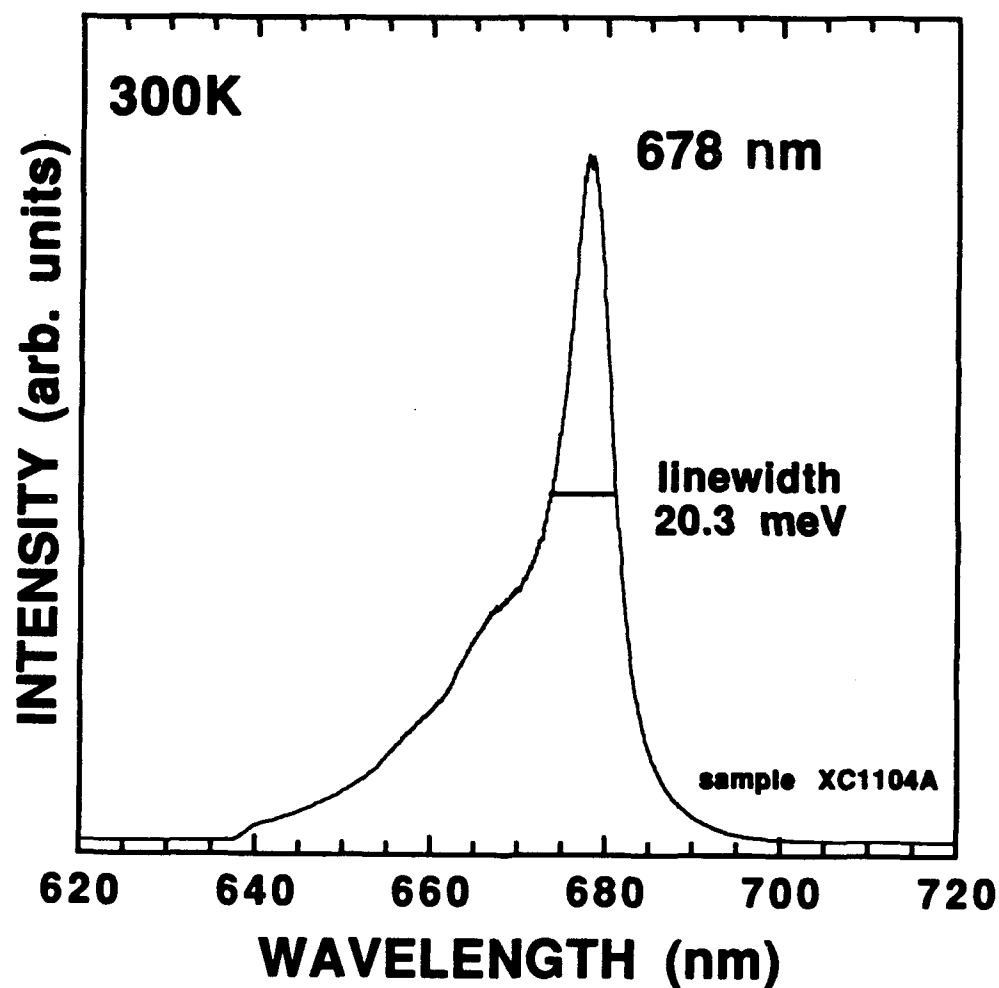


Fig. 3.9 Photoluminescence of an AlGaInP quantum well optical cavity active region calibration sample at 300K, just prior to the growth of the all-AlGaInP visible VCSEL.

Table 3.2 MOVPE Growth List for All-Phosphide Visible VCSEL Sample XC1104C

Thickness (Å)	Material	Index at λ_0	Thickness (Å)	Material	Index at λ_0
(repeat)			continued		
479.8	(Al _{0.2} Ga _{0.8}) _{0.5} In _{0.5} P	3.491	1758.7	(Al _{0.7} Ga _{0.3}) _{0.5} In _{0.5} P	3.316
518.4	Al _{0.5} In _{0.5} P	3.231			
x 45			(repeat)		
1758.7	(Al _{0.7} Ga _{0.3}) _{0.5} In _{0.5} P	3.316	518.4	Al _{0.5} In _{0.5} P	3.231
			479.8	(Al _{0.2} Ga _{0.8}) _{0.5} In _{0.5} P	3.491
			x 60		
(repeat)			518.4	Al _{0.5} In _{0.5} P	3.231
100.0	Ga _{0.44} In _{0.56} P (SQW)	3.577	5000	GaAs	3.81 - i0.16
100.0	(Al _{0.7} Ga _{0.3}) _{0.5} In _{0.5} P	3.316	substrate	(n+) GaAs (311)A	
x 2					
100.0	Ga _{0.44} In _{0.56} P (SQW)	3.577	Bragg wavelength	$\lambda_0 = 670$ nm	
			all epitaxial layers are unintentionally doped		

$\lambda_0 \approx 620$ nm, was etched in H₃PO₄:HCl:H₂O (1:1:1) [Lothian *et al.* 1992a, 1992b] to remove ~half of the top DBR stack. Note that the wet etchant is very rough (the etched surface resembles the Mayan pyramids in Mexico), and that this affects the following reflectance measurement. The measured PL (Ar⁺ laser excitation) and reflectance from a single spot on the etched test piece are shown in Fig. 3.10(a). The calculated emission spectrum and reflectance of the same structure (best estimation) is given in Fig. 3.10(b). The model given in Section 4.3 (Chapter 4) was used for the emission spectrum calculation. The PL is filtered spontaneous emission escaping through what is left of the top DBR. By comparing Fig. 3.10 with Fig. 3.9, it is clear that the peak of the spectral gain from the quantum well active region in the actual visible VCSEL sample occurs in the vicinity of ~675 nm (given the known variations across an unrotated wafer, see Fig. 5.5 in Chapter 5). The PL peak is expected to be ~678 nm or longer at wafer center.

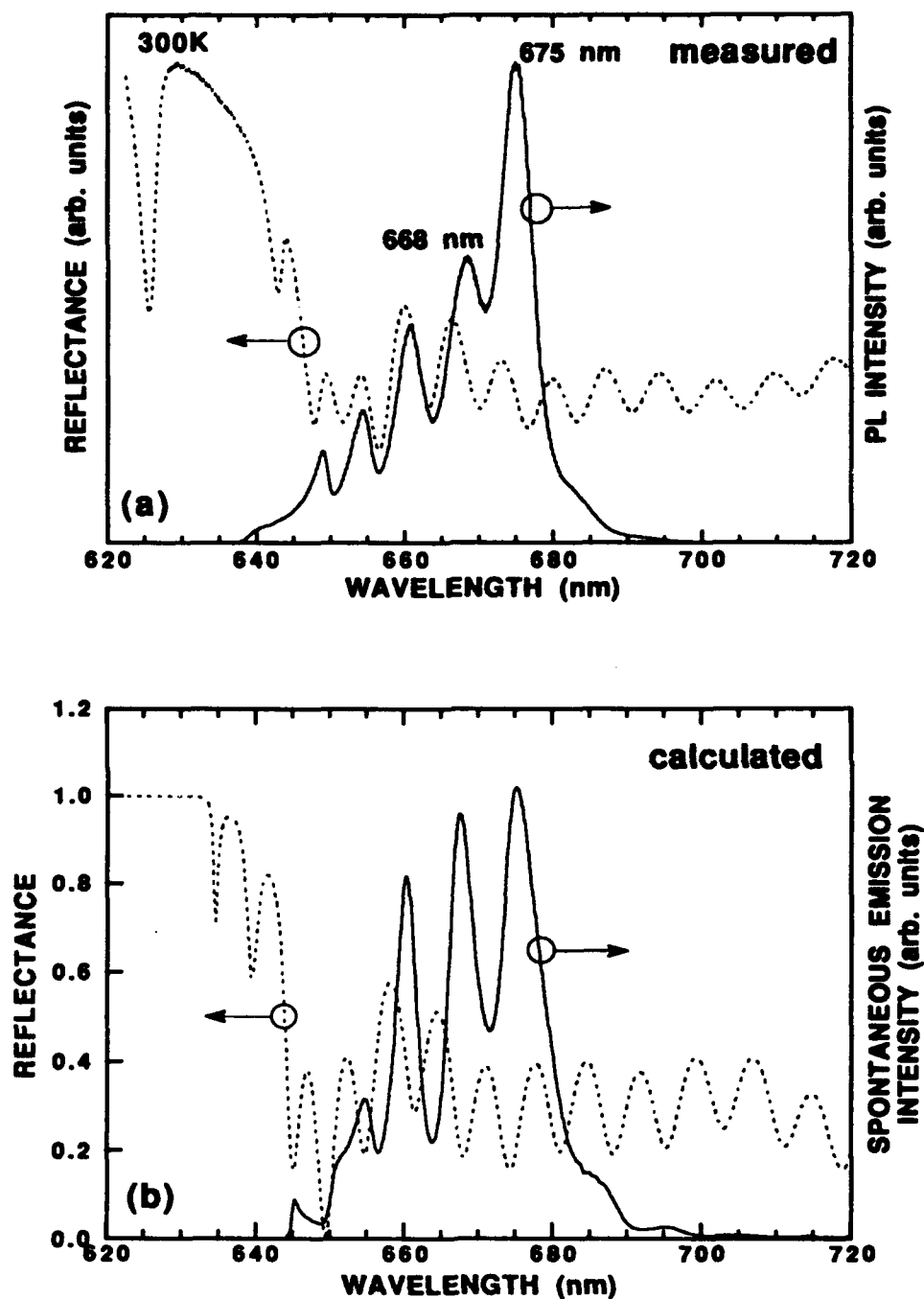


Fig. 3.10 (a) Measured reflectance and photoluminescence from the all-AlGaInP visible VCSEL at the short end of the wafer, with \sim half of the top DBR periods removed, and (b) corresponding calculated reflectance and spontaneous emission spectrum.

As with the hybrid structure described in Section 3.3, the "all-phosphide" VCSEL is grown without rotation, such that the Fabry-Perot resonance wavelength varies ~linearly with centerline position across the two inch wafer from ~690 nm to ~620 nm. This represents a layer thickness variation of ~14% (see Fig. 2.18). The thickness variation is larger than for the AlGaAs DBR structure because a higher growth pressure (110 mbar, instead of 80 mbar) is used to grow AlGaInP. Also, since the differential refractive index of the $\text{Al}_{0.5}\text{In}_{0.5}\text{P}/(\text{Al}_{0.2}\text{Ga}_{0.8})_{0.5}\text{In}_{0.5}\text{P}$ DBRs is smaller than for the $\text{AlAs}/\text{Al}_{0.5}\text{Ga}_{0.5}\text{As}$ DBR (see Chapter 2), the reflectance bandwidth is smaller. Figure 3.11 shows the measured reflectance spectra at several points across the wafer centerline. The range of lasing wavelengths, described below, is within the dashed lines.

Optically pumped lasing is achieved from 668.2 to 676.8 nm. Figure 3.12 is a plot of the lasing spectrum at 676.8 nm (solid curve). Also shown is the attenuated dye laser pump at 637 nm, and the reflectance of the structure (dashed curve) at the same spot on the wafer. The laser emission is shifted (~2 nm) longer than the Fabry-Perot wavelength from the reflectance measurement due to heating. The shift corresponds to an increase in temperature of ~50 °C (see Table 2.7).

The average incident pump power at threshold for the all-phosphide structure in Table 3.2 as a function of emission wavelength (or equivalently wafer position) is plotted in Fig. 3.13(a). The data is for pumping with the mode-locked Nd:YAG/dye lasers with 5 ps pulses at a period of ~11 ns. Similar results were obtained for pumping with the Ar^+ /dye lasers with 100 ns pulses at a period of 1.0 μs , except that device heating decreased the range of observed lasing wavelengths. The results are qualitatively similar to the results of Section 3.4, where the observed range of lasing wavelengths are blue-shifted relative to the peak of the measured PL emission from the quantum well active region. The L-L (light-in vs. light-out) characteristic at $\lambda_0 = 672$ nm is shown in Fig. 3.13(b). The output power quickly rolls over due to heating effects.

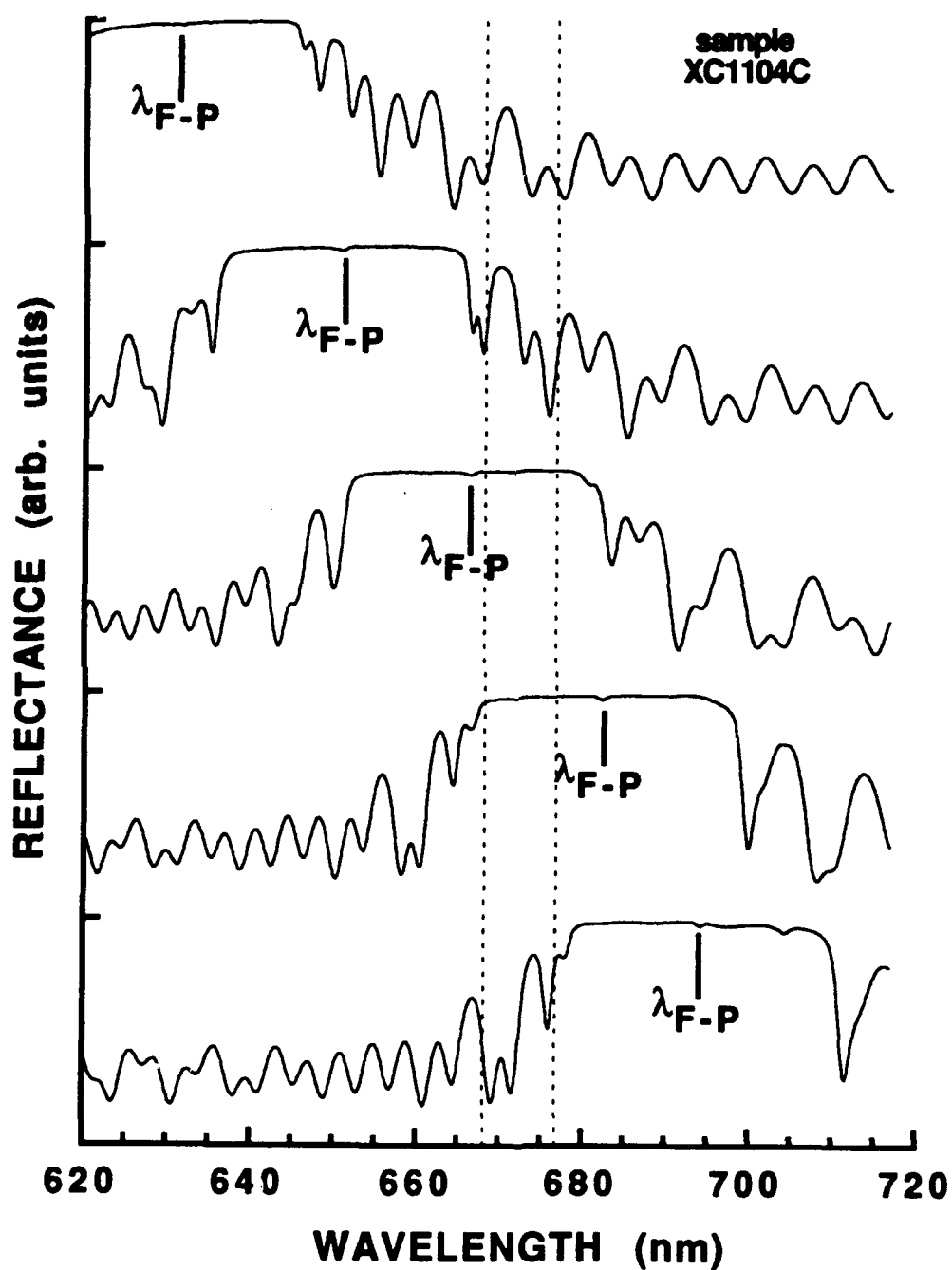


Fig. 3.11 Measured reflectance spectra (at normal incidence) at five approximately equally spaced points across the all-AlGaInP visible VCSEL wafer.

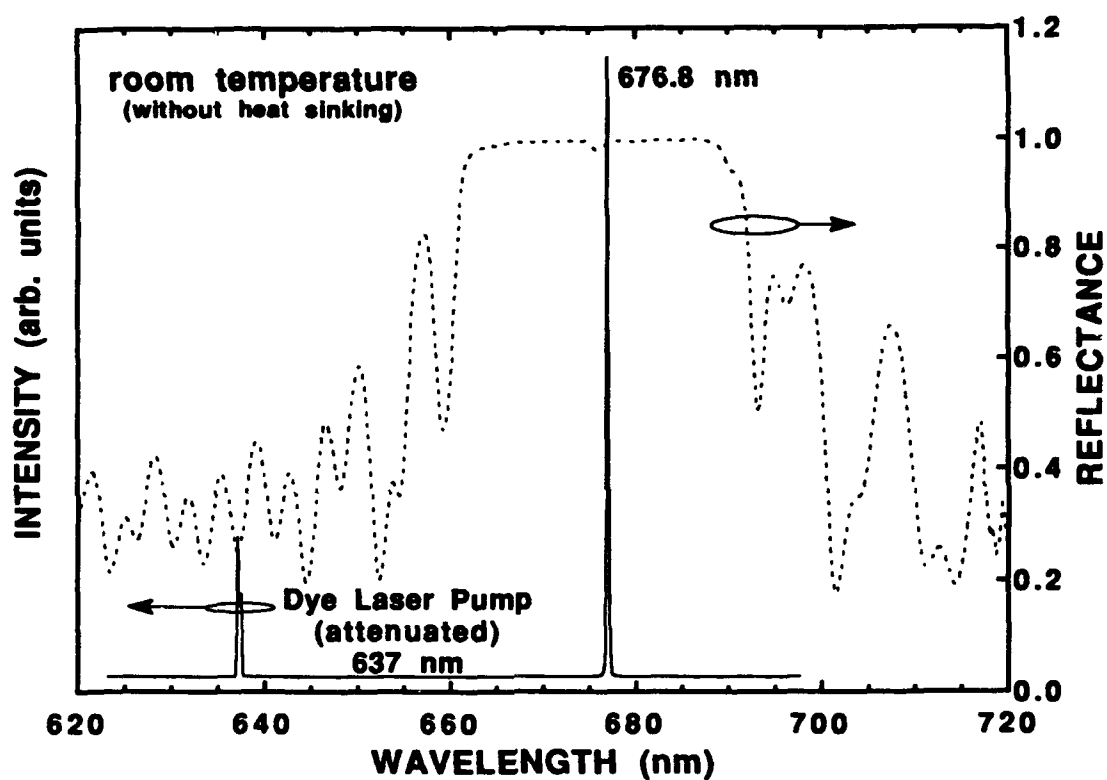


Fig. 3.12 Optically pumped lasing spectrum at $\lambda_0 = 676.8$ nm for the all-AlGaInP visible VCSEL. The attenuated dye laser pump is also shown (at $\lambda_0 = 637$ nm), as is the corresponding reflectance spectrum at normal incidence.

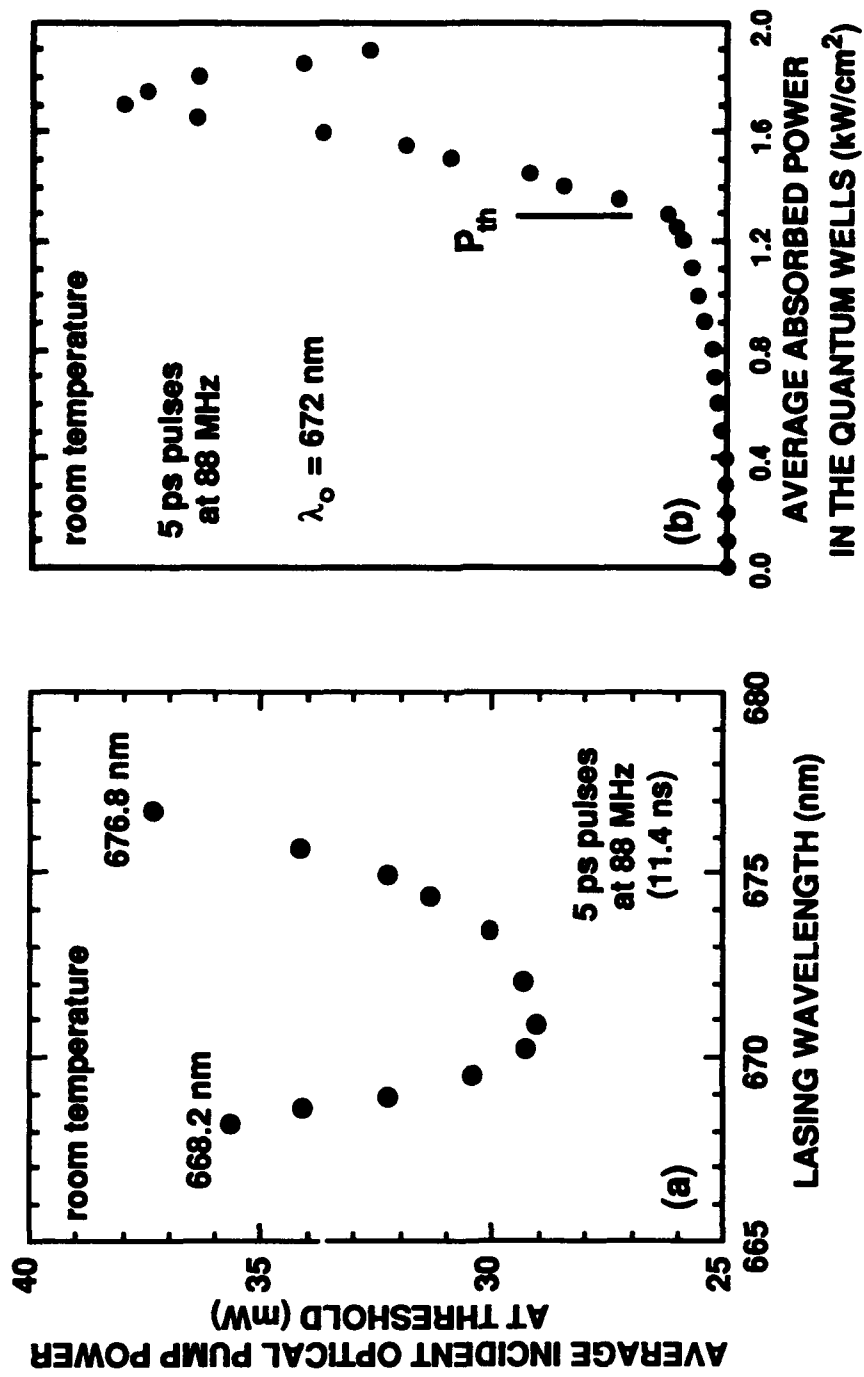


Fig. 3.13 (a) Measured incident power at threshold against lasing wavelength, and (b) L-L (light-in vs. light-out) characteristic of the all-phosphide optically pumped VCSEL.

3.6 Analysis of Results

This Section presents a qualitative analysis of the experimental results presented in Sections 3.4 and 3.5. Figure 3.14(a) shows the calculated central standing wave and real refractive index profile for the hybrid visible VCSEL at resonance wavelengths from 660 to 680 nm. These wavelengths cover the range of lasing observed in Section 3.4 (see Fig. 3.6), and correspond to the thickness variations observed in the unrotated VCSEL wafer. The quantum wells are taken as 10 nm thick, and the step-graded SCH structures are replaced with a conventional SCH, for simplicity. The sets of quantum wells are spatially offset due to the increasing refractive indices with decreasing wavelength. The physical thickness of the DBR periods decreases as the wavelength decreases. The standing wave intensity antinode is highest at 660 nm, and lowest at 680 nm. This is due to the increased reflectance of the DBRs (increased $\Delta n/n$) as the resonance wavelength decreases. The number of DBR periods remains constant, while the differential refractive index increases with decreasing wavelength. The relative confinement factor is essentially constant at $\Gamma_r \approx 1.41 \pm 0.02$, over the given resonance range. In contrast, the DBR reflectivity (and thus the phase penetration lengths, ~ 580 nm at 660 nm, ~ 610 nm at 680 nm) varies with resonance wavelength as shown in Fig. 3.14(b). From Eq. (2.24) with $\alpha_m = 25 \text{ cm}^{-1}$ and 50 cm^{-1} , and neglecting other absorptive losses, the threshold gain versus resonance wavelength is calculated and is shown in Fig. 3.14(b). Although the threshold gain decreases for shorter wavelengths, the behavior does not explain the discrepancy between the experimental peak spectral gain from the active region calibration samples, and the range of observed lasing wavelengths. The experimental results suggest that lasing is achieved with significant gain contributions from the second ($n=2$) quantized state.

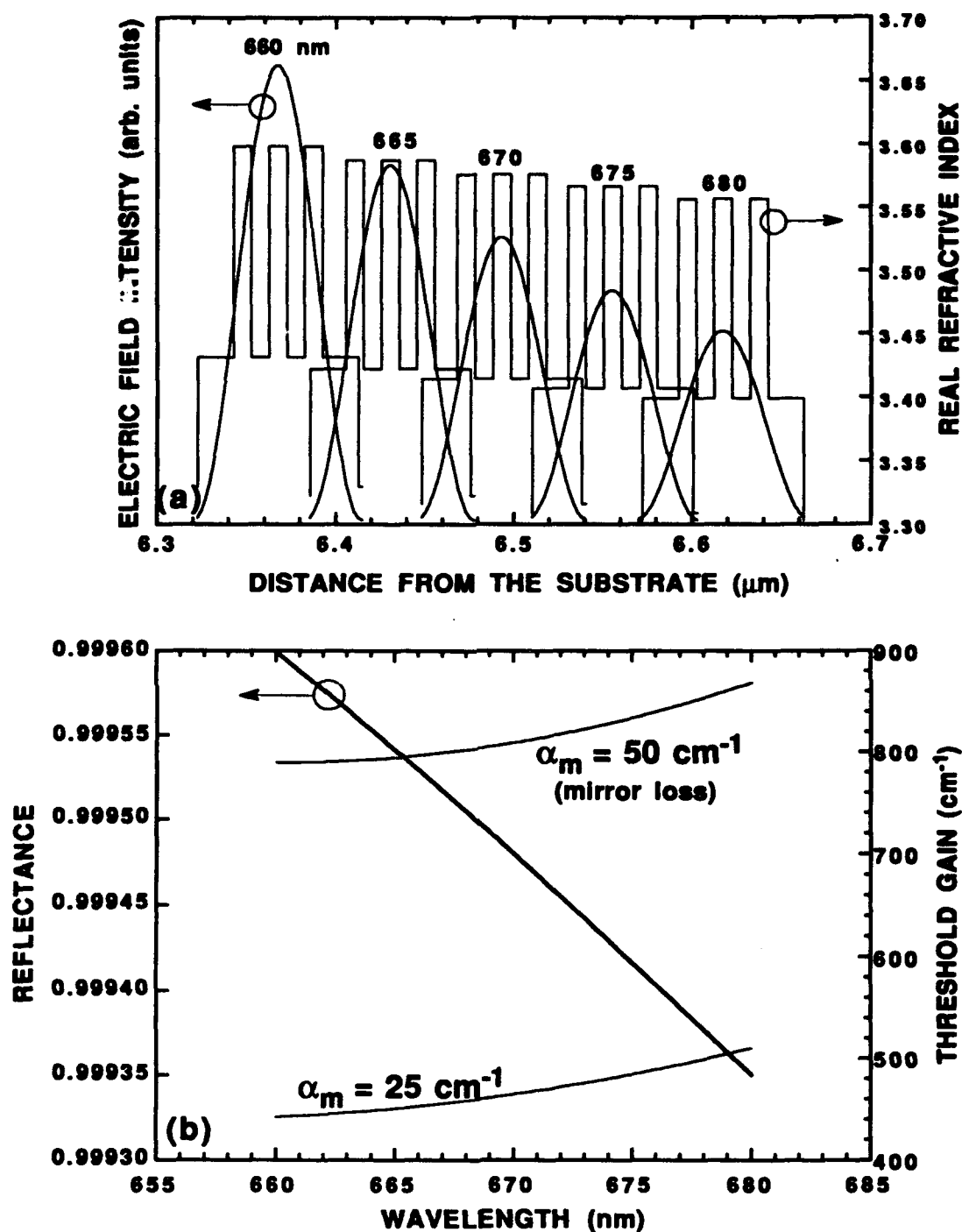


Fig. 3.14 Calculated (a) central standing wave and real refractive index profile at resonance wavelengths from 660 to 680 nm, and (b) corresponding reflectance ($R = \sqrt{R_t R_b}$) and threshold gain (with the given mirror loss) versus resonance wavelength, both for the optically pumped hybrid visible VCSEL.

Figure 3.15(a) qualitatively shows the shape of estimated gain curves in and around the $n=2$ gain peak for a GaInP quantum well with increasing carrier density and temperature (gain curves 1, 2, 3, and 4). The gain curves are similar to those in Fig. 2.33(b). The quasi-parabolic shape of the data in Fig. 3.6 for the hybrid visible VCSEL is reproduced in Fig. 3.15(b). Note that this shape is similar to the inverse shape of the gain curves at the $n=2$ gain peak. It is assumed that the gain at the $n=1$ peak remains below g_{th} due to high cavity losses, or due to insufficient gain. Insufficient gain could be due to a variety of factors such as excess heating causing carrier leakage out of the well. Indeed, much of the incident pumping power is absorbed in the GaAs substrate and converted to heat. In Fig. 3.15(a), curve 1 rises to point A on the threshold gain curve. This corresponds to point A in Fig. 3.15(b) at the threshold minimum. Curves 2 and 3 represent increasing quantum well gain with a red-shift due to heating and due to a high density of carriers in the well. The red-shift overwhelms the small blue-shift in the gain curve that is associated with band filling. Point B in Fig. 3.15(a) is first reached by the shoulder of gain curve 2. In curve 4, the gain decreases and red-shifts further due to excessive device heating. With further increases in carrier density, the gain drops below the required threshold value. Points A, B, and C can be traced out from Fig. 3.15(a) and used to construct the quasi-parabolic curve in Fig. 3.15(b), as shown.

A similar analysis is possible for the all-AlGaInP visible VCSEL, in order to trace out the quasi-parabolic curve shown in Fig. 3.13(a). This type of analysis can also be used to qualitatively explain the shape of the L-L curve in Fig. 3.13(b), with the help of Fig. 2.30 in Chapter 2. Recall that the peak of the quantum well spectral gain red-shifts at a faster rate than does the Fabry-Perot resonance with increasing temperature (or equivalently increasing optical pump power). Once passed threshold, the L-L curve rises sharply and then rolls over with increasing pump power. This correlates to the rising, and red-shifting of the quantum well gain, relative to the Fabry-Perot resonance.

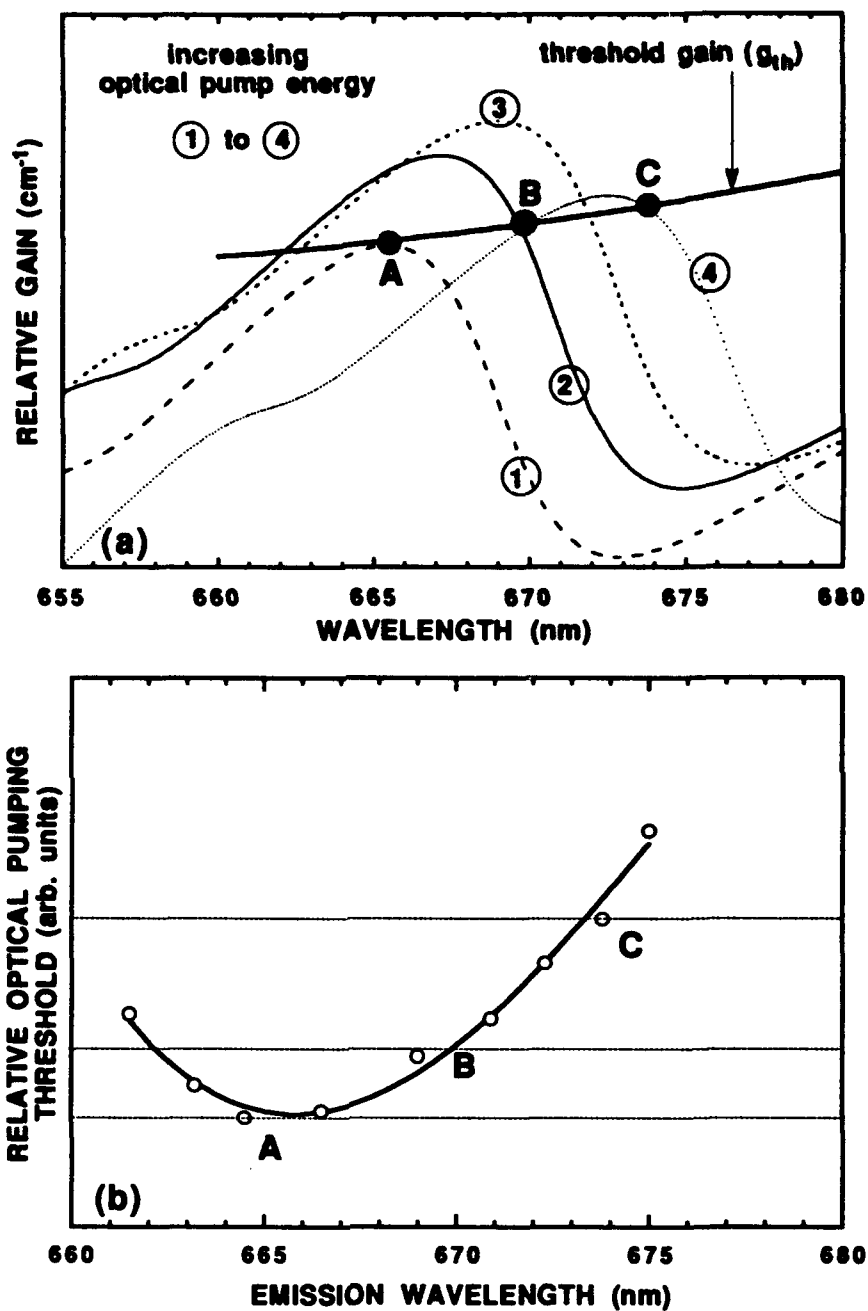


Fig. 3.15 Qualitative analysis of the gain versus lasing wavelength results for the optically pumped hybrid AlGaInP/AlGaAs visible VCSEL. (a) Calculated threshold (thick solid line) and quantum well gain curves 1 to 4 (other lines) in and around the $n=2$ gain peak with increasing pump energy. (b) Repeated Fig. 3.6, showing pumping threshold versus lasing wavelength across an unrotated wafer.

Eventually, the gain peak red-shifts passed the Fabry-Perot resonance and the power output decreases.

The thermal resistivity of $\text{Ga}_{0.5}\text{In}_{0.5}\text{P}$ ($\sim 19 \text{ cm } ^\circ\text{C/W}$) is higher than that for AlGaAs ($< 10 \text{ cm } ^\circ\text{C/W}$) [Bour 1993]. Thus it is not surprising that the operating temperature of the all- AlGaInP visible VCSEL is higher than that for the equivalent hybrid device, and that the range of lasing wavelengths is reduced. To achieve lasing near the $n=1$ gain peak at lower carrier densities, either the device losses must be reduced or the available gain increased. The VCSELs discussed above are undoped, and the losses due to free carrier absorption should be small. Table 3.3 compares the hybrid visible VCSEL discussed in Section 3.4 to three other hybrid visible VCSELs from previous studies. The results are obtained from identical experimental conditions. These structures are similar to the structure in Table 3.1, except for the number of DBR periods, and the thickness of the quantum wells and the separation layers. Also, the optical cavity thickness is 1λ . The results in Table 3.3 suggest that the gain from the 10 nm thick quantum wells with 10 nm thick separation layers is less efficient than the gain achieved from the thinner wells and barriers. As presented in Chapter 5, similar results are obtained for electrically injected visible VCSELs. Visible VCSEL diodes with 10 nm thick quantum wells and barriers are able to lase only with significant gain contributions from the $n=2$ quantum well state, at threshold current densities of $J_{\text{th}} \sim 4.2 \text{ kA/cm}^2$. In contrast, identical devices with thinner 6 nm quantum wells and barriers lase with gain contributions predominantly from the $n=1$ quantum well state, with $J_{\text{th}} \sim 2 \text{ kA/cm}^2$.

3.7 Conclusions

Optically pumped lasing in visible VCSELs with AlGaInP strained quantum well optical cavity active regions and AlAs/AlGaAs and AlInP/AlGaInP DBRs was investigated. For undoped, unrotated (during MOVPE growth) wafers, lasing was

Table 3.3 Comparison of Optically Pumped Hybrid Visible VCSELs

Wafer I.D.	Number of QWs	Thickness QW/Barrier (nm/nm)	Number [‡] of Top DBRs	Number [‡] of Bottom DBRs	PL Peak Emission at 300 K (nm)	Lasing Wavelength at Minimum Threshold (nm)
XB 1024B [†]	3	6/7	31	40.5	~655	~657
XC 0227C	4	6/7	31	40.5	~650	~650
XC 0214B	3	6/7	31	40.5	~660	~665
XC 0915C	3	10/10	33	45.5	~683	~665

[†][R. P. Schneider *et al.* 1992a]

[‡] includes a $\lambda/4$ In_{0.5}Al_{0.5}P layer (see Table 3.1)

achieved at ~room temperature from 661.8 to 675.0 nm in the hybrid structure, and from 668.2 to 676.8 nm in the all-AlGaInP structure. The lasing wavelengths were blue-shifted from the peak of the room temperature PL spectra measured from the quantum well active regions. This phenomena was qualitatively explained by using a conventional quantum well gain model. It was shown that lasing was achieved due to significant gain contributions from the $n=2$ quantized quantum well state. The optically pumped samples were undoped, and the DBRs were conservatively designed (i.e. large numbers of DBR pairs, and thus high values of reflectance). Thus, it was expected that the cavity losses (i.e. absorption) and the gain threshold would be minimal. The measured characteristics, however, suggest that the gain from the active region, composed of 10/10 nm thick quantum well/barrier layers, was inefficient and thus not an optimal design. This hypothesis was corroborated by comparing the present device results to results from similar hybrid visible VCSELs, with 6/7 nm thick quantum well/barrier layers (a more efficient design due to improved standing wave overlap). These latter optically pumped structures operated with gain contributions primarily from the $n=1$ quantized quantum well state.

References for Chapter 3

Bour, D. P., "AlGaInP Quantum Well Lasers", Ch. 9 in *Quantum Well Lasers*, P. S. Zory, Jr., ed., (Academic Press:San Diego, 1993c).

Gourley, P. L., and T. J. Drummond, "Visible, Room-Temperature, Surface-Emitting Laser Using an Epitaxial Fabry-Perot Resonator With AlGaAs/AlAs Quarter-Wave High Reflectors and AlGaAs/GaAs Multiple Quantum Wells", *Applied Physics Letters* 50(18), p. 1225-1227 (4 May 1987).

Lothian, J. R., J. M. Kuo, F. Ren, and S. J. Pearton, "Plasma and Wet Chemical Etching of $\text{In}_{0.5}\text{Ga}_{0.5}\text{P}$ ", *Journal of Electronic Materials*, 21(4), p. 441-445 (1992a).

Lothian, J. R., J. M. Kuo, W. S. Hobson, E. Lane, F. Ren, and S. J. Pearton, "Wet and Dry Etching Characteristics of $\text{Al}_{0.5}\text{In}_{0.5}\text{P}$ ", *Journal of Vacuum Science Technology B*, 10(3), p. 1061-1065 (1992b).

Lott, J. A., R. P. Schneider, Jr., and K. J. Malloy, "All InAlGaP Visible (672 nm) Vertical-Cavity Surface-Emitting Laser", *Digest of the Conference on Lasers and Electro-Optics (CLEO'93)*, Paper CWJ56, Baltimore, MD (2-7 May 1993a).

Saleh, B. E. A., and M. C. Teich, *Fundamentals of Photonics*, (Wiley:New York, 1991).

Schneider, Jr., R. P., R. P. Bryan, J. A. Lott, and G. R. Olbright, "Visible (657 nm) InGaP/InAlGaP Strained Quantum-Well Vertical-Cavity Surface-Emitting Laser", *Applied Physics Letters*, 60(15), p. 1830-1832 (13 April 1992a).

Schneider, Jr., R. P., R. P. Bryan, J. A. Lott, E. D. Jones, and G. R. Olbright, "MOVPE Growth of InAlGaP-Based Visible Vertical-Cavity Surface-Emitting Lasers", *Journal of Crystal Growth*, 124, p. 763-771 (1992b).

Schneider, Jr., R. P., and J. A. Lott, "InAlP/InAlGaP Distributed Bragg Reflectors for Visible Vertical Cavity Surface Emitting Lasers", *Applied Physics Letters*, 62(22), p. 2748-2750 (31 May 1993).

Chapter 4 Resonant Cavity Light Emitting Diodes

4.1 Introduction

Resonant cavity light emitting diodes (RCLEDs) have attracted interest due to their increased output intensities, narrow spectral linewidths, and narrow radiation pattern, as compared to conventional LEDs. These devices consist of an optical cavity active region placed within an asymmetric Fabry-Perot etalon. The etalon mirrors are typically quarter-wave ($\lambda/4$) semiconductor or dielectric distributed Bragg reflectors (DBRs), or metal films over phase matching layers. One DBR has a reflectance (R) near 100% at the Bragg wavelength while the other coupling DBR has $R \leq 97\%$, which determines the etalon cavity quality factor (Q). Spectral linewidth is selected by the cavity Q , and decreases as Q increases. Spatially localized gain layers, such as quantum wells, are placed at the antinodes of the electric field intensity (in the optical cavity), resulting in enhanced spontaneous emission on resonance [Björk *et al.* 1991, Feng 1991, Lei and Deppe 1992, Lei *et al.* 1993]. The thickness of the optical cavity (microcavity) is on the order of the emission wavelength. The RCLED is a potential light source in applications such as wavelength division multiplexing, optical fiber communications, free space optical interconnects, and integrated optical logic. *Visible* (~560 to 690 nm) RCLEDs, composed of AlGaInP quantum well or bulk layer active regions, have potential application in local area networks based on polymer optical fibers [Dutt *et al.* 1988], and for fabrication into densely packed one- or two-dimensional arrays for optical interconnect and monochromatic display applications. Compared to vertical cavity surface emitting lasers (VCSELs), RCLEDs are easier to fabricate and have relaxed

epitaxial growth tolerances, but, they have lower output powers and broader spectral linewidths.

Much like the quantization of energy states in quantum wells, modes are quantized in microcavities. A fundamental quantum electrodynamic effect is the coupling of spontaneous emission, generated within a microcavity, to the modes of the microcavity [De Martini *et al.* 1987, Haroche and Kleppner 1989, Baba *et al.* 1991, Yamamoto and Slusher 1993]. For RCLEDs, the rate of spontaneous emission, for a given wavelength, is increased or decreased (enhanced or inhibited) depending on the parameters of the microcavity at that wavelength. Example parameters include the cavity optical thickness, the mirror reflectance and reflectivity phase, and the exact placement of the gain layers within the microcavity. The first demonstration of enhanced and inhibited spontaneous emission in all-semiconductor microcavity LEDs was achieved in 1990 [Deppe *et al.*, Rogers *et al.*]. This first structure consisted of $\text{Ga}_{0.8}\text{In}_{0.2}\text{As}$ quantum wells surrounded by GaAs barrier layers, and the output was enhanced spontaneous emission at ~ 980 nm. This was followed by IR "RCLEDs" that emitted at ~ 860 nm [Schubert *et al.* 1992] and at ~ 1.3 and 1.55 μm [Hunt *et al.* 1992a, 1992b]. These structures were similar to conventional IR VCSELs, except that the reflectance of the coupling mirror was kept low to prevent lasing. The first visible RCLEDs, composed of an AlGaInP quantum well active region surrounded by AlAs/AlGaAs DBRs, were reported in February 1993 [Lott *et al.* 1993a]. This was soon followed by the first report of all-AlGaInP visible RCLEDs in June 1993 [Lott *et al.* 1993b]. With the all-AlGaInP approach, emission is possible at wavelengths as short as ~ 560 nm by using bulk layers (or a short period superlattice) in the active region. Thus, high density arrays of multi-color (red, orange, yellow, green) RCLEDs should be possible. Devices similar to RCLEDs, called "high-brightness" LEDs, where a DBR high reflector was placed beneath the active region, were also reported [Kato *et al.* 1991, Sugawara *et al.* 1992].

This Chapter presents the fabrication, modeling, and characterization of RCLEDs with both GaInAs/GaAs optical cavity active regions (emitting at ~ 980 nm), and with AlGaInP optical cavity active regions (emitting at ~ 670 nm). The results are significant in that: 1) they include a classical model that predicts the spontaneous emission spectrum for arbitrary RCLEDs, and for the first time considers DBR reflectivity phase, finite photon coherence time, and absorptive cavity losses; 2) they include the first characterization and analysis of an all-semiconductor IR RCLED, before and after some dielectric DBR periods were added to transform the RCLED into a VCSEL; and 3) they include the spectral characterization and analysis of the first visible RCLEDs.

This Chapter is organized as follows. Section 4.2 overviews the fabrication sequences for the RCLEDs. Next, Section 4.3 presents a Classical Wave Interference Model, which is used to model the relative intensity and spectral characteristics (i.e. the enhanced and inhibited spontaneous emission) from one side of an RCLED. Section 4.4 presents the results from an infrared ($\lambda_0 \sim 980$ nm) RCLED composed of GaInAs quantum wells and AlGaAs DBRs. This IR RCLED is transformed into an IR VCSEL by increasing the reflectance of the top coupling DBR, by adding a few dielectric DBR periods. The subsequent characteristics of the hybrid IR VCSEL are presented. Next, Section 4.5 presents the spectral characteristics of hybrid AlGaInP/AlGaAs visible RCLEDs, and Section 4.6 follows with the design and spectral characteristics of all-AlGaInP visible RCLEDs. Finally, Section 4.7 contains the Chapter conclusions.

4.2 Device Fabrication

The RCLEDs were fabricated using the same basic sequences as described for the Quick VCSELs and the ion implanted VCSELs in Chapter 5 (see Section 5.2). These are not the optimal geometries for RCLEDs, but are sufficient to investigate the basic device spectral emission characteristics. A cross-section schematic diagram of a completed IR

RCLED is shown in Fig. 4.1. The device is fabricated as follows. Photoresist, 3 μm thick, is patterned in the reverse image of the top contact pad. Hydrogen ions are implanted with a dose of 1 to 5 $\times 10^{14} \text{ cm}^{-2}$, to a depth just above the top DBR/optical cavity interface (for 10 top $\text{Al}_x\text{Ga}_{1-x}\text{As}$ DBR periods at $\lambda_0 = 980 \text{ nm}$, this depth is $\sim 1.5 \mu\text{m}$, requiring an implant accelerating potential of $\sim 130 \text{ keV}$). After the implant, Ti/Au (30 nm/270 nm) p-contact metal is deposited by e-beam evaporation. The self-aligned top contact is then lifted-off. The contact pads are rectangular (40 \times 60 μm), with optical apertures (holes with circular diameters) of 10, 15, 20, or 30 μm . Next, the rectangular contacts are masked with photoresist, and the exposed material is removed, either by a wet etchant (such as $\text{H}_3\text{PO}_4\text{:H}_2\text{O}_2\text{:H}_2\text{O}$, with a volume ratio of $\sim 1\text{:}1\text{:}10$), or by conventional reactive ion etching using a BCl_3/Cl_2 plasma. The material is etched down just through the optical cavity active region. For wet etching, it is possible to visually count the DBR periods as they are etched by observing the series of light and dark reflections. In contrast to the schematic in Fig. 4.1, the wet-etched sidewalls are sloped. For dry etching, the etch depth is determined in real time by using *in situ* reflectance monitoring (see Fig. 2.12). The etching creates mesas and isolates individual devices. The final step is the deposition, by e-beam evaporation, of n-type contact metal (Ge $\sim 20 \text{ nm}$ / Au $\sim 50 \text{ nm}$ / Ni $\sim 10 \text{ nm}$ / Au $\sim 300 \text{ nm}$) on to the entire back surface of the substrate. This contact is subsequently annealed at $\sim 400^\circ\text{C}$ for 30 seconds to improve the ohmic contact.

A schematic diagram of a completed all-AlGaInP visible RCLED is shown in Fig. 4.2. The devices were fabricated as follows. A photoresist implant mask was patterned in the reverse image of the top contact for implantation with 5×10^{14} hydrogen ions/ cm^2 at an energy of 70 keV. (A recent study revealed that H^+ does not effectively electrically isolate $\text{Al}_{0.5}\text{In}_{0.5}\text{P}$, even at very high doses [Zolper *et al.* 1993]. However, moderate doses ($\sim 1 \times 10^{14} \text{ cm}^{-2}$) of either argon or oxygen were shown to electrically isolate $\text{Al}_{0.5}\text{In}_{0.5}\text{P}$). Next, self-aligned p-electrode metal

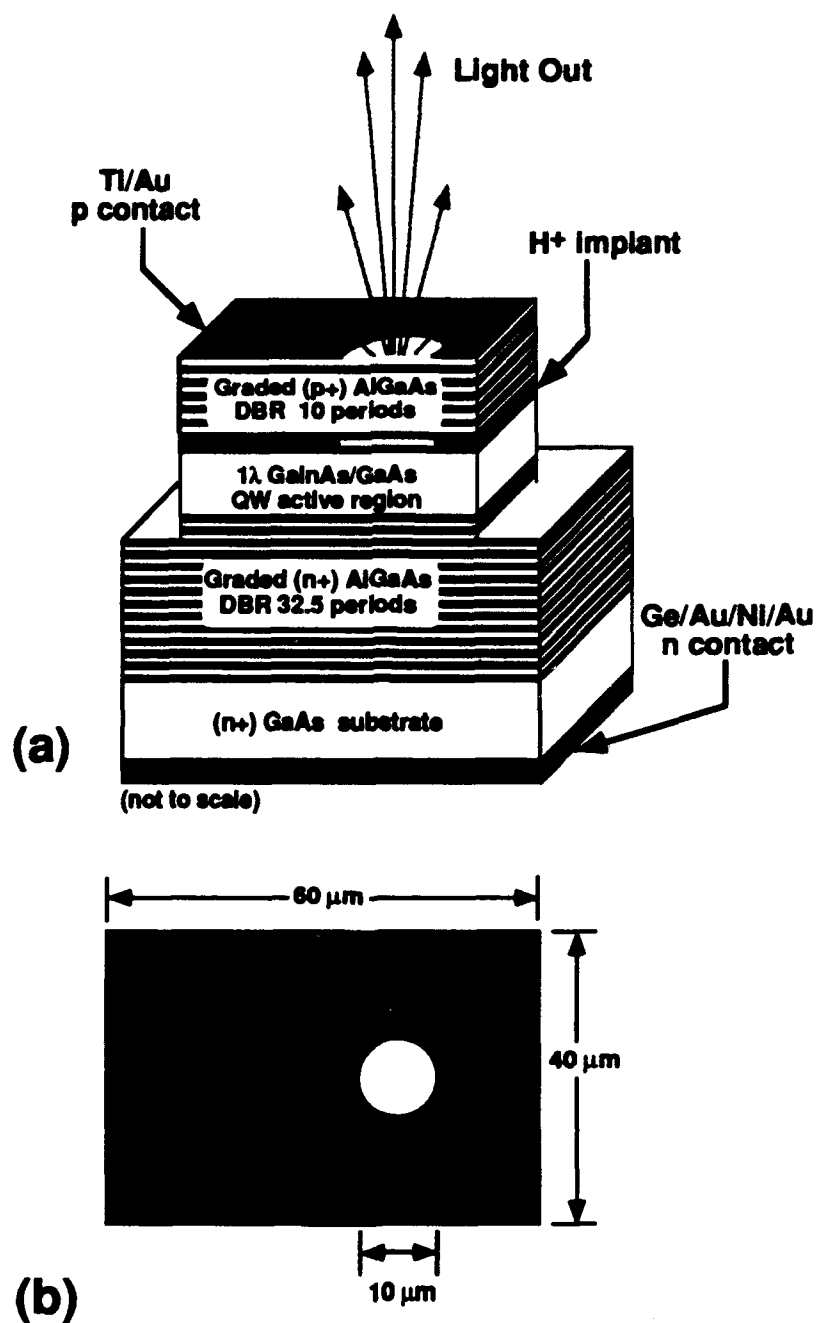


Fig. 4.1 Schematic diagram of (a) a fabricated IR RCLED and (b) the top contact pad. The optical aperture diameter is 10 (shown), 15, 20, or 30 μm.

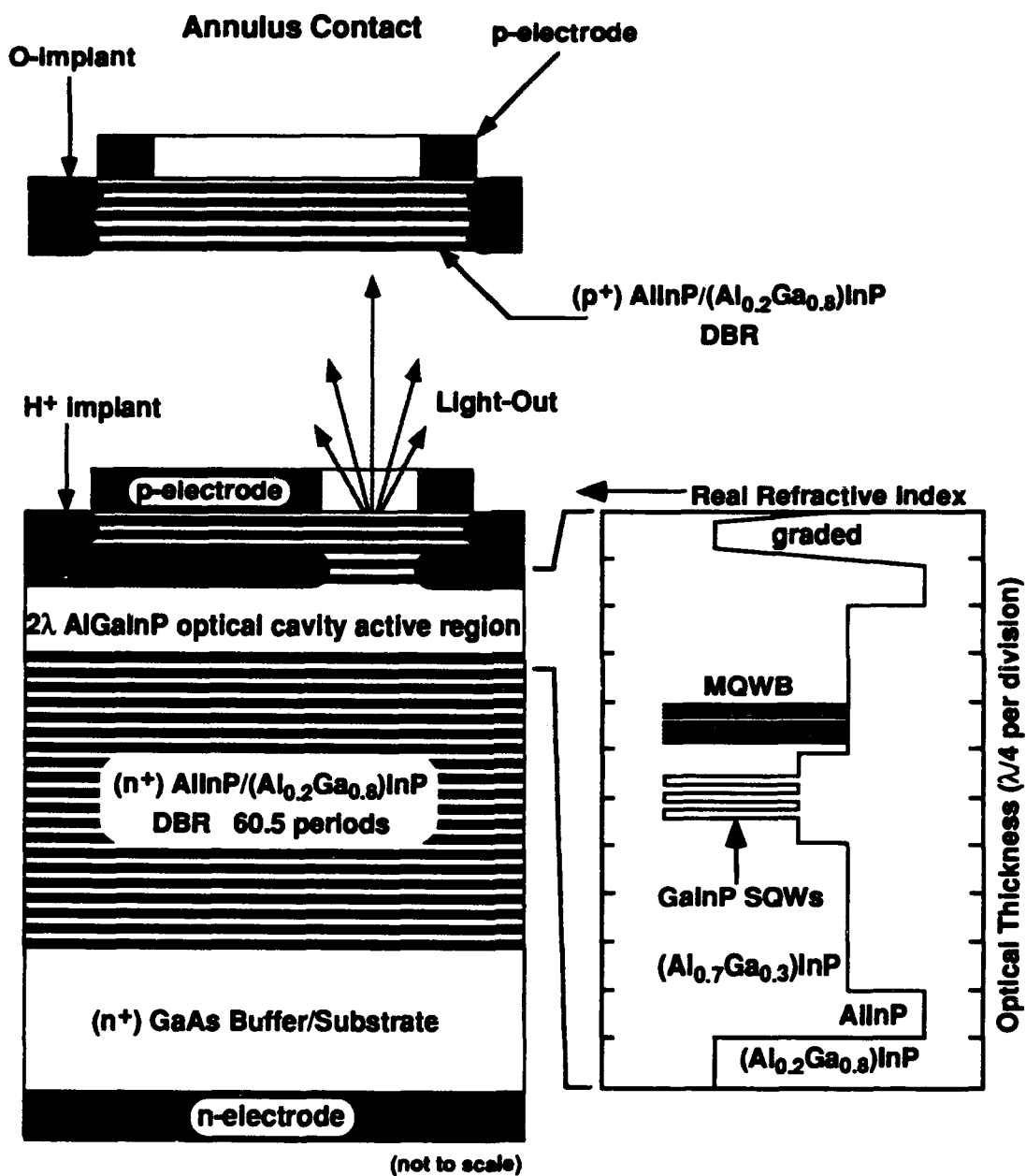


Fig. 4.2 Schematic cross section diagram of the all-AlGaInP visible RCLED. Also shown is the refractive index profile of the optical cavity active region and adjacent pairs of DBRs. The top inset is an alternate annulus top contact geometry

(Ti/Au) was e-beam deposited and lifted-off. The entire p-electrode was then masked with photoresist and a second double hydrogen ion implant was performed at energies of 70 keV and 40 keV to isolate the devices without mesa etching. Finally, n-type ohmic contact metal (GeAu/Ni/Au) was e-beam deposited onto the back surface and annealed as above. For this device geometry, a minimum thickness of about 5 DBR periods is needed to adequately spread current from the top contact into the active emitting area while maintaining a moderately low resistance. For less than 5 periods a phase matching layer could be used as part of the top coupling stack to insure efficient current injection.

4.3 Classical Wave Interference Model

This Section contains the derivation of a Classical Wave Interference Model. This model predicts the relative intensity and spectral characteristics of the emission from one side of an asymmetric multilayer Fabry-Perot etalon structure (see Section 2.5). The active segment in the optical cavity is a quantum well, which in the theory is taken as a spatially localized dipole emitter. The derivation follows that in [Huang *et al.* 1992, Lei *et al.* 1993b, 1993c] but is more general in that it includes the DBR reflectivity phase terms (θ_1 and θ_2). Additionally, analytical equations are given that account for round trip cavity losses, and for finite coherence length. This model is useful for the first order analysis of the (inhibited and enhanced) spontaneous emission spectra emitted from resonant microcavities containing optical cavity (quantum well) active regions. The limitations of the model are also discussed.

Figure 4.3 shows a schematic diagram of the multilayer Fabry-Perot etalon resonant cavity. The quantum well is taken as a spatially isotropic dipole emitter that is placed at an arbitrary distance L_1 and L_2 from the DBR mirrors. The thickness of the optical cavity is $L = L_1 + L_2$. The dipole emits coherent electromagnetic radiation (spontaneous emission) in the form of impulse (single event) wave packets with electric

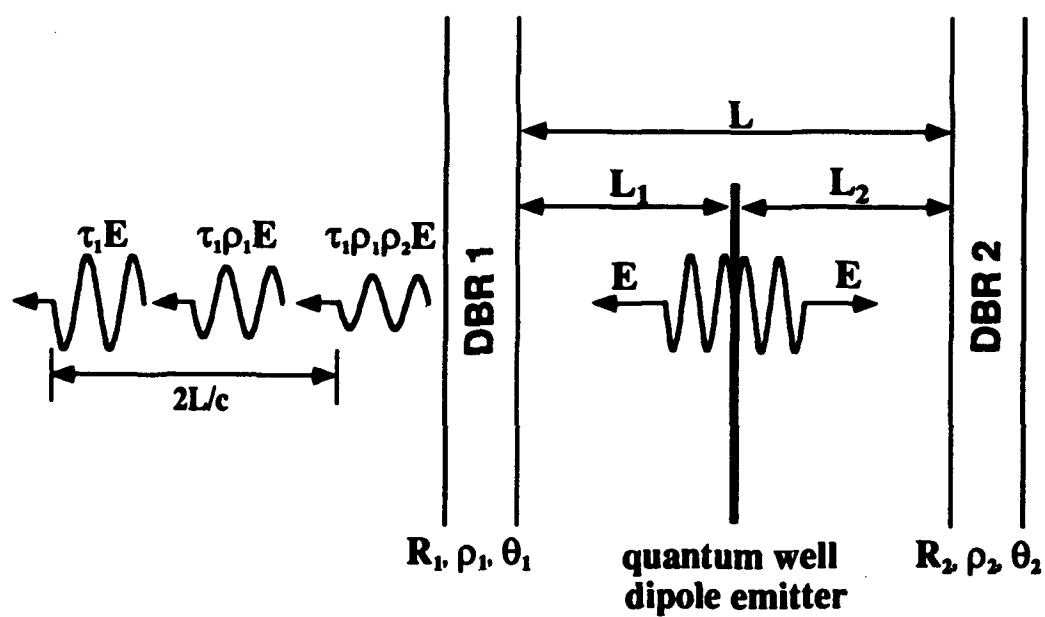


Fig. 4.3 Schematic diagram of a multilayer Fabry-Perot etalon for use with the Classical Wave Interference Model [after Lei *et al.* 1993a].

field amplitude $E(t)$. The wave packet intensity spectrum is approximately Gaussian, and is similar to the electroluminescence spectrum of a conventional light emitting diode, or to the photoluminescence spectrum of a quantum well structure. The coherence time (τ_c) of the spontaneous emission is taken to be much longer than the photon lifetime in the cavity. The DBRs are modeled as mirrors with transmittivity τ , reflectivity ρ , reflectivity phase θ , transmittance T , and reflectance R , all functions of wavelength. These parameters are readily calculated using the matrix method described in Appendix C. For simplicity, the DBRs are treated as single interfaces of negligible spatial extent.

The electric field amplitude emitted out the top (side 1) DBR mirror (E_{R1}) is a summation of wave train pulses due to the repetitive reflections within the optical cavity, analogous to the Airy series that results for conventional Fabry-Perot etalons [MacLeod 1989]. At normal incidence

$$\begin{aligned}
 E_{R1}(t - L_1/c) = & \tau_1 E(t) + \tau_1 \rho_2 E(t + 2L_2/c) \\
 & + \tau_1 \rho_1 \rho_2 E(t + 2L/c) + \tau_1 \rho_1 \rho_2^2 E(t + 2L_2/c + 2L/c) \\
 & + \tau_1 \rho_1^2 \rho_2^2 E(t + 4L/c) + \tau_1 \rho_1^2 \rho_2^3 E(t + 2L_2/c + 4L/c) + \dots
 \end{aligned} \tag{4.1}$$

where τ_1 is the complex transmittivity coefficient of DBR 1 (as seen from inside the optical cavity), ρ_1 and ρ_2 are the complex reflectivity coefficients of DBR 1 and 2, respectively (as seen from within the optical cavity), t is time, $c = c_0/n_{cav}$ is the speed of light in the optical cavity, and n_{cav} is the refractive index of the optical cavity. The frequency spectrum emitted out of DBR 1 is found by taking the Fourier transform of Eq. (4.1)

$$\begin{aligned}
\int_{-\infty}^{\infty} E_{R1}(t - L_1/c) e^{i\omega t} dt &= \int_{-\infty}^{\infty} \tau_1 E(t) e^{i\omega t} dt + \int_{-\infty}^{\infty} \tau_1 \rho_2 E(t + 2L_2/c) e^{i\omega t} dt \\
&+ \int_{-\infty}^{\infty} \tau_1 \rho_1 \rho_2 E(t + 2L/c) e^{i\omega t} dt + \int_{-\infty}^{\infty} \tau_1 \rho_1 \rho_2^2 E(t + 2L_2/c + 2L/c) e^{i\omega t} dt \quad (4.2) \\
&+ \int_{-\infty}^{\infty} \tau_1 \rho_1^2 \rho_2^2 E(t + 4L/c) e^{i\omega t} dt + \int_{-\infty}^{\infty} \tau_1 \rho_1^2 \rho_2^3 E(t + 2L_2/c + 4L/c) e^{i\omega t} dt + \dots
\end{aligned}$$

where a factor of $1/2\pi$ has been canceled from each term. The electric field impulse emerging from DBR 1 is more precisely given by

$$\delta(t - t_0) E(t) \quad (4.3)$$

where t_0 is the time the pulse first appears and δ is the Kronecker (delta) function

$$\int_{-\infty}^{\infty} \delta(t - t_0) dt \equiv 1 \quad (4.4)$$

The first term on the left hand side (L. H. S.) of Eq. (4.2) is thus

$$\text{L. H. S.} = \int_{-\infty}^{\infty} \delta(t - t_0) E_{R1}(t - L_1/c) e^{i\omega t} dt \quad (4.5)$$

Since $e^{i\omega t}$ is slowly varying in the vicinity of $t_0 = t - L_1/c$, it can be taken out of the integral as the constant $e^{i\omega t_0} = e^{i\omega(t - L_1/c)}$, resulting in

$$e^{i\omega(t - L_1/c)} E_{R1}(\omega) \int_{-\infty}^{\infty} \delta(t - t_0) dt = e^{i\omega(t - L_1/c)} E_{R1}(\omega) \quad (4.6)$$

This same integration scheme is performed on every term on the right hand side of Eq. (4.2). The resulting relation at $t = 0$ is

$$\begin{aligned} E_{R1}(\omega) e^{-i\omega L_1/c} = E(\omega) & \left[\tau_1 + \tau_1 \rho_2 e^{i\omega 2L_2/c} + \tau_1 \rho_1 \rho_2 e^{i\omega 2L/c} \right. \\ & \left. + \tau_1 \rho_1 \rho_2^2 e^{i\omega(2L_2/c + 2L/c)} + \tau_1 \rho_1^2 \rho_2^2 e^{i\omega(4L/c)} + \dots \right] \end{aligned} \quad (4.7)$$

The right hand side (R. H. S) of Eq. (4.7) may also be written as

$$\text{R. H. S.} = E(\omega) \tau_1 \left\{ \sum_{u=0}^{\infty} \left[\rho_1^u \rho_2^u e^{i\omega(2uL/c)} + \rho_1^u \rho_2^{(u+1)} e^{i\omega(2L_2/c + 2uL/c)} \right] \right\} \quad (4.8)$$

The magnitude $|E(\omega)|^2$ is the frequency intensity spectrum of an initial wave packet inside the cavity. The variables τ and ρ are in general complex, for example $\rho = \alpha + i\beta$. In phasor notation $\rho = |\rho|e^{i\theta}$, where $|\rho| = \sqrt{\alpha^2 + \beta^2}$ and $\theta = \tan^{-1}(\beta/\alpha)$.

The infinite series in Eq. (4.7) is made recurrent by dividing through by $\rho_1 \rho_2 e^{i\omega 2L/c}$, resulting in

$$\frac{E_{R1}(\omega) e^{-i\omega L_1/c}}{\rho_1 \rho_2 e^{i\omega 2L/c}} = \tau_1 E(\omega) \left[\frac{1}{\rho_1 \rho_2 e^{i\omega 2L/c}} + \frac{e^{i\omega 2L_2/c}}{\rho_1 e^{i\omega 2L/c}} \right] + E_{R1}(\omega) e^{i\omega(t - L_1/c)} \quad (4.9)$$

Rearranging Eq. (4.9)

$$E_{R1}(\omega) e^{-i\omega L_1/c} [1 - \rho_1 \rho_2 e^{i\omega 2L/c}] = \tau_1 E(\omega) [1 + \rho_2 e^{i\omega 2L_2/c}] \quad (4.10)$$

Replacing ρ_1 and ρ_2 with phasor notation in Eq. (4.10) results in

$$E_{R1}(\omega) e^{-i\omega L_1/c} [1 - |\rho_1| |\rho_2| e^{i(\omega 2L/c + \theta_1 + \theta_2)}] = \tau_1 E(\omega) [1 + |\rho_2| e^{i(\omega 2L_2/c + \theta_2)}] \quad (4.11)$$

The intensity of the emission spectrum is found by squaring (using the complex conjugates) both sides of Eq. (4.11) and solving for $|E_{R1}(\omega)|^2$. The left hand side of Eq. (4.11) reduces to

$$L. H. S. = |E_{R1}(\omega)|^2 [1 - 2 |\rho_1| |\rho_2| \cos(\omega 2L/c + \theta_1 + \theta_2) + R_1 R_2] \quad (4.12)$$

and the right hand side of Eq. (4.11) reduces to

$$R. H. S. = T_1 |E(\omega)|^2 [1 + 2 |\rho_2| \cos(\omega 2L_2/c + \theta_2) + R_2] \quad (4.13)$$

Solving for $|E_{R1}(\omega)|^2$ by equating Eqs (4.12) and (4.13) results in

$$|E_{R1}(\omega)|^2 = \frac{T_1 |E(\omega)|^2 [1 + 2 |\rho_2| \cos(\omega 2L_2/c + \theta_2) + R_2]}{[1 - 2 |\rho_1| |\rho_2| \cos(\omega 2L/c + \theta_1 + \theta_2) + R_1 R_2]} \quad (4.14)$$

The value of $|E_{R1}(\omega)|^2/|E(\omega)|^2$ represents a spontaneous emission enhancement factor.

Loss mechanisms such as scattering and absorption are neglected in the derivation of Eq. (4.14), except for those that are included in the matrix calculations. Consider a

phenomenological loss, where $e^{2\zeta}$ is the loss due to one round trip pass in the optical cavity. For example, ζ could equal $-\alpha L_{\text{eff}}$, where α is the material absorption coefficient and L_{eff} is the effective cavity length (see Section 2.2). With this simple loss mechanism, Eq. (4.14) becomes

$$|E_{R1}(\omega)|^2 = \frac{T_1 |E(\omega)|^2 [1 + 2e^{\zeta} |\rho_2| \cos(2\omega L_2/c + \theta_2) + e^{2\zeta} R_2]}{[e^{\zeta/2} - 2e^{\zeta} |\rho_1| |\rho_2| \cos(2\omega L/c + \theta_1 + \theta_2) + e^{3\zeta/2} R_1 R_2]} \quad (4.15)$$

Note that ζ (through α) is wavelength dependent.

Equation (4.14) is valid for infinite τ_c . For an actual quantum well microcavity structure, the value of τ_c is given by [Saleh and Teich 1991]

$$\tau_c = \frac{1}{\Delta\nu} \quad (4.16)$$

where $\Delta\nu$ is the spectral half width frequency of the quantum well emission without the presence of the microcavity (equal to the spectral half width of $|E(\omega)|^2$ for the present case). For GaInP quantum well structures emitting in the visible (620 to 690 nm), $\Delta\nu \sim 1 \times 10^{13} \text{ s}^{-1}$, and thus from Eq. (4.16) $\tau_c \sim 100 \text{ fs}$. The coherence length (l_c) is given by [Saleh and Teich 1991]

$$l_c = c_0 \tau_c / n_{\text{cav}} \quad (4.17)$$

For an AlGaInP semiconductor optical cavity with a refractive index of $n_{\text{cav}} \approx 3.3$, the coherence length for the above example is $l_c \sim 9 \mu\text{m}$. The microcavities of interest in this dissertation are typically $d_{\text{oc}} \approx 0.1$ to $1.5 \mu\text{m}$ thick (not including the phase penetration lengths). The corresponding number of round trips in the optical cavity for which

coherence is maintained is $l_c/2d \approx 9/0.2 = 45$ or less. Consider a 2λ cavity ($\lambda_0 = 650$ nm, thus $d_{oc} \sim 0.4$ μm thick) with $R_2 = 1.0$ and $R_1 = 0.5$. The field amplitude (neglecting absorption) after 10 round trips is about $\tau_1(\rho_1)^{10}(\rho_2)^{10}E \approx 0.016E$ and the extra terms beyond this point that are included in Eq. (4.7) are negligible. Thus, Eq. (4.14) should be a good estimate of the emission spectrum for this case. In contrast, if $R_2 = 1.0$ and $R_1 = 0.9$, the field amplitude after 10 round trips is about $0.53E$ and Eq. (4.14) will over estimate the intensity of the spectrum.

For short coherence lengths or for cavities with high DBR reflectances, a phenomenological correction to the predicted spectral intensity given by Eq. (4.14) is possible by subtracting from it the spectral contributions of the wave train pulses that exit DBR 1 after a certain number of round trip passes in the cavity. If $u-1$ round trips are allowed (round $u-1$ down to the nearest integer), then

$$\frac{|E_{R1}(\omega)|^2}{|E(\omega)|^2} = \frac{T_1 |\rho_1|^{2u} |\rho_2|^{2u} [1 + 2 |\rho_2| \cos(2\omega L_2/c + \theta_2) + R_2]}{[1 - 2 |\rho_1| |\rho_2| \cos(2\omega L/c + \theta_1 + \theta_2) + R_1 R_2]} \quad (4.18)$$

represents the relative spectral intensity that should be subtracted from the value obtained with Eq. (4.14). Since the loss of phase coherence is not abrupt but gradual, this procedure is strictly an approximation and represents a lower limit for the emitted spectral intensity.

The results of an example calculation using Eqs (4.14) and (4.18) are shown in Fig. 4.4. The details of the example visible VCSEL structure are given in Table 5.1 (Chapter 5). The dashed line, which is $|E(\omega)|^2$ in the calculation, represents the emission spectra of the quantum well active region without the DBRs (this is measured data (normalized to a peak value of 1) from an LED test structure). The solid line is the calculated spontaneous emission (i.e. the electroluminescence) expected from the top

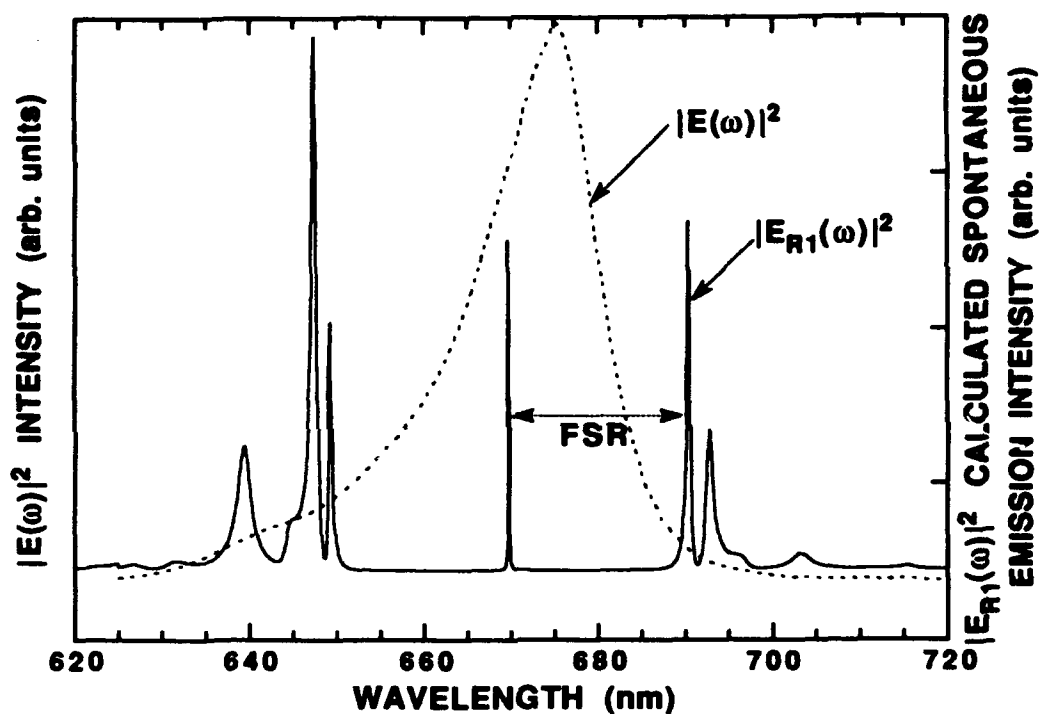


Fig. 4.4 Example calculation using the Classical Wave Interference Model. The modeled structure is the hybrid visible VCSEL given in Table 5.1. The dashed line is the intensity spectrum of the quantum well active region without the DBRs in place. The solid line is the expected spontaneous emission spectrum emitted from the top of the visible VCSEL. The excitation current is assumed to be below lasing threshold. (For comparison, see Figs 5.3, 5.7. and 5.8 in Chapter 5). For this calculation, absorption was neglected.

DBR, measured normal to the surface. The shape of the spontaneous emission spectrum is a sensitive function of $|E(\omega)|^2$, the absorption parameters used in the matrix calculations, and the exact multilayer structure (i.e. many of the sharp features in Fig. 4.4 appear distorted in the actual structure due to natural growth fluctuations). The model gives a good (semi-quantitative) estimate of the expected emission spectrum (compare Fig. 4.4 with Figs 5.3, 5.7, and 5.8 in Chapter 5). Deviations from measured data are expected since the parameters in the given model have finite accuracy. The phenomenological corrections (Eqs (4.15) and (4.18)), along with $|E(\omega)|^2$, essentially act as fitting parameters.

4.4 Infrared RCLEDs/Hybrid VCSELs

The IR RCLED was grown using molecular beam epitaxy (MBE) by S. A. Chalmers [1993]. The structure consisted of a 1λ optical cavity active region with three 3.2 nm thick $\text{Ga}_{0.7}\text{In}_{0.3}\text{As}$ strained quantum wells, surrounded by 10 nm thick GaAs barrier layers, in-turn surrounded by $\text{Al}_x\text{Ga}_{1-x}\text{As}$, $x = 0.2$ to 0.4 linearly graded layers forming a GRINSCH (graded index separate confinement heterostructure) active region. The Bragg design wavelength was $\lambda_0 \sim 980$ nm. The DBRs consisted of $\text{Al}_{0.1}\text{Ga}_{0.9}\text{As}$ (high index) and $\text{Al}_{0.9}\text{Ga}_{0.1}\text{As}$ (low index) layers, each ~ 19 nm thick, with a 3 linear segment $\text{Al}_x\text{Ga}_{1-x}\text{As}$ (graded $x = 0.1$ to 0.3, $x = 0.3$ to 0.7, $x = 0.7$ to 0.9) intermediate layer. The grading scheme approximates a sinusoid, and results in low series resistance [Chalmers *et al.* 1993]. The bottom (n+)DBR is Si-doped to $\sim 2 \times 10^{18} \text{ cm}^{-3}$ and has 32.5 periods. The top coupling (p+)DBR is Be-doped to $\sim 2 \times 10^{18} \text{ cm}^{-3}$ and has 10 periods, including an ~ 20 nm (n+)GaAs capping layer to reduce the contact resistance. The growth temperature is $\sim 585^\circ\text{C}$, except for the GaAs and $\text{Ga}_{0.7}\text{In}_{0.3}\text{As}$ active region layers which are grown at $\sim 540^\circ\text{C}$. The structure is based on similar IR VCSEL

structures [Lear *et al.* 1993], except that the number of top coupling DBR periods is reduced.

Although the 2 inch (n+)GaAs wafer is rotated during MBE growth, a variation in layer thickness exists from wafer center toward the edge. The reflectance spectra of the as-grown IR RCLED at six approximately equally spaced (~ 3 mm) points from wafer center toward an edge, are shown in Fig. 4.5. The Fabry-Perot resonance varies from ~ 985 nm (at wafer center), to ~ 905 nm (toward the wafer edge). Also, it is seen that the resonance is slightly off from the center of the DBR, toward longer wavelengths, indicating that the thickness of the optical cavity is slightly long.

Implanted, mesa isolated structures are fabricated as described in Section 4.2. The electroluminescence (EL) from the RCLEDs at three different points on the wafer are shown in Fig. 4.6. The linewidth of the EL peaks (~ 4.5 nm) is equal to the linewidths of the Fabry-Perot resonance "dips" in Fig. 4.5. The EL peak is most intense when the peak of the spectral gain from the quantum well is aligned to the cavity mode, and this occurs at ~ 984 nm. The L-I (power out versus current in) characteristics of the IR RCLED at ~ 984 nm are shown in Fig. 4.7(a), for devices with optical aperture diameters from 10 to 30 μm . The power was measured with a $1 \times 1 \text{ cm}^2$ calibrated Si photodetector placed ~ 1.5 cm above the given device.

The next step was the deposition of a dielectric $\lambda/4$ stack to increase the reflectance of the top DBR (see Subsection 2.4.4). Photoresist, $\sim 6 \mu\text{m}$ thick, was patterned around the apertures by using the inverse of the mesa mask, but off-setting the mask such that part of the top metal contact remained covered in photoresist. Five periods of Nb_2O_5 (high index)/ SiO_2 (low index) were deposited onto the RCLEDs using DC magnetron sputtering (deposition temperature $\leq 50^\circ\text{C}$, such that the photoresist was unaffected) with *in situ* reflectance monitoring. (The $(\text{LH})^5$ coating was also deposited onto a glass (SiO_2) slide during the coating run. From transmission measurements on this

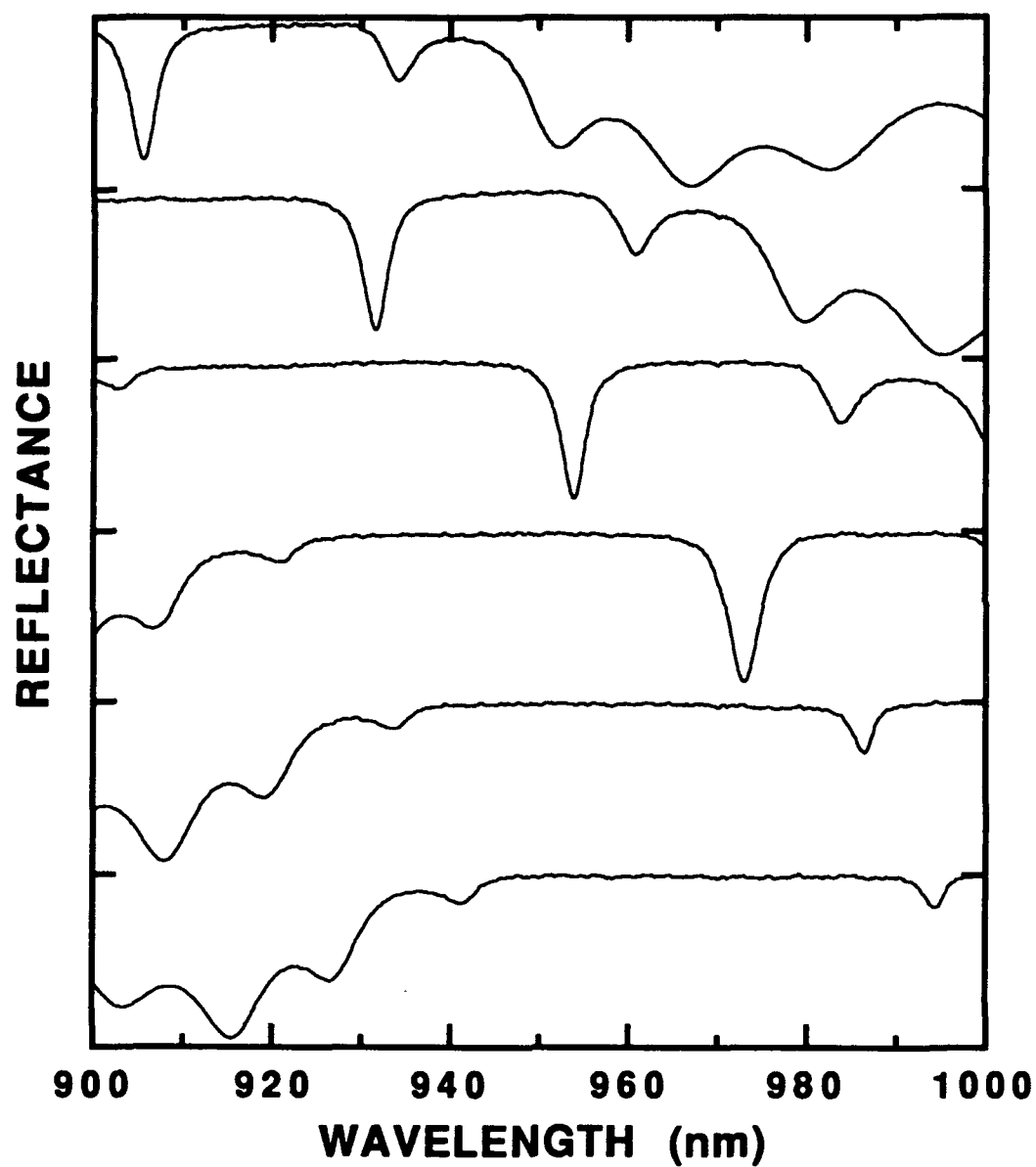


Fig. 4.5 Reflectance spectra at six approximately equally spaced (~ 3 mm) points on the as-grown IR RCLED structure (sample HC161).

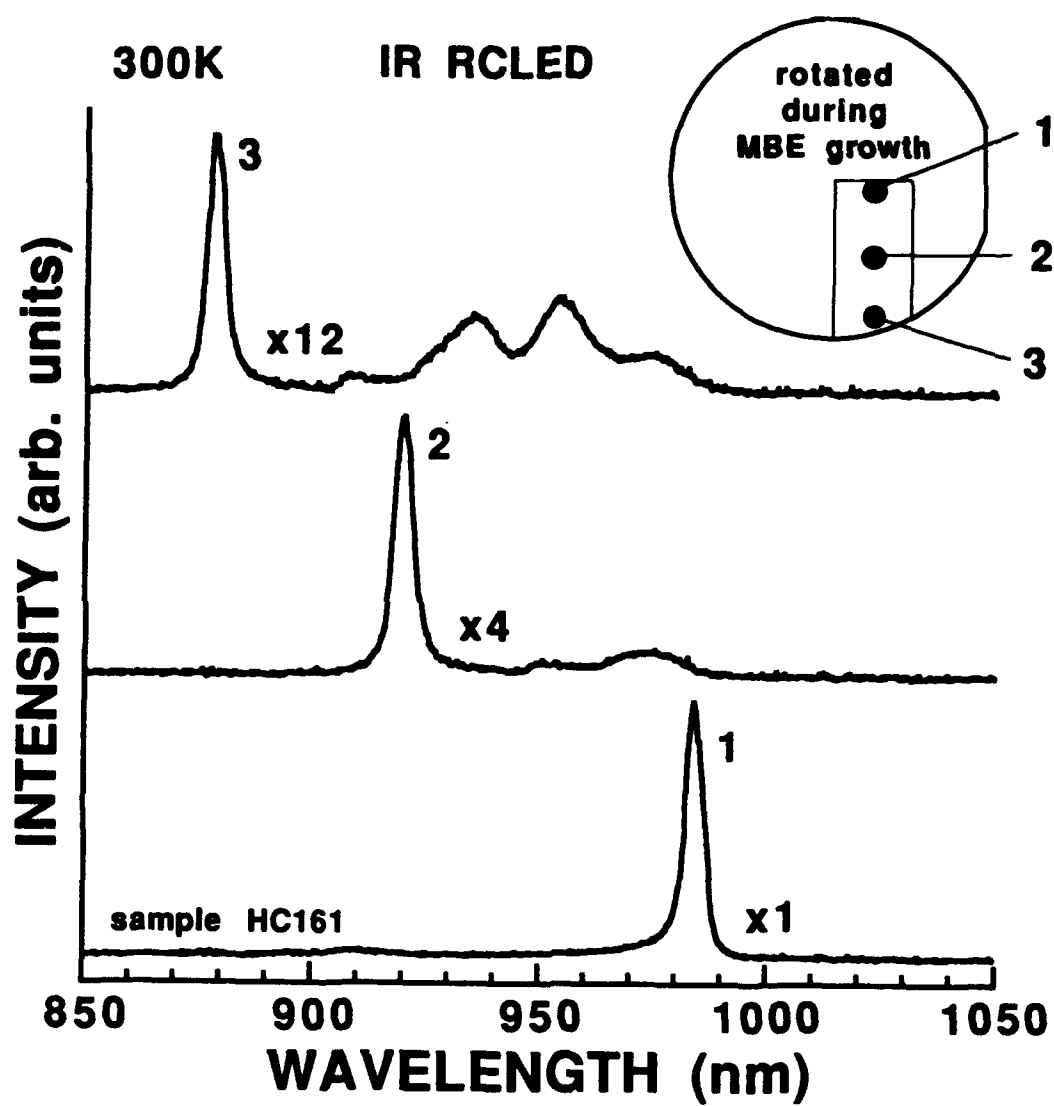


Fig. 4.6 Electroluminescence of the IR RCLED at three points on a fabricated sample. The inset shows the location of the measurements.

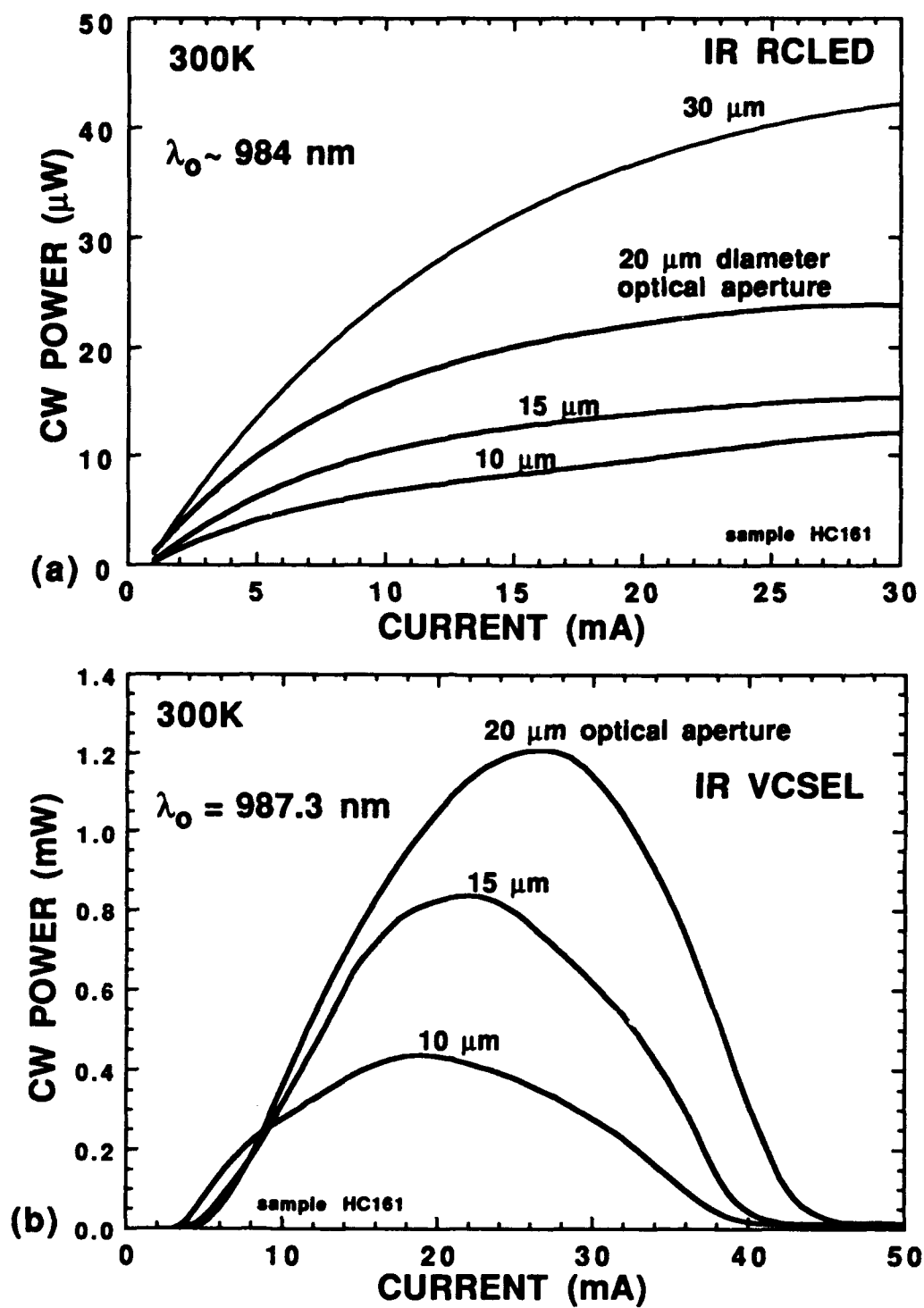


Fig. 4.7 L-I characteristics for (a) an IR RCLED and (b) the same IR RCLED (now an IR VCSEL) with a five period dielectric stack added to the top DBR.

monitor sample, the Bragg wavelength of the dielectric DBR was $\lambda_0 = 970.2$ nm). The optical coating was lifted-off, remaining over the optical apertures. For this configuration, the calculated reflectance at λ_0 , as seen from the optical cavity, was > 0.996 . The L-I characteristics of the now hybrid IR VCSEL are shown in Fig. 4.7(b). The continuous wave (CW) threshold current was 4 to 6 mA ($J_{th} \sim 2$ to 5 kA/cm²), and the voltage at threshold was $V_{th} \sim 1.8$ V. The device characteristics, including the maximum output power of ~ 1 mW, are comparable to those previously reported for similar IR VCSEL structures [Lei *et al.* 1991].

4.5 Hybrid AlGaInP/AlGaAs Visible RCLEDs

A hybrid AlGaInP/AlGaAs visible RCLED was grown with an epitaxial structure as given in Table 3.1 (Chapter 3), except that the bottom Si-doped ($\sim 2 \times 10^{18}$ cm⁻³) (n+)DBR had 50 AlGaAs periods, and the top coupling C-doped ($\sim 4 \times 10^{18}$ cm⁻³) (p+)DBR had 10.5 AlGaAs periods. The (n) and (p)Al_{0.5}In_{0.5}P $\lambda/4$ layers adjacent to the 2λ thick optical cavity, were doped with Si ($\sim 2 \times 10^{18}$ cm⁻³) and Mg ($\sim 7 \times 10^{17}$ cm⁻³), respectively. Three, 10 nm thick, \sim Ga_{0.44}In_{0.56}P strained quantum wells were used, with peak emission at $\lambda_0 \sim 675$ nm (as determined from photoluminescence measurements on calibration samples). As for the optically pumped experiments described in Section 3.4 and 3.5, the structures were grown without wafer rotation. In order to investigate the spontaneous emission properties of this structure, the devices were fabricated with top annulus contacts (Fig. 4.2 inset), but without an ion implant and without mesa etching. With this geometry, all of the measured EL is filtered through the top DBR. The only consequence is that the I-V (current-voltage) characteristics of the devices are nonideal, since the current is not confined but spreads from the top contact in all directions.

Figure 4.8 shows the normalized EL (solid lines) (constant 10 mA bias current) and reflectance (dashed lines) at several points across the wafer centerline. (The measurement is performed with the equipment shown in Fig. 2.7). Each measurement point corresponds to the listed Fabry-Perot resonances of 620 to 670 nm, in 10 nm steps. The linewidth of the resonance spectral features is ~ 1.9 nm (5.2 meV). The peak of the quantum well spectral gain aligns with the Fabry-Perot mode at about $\lambda_0 \sim 675$ nm. The spectral gain varies about 7.5 nm across the wafer centerline (see Fig. 5.5 in Chapter 5). Enhanced spontaneous emission on resonance is most noticeable at a resonance of 640 nm, where the spectral EL feature at 640 nm has a higher intensity than the spectral feature at ~ 675 nm. Figure 4.9 shows the calculated spontaneous emission (solid lines) at resonances of 620, 640, and 660 nm, corresponding to the measured data in Fig. 4.8. Despite the modeling difficulties discussed above, the calculated spectra are qualitatively similar to the measured data.

Example EL and reflectance measurements for another set of hybrid visible RCLEDs, fabricated on an unrotated wafer, are shown in Fig. 4.10. The device structure is similar to the structure above, except that the top coupling DBR has just 5 periods. The resonance feature at 640 nm in Fig. 4.10(c) is 1/10 as intense as the resonance feature at ~ 672 nm in Fig. 4.10(a). The linewidth of the resonance features is ~ 4.0 nm (10.8 meV).

The characteristics of a final example hybrid visible RCLED are shown in Fig. 4.11. This structure is identical to the hybrid visible VCSELs (i.e. sample XD0701C) described in detail in Section 5.4, except that the top coupling DBR has just 5 periods (including the 10 nm thick (p+)GaAs cap). The devices are fabricated with the mask set shown in Fig. 4.1, and include a "proton" implantation step and a mesa isolation etch. The EL measurements (taken at a constant bias of 10 mA for each device) across the unrotated wafer centerline are given in Fig. 4.11(a). For this particular wafer, the peak quantum well gain aligns with the Fabry-Perot mode at about $\lambda_0 \sim 660$ nm. The L-I

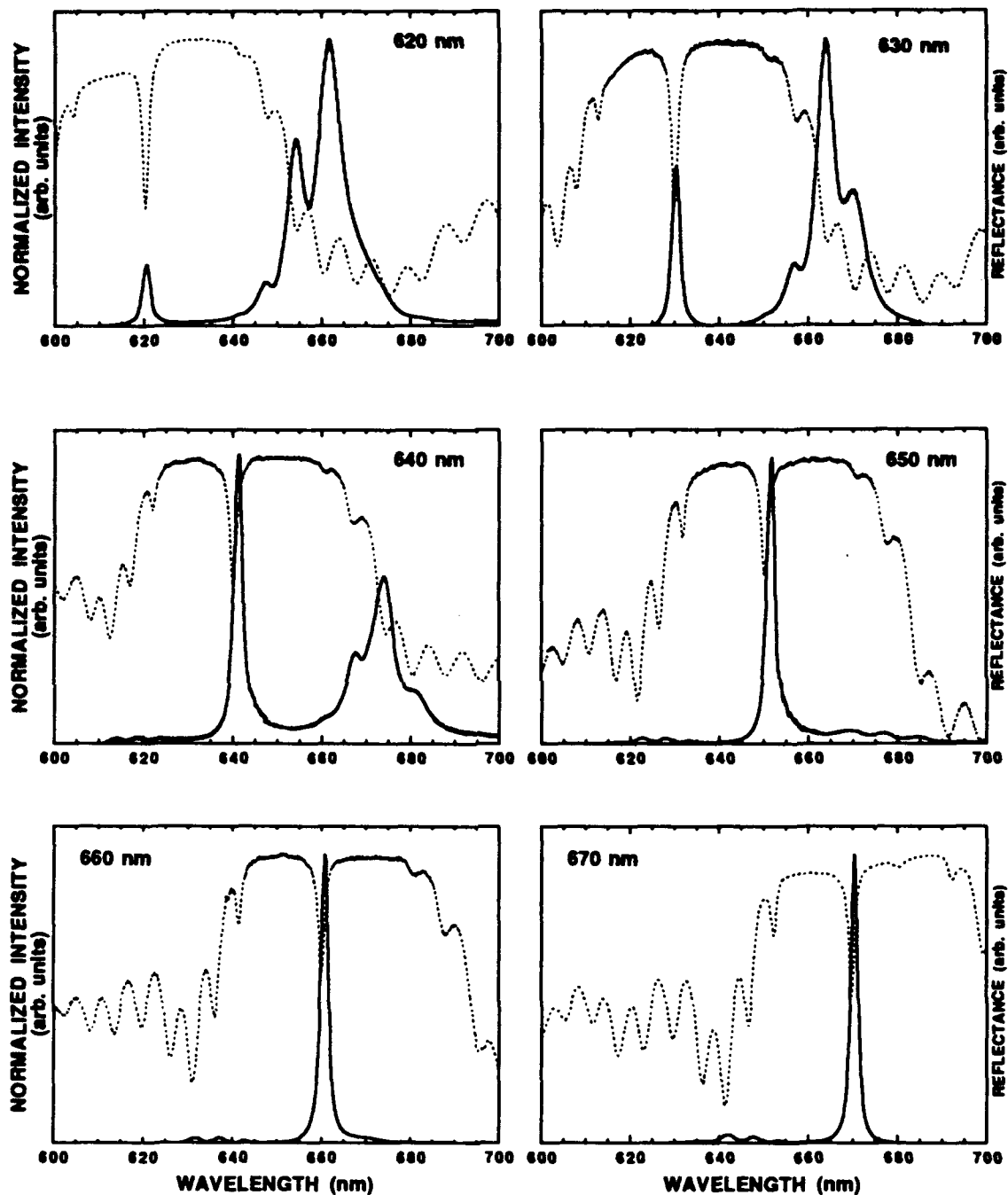


Fig. 4.8 Measured electroluminescence (solid lines) and reflectance (dashed lines) at several points across the centerline of a hybrid AlGaInP/AlGaAs visible RCLED unrotated wafer. The Fabry-Perot resonance wavelength is indicated in each plot. The peak spectral gain from the quantum well active region, without the DBRs, is $\lambda_0 \sim 675$ nm.

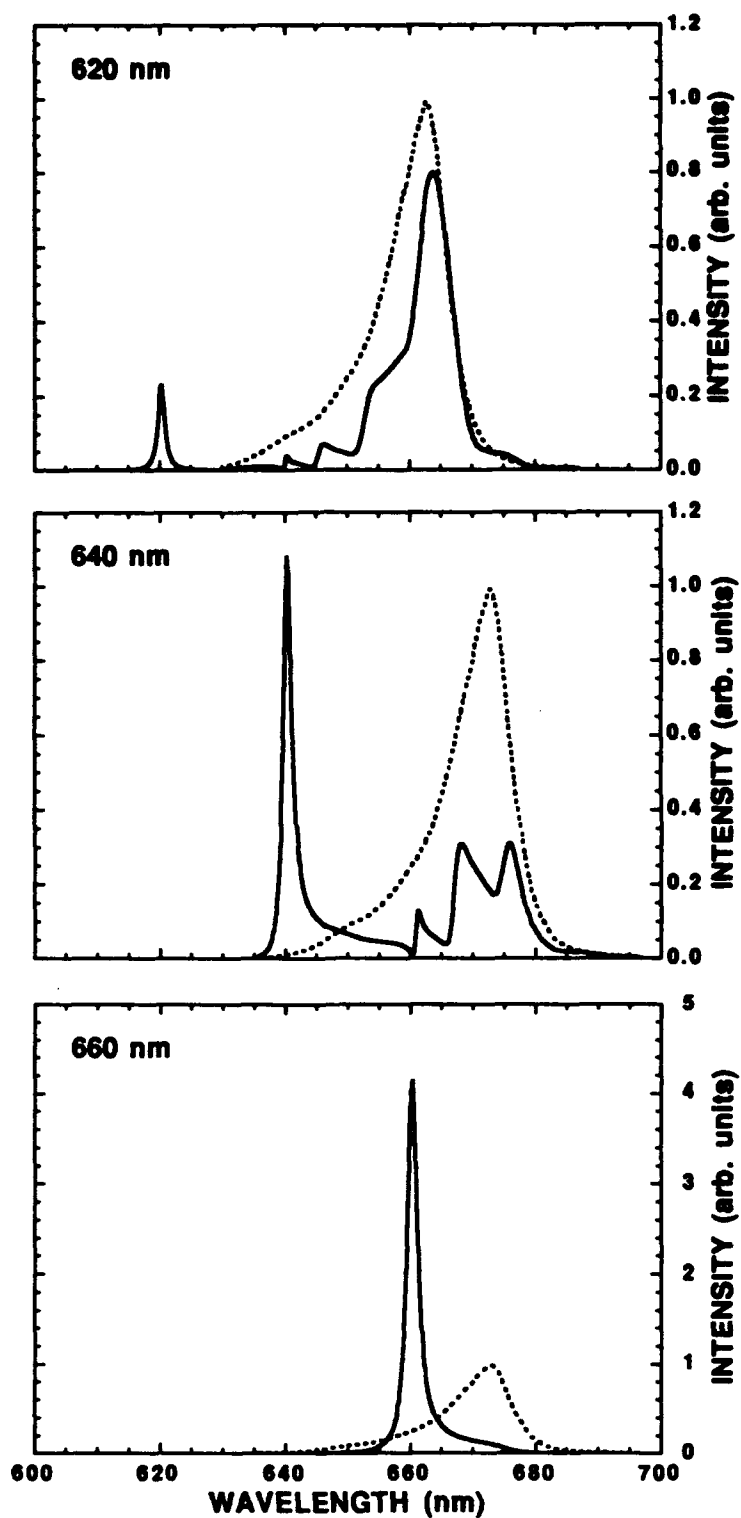


Fig. 4.9 Calculated spontaneous emission spectra (solid lines) for the hybrid visible VCSEL at Fabry-Perot resonances of 620, 640, and 660 nm. The dashed lines are the quantum well active region gain spectra without the DBRs (equal to $|E(\omega)|^2$).

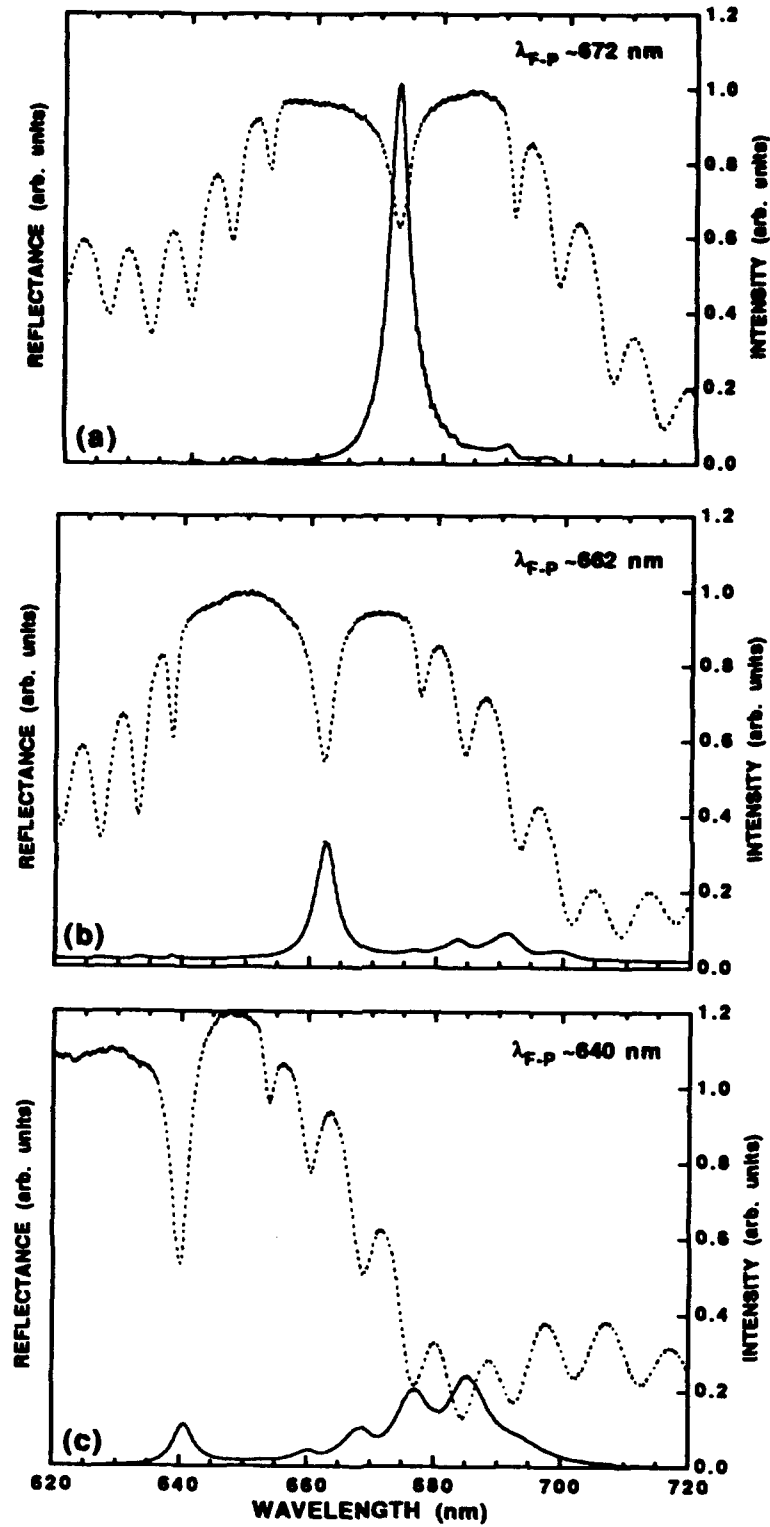


Fig. 4.10 Measured reflectance (dashed lines) and electroluminescence (EL) (solid lines) for an example hybrid visible RCLED with five top coupling DBR periods. The EL intensity is relative, and increases as the Fabry-Perot mode moves closer into alignment with the peak of the quantum well spectral gain (at ~ 675 nm).

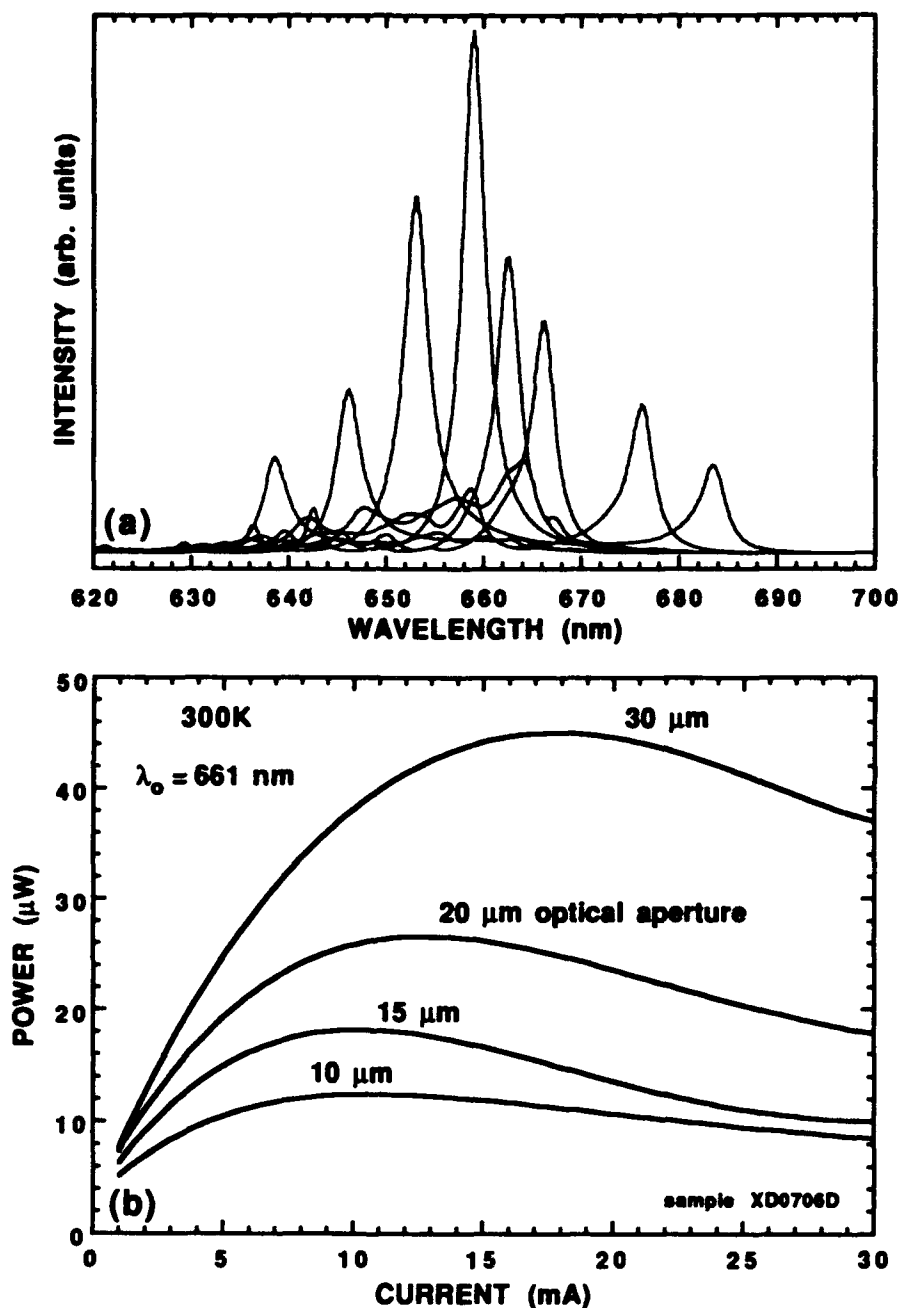


Fig. 4.11 (a) Measured electroluminescence at several points across an unrotated wafer, and (b) L-I characteristics at $\lambda_o = 661$ nm, for hybrid visible RCLEDs. The device structure is similar to that given in Table 5.1 (Chapter 5), except that the top coupling DBR has just five periods (including the (p+)GaAs cap), the DBR interfaces are graded (~biparabolic), and the GaInP quantum wells and the AlGaInP barrier layers are all 6 nm thick. The peak spectral gain from the quantum well active region occurs at $\lambda_o \sim 660$ nm.

characteristics are shown in Fig. 4.11(b). The maximum output powers are comparable to those in Fig. 4.7 for the IR RCLEDs. However, the curves roll over at lower currents due most likely to heating effects.

4.6 All-AlGaInP Visible RCLEDs

A schematic cross-section diagram of a fabricated all-AlGaInP visible RCLED was shown in Fig. 4.2, along with the real refractive index profile in and around the optical cavity active region. The lattice-matched epitaxial layers were grown by low pressure MOVPE on (311)A oriented (n+) GaAs substrates, with thicknesses corresponding to a Bragg wavelength (λ_0) of 670 nm. The bottom Si-doped ($\sim 10^{18} \text{ cm}^{-3}$) DBR consisted of 60.5 periods of alternating $\text{Al}_{0.5}\text{In}_{0.5}\text{P}$ (low index) and $(\text{Al}_{0.2}\text{Ga}_{0.8})_{0.5}\text{In}_{0.5}\text{P}$ (high index) $\lambda/4$ layers. Similarly, the Mg-doped ($\sim 10^{18} \text{ cm}^{-3}$) top output coupling DBR consisted of 5 periods of alternating $(\text{Al}_y\text{Ga}_{1-y})_{0.5}\text{In}_{0.5}\text{P}$ ($y = 1.0$) and $(\text{Al}_y\text{Ga}_{1-y})_{0.5}\text{In}_{0.5}\text{P}$ ($y = 0.2$) $\lambda/4$ layers, and included 10 nm thick linearly graded interface regions ($1.0 \geq y \geq 0.2$) to reduce series resistance. The last $\lambda/4$ layer was a composite and concluded with 10 nm-thick C-doped ($\sim 10^{19} \text{ cm}^{-3}$) $\text{Al}_{0.5}\text{Ga}_{0.5}\text{As}$ and GaAs layers to improve the top ohmic contact. The 2λ optical cavity active region included three 10 nm thick $\text{Ga}_{0.44}\text{In}_{0.56}\text{P}$ strained quantum wells with $y = 0.5$ barriers and $y = 0.7$ spacer layers doped with Si and Mg adjacent to the DBRs. Additionally, a 10 period ($y = 0.0/y = 0.7$) multiquantum well barrier (MQWB) electron reflector was included on the p-side of the optical cavity to increase electron confinement.

The measured reflectance spectrum at normal incidence for the as-grown all-AlGaInP RCLED is given in Fig. 4.12 (solid curve). A broad reflectance minima at 668.6 nm is the Fabry-Perot cavity resonance. The measured mirror center and the Fabry-Perot resonance are both within 1% of the target design (670 nm). For comparison, the reflectance spectrum was calculated (with $\lambda_0 = 668 \text{ nm}$) by using standard matrix

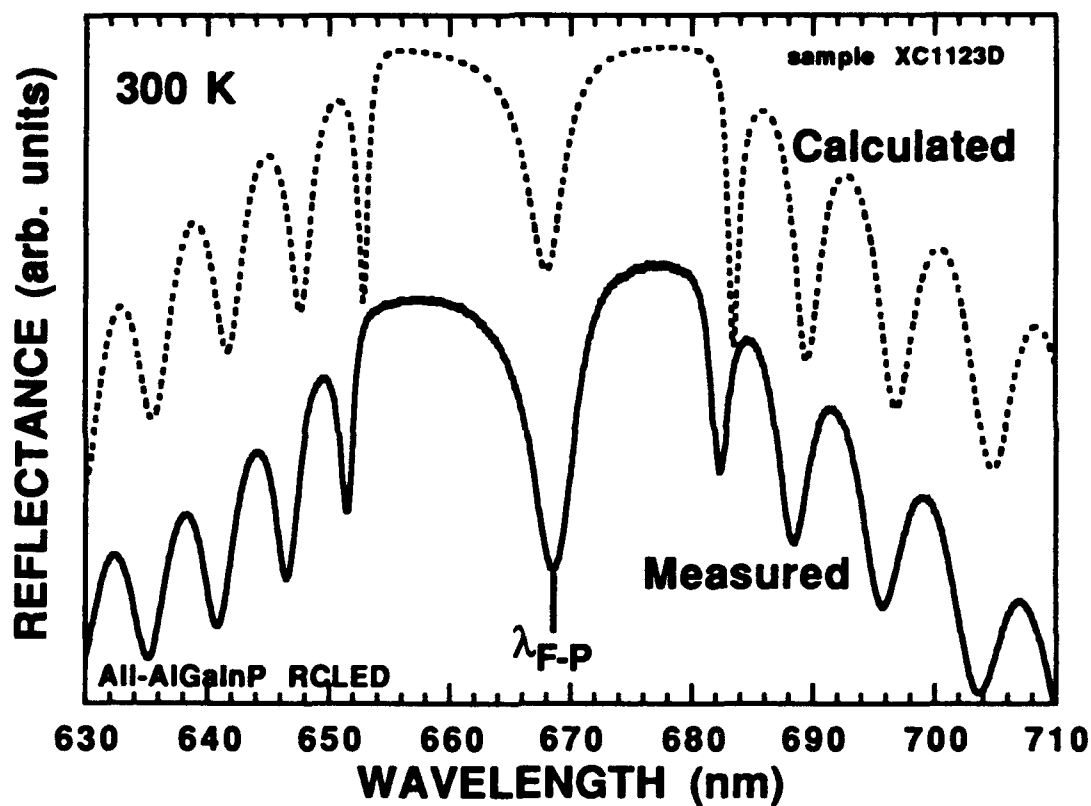


Fig. 4.12 Measured (solid line) and calculated (dashed line) reflectance spectra, normal to the surface, for the as-grown all-AlGaInP visible RCLED at room temperature. The measured mirror center and Fabry-Perot resonance (at 668.6 nm) are both within 1% of the target design (670 nm). The calculated spectrum (with $\lambda_0 = 668$ nm) is offset along the y-axis for clarity.

methods [MacLeod 1989] and refractive index dispersion curves [Tanaka *et al.* 1986], and is also shown in Fig. 4.12 (dashed curve). Absorption is neglected in the calculation since the $y = 0.2$ layers in the DBRs should not begin absorbing until $\lambda \leq 615$ nm (~ 2.02 eV).

The EL at room temperature for a typical all-AlGaInP visible RCLED biased with 5 mA CW current is given in Fig. 4.13(a). The corresponding calculated spontaneous emission spectrum is shown in Fig. 4.13(b). The peak output wavelength was 669.7 nm with a linewidth of 4.8 nm (13.3 meV). Since the peak wavelength shortens with increasing angle from the normal, the sampled emission angle was adjusted to find the longest peak wavelength. This EL was obtained by using a lens that collected the emission within a 24° solid angle and thus some linewidth spectral broadening, calculated to be 0.4 nm, was expected. The EL in Fig. 4.13(a) was from a device immediately adjacent to the nonmetallized area used for the reflectance measurement in Fig. 4.12. The peak emission and the cavity resonance wavelengths differ by 1.1 nm due to cavity heating effects [Hasnain *et al.* 1991]. The inset in Fig. 4.13(a) shows the EL at three different drive currents. Though the peak wavelength shifts longer as the current increases, the linewidth remains essentially constant up to 10 mA CW since the emission spectrum is determined primarily by the cavity parameters.

When designing RCLEDs it is useful to estimate the emission linewidth ($\Delta\lambda_{1/2}$) for a given device structure, such as when the reflectance of the coupling mirror is a variable parameter. The linewidth could be estimated from the width of the Fabry-Perot resonance dip in Fig. 4.12. Here we have estimated the linewidth with an alternate approach. The cavity finesse (\mathcal{F}) is determined, after calculating the DBR reflectances, by using Eq. (2.17). The phase penetration length into the DBRs is found analytically [Babic and Corzine 1992] and added to the optical cavity length to determine a total effective cavity length (L_{eff}). For a high Q cavity, the linewidth is then given by

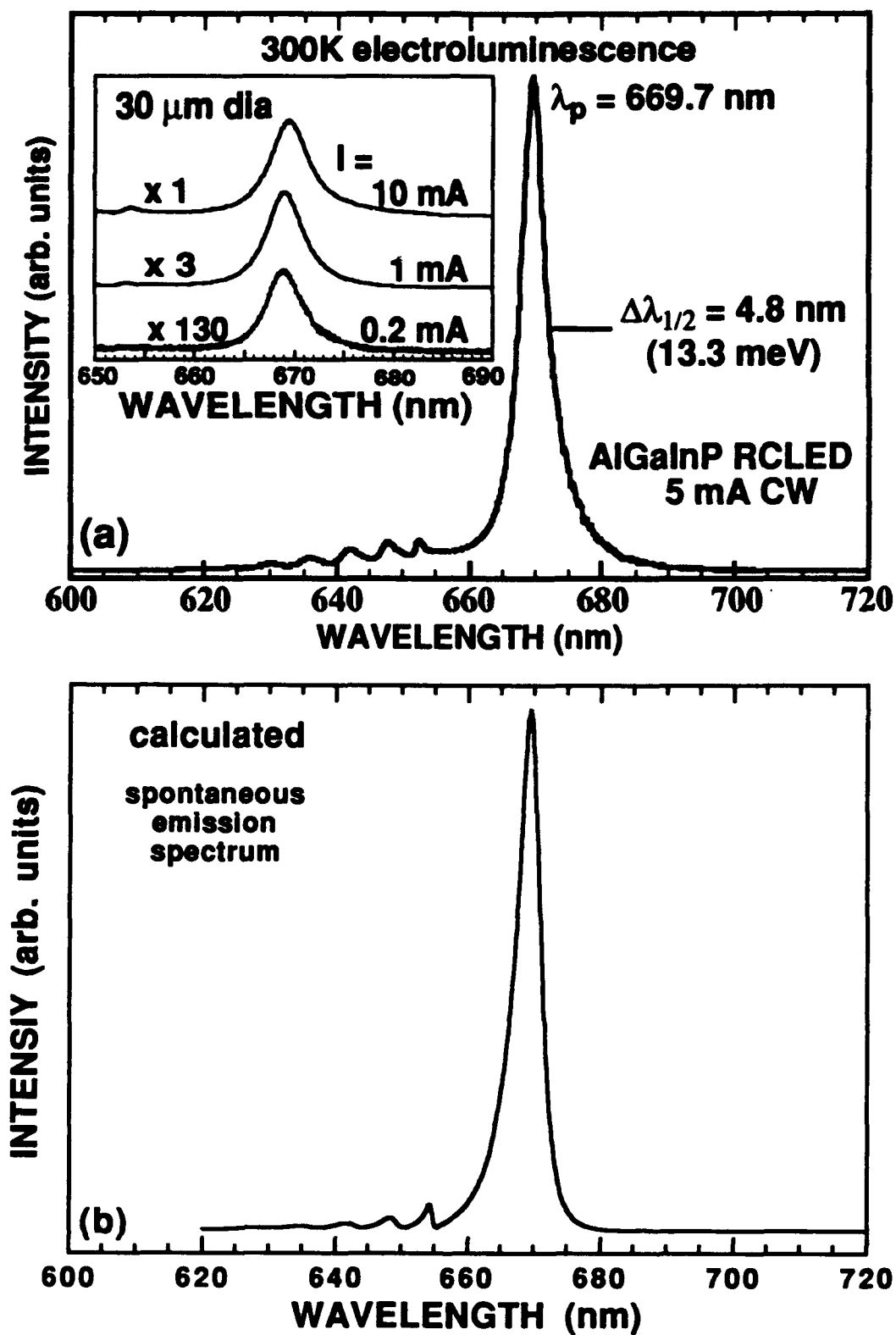


Fig. 4.13 Electroluminescence (EL) spectra of the all-AlGaInP visible RCLED, (a) measured, and (b) calculated. The inset shows EL spectra at three different current levels.

Eq. (2.18) where $\Delta\lambda_{1/2}/\lambda_0 = 1/Q = \lambda/(2L_{\text{eff}}n_{\text{cav}}F)$. Figure 4.14 shows a plot of the calculated linewidth versus the number of top coupling DBR periods for the all-AlGaInP RCLED structure with three different optical cavity thicknesses. For the current structure with 5 top DBR periods and a 2λ optical cavity thickness, the calculated linewidth is 4.3 nm. This agrees with the measured value in Fig 4.14 (4.8 nm) corrected for the effects of spectral broadening due to the measurement optics.

4.7 Conclusions

This Chapter has explored the design and spectral characteristics of a new type of photonic device, the resonant cavity light emitting diode (RCLED). A classical model was introduced and shown to provide a good, semi-quantitative estimate of the expected emission spectrum from an arbitrary RCLED structure. Previous studies on the quantum electrodynamic effects in semiconductor microcavities have concentrated on the placement of the quantum well(s) in the optical cavity active region and the resulting enhanced or inhibited spontaneous emission. The studies presented here, however, treated primarily the effects of misalignment between the quantum well spectral gain and the microcavity resonance mode. This was accomplished by not rotating the wafers during MOVPE growth, which resulted in an ~ 50 nm linear shift in the mode wavelength across the centerline of the wafer (due to an $\sim 10\%$ linear variation in the epitaxial layer thicknesses), while the quantum well peak spectral gain varied by ~ 7.5 nm or less (e.g. for the hybrid AlGaInP/AlGaAs devices). The spectral characteristics at several points across the example wafers showed clearly the enhanced spectral intensity for on-resonance wavelengths. The narrowed linewidth of the emission spectra was correlated with the design of the given RCLED, and related to the number of top coupling DBR pairs.

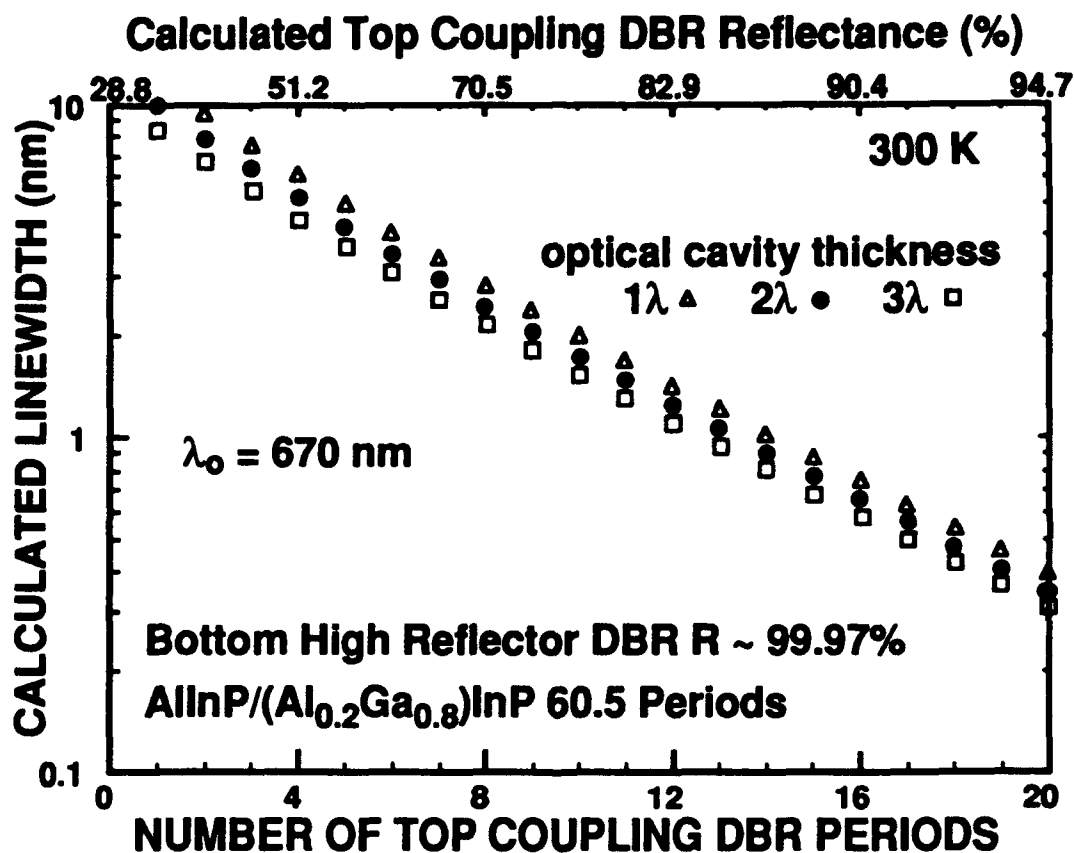


Fig. 4.14 Calculated linewidth versus number of top coupling Al_{0.5}In_{0.5}P/(Al_{0.2}Ga_{0.8})_{0.5}In_{0.5}P DBR periods for an all-AlGaInP visible RCLED with three different optical cavity thicknesses. The bottom DBR is a 60.5 period high reflector, and the Bragg wavelength is 670 nm.

A straight forward extension of the basic RCLED for emission in the visible (~670 nm) was accomplished by employing AlGaInP optical cavity active regions, and both AlGaAs and AlGaInP DBRs. With AlGaInP bulk or short period superlattice active regions, and AlGaInP DBRs, the RCLED emission wavelength is potentially as short as ~560 nm. Because of difficulty in the p-doping of $(\text{Al}_y\text{Ga}_{1-y})_{0.5}\text{In}_{0.5}\text{P}$ with $y \geq 0.7$ and the associated high series resistance (see Subsection 2.6.1), shorter wavelength (≤ 630 nm) RCLEDs most likely will have to forgo a top coupling all-semiconductor DBR, and use instead a thick (3λ or more) nonabsorbing phase matching/current spreading layer, capped with $\gamma\text{-GaAs}$ for contacting to an annulus or similar aperture metal contact (The GaAs could be selectively etched after depositing the metal, to prevent absorption of the emitted light). The emission linewidth could then be controlled by depositing additional dielectric DBRs if desired. The reflectivity of the bottom DBR need not be ~100% (unless a visible VCSEL was the goal), rather, ~90% would be adequate. This would greatly cut-down the number of required bottom DBR periods while still keeping most of the generated emission away from the absorbing GaAs substrate. For example, at $\lambda_0 = 590$ nm, 96 periods (~8.2 μm thick) of an $(\text{Al}_{0.5}\text{Ga}_{0.5})_{0.5}\text{In}_{0.5}\text{P}/\text{Al}_{0.5}\text{In}_{0.5}\text{P}$ DBR would be required to (theoretically) reach $R \geq 0.9999$, while only 30 periods are needed to reach $R \geq 0.93$. Further investigations of visible RCLEDs should concentrate on the measurement/optimization of quantum efficiency, thermal stability, modulation bandwidth, and on practical applications such as sources for short-distance plastic optical fiber communication systems.

The visible RCLED has also proven very useful in the development of the visible vertical cavity surface emitting laser (VCSEL). The as-grown structures served as optical calibrations for subsequent full top stack VCSEL growths, providing critical information on the optical cavity thickness, DBR mirror center, and peak spectral gain of the quantum well active region.

References for Chapter 4

- Baba, T., T. Hamano, F. Koyama, and K. Iga, "Spontaneous Emission Factor of a Microcavity DBR Surface-Emitting Laser", *IEEE Journal of Quantum Electronics*, 27(6), p. 1347-1358 (June 1991).
- Babic, D. I., and S. W. Corzine, "Analytic Expressions for the Reflection Delay, Penetration Depth, and Absorptance of Quarter-Wave Dielectric Mirrors," *IEEE Journal of Quantum Electronics*, 28, p. 514-524 (1992).
- Björk, G., S. Machida, Y. Yamamoto, and K. Igeta, "Modification of Spontaneous Emission Rate in Planar Dielectric Microcavity Structures", *Physical Review A*, 44(1), p. 669-681 (1 July 1991).
- Chalmers, S. A., Postdoctoral Member of Technical Staff, Sandia National Laboratories, Albuquerque, New Mexico, private communication (1993).
- Chalmers, S. A., K. L. Lear, and K. P. Killeen, "Low Resistance Wavelength-Reproducible p-Type (Al,Ga)As Distributed Bragg Reflectors Grown by Molecular Beam Epitaxy", *Applied Physics Letters*, 62(14), p. 1585-1587 (5 April 1993).
- De Martini, F., G. Innocenti, G. R. Jacobovitz, and P. Mataloni, "Anomalous Spontaneous Emission Time in a Microscopic Optical Cavity", *Physical Review Letters*, 59(26), p. 2955-2958 (28 December 1987).
- Deppe, D. G., J. C. Campbell, R. Kuchibhotla, T. J. Rogers, and B. G. Streetman, "Optically-Coupled Mirror-Quantum Well InGaAs-GaAs Light Emitting Diode", *Electronic Letters*, 26(20), p. 1665-1666 (27 September 1990).
- Dutt, B. V., J. H. Racette, S. J. Anderson, F. W. Scholl, and J. R. Shealy, "AlGaInP/GaAs Red Edge-Emitting Diodes for Polymer Optical Fiber Applications," *Applied Physics Letters*, 53(21), p. 2091-2092 (1988).
- Feng, X.-P., "Theory of a Short Optical Cavity With Dielectric Multilayer Film Mirrors," *Optics Communications*, 83(1, 2), p. 162-176 (15 May 1991).
- Haroche, S., and D. Kleppner, "Cavity Quantum Electrodynamics", *Physics Today*, p. 24-30 (January 1989).
- Huang, Z., C. Lei, D. G. Deppe, C. C. Lin, C. J. Pinzone, and R. D. Dupuis, "Spectral and Intensity Dependence on Dipole Localization in Fabry-Perot Cavities", *Applied Physics Letters*, 61(25), p. 2961-2963 (21 December 1992).
- Hunt, N. E. J., E. F. Schubert, R. A. Logan, and G. J. Zydzik, "Enhanced Spectral Power Density and Reduced Linewidth at 1.3 μm in an InGaAsP Quantum Well Resonant-Cavity Light-Emitting Diode," *Applied Physics Letters*, 61(19), p. 2287-2289 (9 November 1992a).

Hunt, N. E. J., E. F. Schubert, R. A. Logan, and G. J. Zydzik, "Extremely Narrow Spectral Widths from Resonant Cavity Light-Emitting Diodes (RCLEDs) Suitable for Wavelength-Division Multiplexing at 1.3 μm and 1.55 μm ," Digest of the IEEE International Electron Devices Meeting, San Francisco, CA, p. 651-654 (13-16 December 1992b).

Kato, T., H. Susawa, M. Hirotsu, T. Saka, Y. Ohashi, E. Shichi, and S. Shibata, "GaAs/GaAlAs Surface Emitting IR LED With Bragg Reflector Grown by MOCVD", Journal of Crystal Growth, 107, p. 832-835 (1991).

Keller, U., G. R. Jacobovitz-Veselka, J. E. Cunningham, W. Y. Jan, B. Tell, K. F. Brown-Goebeler, and G. Livescu, "Microcavity Enhanced Vertical Cavity Light-Emitting Diodes", Applied Physics Letters, 62(24), p. 3085-3087 (14 June 1993).

Lear, K. L., and S. A. Chalmers, "High Single-Mode Power Conversion Efficiency Vertical-Cavity Top-Surface-Emitting Lasers", IEEE Photonics Technology Letters, (to be published September 1993)

Lei, C., T. J. Rogers, D. G. Deppe, and B. G. Streetman, "ZnSe/CaF₂ Quarter-Wave Bragg Reflector for the Vertical Cavity Surface-Emitting Laser", Journal of Applied Physics, 69(11), p. 7430-7434 (1 June 1991).

Lei, C., and D. G. Deppe, "Optical Gain Enhancement in Fabry-Perot Microcavity Lasers", Journal of Applied Physics, 71(6), p. 2530-2535 (15 March 1992).

Lei, C., Z. Huang, D. G. Deppe, C. J. Pinzone, and R. D. Dupuis, "Spectral Interference Effects in the Light Emission from Fabry-Perot Cavities", Journal of Applied Physics, 73(6), p. 2700-2704 (15 March 1993a).

Lei, C., D. G. Deppe, Z. Huang, and C. C. Lin, "Emission Characteristics from Dipoles with Fixed Positions in Fabry-Perot Cavities", IEEE Journal of Quantum Electronics, 29(5), p. 1383-1386 (May 1993b).

Lei, C., "Spontaneous Emission in Semiconductor Microcavities and Its Role in Vertical Cavity Surface Emitting Lasers", Doctoral Dissertation, University of Texas at Austin (May 1993c).

Lott, J. A., R. P. Schneider, Jr., G. A. Vawter, J. C. Zolper, and K. J. Malloy, "Visible (660 nm) Resonant Cavity Light-Emitting Diodes", Electronics Letters, 29(4), p. 328-329 (18 February 1993a).

Lott, J. A., R. P. Schneider, Jr., J. C. Zolper, and K. J. Malloy, "AlGaInP Visible Resonant Cavity Light-Emitting Diodes," Photonics Technology Letters, 5(6), p. 631-633 (June 1993b).

MacLeod, H. A., *Thin-Film Optical Coatings*, 2nd ed. (New York:McGraw-Hill, 1989).

Rogers, T. J., D. G. Deppe, and B. G. Streetman, "Effect of an AlAs/GaAs Mirror on the Spontaneous Emission of an InGaAs-GaAs Quantum Well", Applied Physics Letters, 57(18), p. 1858-1860 (29 October 1990).

Saleh, B. E. A., and M. C. Teich, *Fundamentals of Photonics*, (Wiley:New York, 1991).

Schubert, E. F., Y.-H. Wang, A. Y. Cho, L.-W. Tu, and G. J. Zydzik, "Resonant Cavity Light-Emitting Diode", *Applied Physics Letters*, 60(8), p. 921-923 (24 February 1992).

Sugawara, H., K. Itaya, H. Nozaki, and G. Hatakoshi, "High-Brightness InGaAlP Green Light-Emitting Diodes", *Applied Physics Letters*, 61(15), p. 1775-1777 (12 October 1992).

Takagi, T., F. Koyama and K. Iga, "Design and Photoluminescence Study on a Multiquantum Barrier", *IEEE Journal of Quantum Electronics*, 27, p. 1511-1519 (1991).

Tanaka, H., Y. Kawamura, and H. Asahi, "Refractive Indices of $\text{In}_{0.49}\text{Ga}_{0.51-x}\text{Al}_x\text{P}$ Lattice Matched to GaAs", *Journal of Applied Physics*, 59, p. 985-986 (1986).

Yamamoto, Y., and R. Slusher, "Optical Processes in Microcavities", *Physics Today*, p. 66-73 (June 1993).

Yokoyama, H., K. Nishi, T. Anan, H. Yamada, S. D. Brorson, and E. P. Ippen, "Enhanced Spontaneous Emission from GaAs Quantum Wells in Monolithic Microcavities", *Applied Physics Letters*, 57(26), p. 2814-2816 (24 December 1990).

Zolper, J. C., R. P. Schneider, Jr., and J. A. Lott, "Formation of High Resistivity Regions in p-Type $\text{Al}_{0.5}\text{In}_{0.5}\text{P}$ by Ion Implantation", *Applied Physics Letters* (to be published December 1993).

Chapter 5 Electrically Injected Visible Vertical Cavity Surface Emitting Lasers

5.1 Introduction

Visible (620 to 690 nm) AlGaInP vertical cavity surface emitting lasers (VCSELs) are attractive for a number of applications including low cost plastic fiber communications, optical data storage and retrieval, optical interconnections and computing, projection displays, distance measurements, holographic memories, medical diagnostics, replacement of HeNe lasers for barcode scanning, and high resolution printing, to name just a few. Infrared (IR) VCSEL diodes have been studied for over a decade [Soda *et al.* 1979, Iga *et al.* 1988, Koyama *et al.* 1989, Lee *et al.* 1989, Geels *et al.* 1991, Hasnain *et al.* 1991, Baba *et al.* 1993, Lear *et al.* 1993]. Arrays of continuous wave (CW) IR VCSEL diodes emitting at 780 to 1000 nm reached the market place for the first time last year (1992)[†]. In contrast, visible AlGaInP VCSEL diodes were demonstrated for the first time this year (1993). The commercialization of visible VCSELs requires the development of practical (low cost and robust), high efficiency, electrically injected devices.

The first electrically injected "shorter wavelength" VCSELs emitted at 770 nm (deep red) [Lee *et al.* 1991] and at 699 nm [Tell *et al.* 1992]. These devices were fabricated entirely from Al_xGa_{1-x}As epitaxial layers (including a GaAs/AlAs short period superlattice active region), and hence were limited to emission wavelengths greater than ~695 nm. These devices operated with pulsed current excitation at room temperature, and

[†]see page 223, *Laser Focus World* (May 1992)

the latter device was shown to operate with CW current excitation below -25°C [Tell *et al.* 1993]. Visible (~ 620 to 690 nm) light emission is more commonly achieved with AlGaInP quantum well active regions, as described in Appendix A. In fact, the study of AlGaInP visible edge emitting lasers is currently one of the most active areas in semiconductor device research [Brueck 1991, Bour 1992a, Hecht 1993].

The first electrically injected visible VCSELs composed of an AlGaInP quantum well active region were demonstrated on 25 February 1993 and first published in March 1993 [Lott and Schneider 1993a]. Several key aspects of growth and device design were published shortly thereafter [Schneider and Lott 1993a]. The devices were fabricated into an unoptimized, etched post geometry with a top annular contact (called Quick VCSELs). These prototype devices used AlAs/Al_{0.5}Ga_{0.5}As DBRs and operated with pulsed current excitation at room temperature over the range 639.1 to 660.9 nm. Due to cavity losses and unoptimized gain layers, gain contributions from the second ($n=2$) quantized quantum well state were required to achieve lasing [Lott *et al.* 1993b]. The threshold current density was $J_{\text{th}} \sim 4.2$ kA/cm² for devices with a 20 μm diameter optical aperture in a 30 μm diameter mesa, and the maximum pulsed output power was 3.38 mW at a wavelength of ~ 650 nm. (For Quick visible VCSELs made from the same material as above, but with 10 μm apertures in 20 μm mesas, with pulsed current excitation of 100 ns at 10 μs , at room temperature, the lasing range was 635.7 to 666.9 nm).

Subsequently, several design improvements were implemented to reduce the cavity losses and increase the available gain. The second round of Quick visible VCSELs, with 10 μm diameter optical apertures in a 20 μm diameter mesa, operated at room temperature with pulsed excitation over the very broad range of 629.6 to 691.4 nm [Lott *et al.* 1993d]. The devices with lasing wavelength above ~ 665 nm operated primarily with gain contributions from the first ($n=1$) quantized quantum well state. In contrast, the devices with lasing wavelength below ~ 665 nm operated with gain

contributions from both the $n=1$ and the $n=2$ quantized quantum well state. Room temperature CW operation was achieved for devices with a $5\text{ }\mu\text{m}$ diameter optical aperture in a $15\text{ }\mu\text{m}$ diameter mesa with emission at $\sim 670\text{ nm}$ and with $J_{\text{th}} \sim 2.8\text{ kA/cm}^2$ [Lott *et al.* 1993d]. The same material, when fabricated into conventional ion implanted top surface emitting devices, operated CW at room temperature with $J_{\text{th}} \sim 2\text{ kA/cm}^2$ at $V_{\text{th}} \sim 3\text{ V}$, with a maximum output power of $\sim 0.5\text{ mW}$.

This Chapter presents the fabrication, characterization, and analysis of electrically injected visible VCSELs with an AlGaInP optical cavity active region and AlGaAs DBRs. The results are significant in that: 1) they include the first demonstration of electrically injected visible VCSELs with an AlGaInP optical cavity active region; 2) they include the first observation and analysis of lasing with contributions from the $n=2$ quantum well transition in electrically injected VCSELs at any wavelength; and 3) they include the first demonstration of room temperature CW operation of electrically injected visible VCSELs.

This Chapter is organized as follows. Section 5.2 overviews the fabrication sequences for the visible VCSELs. Next, Section 5.3 presents the results from the initial set of prototype devices, where lasing was achieved for the first time in visible VCSEL diodes. It is shown that lasing was achieved with significant gain contributions from the $n=2$ quantum well state. Section 5.4 presents the results from the much improved second round of devices which incorporated several design changes to improve device performance. (These changes were based on the lessons learned from the first round of devices). For the second round devices, lasing is achieved primarily with gain contributions from the $n=1$ quantum well state with much reduced threshold currents. In Section 5.5, the characteristics and analysis of the first room temperature CW visible VCSEL diodes are presented. Finally, Section 5.6 contains the Chapter conclusions.

5.2 Device Fabrication

The visible VCSELs were fabricated using one of two different fabrication sequences, both of which result in top surface emitting devices. The first fabrication sequence is the Quick VCSEL process. This process was developed to quickly fabricate devices to characterize VCSEL epitaxial material. This process takes ~8 to 12 continuous hours to complete, and results in etched post test devices with annular top contacts. The second processing sequence is more elaborate and involves a high energy ion implantation step. This process takes ~24 to 40 continuous hours to complete, and is based on previous research on similar top emitting IR VCSELs [Lee *et al.* 1990, Orenstein *et al.* 1990].

A cut-away schematic diagram of a completed Quick visible VCSEL test device is shown in Fig. 5.1. The device is fabricated as follows. First, top p-type annular contacts are placed onto the surface by using a standard photoresist lift-off technique. The metal is ~30 nm of Ti, followed by ~270 nm of Au (thus a Schottky tunnel contact is formed). The outer diameters of the annular contacts vary from 10 up to 60 μm , while the inner diameters, which define the optical apertures, vary from 2 to 50 μm . The next two steps are performed in either order. The annular contacts are masked with photoresist and circular mesas are etched down to the top of the AlGaInP optical cavity active region using either BCl_3 or a combination of BCl_3 and Cl_2 in a reactive ion etching system. The plasma selectively etches the AlGaAs DBRs, stopping on the AlGaInP. Next, n-type metal (Ge ~20 nm/ Au ~50 nm/ Ni ~10 nm/ Au ~300 nm) is deposited onto the back surface by electron beam evaporation. Finally, the metal contacts are annealed at ~400 °C for 30 seconds.

For device operation, hole current is injected from the top annular contact down through the DBR and into the quantum well active region, while electron current is

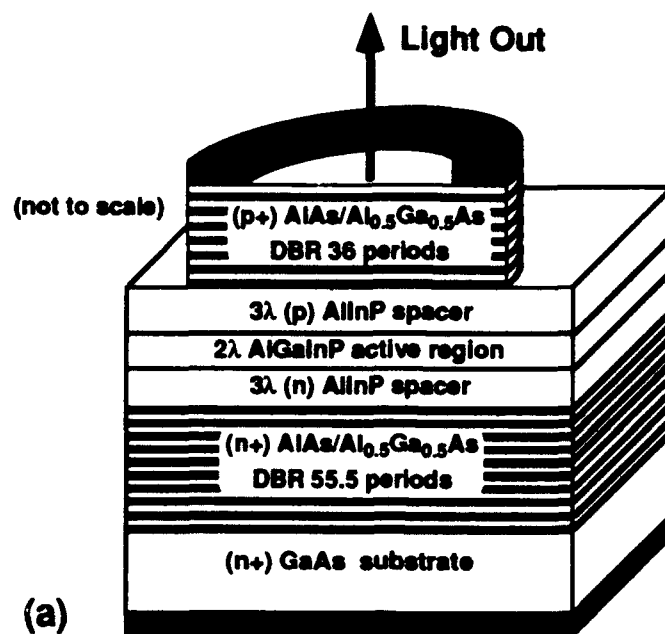


Fig. 5.1 Quick visible VCSELs. (a) Schematic diagram and, (b) and (c) scanning electron micrographs. In (b), the diameter of the optical aperture/mesa is 20/30 μm . In (c), the diameter of the optical aperture/ mesa is 3/10 μm .

injected through the bottom DBR stack and into the quantum wells. The hole current is restricted by the etched post, which isolates the individual devices. Once into the AlGaInP optical cavity, some of the current spreads outward and is essentially wasted. Gain guided lasing is achieved by filling to inversion, the entire quantum well area beneath the etched post. Although not an optimum VCSEL geometry, especially for thick optical cavities, Quick VCSELs have proven very useful for the initial characterization of the visible VCSEL epitaxial structures. Furthermore, several significant aspects of visible VCSEL performance (including the underlying device physics) have been ascertained from Quick VCSELs, as is demonstrated in the Sections that follow.

A cut-away schematic diagram of a completed ion implanted visible VCSEL is shown in Fig. 5.2. The device is fabricated as follows. Top square or rectangular contact pads are defined by photoresist lift-off. The metal, evaporated by electron beam, is 30 nm Ti, followed by 70 to 170 nm Au. Within the metal contacts are circular openings (optical apertures) with diameters of 12 μm (square contact), or 10, 15, 20, or 30 μm (rectangular contact). Next, thick (6 to 8 μm thick) photoresist dots are patterned over the apertures to serve as ion implant masks. Hydrogen ions ("protons") are implanted through the top metal contact deep into the structure. Typical doses of ~ 1 to $5 \times 10^{14} \text{ cm}^{-2}$ are used, at an accelerating potential of 350 to 420 keV. (The peak implant depth is $\sim 1 \mu\text{m}/100 \text{ keV}$ in the AlGaAs DBR). The peak range of the implant is slightly above the top AlGaAs DBR/AlGaInP optical cavity heterointerface, typically 3 to 4 μm from the surface depending on the number of DBRs (one DBR period is $\sim 100 \text{ nm}$ thick). The protons create areas of high resistivity in the AlGaAs, forcing current to flow in a funnel path from the top contact down through the unimplanted regions beneath the optical apertures. The protons also produce regions of minor damage beneath the top contact. This injection scheme is more efficient than that for the Quick VCSELs, since only the quantum well area beneath the aperture must be inverted to achieve lasing. Protons do not create high

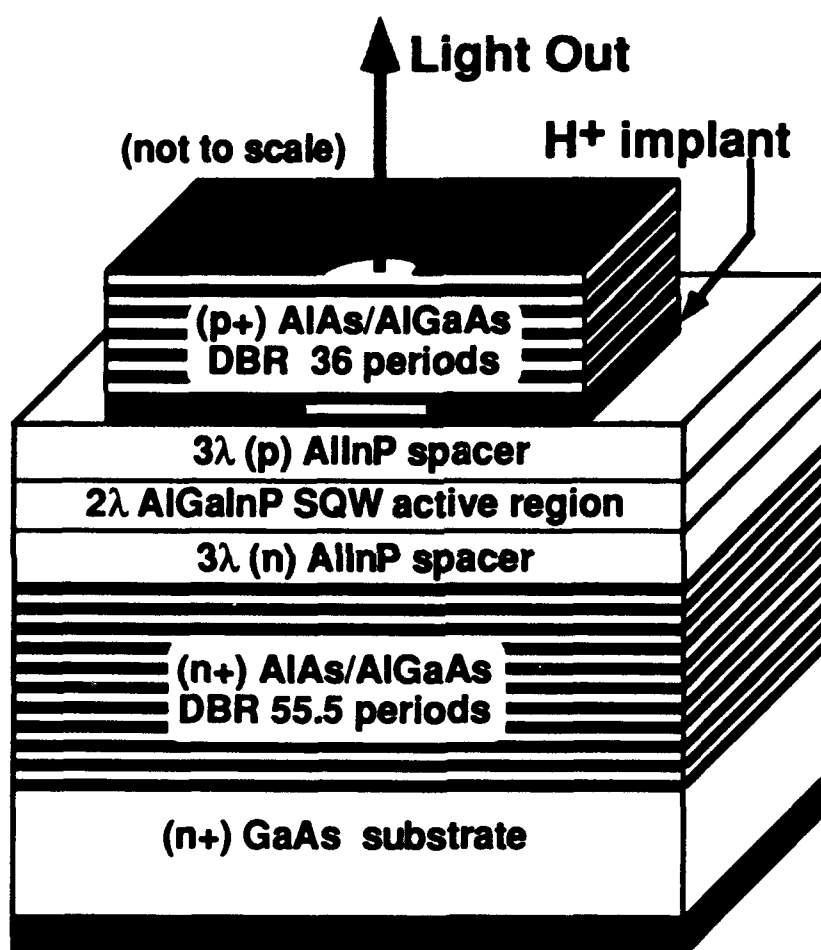


Fig. 5.2 Schematic diagram of an ion implanted visible VCSEL.

resistivity regions in the AlGaInP [Zolper *et al.* 1993]. Thus, it is not beneficial to place the peak of the implant in the AlGaInP optical cavity, and consequently a small fraction of injected current spreads out in the AlGaInP layers beneath the AlGaAs DBR and does not contribute directly to lasing. However, the lateral current spreading is minimal due to the relatively high resistivity of the (p)Al_{0.5}In_{0.5}P. While implanted oxygen (or argon) effectively increases the resistance of doped AlGaInP, it is not possible to implant this specie more than $\sim 1\mu\text{m}$ from the surface because of its size. Mesa isolation is achieved, as for the Quick visible VCSELs above, either with a plasma etch, or with a wet chemical etch using H₃PO₄:H₂O₂:H₂O.

Many other device geometries are possible. One example is the bottom emitting device where an etched post or ion implant define the device size, as above, except that the metal contact to the top DBR is a solid circle. This metal contact is part of the DBR reflector and fewer DBR periods are needed to obtain an equivalent reflectance. Additionally, the current is uniformly injected and current spreading is much less of a factor. For the visible VCSELs, bottom emitters are possible except that the substrate must be removed since it will absorb visible radiation. Another possibility is a composite device, where part or all, of one or both of the DBRs are composed of dielectric quarter wave stacks, as described in Section 2.4.3.

5.3 Operation with Gain Contributions from the $n=2$ Quantum Well State

The first round of studies on visible VCSEL diodes were based on the hybrid optically pumped structures described in Chapter 3. This took advantage of the many growth and fabrication refinements already developed for GaInAs and GaAs quantum well near infrared (IR) VCSELs, which use similar AlAs/GaAs and AlAs/Al_xGa_{1-x}As ($x \sim 0.15$) DBRs, respectively. The development of visible VCSEL diodes required

extensive optical studies of AlGaInP quantum well active regions, and of doping in both AlGaInP optical cavities and in AlGaAs DBRs. These studies were performed in concert with the VCSEL design issues discussed in Chapter 2, and with the limitations imposed by the state-of-the-art metalorganic vapor phase epitaxy (MOVPE) growth technology. Initially, the injection conditions present in visible VCSELs were studied by characterizing conventional strained quantum well AlGaInP visible edge-emitting lasers, but with variable $\text{Al}_{0.5}\text{In}_{0.5}\text{P}$ cladding layer thickness. Also, these conventional cladding layers were surrounded in-turn with additional AlAs/ $\text{Al}_{0.5}\text{Ga}_{0.5}\text{As}$ DBR "cladding" layers [Schneider and Lott 1993]. This study revealed that improved carrier injection efficiency resulted from the use of an extended 8λ optical cavity, consisting of cladding (doped) 3λ -thick $\text{Al}_{0.5}\text{In}_{0.5}\text{P}$ spacer layers surrounding a (undoped) 2λ -thick quantum well active region. This 8λ thick optical cavity was in-turn surrounded by the AlGaAs DBRs. These results were incorporated into the first successful visible VCSEL diodes.

Compared to AlGaAs infrared (IR) edge-emitting lasers, AlGaInP lasers have higher threshold current density (J_{th}), and smaller characteristic temperature. This is attributed to intrinsic material parameters such as small energy band offsets (thus reduced carrier confinement), high effective masses (thus increased transparency carrier density), and difficulty in the p-doping of AlInP alloys. Shorter wavelength operation, achieved for example by adding Al to the GaInP quantum well(s), by increasing the Ga/In ratio (biaxial tension), or by reducing the well thickness, further reduces the carrier confinement [Bour 1992b, 1993].

Similar trends are expected for quantum well AlGaInP VCSELs, where cavity heating effects compound the carrier leakage problem and lead to a reduction in the available gain at a given current density. Moreover, cavity and distributed Bragg reflector (DBR) losses (i.e. free carrier absorption) could increase the amount of gain required to reach threshold, to a point where the available gain from the first quantized state ($n=1$) is

insufficient to overcome the losses, even at high injected carrier densities. To achieve lasing in this case, the available gain must be increased for example by increasing the number of quantum wells in the active region. An alternate solution is to operate at shorter wavelengths with gain contributions from the second quantized state ($n=2$), where the maximum available gain is higher due to a higher joint optical density of states.

The growth list for a visible VCSEL with an extended 8λ thick optical cavity, is given in Table 5.1. The lattice-matched epitaxial layers are grown by MOVPE on (100) (n+) GaAs substrates misoriented 6° toward the nearest $\langle 111 \rangle$ A. The growth conditions

Table 5.1 MOVPE Growth List for Hybrid Visible VCSEL Sample XD0222B

~Thickness (Å)	Material	~Index	~Thickness (Å)	Material	~Index
100.0	(p+)GaAs	3.83-i0.194	continued		
308.9	(p+)Al _{0.5} Ga _{0.5} As	3.541	200.0	(Al _{0.4} Ga _{0.3}) _{0.5} In _{0.5} P	3.450
(repeat)			200.0	(Al _{0.5} Ga _{0.3}) _{0.5} In _{0.5} P	3.413
100.0	(p+)Al _{0.75} Ga _{0.25} As	3.299	200.0	(Al _{0.6} Ga _{0.3}) _{0.5} In _{0.5} P	3.378
416.3	(p+)AlAs	3.111	1066.3	(Al _{0.7} Ga _{0.3}) _{0.5} In _{0.5} P	3.345
100.0	(p+)Al _{0.75} Ga _{0.25} As	3.299	5988.9	(n)Al _{0.5} In _{0.5} P (3λ spacer)	3.256
365.7	(p+)Al _{0.5} Ga _{0.5} As	3.541	469.3	(n+)AlAs	3.111
x 35			100.0	(n+)Al _{0.75} Ga _{0.25} As	3.299
100.0	(p+)Al _{0.75} Ga _{0.25} As	3.299	(repeat)		
469.3	(p+)AlAs	3.111	365.7	(n+)Al _{0.5} Ga _{0.5} As	3.541
5988.9	(p)Al _{0.5} In _{0.5} P (3λ spacer)	3.256	100.0	(n+)Al _{0.75} Ga _{0.25} As	3.299
1066.3	(Al _{0.7} Ga _{0.3}) _{0.5} In _{0.5} P	3.345	416.3	(n+)AlAs	3.111
200.0	(Al _{0.6} Ga _{0.3}) _{0.5} In _{0.5} P	3.378	100.0	(n+)Al _{0.75} Ga _{0.25} As	3.299
200.0	(Al _{0.5} Ga _{0.3}) _{0.5} In _{0.5} P	3.413	x 54		
200.0	(Al _{0.4} Ga _{0.3}) _{0.5} In _{0.5} P	3.450	365.7	(n+)Al _{0.5} Ga _{0.5} As	3.541
(repeat)			100.0	(n+)Al _{0.75} Ga _{0.25} As	3.299
100.0	Ga _{0.44} In _{0.56} P (SQW)	3.622	416.3	(n+)AlAs	3.111
100.0	(Al _{0.4} Ga _{0.3}) _{0.5} In _{0.5} P	3.450	50.0	(n+)Al _{0.75} Ga _{0.25} As	3.299
x 2			5000	(n+)GaAs	3.83-i0.194
100.0	Ga _{0.44} In _{0.56} P (SQW)	3.622	substrate	(n+) GaAs (100) 6°	3.83-i0.194
			Bragg wavelength	λ ₀ = 650 nm	

are similar to those previously reported [Schneider *et al.* 1992a, 1992b]. The structures consist of a strained quantum well $(\text{Al}_y\text{Ga}_{1-y})_{0.5}\text{In}_{0.5}\text{P}$ optical cavity active region surrounded by $\text{AlAs}/\text{Al}_{0.5}\text{Ga}_{0.5}\text{As}$ DBRs. The bottom Si-doped ($\sim 2 \times 10^{18} \text{ cm}^{-3}$) DBR consists of 55.5 periods of alternating AlAs and $\text{Al}_{0.5}\text{Ga}_{0.5}\text{As}$ quarter-wave layers with 10 nm thick $\text{Al}_{0.75}\text{Ga}_{0.25}\text{As}$ barrier reduction layers at each interface. An identical 36 period C-doped ($\sim 4 \times 10^{18} \text{ cm}^{-3}$) top output-coupling DBR is used and concludes with a 10 nm thick (p+) ($\sim 7 \times 10^{19} \text{ cm}^{-3}$) GaAs layer to reduce contact resistance. An 8λ -thick $(\text{Al}_y\text{Ga}_{1-y})_{0.5}\text{In}_{0.5}\text{P}$ optical cavity contains three 10 nm thick $\text{Ga}_{0.44}\text{In}_{0.56}\text{P}$ compressively strained ($\sim 0.56\%$) quantum wells in a step graded-barrier separate confinement heterostructure (SCH). Surrounding the wells are $y = 0.4$ barrier layers, stepped to $y = 0.7$ in 0.1 increments. This portion of the active region has a 2λ optical thickness. The remaining optical cavity consists of 3λ thick Mg-doped ($\sim 6\text{--}8 \times 10^{17} \text{ cm}^{-3}$) and Si-doped ($\sim 2 \times 10^{18} \text{ cm}^{-3}$) $\text{Al}_{0.5}\text{In}_{0.5}\text{P}$ spacer layers on the n-side and p-side, respectively.

The calculated reflectance and reflectivity phase spectra (at $\lambda_0 = 650 \text{ nm}$) for the hybrid visible VCSEL structure at normal incidence are shown in Fig. 5.3. The primary Fabry-Perot resonance occurs at $\sim 650 \text{ nm}$, while other cavity resonances occur near 626.8, 631.4, 668.6, and 673.6 nm. As described in Chapter 2, a resonance occurs when the optical cavity round trip phase is 2π . To further illustrate this point, Fig. 5.4 is a high resolution (calculated) plot of the reflectance and reflectivity phase spectra at (a) $\sim 650 \text{ nm}$ (defined here as a primary Fabry-Perot resonance or mode) (b) $\sim 668.6 \text{ nm}$ (defined here as a secondary Fabry-Perot resonance or mode), and (c) $\sim 673.7 \text{ nm}$ (defined here as a natural resonance or mode) for the structure in Table 5.2 at normal incidence. Since the plots are the reflectivity of the entire structure, a 2π round trip phase corresponds to the wavelengths in Fig. 5.4, where the reflectivity phase equals zero. A 2π round trip phase at $\sim 649.97 \text{ nm}$ occurs since the reflectivity phase of the DBR mirrors are

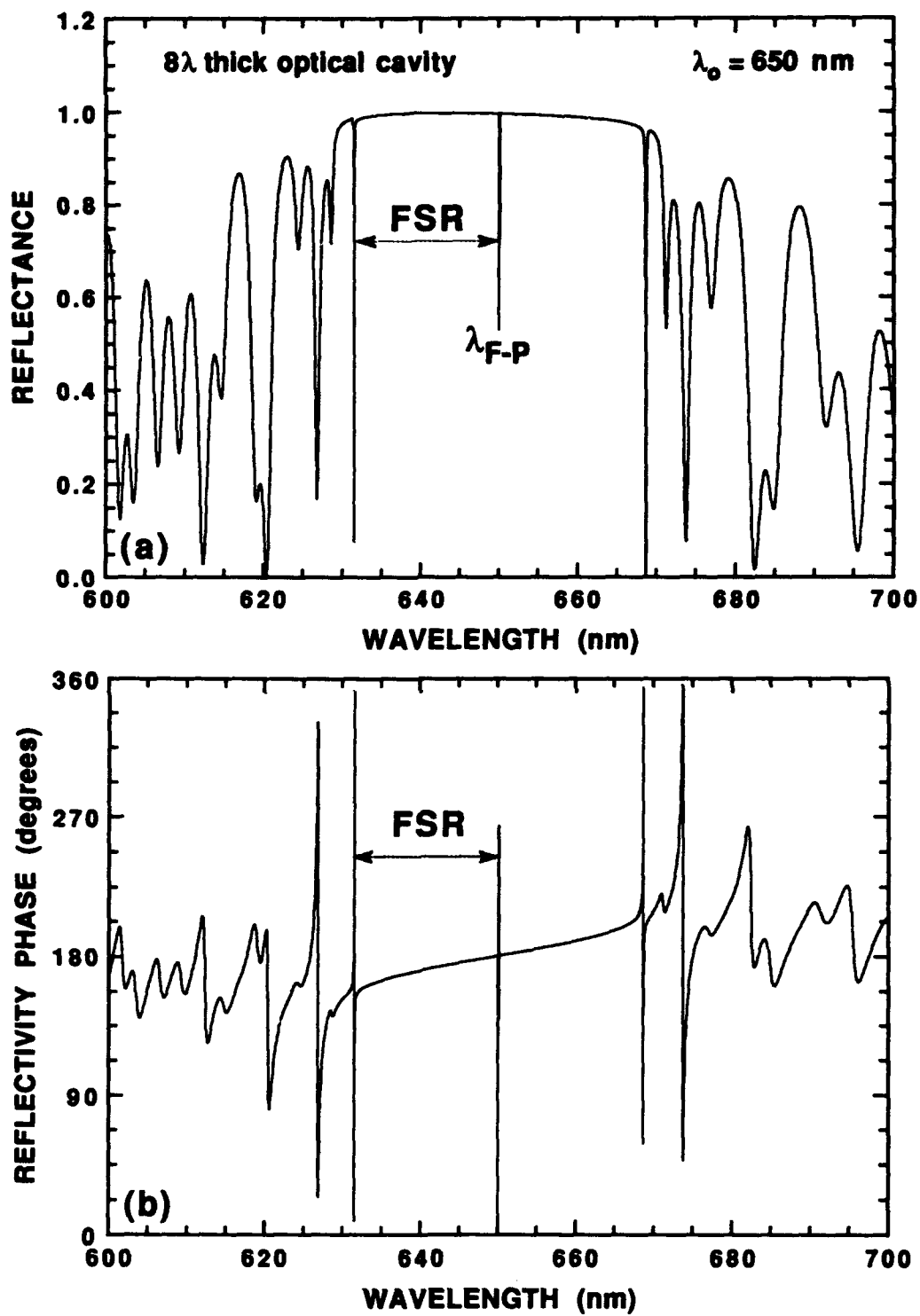


Fig. 5.3 Calculated (a) reflectance and (b) reflectivity phase for the hybrid visible VCSEL in Table 5.1. The free spectral range (FSR) is indicated.

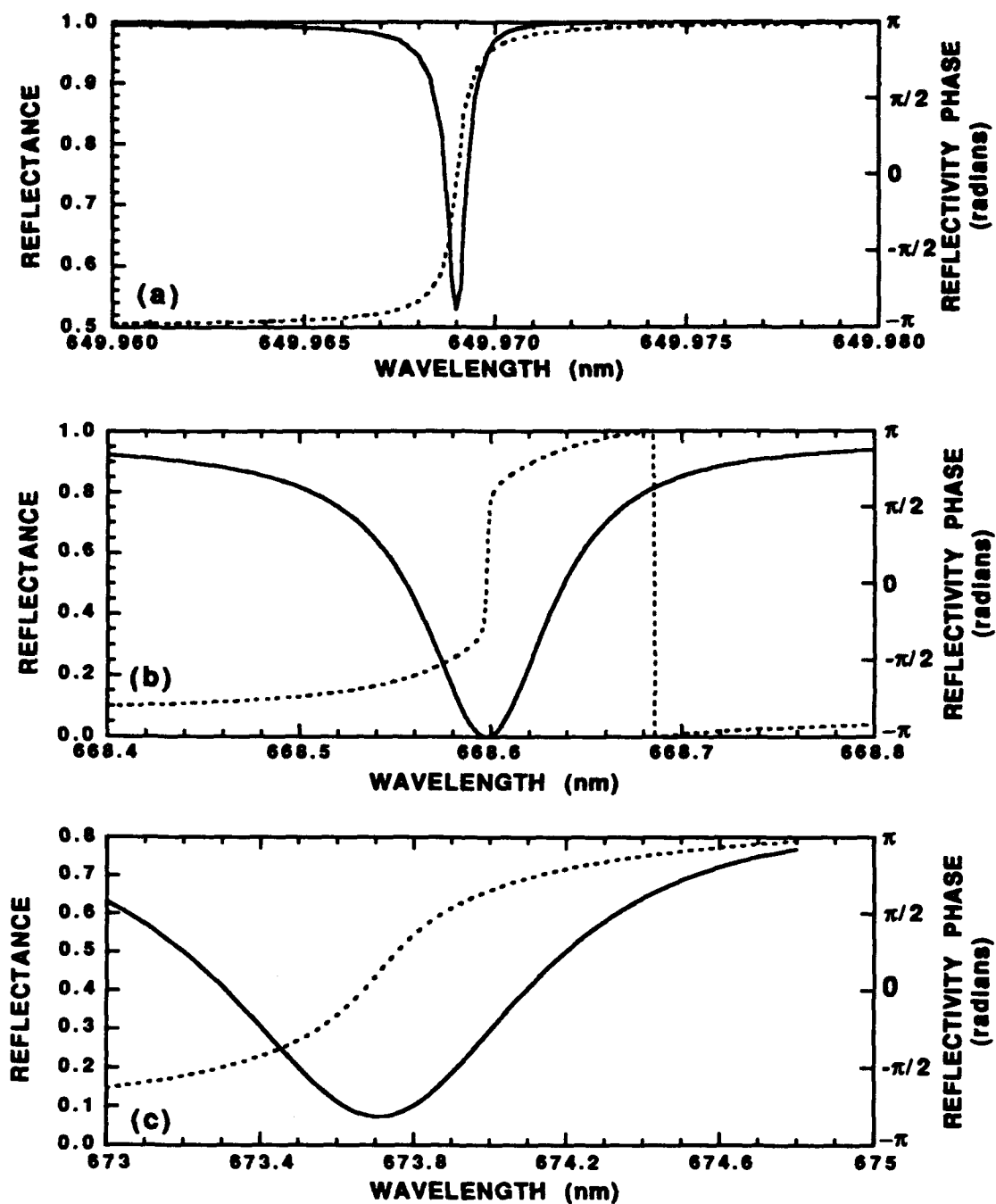


Fig. 5.4 Calculated reflectance (solid line) and reflectivity phase (dashed line) in and around the (a) primary Fabry-Perot mode (b) secondary Fabry-Perot mode, and (c) natural mode, for the hybrid visible VCSEL in Table 5.1. (Expanded, higher resolution plots of Fig. 5.3).

each π , and the optical cavity is exactly $8\lambda_0$ thick. (The slight deviation from 650.0 nm is due to the precision of the layer thicknesses used in the matrix calculation). In contrast at 668.6 nm, the reflectivity phase of the top and bottom DBRs, as seen from the optical cavity, are 1.347 and 1.408 radian, respectively. The optical cavity thickness is $\sim 7.72\lambda_0$, and the phase due to propagation through the cavity is ~ 1.763 radian. The total round trip phase is thus $2(1.763) + 1.347 + 1.408 = 2\pi$. At 668.6 nm, the reflectivity phase of the top and bottom DBRs, as seen from the optical cavity, are 0.0175 and 1.737 radian, respectively. The optical cavity thickness is $\sim 7.64\lambda_0$, and the phase due to propagation through the cavity is ~ 2.262 radian. The total round trip phase is thus $2(2.262) + 0.0175 + 1.737 = 2\pi$.

As discussed for the hybrid optically pumped structure in Section 3.4, the VCSEL wafers (2 inch diameter) are not rotated during growth, resulting in an $\sim 10\%$ variation in centerline layer thickness. Thus, the Fabry-Perot resonance changes with wafer position as in Figs 2.18, 3.4, and 3.11. Despite this, the active region peak spectral gain changes by less than 7.5 nm from front to back along the wafer centerline. (In contrast for rotated wafers, the variation is < 3 nm). Figure 5.5 is a plot of the room temperature PL from an unrotated optical cavity active region calibration wafer. The calibration wafer consists of the structure in Table 5.1, except without the bottom and top DBRs. Note that the "design" emission wavelength for the quantum well active region in Fig. 5.5 is ~ 670 nm. This corresponds to the $n=1$ (e1 to hh1) quantum well transition.

The variation of the PL peak spectral gain is primarily a result of a larger decrease in In incorporation, compared to Ga, when moving from front to back along the wafer centerline. This is a fundamental characteristic of the MOVPE growth process. As a result, the compressive quantum well strain is lower near the back of the wafer and increases toward the front. The energy bandgap of the quantum well layers correspondingly increases when moving from the front toward the back. The small

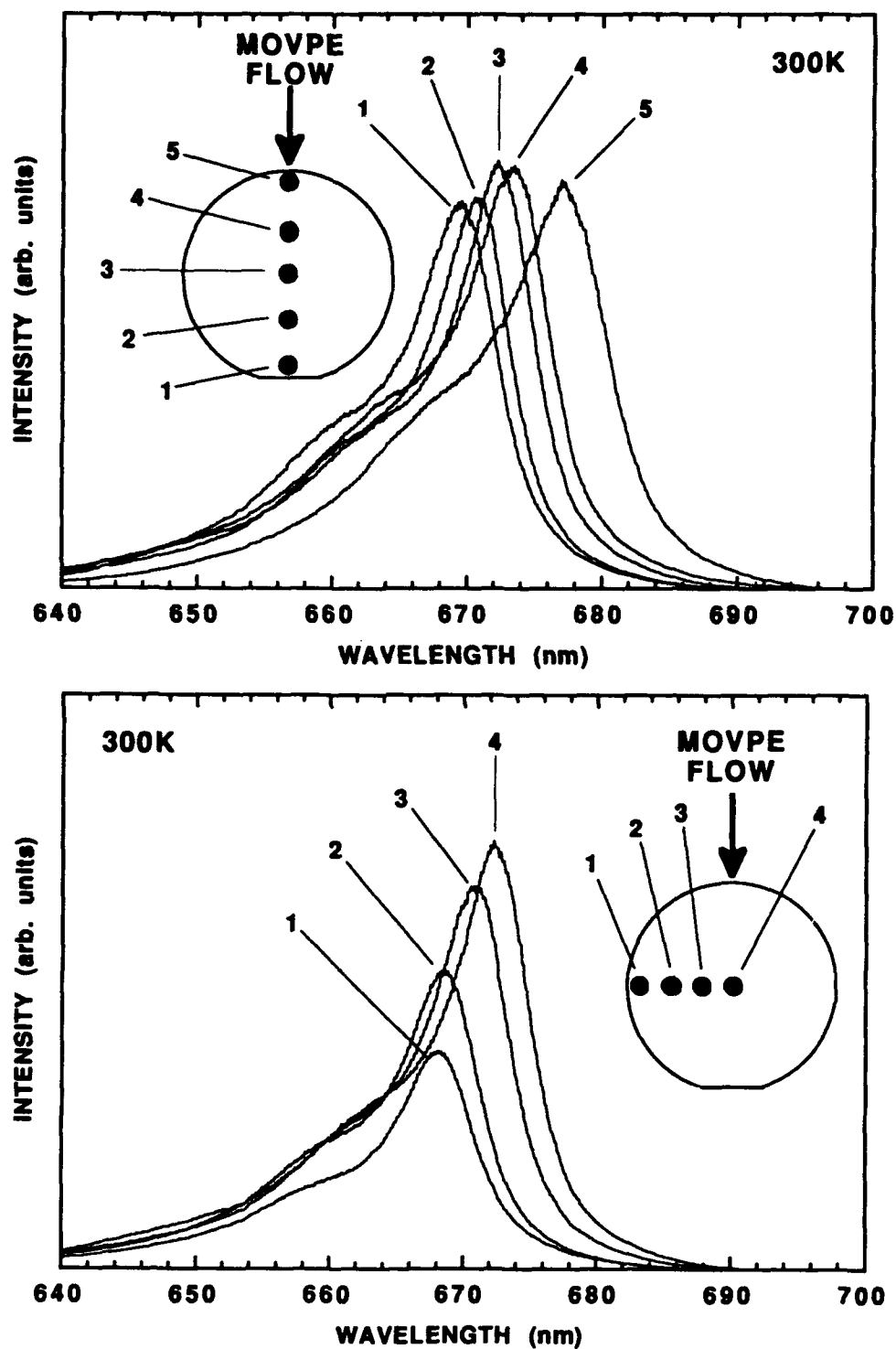


Fig. 5.5 Photoluminescence (PL) spectra at several points on an unrotated, strained quantum well, optical cavity active region calibration wafer. (The structure is given in Table 5.1, except without the top and bottom DBRs).

thickness variation in the quantum wells also results in a blue-shift of the PL emission peak when moving from front to back, but this shift is much smaller than that due to the compositional variation. The net result of the thickness and compositional variation is a large range of possible lasing emission wavelengths. Figure 5.6 is a schematic plot of the Fabry-Perot resonance wavelength across wafer XD0222B, where the resonance is at ~ 670 nm at wafer center. Also shown is the range of peak transition wavelengths at the peak of the $n=1$ and $n=2$ quantum well transitions, roughly corresponding to the PL data in Fig. 5.5.

The measured reflectance spectra from two points ($\lambda_0 \approx 650$, and 670 nm) for the hybrid visible VCSEL structure, are given in Fig. 5.7(a). The resonant features described in the reflectance calculation (Fig. 5.3) above are difficult to locate, due primarily to the resolution of the measurement system. Additionally, the structures deviate from the exact thickness and compositions listed in Table 5.1 due to natural growth fluctuations. Thus, the measured reflectance spectra will not precisely mimic the calculated spectra. In spite of this, the primary Fabry-Perot mode is present as shown (λ_{F-P}). Also, the secondary Fabry-Perot mode and the natural mode, defined above, are located to the right (toward longer wavelengths) of the primary Fabry-Perot mode, between the edge of the high reflectance zone and the hunchback feature.

Quick visible VCSELs were fabricated as described in Section 5.3, with the backside metal deposited before the mesa etch. Prior to the mesa etch step, the room temperature electroluminescence (EL) was sampled from several equally-spaced devices at a constant low bias current (~ 10 mA). An example (normalized intensity) EL spectra is given in Fig. 5.7(b), along with the reflectance (normal incidence) at the same point on the wafer. The EL measurement system is described in Subsection 2.4.1 (Fig. 2.7). The EL spectra contains spikes corresponding to the primary Fabry-Perot mode, and to the secondary mode on the long wavelength side. The EL spectra at several equally spaced

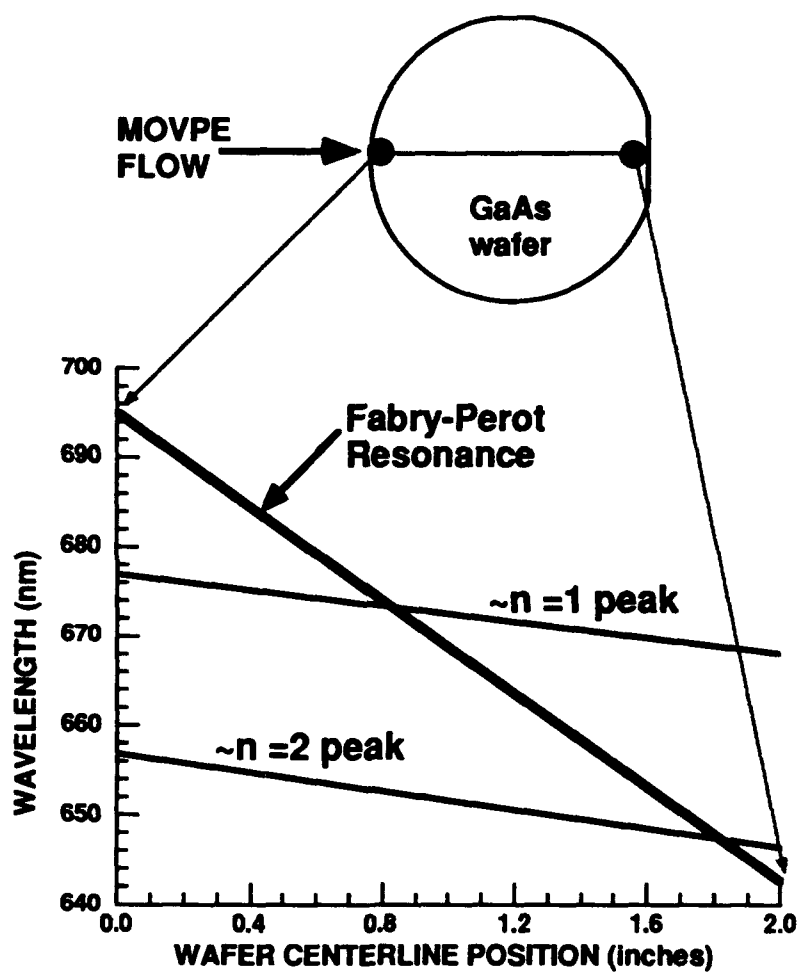


Fig. 5.6 Schematic plot of the variation in Fabry-Perot resonance wavelength (thick solid line) and peak quantum well transition wavelengths across unrotated visible VCSEL wafer number XD0222B. The transition wavelengths ($n=1$ and $n=2$) refer to the first and second quantized state transitions.

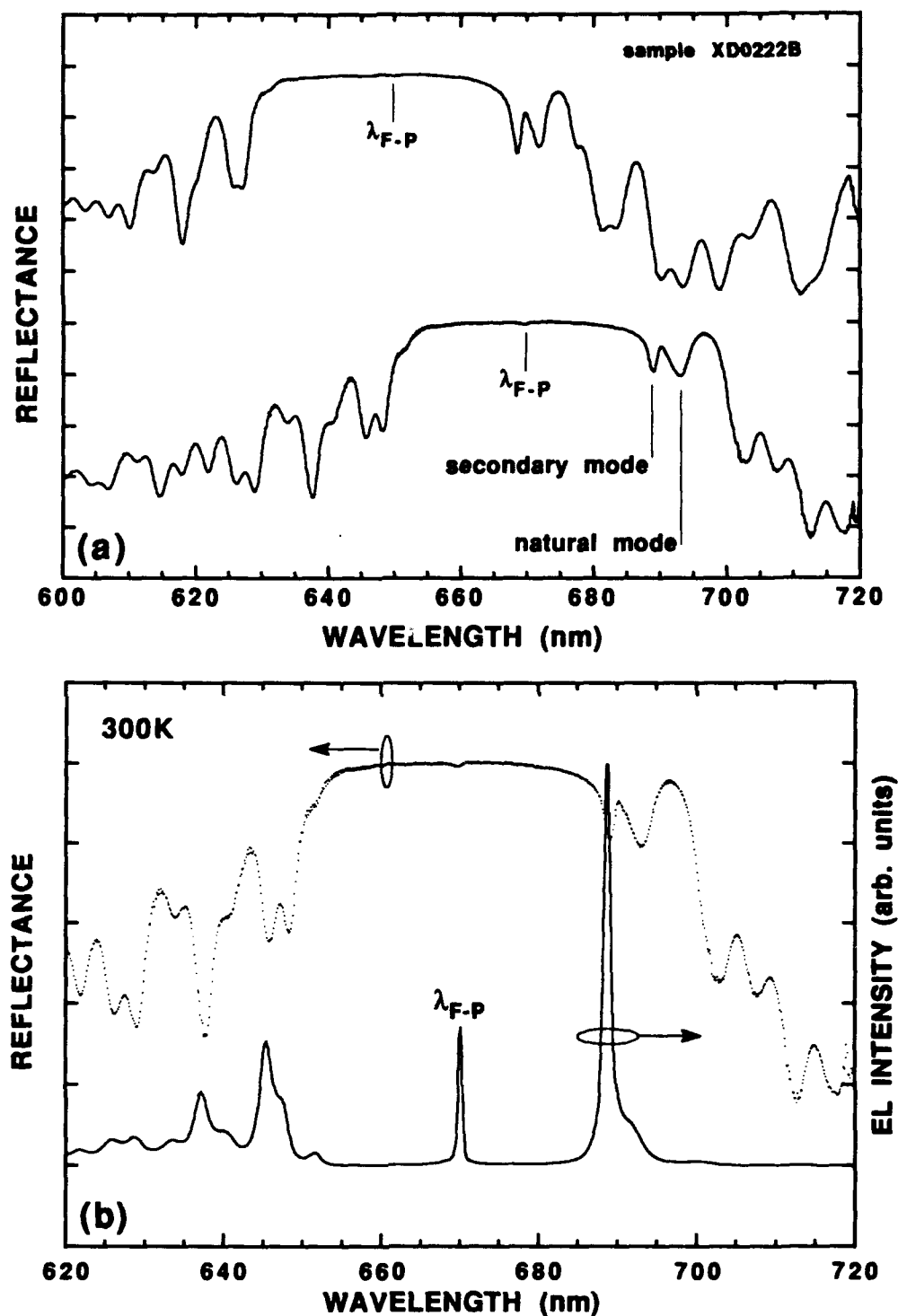


Fig. 5.7 (a) Measured reflectance at $\lambda_0 \approx 650$ and 670 nm for the hybrid visible VCSEL structure, and (b) reflectance (dotted line) and electroluminescence (solid line) for a fabricated Quick visible VCSEL prior to the mesa etch step.

points across the wafer are given in Fig. 5.8. Because the top DBR is still fully in place, all of the measured emission spectra consists of filtered/enhanced spontaneous emission, and can be modeled by using the wave interference model described in Section 4.3 (Chapter 4). In the bottom spectrum in Fig. 5.8, the primary Fabry-Perot resonance is at ~ 690 nm and the secondary Fabry-Perot resonance is at ~ 710 nm. Figure 5.9 is a plot of the Fabry-Perot resonance peak spectral features, taken at several equally-spaced points, across the sample. The emission intensity goes through a peak at ~ 670 nm, corresponding to the $n=1$ optical gain peak of the quantum well active region. (Note that the envelope of the resonance peaks correlates to the quantum well spectral gain, with the maximum intensity roughly at the $n=1$ gain peak (as for a PL measurement of the active region).

Using pulsed excitation at room temperature and without heat sinking, lasing wavelengths from 639.1 nm to 660.7 nm are measured (sample XD0222B). As for the optically pumped structures described in Chapter 3, lasing is achieved with significant gain contributions from the $n=2$ quantum well state. The pulsed excitation is ~ 200 ns pulses at a period of 1 μ s. Many devices continue to lase with up to a 40% duty cycle at a 1 μ s period. The 20 μ m diameter devices (in a 30 μ m diameter mesa) typically have a threshold current (I_{th}) of 30 mA ($J_{th} \sim 4.2$ kA/cm²) at 2.7 V with a resistance of ~ 15 Ω at $> 1.5 I_{th}$. This low resistance is due to the small energy band offsets within the DBR, the heavy doping, and the large number of DBR periods allowing uniform current spreading. Lasing spectra below ($0.9 I_{th}$), at ($1.0 I_{th}$), and just above ($1.1 I_{th}$) current threshold for a device emitting at 650.4 nm are shown in Fig. 5.10. A red-shift in the emission wavelength occurs with increasing current due to heating effects. The side peak at 667 nm is due to EL escaping through the top DBR at the secondary Fabry-Perot resonance. A bump near 644 nm below threshold is EL escaping from the sides of the etched post, and corresponds to gain contributed from the $n=2$ quantum well transition.

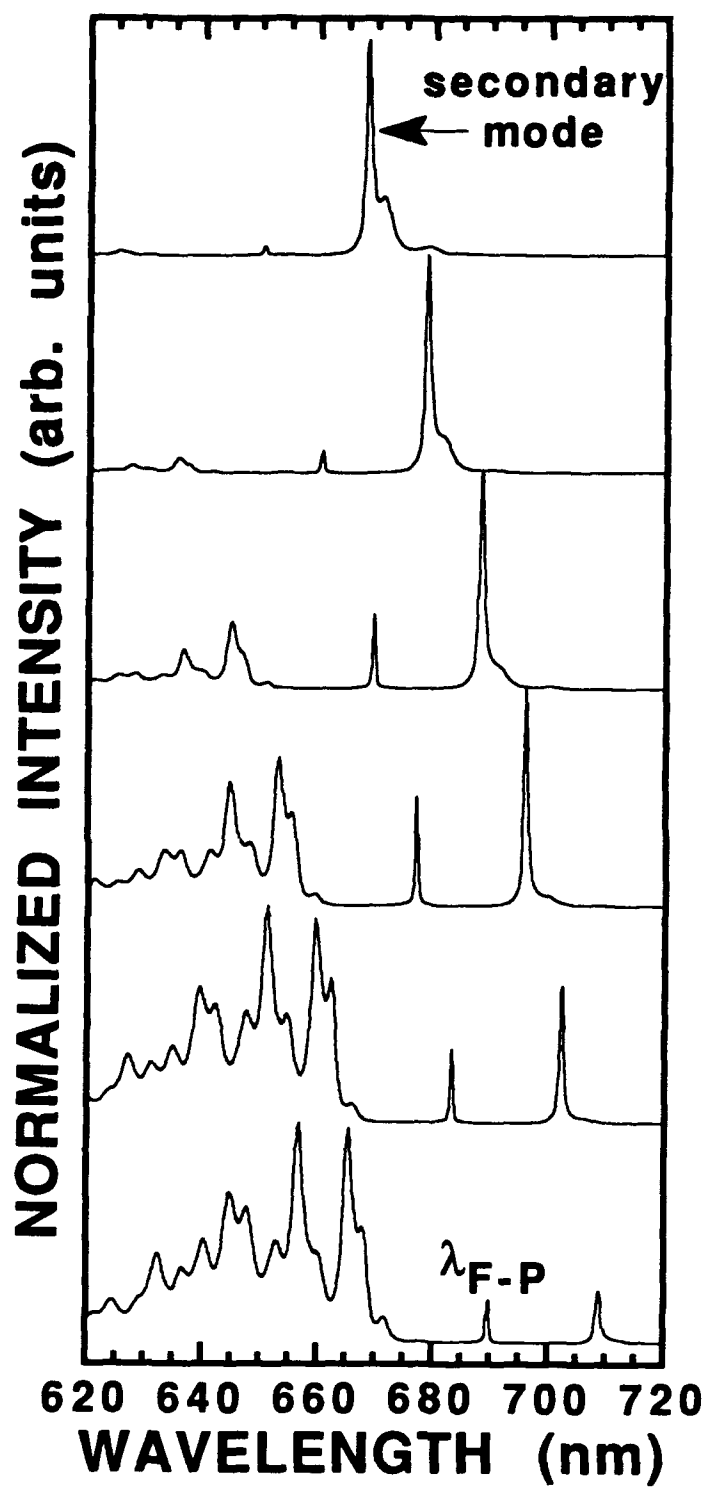


Fig. 5.8 Electroluminescence spectra for fabricated Quick visible VCSELs, prior to the mesa etch step, at several equally spaced points across the hybrid visible VCSEL wafer.

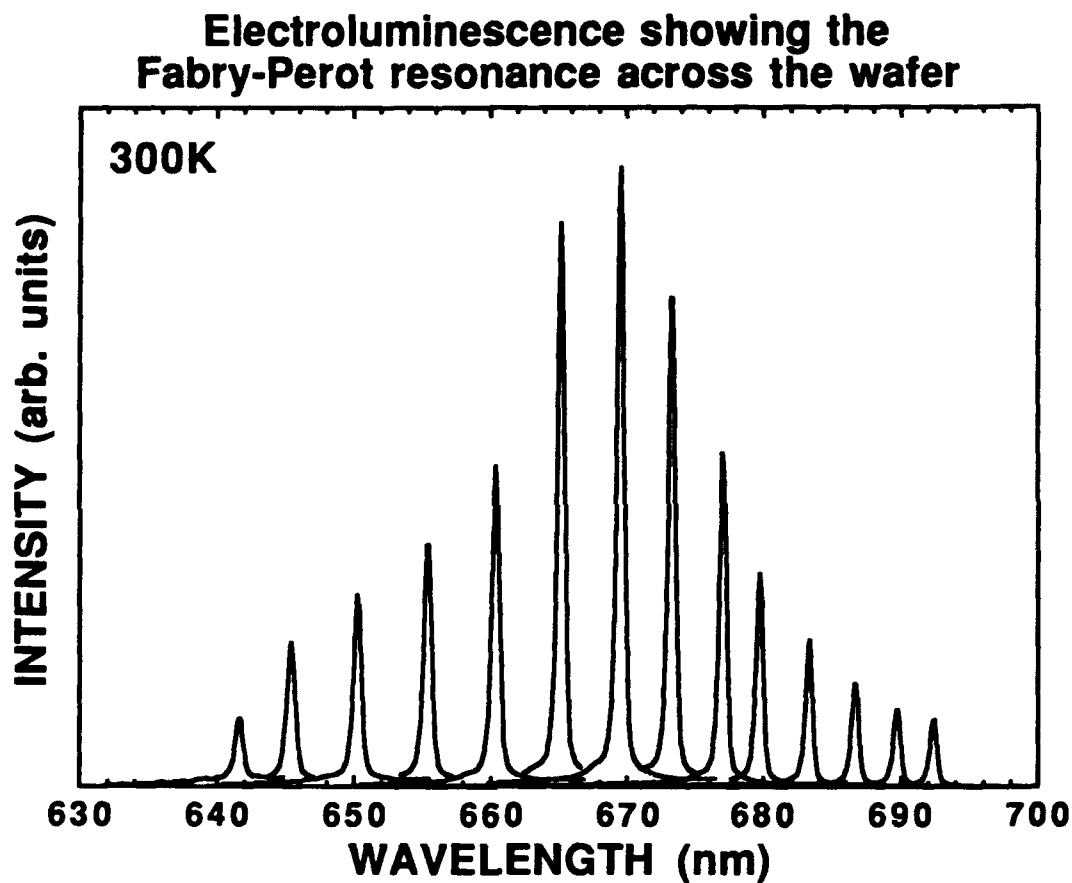


Fig. 5.9 Electroluminescence spectra corresponding to the Fabry-Perot resonances at several equally spaced points across the hybrid visible VCSEL wafer. The measurements were performed on Quick visible VCSELs prior to the mesa etch step (see Figs 5.7 and 5.8), with a direct current bias of ~ 10 mA. The envelope of the resonance peaks correlates to the quantum well spectral gain, with the maximum intensity roughly at the $n=1$ gain peak.

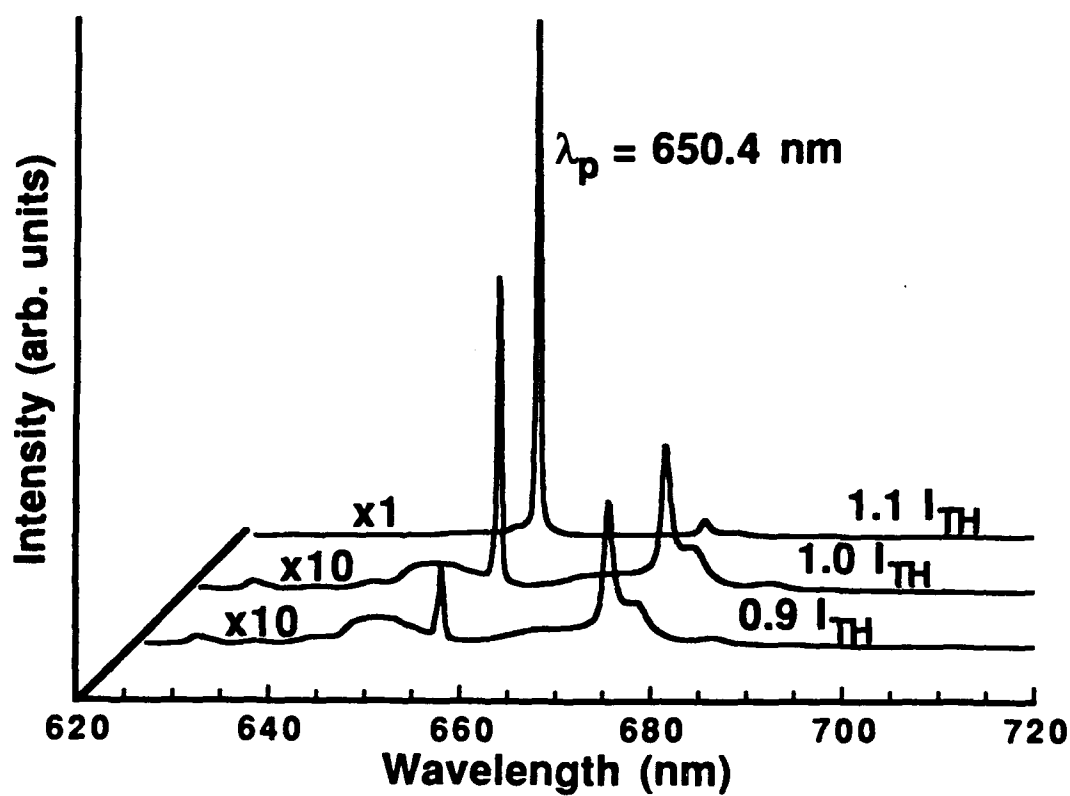


Fig. 5.10 Visible VCSEL lasing spectra below, at, and just above threshold at room temperature. The Quick visible VCSELs have an optical aperture diameter of $20\ \mu\text{m}$ in a mesa diameter of $30\ \mu\text{m}$. The threshold current $I_{\text{th}} \sim 30\ \text{mA}$.

A light-current (L-I) characteristic for a device with a 20 μm optical aperture, emitting at ~ 650 nm, is shown in Fig. 5.11. A distinct threshold is seen at about 30 mA. The differential slope efficiency is 6% just past threshold and the external quantum efficiency is 1.8% at 80 mA. The maximum peak output power is limited to 3.38 mW due to thermal roll-over. The inset in Fig. 5.11 is the measured far-field intensity (fit to a Gaussian distribution) at 70 mA and a divergence (full angle) of 6.5° is indicated. The far field (full angle) angular divergence is expected to be $\approx \lambda_0/d \sim 1.9^\circ$, where $d = 20 \mu\text{m}$ is the aperture diameter [Saleh and Teich 1991]. The discrepancy is partially due to a thermal lensing effect [Hasnain *et al.* 1991], where only the central area of the aperture is lasing. This effectively reduces the diameter of the optical aperture and thus increases the angular divergence of the Gaussian emission.

Lasing does not occur above a wavelength of ~ 661 nm (for the given pulse conditions and device size). This may be due to high cavity losses, such that the gain provided at $n=1$ (i.e. gain contributed from the $n=1$ quantized quantum well state) is insufficient for lasing. Indeed, devices identical to those described above but with two quantum wells (thus lower gain) in the active region did not lase at any wavelength. While the high doping and relatively small band offsets in the DBRs lead to a low series resistance ($\sim 15 \Omega$ above threshold), the small refractive index differential (i.e. $\Delta n/n \approx 13\%$ at $\lambda_0 = 650$ nm) results in deep penetration of the standing wave into the DBRs. This increases the effective cavity length [Babic and Corzine 1992] and results in higher losses. Moreover, it is uncertain how much loss is associated with the AlAs-Al_{0.5}In_{0.5}P heterointerfaces (i.e. where a change in column V element occurs) which reside at the critical optical cavity/DBR boundary in the present design. In contrast, the data on similar undoped optically pumped structures in Chapter 3 suggests that the 10 nm thick quantum wells used in the present study are not optimized for maximum utilization of gain, especially at shorter emission wavelengths. Calculations of

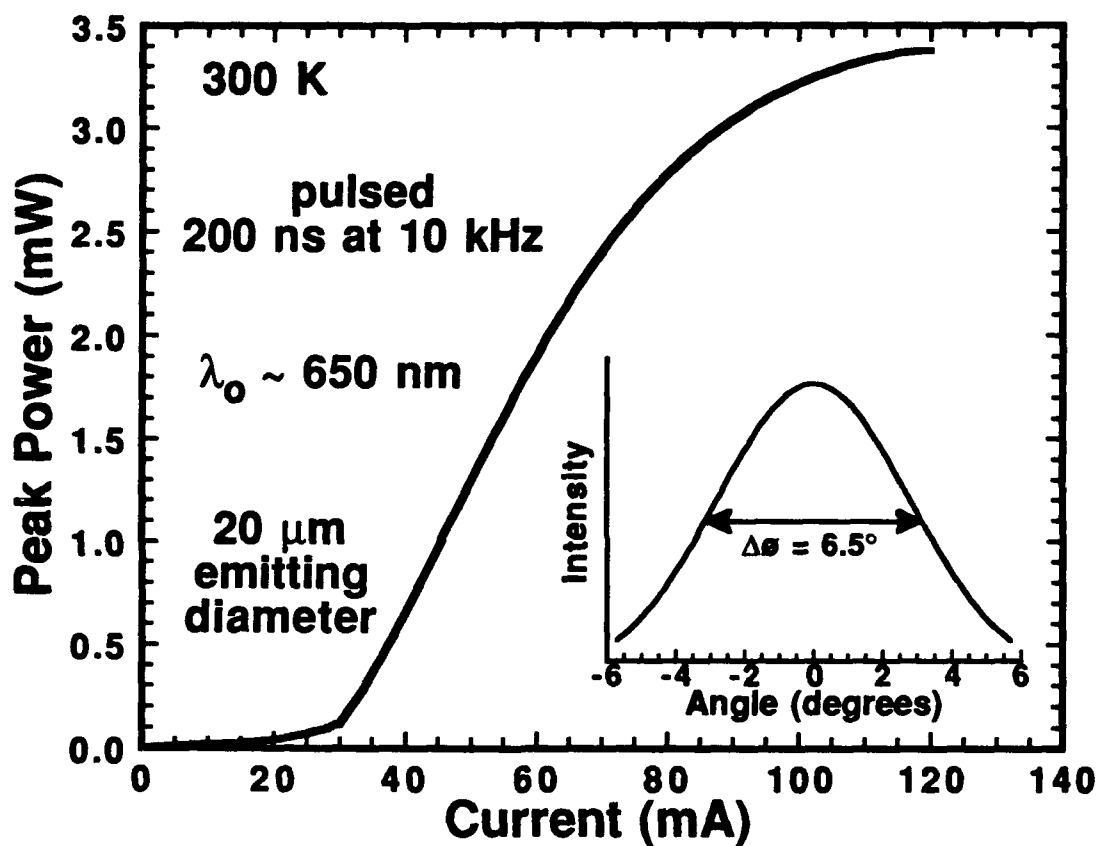


Fig. 5.11 Light-current (L-I) characteristic at room temperature of a Quick visible VCSEL diode. The inset is the far-field emission intensity fit to a Gaussian distribution.

the longitudinal confinement factor (see Table 2.6) reveal that thinner (~6 to 8 nm) quantum wells spaced closer together should result in a reduced threshold and higher optical gain, for equal total gain length.

Insight into the operation of the visible VCSELs can be obtained by examining "n=2 lasing" in quantum well edge-emitter lasers [Holonyak *et al.* 1980, Middlestein *et al.* 1986]. At threshold, the round trip gain equals the round trip loss, $g_{th} = 1/\Gamma[\alpha + (1/L)\ln(1/R)]$, where g_{th} is the gain threshold, Γ is the confinement factor, α is the cavity loss, L is the length, and R is the facet reflectance. For small α , g_{th} is selected by varying L . For short length devices, the g_{th} exceeds the gain available from the first quantized state, and gain contributions from the second quantized state are required for lasing. At intermediate L , it is possible to achieve lasing at first $n=1$ (i.e. lasing due primarily to gain contributions from the $n=1$ quantized quantum well state, since $n=2$ contributions, however small, are always present), then as the injected current density increases (filling higher lying subbands), at $n=2$. In our conventional broad area stripe geometry, gain guided red edge-emitting lasers (single strained ~Ga_{0.44}In_{0.56}P quantum well with (Al_{0.4}Ga_{0.6})_{0.5}In_{0.5}P barriers and ~1 μ m thick AlInP cladding layers, capped with (p+)GaAs, and grown on (n+)GaAs substrates), lasing occurs only at $n=1$ for $L \geq 300 \mu$ m ($J_{th} \sim 200$ A/cm²) due to gain saturation and heating. Figure 5.12 is a plot of the electroluminescence sampled from the top of an AlGaInP red edge-emitter with a 50 μ m x 250 μ m stripe. Multimode lasing first occurs near 680 nm, then blue-shifts to near 660 nm when the peak gain from $n=2$ exceeds that at $n=1$ (see Figs 2.33 and 2.34 in Chapter 2). For $L < 200 \mu$ m, lasing is achieved only at $n=2$.

Figure 5.13(a) is a plot of the threshold current versus lasing wavelength for several Quick visible VCSELs across sample XD0222B. The devices have an optical aperture diameter of 10 μ m, in a mesa diameter of 20 μ m. The room temperature current excitation is 100 ns pulses at a repetition rate of 10 μ s (i.e. 1% duty cycle). A low duty

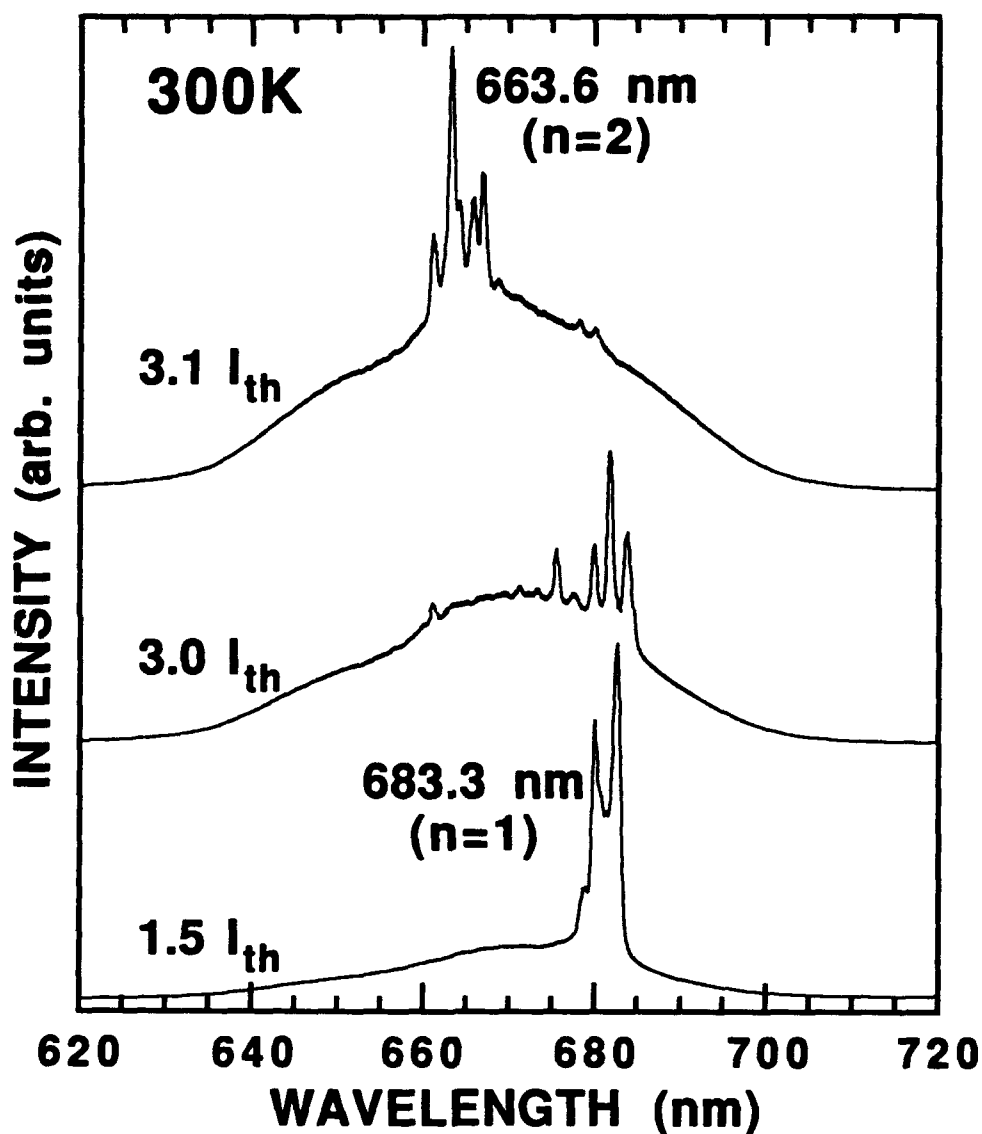


Fig. 5.12 Electroluminescence sampled from the top of a $50\text{ }\mu\text{m} \times 250\text{ }\mu\text{m}$ broad area, stripe geometry, AlGaInP visible edge-emitting laser. Multimode lasing at the $n=1$ gain peak (near 680 nm) blue-shifts $\sim 20\text{ nm}$ to the $n=2$ gain peak (near 660 nm) as the current increases. The threshold current (I_{th}) is $\sim 37\text{ mA}$, corresponding to a $J_{th} \sim 300\text{ A/cm}^2$. The room temperature pulsed current excitation is 100 ns pulses at 1.0 μs .

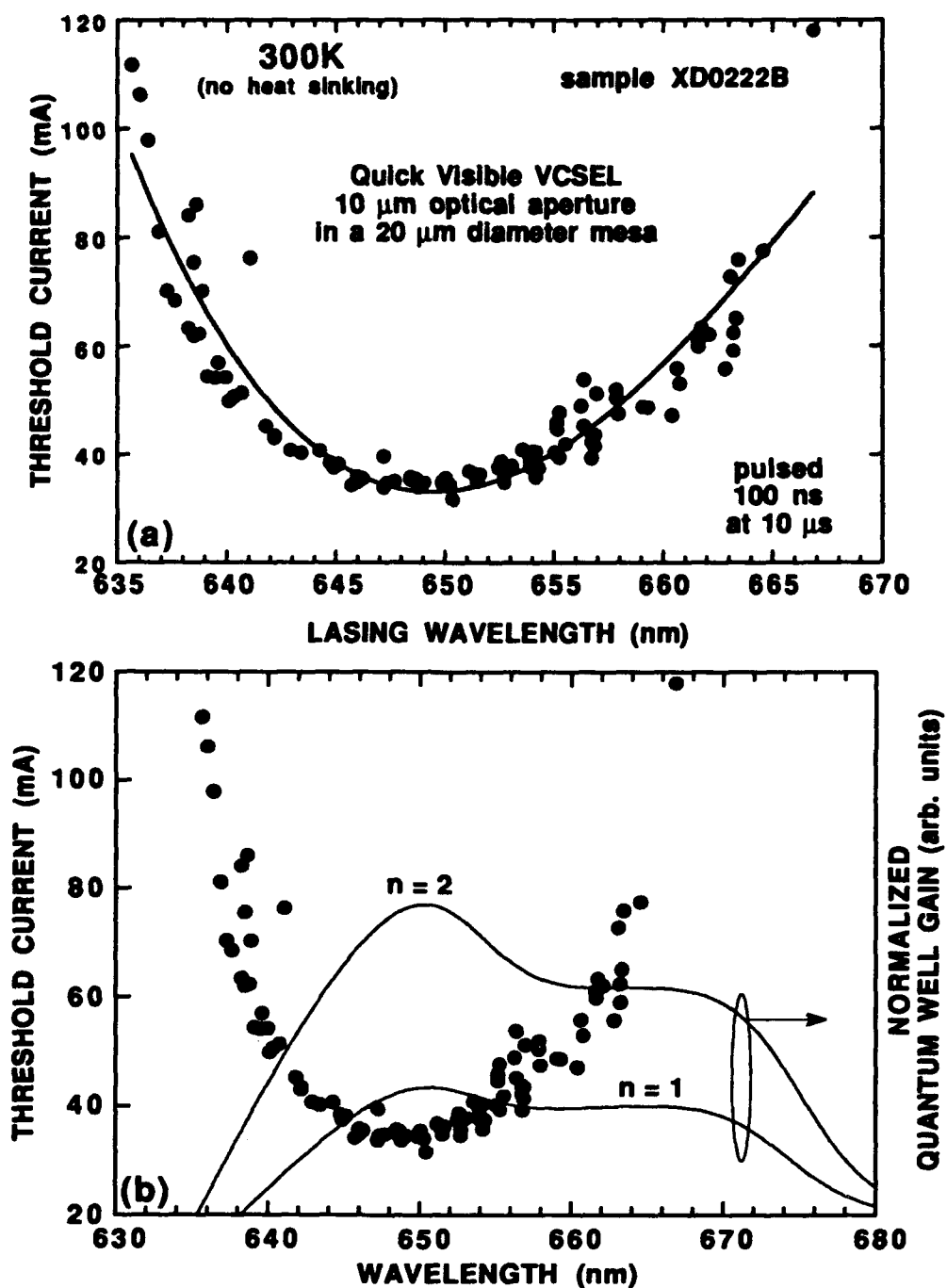


Fig. 5.13 (a) Threshold current versus lasing wavelength (or equivalently wafer position) for Quick visible VCSELs fabricated across sample XD0222B, and (b) the same data overlaid with semi-quantitative quantum well gain spectra.

cycle is used for the pulsed excitation to minimize heating effects. It is clear that the threshold minimum is at ~ 650 nm. The \sim parabolic shape of the curve is qualitatively similar to the shape of the curves in Figs 3.6 and 3.13(a), and a similar "n=2" lasing argument applies. This is especially true since it was proven in Fig. 5.9 that the n=1 gain peak occurs at ~ 670 nm.

Figure 5.13(b) shows the same threshold current versus wavelength data, along with two estimated (and normalized to remove the units) quantum well gain curves where the n=2 gain peak coincides with ~ 650 nm. The gain curves are calculated by using the semi-quantitative gain model in Appendix D. The top gain curve, relative to the lower gain curve, represents increased injected carrier density in the quantum wells. If the gain at ~ 665 to 670 nm is high enough for lasing, the lowest threshold current (I_{th}) should occur at this wavelength corresponding to the n=1 transition. For the visible VCSELs however, the lowest I_{th} is near ~ 650 nm, and the I_{th} increases elsewhere. This suggests that lasing occurs in and around the n=2 gain peak. (Lasing is not strictly "at n=2", but rather occurs due to gain contributions from the n=2 state. This is most noticeable at wavelengths ≥ 660 nm in 5.13(b)). The small ~ 20 nm separation between n=1 and n=2 is a consequence of the small band offsets and the large effective masses of the $(Al_yGa_{1-y})_{0.5}In_{0.5}P$ quantum well system. For an analogous GaAs/AlGaAs quantum well, the separation is larger at 50 to 60 nm.

5.4 Operation with Gain Contributions Primarily from the n=1 Quantum Well State

The second round of visible VCSELs are similar to those in Section 5.3. Several design improvements were made, however, based on the experimental results from the optically pumped structures (in Chapter 3) and the first round of diodes (in Section 5.4). First, the thickness of the quantum wells and separation layers in the optical cavity active

region were decreased (6 or 8 nm rather than 10 nm) to improve the overlap between the standing wave and the gain layers, and to reduce the threshold current. Due to the thinner quantum wells and corresponding blue shift in the peak spectral gain, the design wavelength (λ_0) was decreased to ~ 665 nm. Second, the doping density in the (p)AlGaAs DBR was decreased to reduce losses associated with free carrier absorption. Third, the $\text{Al}_x\text{Ga}_{1-x}\text{As}$ DBR heterointerfaces were compositionally graded (\sim biparabolic from $x = 1.0$ to 0.75 , then $x = 0.75$ to 0.50 , and vice versa) to help reduce the series resistance, while counter balancing the reduced p-doping in the DBR which increases the series resistance.

The structures were grown by MOVPE without wafer rotation as before. The bottom Si-doped (n)DBR ($2 \times 10^{18} \text{ cm}^{-3}$) consists of 55.5 periods of alternating 0.15λ -thick AlAs and $\text{Al}_x\text{Ga}_{1-x}\text{As}$ $x = 0.5$ layers with 0.1λ -thick $x = 1.0$ to 0.5 continuous parabolic graded layers at each interface (samples XD0623E and XD0624B have the original step grade as in Table 5.1, while samples XD0630C and XD0701C have the \sim biparabolic grade). The top output-coupling C-doped (p)DBR is identical, with 36 periods. The C-doping, $\sim 2 \times 10^{18} \text{ cm}^{-3}$, is one-half the value for the round 1 devices. Additionally (for samples XD0630C and XD0701C), the C-doping is reduced to ~ 5 to $10 \times 10^{17} \text{ cm}^{-3}$ in the 5 (p)DBR periods adjacent to the optical cavity, and increased to ~ 0.5 to $2 \times 10^{20} \text{ cm}^{-3}$ in the uppermost 2 DBRs periods (the last $\text{Al}_{0.5}\text{Ga}_{0.5}\text{As}$ $\lambda/4$ layer is a composite, and includes a 10 nm thick (p+)GaAs layer). The 8λ -thick AlGaInP optical cavity active region contains three 6 nm-thick ($x \sim 0.57$, $\epsilon \sim 0.65\%$) or 8 nm-thick ($x \sim 0.55$, $\epsilon \sim 0.49\%$) $\text{Ga}_{1-x}\text{In}_x\text{P}$ compressively strained quantum wells, separated by 6 nm-thick $(\text{Al}_{0.5}\text{Ga}_{0.5})_{0.5}\text{In}_{0.5}\text{P}$ barrier layers, in a step graded-barrier separate confinement heterostructure (SCH) (sample XD0623E has 4 quantum wells). Just prior to the VCSEL growth, an optical cavity active region calibration sample was grown without the DBRs. The peak room temperature photoluminescence emission wavelength was

~665 nm. Figure 5.14 shows the measured reflectance spectra for (a) sample XD0624B and (b) sample XD0701C, near wafer center.

Etched post Quick VCSEL test devices were fabricated as before, on strips cleaved from the 2 inch diameter wafers. The strips ran from one side of the wafer to the other, along the wafer centerline. Figure 5.15 is a plot of the threshold current versus lasing wavelength under pulsed excitation (100 ns pulses at a 1 μ s period) at room temperature (without heat sinking) for (a) samples XD0623E and XD0624B, and (b) samples XD0630C and XD0701C, for several devices positioned across the wafer strips. The devices had 10 μ m diameter optical apertures in a 20 μ m diameter mesa. The threshold current minima correlate well to the peak of the room temperature PL (~665 nm) measured on the active region calibration sample, allowing for a small red-shift due to heating. Additionally, the threshold minima correlate to lasing at the $n=1$ quantum well transition, in contrast to the results in Section 5.4. Lasing at wavelengths shorter than ~665 nm was achieved as before, with gain contributions from the $n=2$ quantum well state. Table 5.2 is a performance comparison of the hybrid visible VCSEL diodes.

In Fig. 5.15(a), the threshold current is higher for sample XD0623E (with four 8 nm thick quantum wells), as compared to sample XD0624B (with three 8 nm thick quantum wells). This is because the larger number of wells require a larger injected carrier density to reach threshold. In contrast, the threshold current is about equal for sample XD0630C (with three 8 nm thick quantum wells), as compared to sample XD0701C (with three 6 nm thick quantum wells), except at > 670 nm. In all samples, the long wavelength cut-off occurs at the edge of the wafer, so it was not possible to test for lasing at longer wavelengths. For this reason, a growth adjustment was made for the latter two samples (in Fig. 5.15(b)), such that the ~665 nm Fabry-Perot resonance occurred at wafer center.

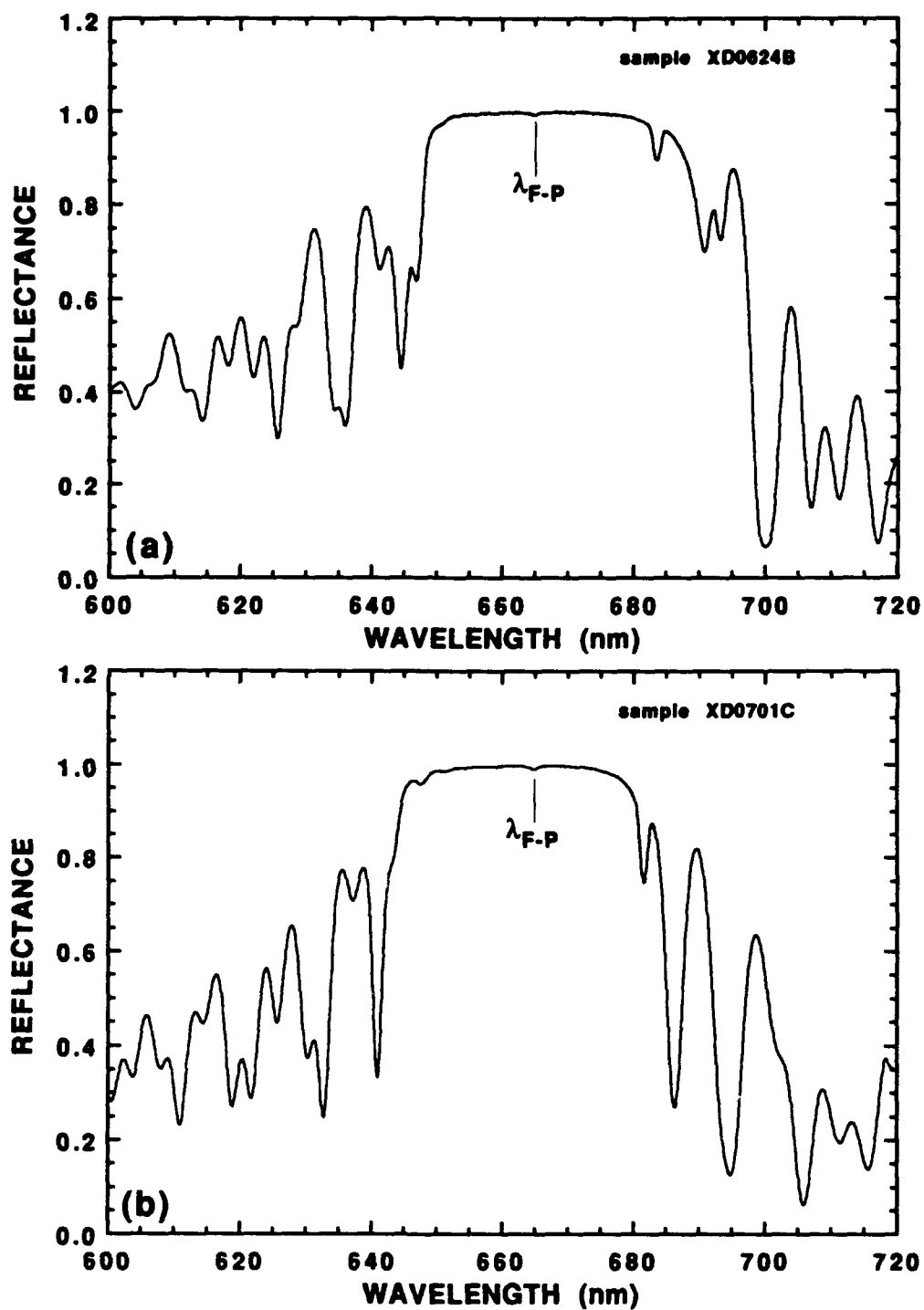


Fig. 5.14 Measured reflectance spectra near wafer center for (a) sample XD0624B, and (b) sample XD0701C.

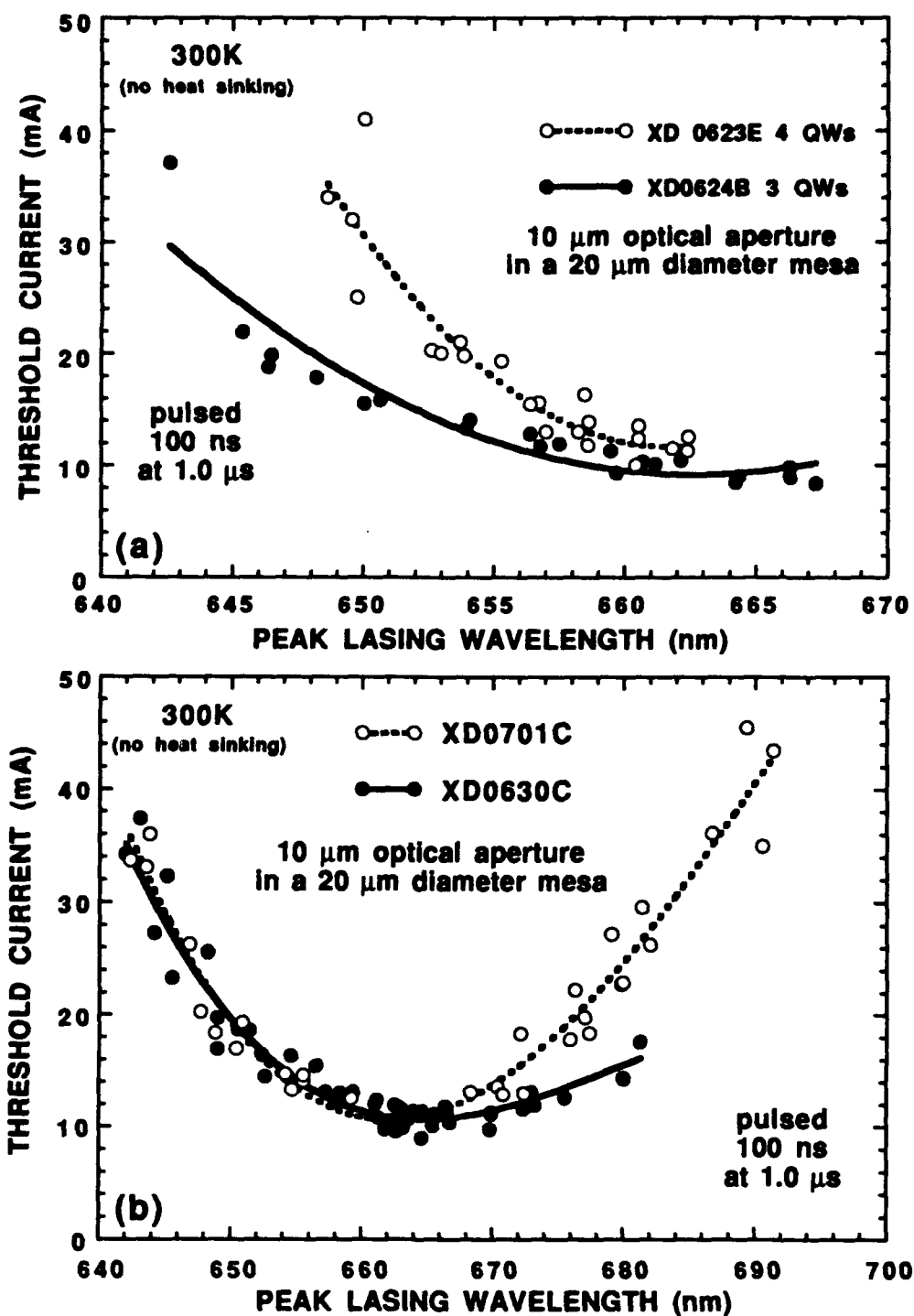


Fig. 5.15 Threshold current versus lasing wavelength for Quick visible VCSEL (a) samples XD0623E and XD0624B, and (b) samples XD0630C and XD0701C.

Table 5.2 Comparison of Hybrid Visible VCSEL Diodes

Sample Number	DBR top/bottom	Quantum Wells number/ thickness $\text{Ga}_{1-x}\text{In}_x\text{P}$	Pulsed Lasing Range low to high (nm)	Thickness of the Optical Cavity	I_{th} (mA) at \sim wavelength (nm)
Round Number 1:					
XD0222B	36/55.5	3/ 10 nm $x \sim 0.56$	639 to 661 ^{‡, ¶}	8 λ	30 647.3
XD0223A	36/55.5	2/ 10 nm $x \sim 0.56$	no lase	8 λ	∞ none
XD0310A [§]	36/55.5	3/ 10 nm $x \sim 0.56$	646.0 to 664.1 [¶]	10 λ	24 656.2
XD0310B [§]	36/55.5	3/ 10 nm $x \sim 0.56$	655.2 to 662.8 [¶]	4 λ	32 659.0
XD0310C [§]	36/55.5	3/ 10 nm $x \sim 0.56$	643.3 to 663.6 [¶]	8 λ	32 650.0
Round Number 2:					
XD0623E ¹	36/55.5	4/ 8 nm $x \sim 0.55$	648.6 to 662.4 [†]	8 λ	9.8 660.4 [†]
XD0624B ¹	36/55.5	3/ 8 nm $x \sim 0.55$	642.6 to 667.3 [†]	8 λ	9.7 665.3
XD0630C ^{1, 2}	36/55.5	3/ 8 nm $x \sim 0.55$	637.4 to 680.9 [†]	8 λ	9.0 664.6
XD0701C ^{1, 2}	36/55.5	3/ 6 nm $x \sim 0.57$	629.6 to 691.4 [†]	8 λ	10.7 662

Wafers are not rotated during MOVPE growth;

Devices are Quick visible VCSELs with a 10 μm diameter optical aperture in a 20 μm diameter mesa;

Structures grown on (100) (n+) GaAs substrates, misoriented 6° toward the nearest <111>A;

Room Temperature ($\sim 300\text{K}$) pulsed current excitation, 10 ns to 100 ns pulses at 100 ns to 1 μs period;

[‡]: Quick visible VCSELs with a 20 μm diameter optical aperture in a 30 μm diameter mesa;

[§]: grown on a (311)A (n+) GaAs substrate

[†]: long wavelength cut-off occurs at the edge of the wafer ;

[¶]: Lasing only with $n=2$ gain contributions;

¹: reduced p-doping in the DBRs (cut in half to $\sim 2 \times 10^{18} \text{ cm}^{-3}$) to reduce free carrier absorption;

²: \sim biparabolic graded DBRs

For the 10 μm aperture devices from wafer XD0701C, lasing is achieved at up to a 70% duty cycle (700 ns pulses at 1 μs) from ~ 660 to 670 nm. This decreases to a 10 % duty cycle at 642.3 nm due to heating effects. Lasing was achieved down to 629.6 nm by using 10 ns pulses at a period of 100 ns. As mentioned above, the long wavelength cut-off at 691.4 nm occurred at the edge of the wafer. For devices with 20 and 40 μm optical apertures emitting near 665 nm with pulsed excitation (100 ns at 1 μs), the maximum peak output power was 3 and 7 mW, respectively, while the maximum duty cycle was 50 and 40%, respectively.

The shape of the threshold current versus lasing wavelength curves in Fig. 5.15 can be qualitatively explained with the quantum well gain model in Appendix D (as is done in Section 3.6). Figure 5.16(a) shows the threshold current versus lasing wavelength results for Quick visible VCSELs (sample XD0701C) with 5 and 10 μm diameter optical apertures, in 15 and 20 μm diameter mesas, respectively. Superimposed on the plot is the calculated (normalized) gain spectrum for a 6 nm thick $\text{Ga}_{0.43}\text{In}_{0.57}\text{P}$ quantum well, surrounded by $(\text{Al}_{0.5}\text{Ga}_{0.5})_{0.5}\text{In}_{0.5}\text{P}$ barrier layers. Figure 5.16(b) shows the calculated gain spectra at different quantum well carrier densities. As the quantum well carrier density increases, the spectral gain rises and first reaches threshold at the $n=1$ gain peak near ~ 665 nm (a small red shift due to heating is expected). With further increases in current (and thus carrier density), the spectral gain increases and lasing is achieved at wavelengths on either side of ~ 665 nm. As a result, the threshold current versus lasing wavelength curve is roughly the inverse of the spectral gain curve, around the $n=1$ gain peak. The asymmetry in the curve is due to heating effects. As the carrier density increases with injection current, the device temperature increases. The increased temperature, along with exchange and correlation effects, decrease the energy bandgap of the quantum well(s). This causes a red shift in the spectral gain, along with a reduction in the gain (compared to the gain at the original temperature).

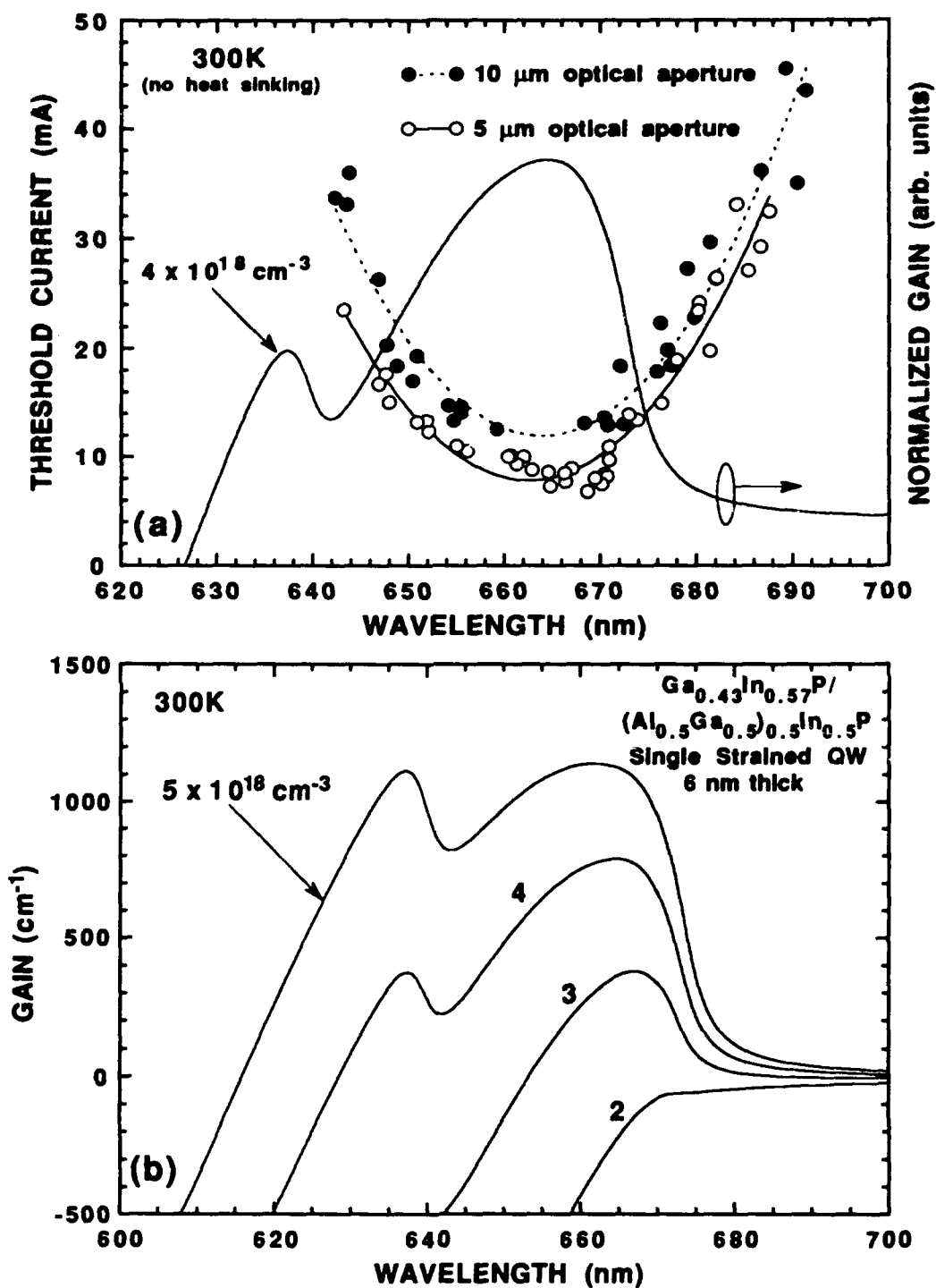


Fig. 5.16 (a) Threshold current versus lasing wavelength (or equivalently wafer position) for Quick visible VCSEL sample XD0701C, superimposed with a normalized calculated quantum well gain spectrum, and (b) calculated quantum well gain spectra.

5.5 Continuous Wave Operation

The Quick visible VCSELs in Section 5.4 were tested with CW current excitation. Figure 5.17 shows the room temperature (23 °C) CW output power and voltage against current curves (L-I-V) for a device with a 5 μm optical aperture centered in a 15 μm diameter mesa, emitting at 670.4 nm. The threshold current (I_{th}) is 5 mA ($J_{\text{th}} \approx 2.8 \text{ kA/cm}^2$) at a voltage (V_{th}) of 2.4 V. The resistance remains below 40 Ω past threshold. The L-I curve rolls over quickly at $< 2I_{\text{th}}$ due to heating effects. Lasing with CW excitation is obtained over the limited peak emission wavelength range of $670 \text{ nm} \pm 1 \text{ nm}$.

Larger optical aperture Quick visible VCSELs operate CW only at reduced temperatures. Figure 5.18 shows typical CW L-I-V curves for a device with a 40 μm optical aperture in a 50 μm diameter mesa. The peak output power is 3 mW at 100K ($I_{\text{th}} = 22 \text{ mA}$, $V_{\text{th}} = 3.7 \text{ V}$) and drops to $\sim 200 \mu\text{W}$ at 260 K ($I_{\text{th}} = 35 \text{ mA}$, $V_{\text{th}} = 2.7 \text{ V}$). For this device with peak emission at $\sim 661 \text{ nm}$, the lowest current threshold (18 mA, curve c) occurs at $\sim 200\text{K}$, suggesting that some refinement (shift of the Fabry-Perot resonance toward the spectral gain peak) for more efficient room temperature operation is possible. The CW power is $> 4 \text{ mW}$ for several devices emitting at longer wavelengths.

The second round of visible VCSELs, described in Section 5.4, were also fabricated into proton implanted structures, as outlined in Section 5.2. A double proton implant was used for lateral current confinement, with doses of 4 and $1 \times 10^{14} \text{ cm}^{-2}$, at energies of 410 and 370 keV, respectively. The top contact was rectangular ($\sim 75 \times 125 \mu\text{m}$), with optical apertures of 10, 15, 20, and 30 μm . The implant defined apertures were 10, 15, 20, and 30 μm , and thus several combinations of optical and implanted apertures were available.

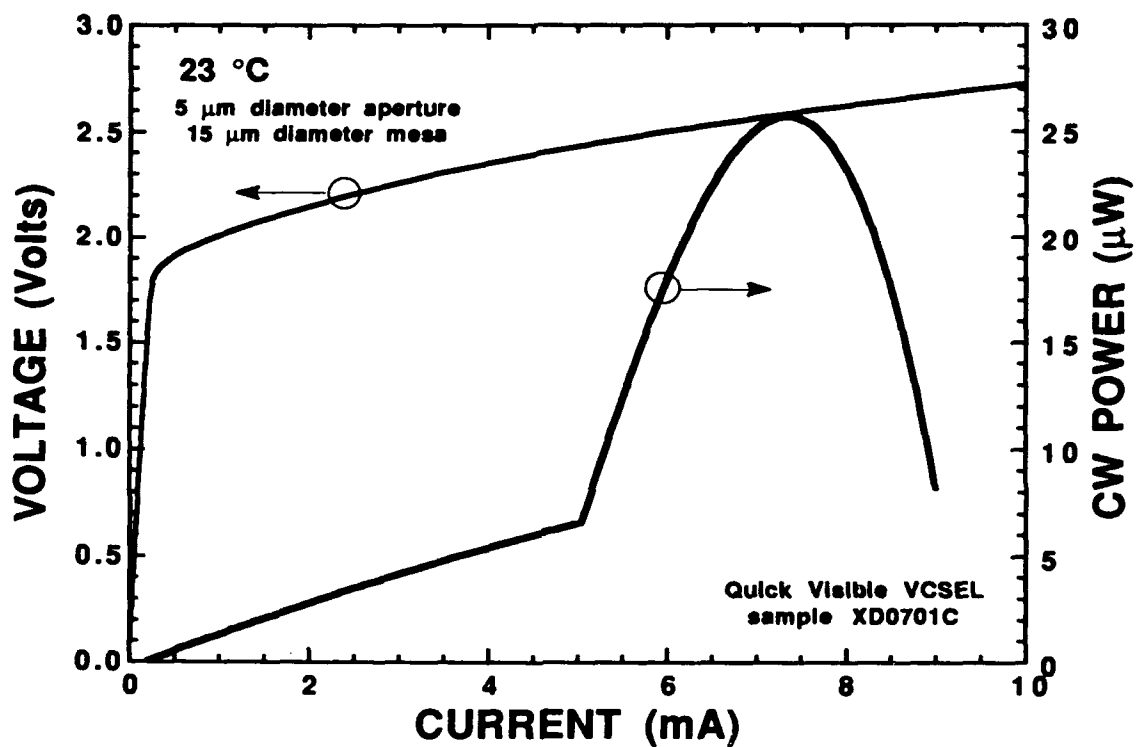


Fig. 5.17 Room temperature (23 °C) continuous wave L-I-V curves for a Quick visible VCSEL (wafer XD0701C). The lasing emission wavelength is $\lambda_0 = 670.4$ nm.

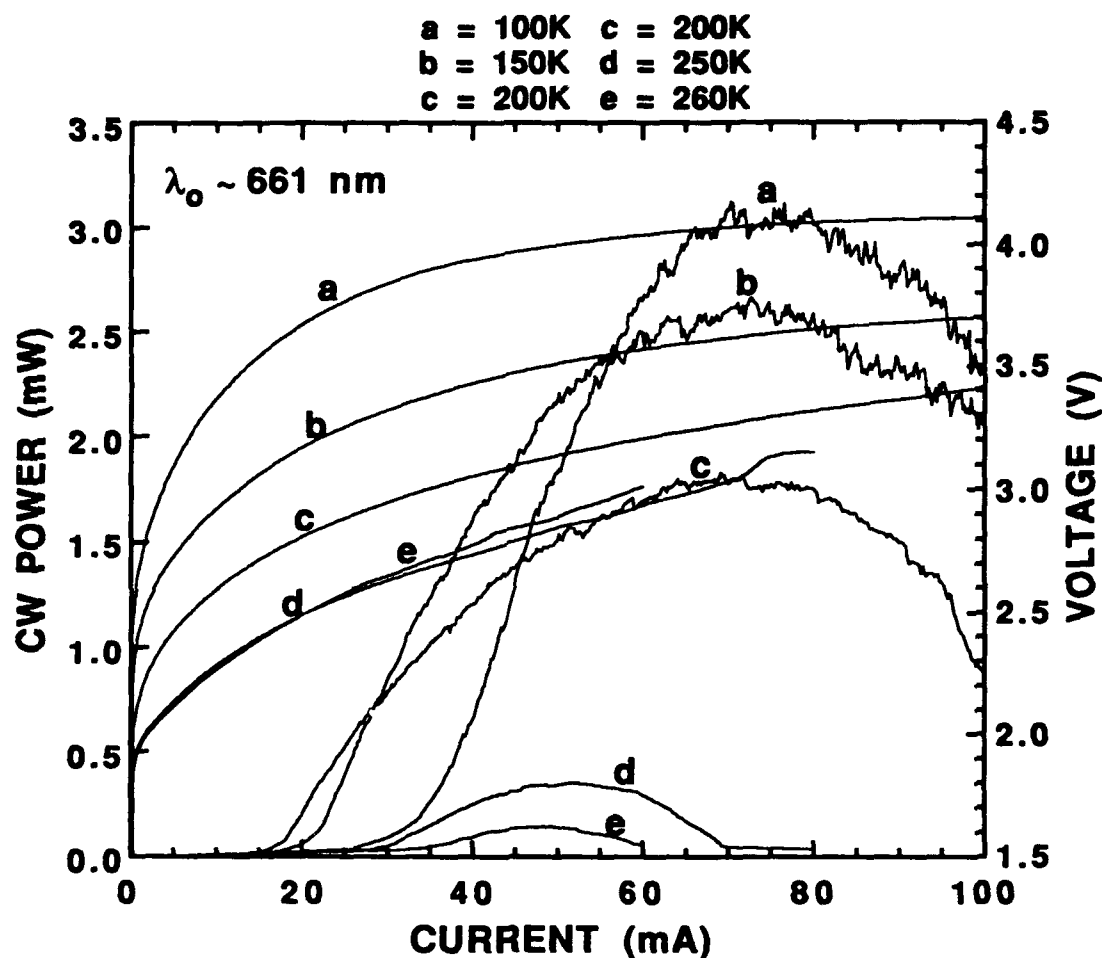


Fig. 5.18 Low temperature continuous wave L-I-V curves for a Quick visible VCSEL (wafer XD0701C). The optical aperture diameter is 40 μm , in a 50 μm diameter mesa. (Measurement courtesy of K. D. Choquette [1993]).

The L-I-V characteristics for implanted visible VCSELs with 10/10 μm and 15/20 μm optical aperture/implant aperture are shown in Fig. 5.19(a) and (b), for lasing at ~ 670 nm. The temperature is held at 20°C using a thermoelectric cooler. The 10 μm aperture device has a threshold current of 1.6 mA ($J_{\text{th}} \sim 2.0 \text{ kA/cm}^2$) at $V_{\text{th}} \sim 3\text{V}$, with a maximum output power of ~ 0.2 mW. The device resistance remains at $\sim 300 \Omega$ with $I > 2I_{\text{th}}$. The differential quantum efficiency $\eta = (1/h\nu)(\Delta P/\Delta I)$ is $\sim 5\%$ between 2 to 3 mA, and the peak power conversion efficiency is $\sim 3\%$ at 3 mA. On similar devices near $\lambda_0 \sim 670$ nm, the threshold current was as low as 1.25 mA ($J_{\text{th}} \sim 1.6 \text{ kA/cm}^2$), and as high as 2.2 mA ($J_{\text{th}} \sim 2.8 \text{ kA/cm}^2$). The 15 μm aperture device has a threshold current of 4.6 mA ($J_{\text{th}} \sim 1.5 \text{ kA/cm}^2$) at $V_{\text{th}} \sim 2.4\text{V}$, with a maximum output power of ~ 0.44 mW. The device resistance remains below $\sim 100 \Omega$ with $I > I_{\text{th}}$. The value of η is $\sim 4\%$ between 5 to 10 mA, and the peak power conversion efficiency is $\sim 3\%$ at 8 mA. A few similar devices with 20 μm apertures and 20 μm implant diameters (implanted at ~ 340 keV with $5 \times 10^{14} \text{ cm}^{-2}$) had maximum output powers of 0.45 to 0.55 mW.

Typical L-I-V characteristics for a visible VCSEL with 10/10 μm optical aperture/implant aperture as a function of temperature is shown in Fig. 5.20. Continuous wave lasing is achieved for heat sinking temperatures up to 45°C . This indicates that the heat dissipation in the implanted devices is far superior to that in the Quick VCSELs. The threshold current continuously decreases with decreasing temperature, indicating that the optimal overlap between the Fabry-Perot mode and the gain peak, for this particular device, occurs at reduced temperatures ($< 20^\circ\text{C}$). The kink in the L-I curves below 35°C represent changes in the transverse modes.

The CW threshold current versus lasing wavelength for sample XD0701C is shown in Fig. 5.21, for devices with 10 μm optical and implant apertures. The threshold current varies slowly with lasing wavelength as compared to the data in Fig. 5.16, with a minimum threshold (1.9 mA) at ~ 670 nm, and abrupt cut-offs at 656.6 and 684.9 nm. The

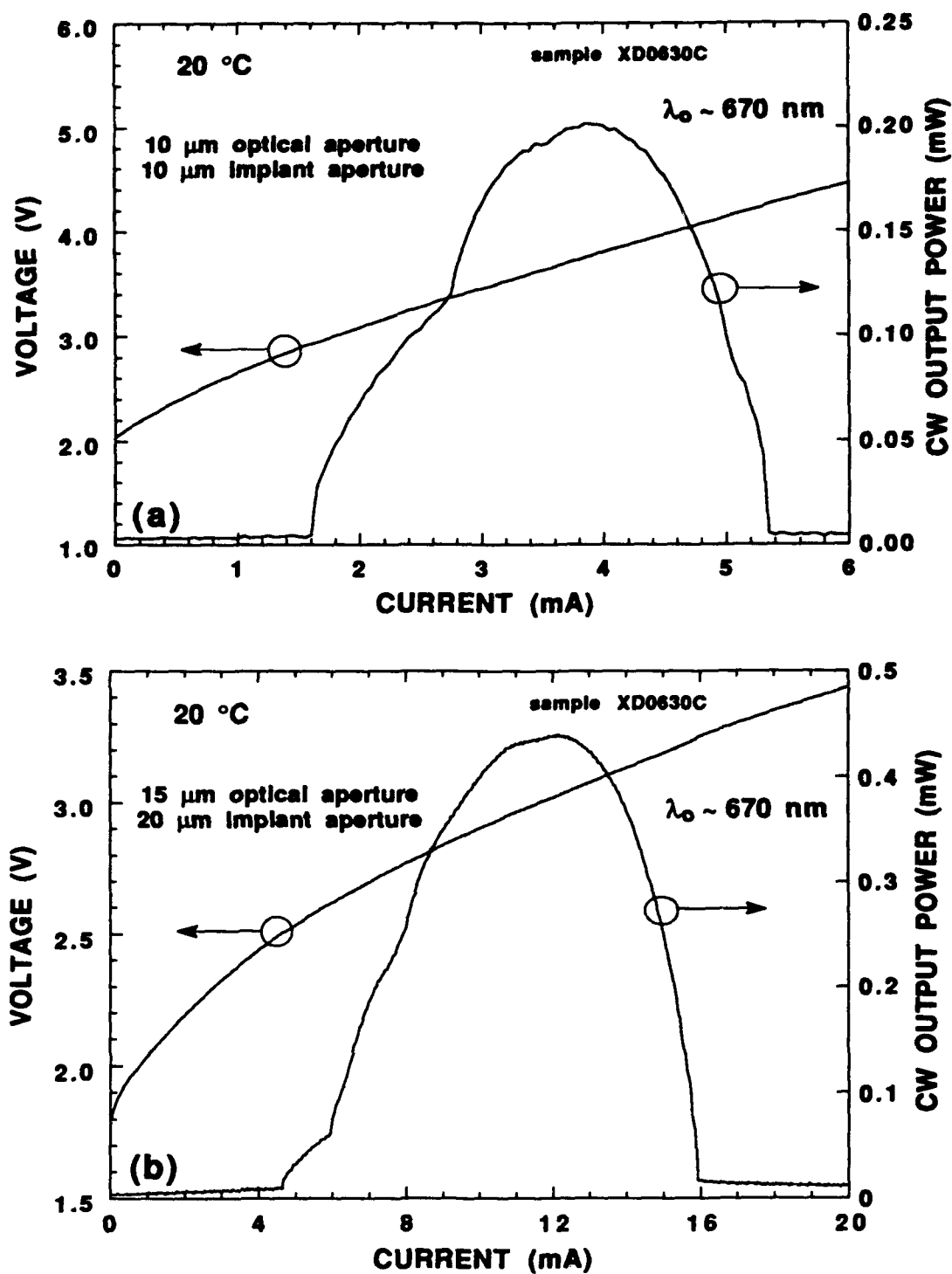


Fig. 5.19 L-I-V characteristic at 20°C for ion implanted visible VCSELs with (a) a 10 μm optical aperture and a 10 μm implant aperture, and (b) a 15 μm optical aperture and a 20 μm implant aperture.

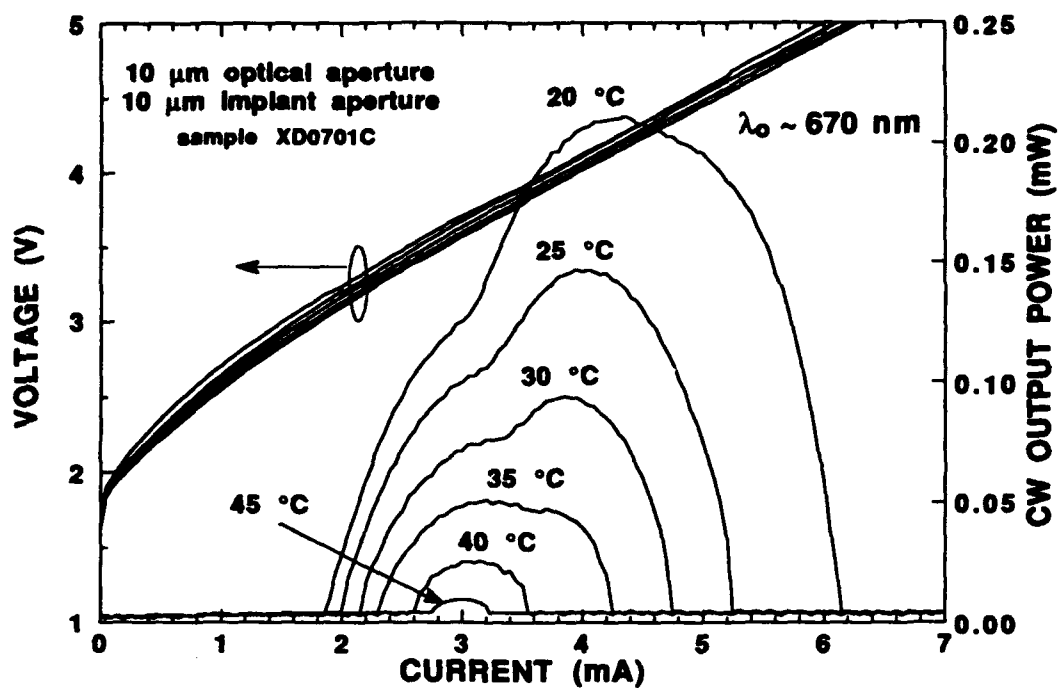


Fig. 5.20 L-I-V characteristics for an ion implanted visible VCSEL with a 10 μm optical aperture and a 10 μm implant aperture as a function of heatsink temperature from 20 to 45 °C.

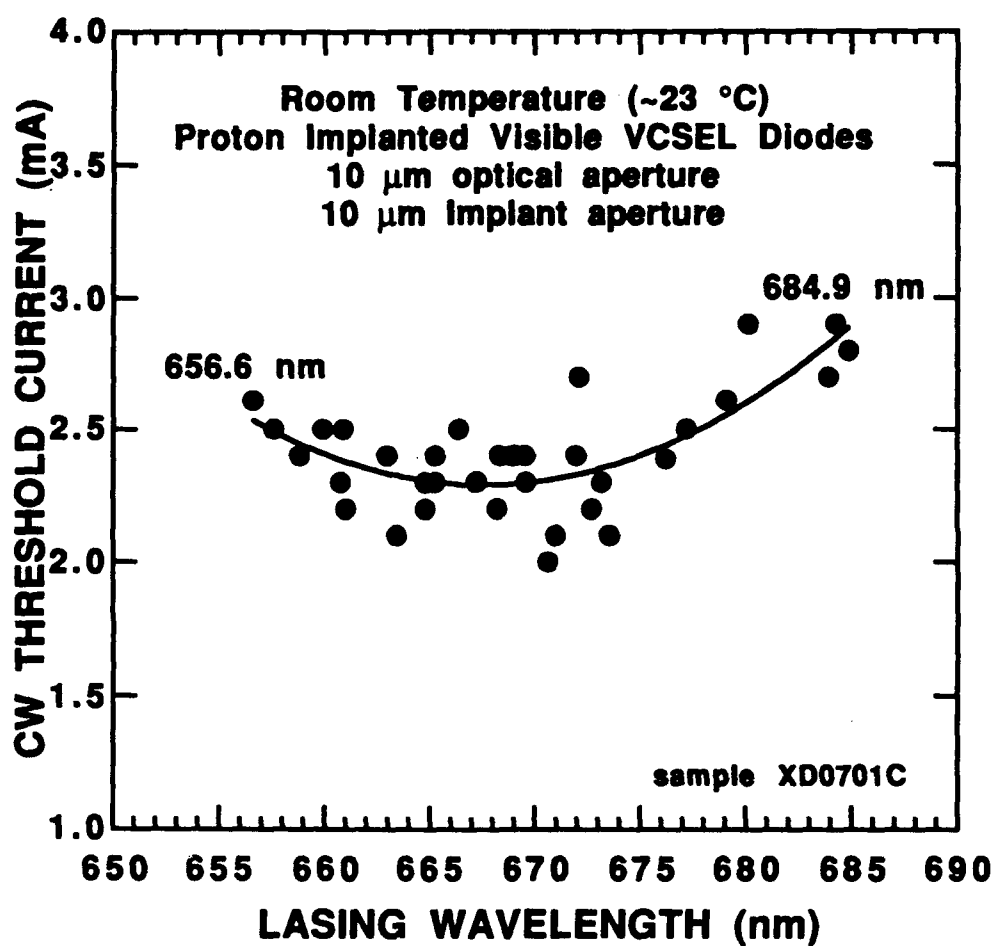


Fig. 5.21 Continuous wave threshold current versus lasing wavelength (or equivalently wafer position) for ion implanted visible VCSELs across sample XD0701C.

shallower curve indicates that the temperature of the implanted visible VCSEL is not as variable as is the temperature of the Quick visible VCSEL. Also, a larger fraction of the injected current goes toward radiative recombination, thus increasing the differential gain and overall efficiency.

5.6 Conclusions

This Chapter presented the fabrication, characterization, and analysis of the first electrically injected visible VCSELs with a strained quantum well AlGaInP optical cavity active region surrounded by AlGaAs DBRs. The Quick VCSEL fabrication process was developed and proven useful for the rapid (≤ 1 day) evaluation of VCSEL epitaxial material. As demonstrated with the second round devices, the performance of ion implanted visible VCSELs is far superior to that of Quick visible VCSELs (e.g. the threshold current dropped from ~ 10 mA to ~ 2 mA, and the maximum output power increased from ~ 25 μ W to ~ 200 μ W, for \sim equivalent size devices). This is due largely to improved thermal management (i.e. lower currents generate less heat, and the heat is more effectively dissipated in the implanted device geometry as compared to the etched air-post geometry).

Also proven very useful for the evaluation of VCSEL wafers, and for studies of VCSEL device physics, was MOVPE growth without rotation. For the commercial production of two-dimensional arrays, however, the rotation would most likely be employed to yield thickness variations of about $\pm 1\%$ or less (i.e. uniform lasing emission across the wafer), unless a specific application required a range of emission wavelengths from a group of closely spaced devices. Note from Fig. 2.18 that a 1% thickness variation roughly corresponds to a 5 nm range of emission wavelengths.

The first round of visible VCSEL diodes were shown to operate with significant gain contributions from the $n=2$ quantum well state, with emission wavelengths shifted

by ~20 nm from what would be expected from "n=1 lasing". While this is a novel approach for shorter wavelength operation in visible quantum well lasers, a high price is paid. The threshold current is 3 or more times higher (since the wells must be filled to higher carrier densities). The increased current density increases the device temperature which increases carrier leakage from the quantum wells, and in-turn decreases efficiency. Lasing with n=2 gain contributions was found in both optically and electrically pumped/injected visible VCSELs and, based on the measured characteristics, was attributed to unoptimized utilization of the available gain (i.e. poor overlap between the quantum well active region and the central standing wave). Except for specialized short wavelength or two mode switching applications (yet to be proven viable), it is unlikely that commercial devices would benefit from "n=2 lasing".

With some design "tweaking": 1) to reduce the cavity losses (by reducing the p-doping in the DBRs and near the optical cavity), 2) to improve the utilization of the available gain (by reducing the thickness of the quantum wells, and/or the barrier layers to improve the overlap between the wells and the standing wave peak), and 3) to keep the series resistance low (by grading the DBR interfaces), the second round devices were shown to operate with gain contributions primarily from the n=1 quantum well state. (The effect on device performance due to each of the changes cited above deserves further study). For the first time, efficient CW room temperature operation was demonstrated with ion implanted versions of these devices (i.e. thresholds below 2 mA with maximum output powers ≥ 0.2 mW). This last result has proven that the technology is viable, and has opened the door for large scale development. Much improved device performance is expected over the next few years (i.e. submilliamp thresholds, maximum powers ≥ 5 mW, demonstration of high density arrays, CW lasing at $\lambda_0 \sim 633$ nm, etc.).

Though the developmental path was arduous, red VCSELs have indeed emerged from the laboratory, progressing from optically pumped structures in the Fall of 1991, to efficient diodes that operate CW at room temperature by the Summer of 1993.

References for Chapter 5

Babic, D. I., and S. W. Corzine, "Analytic Expressions for the Reflection Delay, Penetration Depth, and Absorptance of Quarter-Wave Dielectric Mirrors", *IEEE Journal of Quantum Electronics*, 28(2), p. 514-524 (February 1992).

Bour, D. P., D. W. Treat, R. L. Thornton, T. L. Paoli, R. D. Bringans, B. S. Krusor, R. S. Geels, D. F. Welch, and T. Y. Wang, "Low Threshold $\text{Ga}_x\text{In}_{1-x}\text{P}/(\text{Al}_y\text{Ga}_{1-y})_{0.5}\text{In}_{0.5}\text{P}$ Strained Quantum Well Lasers", *Journal of Crystal Growth*, 124, p. 751-756 (1992a).

Bour, D. P., D. W. Treat, R. L. Thornton, R. D. Bringans, T. L. Paoli, R. S. Geels, and D. F. Welch, "Characteristics of Short-Wavelength ($617 < \lambda < 640$ nm) $\text{Ga}_{0.4}\text{In}_{0.6}\text{P}/(\text{Al}_y\text{Ga}_{1-y})_{0.5}\text{In}_{0.5}\text{P}$ Strained, Thin Multiple-Quantum-Well Lasers", *IEEE Photonics Technology Letters*, 4(10), p. 1081-1083 (October 1992b).

Bour, D. P., D. W. Treat, R. L. Thornton, R. S. Geels, and D. F. Welch, "Drift Leakage Current in AlGaInP Quantum-Well Lasers", *IEEE Journal of Quantum Electronics*, 29(5), p. 1337-1343 (May 1993).

Brueck, S. R. J., ed., Special Issue on Semiconductor Lasers, *IEEE Journal of Quantum Electronics*, 27(6), pp. 1332-1425 (1991).

Choquette, K. D., Postdoctoral Member of Technical Staff, Sandia National Laboratories, Albuquerque, NM, unpublished (1993).

Geels, R. S., S. W. Corzine, and L. A. Coldren, "InGaAs Vertical-Cavity Surface-Emitting Lasers", *IEEE Journal of Quantum Electronics*, 27(6), p. 1359-1367 (June 1991).

Hasnain, G., K. Tai, L. Yang, Y. H. Wang, R. J. Fischer, J. D. Wynn, B. Weir, N. K. Dutta, and A. Y. Cho, "Performance of Gain-Guided Surface Emitting Lasers with Semiconductor Distributed Bragg Reflectors", *IEEE Journal of Quantum Electronics*, 27(6), p. 1377-1385 (June 1991).

Hecht, J., "Semiconductor Diode Lasers Span the Rainbow", *Laser Focus World*, p. 199-211 (April 1993).

Holonyak, Jr., N., R. M. Kolbas, R. D. Dupuis, and P. D. Dapkus, "Quantum-Well Heterostructure Lasers", *IEEE Journal of Quantum Electronics*, 16(2), p. 170-186 (1980).

Huang, K. F., K. Tai, K., C. C. Wu, and J. D. Wynn, "Continuous Wave Visible InGaP/InGaAlP Quantum Well Surface Emitting Laser Diodes", *Digest of the Device Research Conference, Santa Barbara, CA, Post Deadline Paper IIIB-7* (21-23 June 1993).

Iga, K., F. Koyama, and S. Kinoshita, "Surface Emitting Semiconductor Lasers", *IEEE Journal of Quantum Electronics* 24(9), p. 1845-1855 (September 1988).

Koyama, F., S. Kinoshita, and K. Iga, "Room-Temperature Continuous Wave Lasing Characteristics of a GaAs Vertical Cavity Surface-Emitting Laser", *Applied Physics Letters*, 55(3), p. 221-222 (17 July 1989).

Lear, K. L., and S. A. Chalmers, "High Single-Mode Power Conversion Efficiency Vertical-Cavity Top-Surface-Emitting Lasers", IEEE Photonics Technology Letters, (to be published September 1993)

Lee, Y. H., J. L. Jewell, A. Scherer, S. L. McCall, J. P. Harbison, L. T. Florez, "Room-Temperature Continuous-Wave Vertical-Cavity Single-Quantum-Well Microlasers", Electronics Letters, 25(20), p. 1377-1378 (28 September 1989).

Lee, Y. H., B. Tell, K. Brown-Goebeler, J. L. Jewell, and J. V. Hove, "Top Surface-Emitting GaAs Four Quantum-Well Lasers Emitting at 0.85 μm ", Electronics Letters, 26(11), p. 710-711 (24 May 1990).

Lee, Y. H., B. Tell, K. F. Brown-Goebeler, R. E. Leibenguth, and V. D. Matterna, "Deep-Red Continuous Wave Top-Surface-Emitting Vertical-Cavity AlGaAs Superlattice Lasers", IEEE Photonics Technology Letters, 3(2), p. 108-109 (1991).

Lott, J. A., and R. P. Schneider, Jr., "Red (639-661 nm) InAlGaP/AlGaAs Vertical Cavity Surface Emitting Laser Diodes", Digest of the Quantum Optoelectronics Topical Meeting (3rd Biennial Meeting, sponsored by the Optical Society of America), Palm Springs, CA, Post Deadline Paper PD1 (17-19 March 1993a).

Lott, J. A., R. P. Schneider, Jr., and K. J. Malloy, "Electrically Injected AlGaInP Visible Vertical Cavity Surface Emitting Lasers Operating at the $n=2$ Quantum Well Transition", Digest of the 1993 Conference on Lasers and Electro-Optics (CLEO'93), Baltimore, MD, Post Deadline Paper CPD3 (2-7 May 1993b).

Lott, J. A., and R. P. Schneider, Jr., "Electrically Injected Visible (639-661 nm) Vertical Cavity Surface Emitting Lasers", Electronics Letters, 29(10), pp. 830-832 (13 May 1993c)

Lott, J. A., R. P. Schneider, Jr., K. D. Choquette, S. P. Kilcoyne, J. J. Figiel, and K. J. Malloy "Room Temperature Continuous Wave Operation of Red Vertical Cavity Surface Emitting Laser Diodes", Electronics Letters, (to be published September 1993d).

Mittelstein, M., Y. Arakawa, A. Larsson, and A. Yariv, "Second Quantized State Lasing of a Current Pumped Single Quantum Well Laser", Applied Physics Letters, 49(25), p. 1689-1691 (1986).

Orenstein, M., A. C. Von Lehmen, C. Chang-Hasnain, N. G. Stoffel, J. P. Harbison, L. T. Florez, E. Clausen, and J. L. Jewell, "Vertical-Cavity Surface-Emitting InGaAs/GaAs Lasers with Planar Lateral Definition", Applied Physics Letters 56(24), p. 2384-2386 (11 June 1990).

Saleh, B. E. A., and M. C. Teich, *Fundamentals of Photonics*, (Wiley:New York, 1991).

Schneider, Jr., R. P., R. P. Bryan, J. A. Lott, E. D. Jones, and G. R. Olbright, "MOVPE Growth of InAlGaP-Based Visible Vertical-Cavity Surface-Emitting Lasers," Journal of Crystal Growth, 124, p. 763-771 (1992a).

Schneider, Jr., R. P., E. D. Jones, J. A. Lott, and R. P. Bryan, "Photoluminescence Linewidths in Metalorganic Vapor Phase Epitaxially Grown Ordered and Disordered InAlGaP Alloys", *Journal of Applied Physics*, 72(11), p. 5397-5400 (1 December 1992b).

Schneider, Jr., R. P., and J. A. Lott, "Cavity Design For Improved Electrical Injection in InAlGaP/AlGaAs Visible (639-661 nm) Vertical Cavity Surface-Emitting Laser Diodes", *Applied Physics Letters*, 63(7), p. 917-919 (16 August 1993a).

Schneider, Jr., R. P., J. A. Lott, K. L. Lear, M. Ludowise, and A. A. Anyname, "Mg Doping in AlGaInP/AlGaAs Visible Edge- and Surface-Emitting Laser Diodes", *Digest of the Materials Research Society Fall Meeting, Boston, MA* (November/December 1993b).

Schneider, Jr., R. P., J. A. Lott, and K. L. Lear, unpublished (1993c).

Soda, H., K. Iga, C. Kitahara, and Y. Suematsu, "GaInP/InP Surface Emitting Injection Lasers", *Japanese Journal of Applied Physics*, 18(12), p. 2329-2330 (1979).

Tell, B., R. E. Leibenguth, K. F. Brown-Goebeler, and G. Livescu, "Short Wavelength (699 nm) Electrically Pumped Vertical-Cavity Surface-Emitting Lasers", *IEEE Photonics Technology Letters*, 4(11), p. 1195-1196 (November 1992).

Tell, B., K. F. Brown-Goebeler, and R. E. Leibenguth, "Low Temperature Continuous Operation of Vertical-Cavity Surface-Emitting Lasers with Wavelength Below 700 nm", *IEEE Photonics Technology Letters*, 5(6), p. 637-639 (June 1993).

Zolper, J. C., R. P. Schneider, Jr., and J. A. Lott, "Formation of High Resistivity Regions in p-Type $\text{Al}_{0.5}\text{In}_{0.5}\text{P}$ by Ion Implantation", *Applied Physics Letters* (to be published December 1993).

Zory, Jr., P. S., ed., *Quantum Well Lasers*, (Academic, New York, 1993).

Chapter 6 Conclusions

"One moment there had been nothing but darkness; next moment a thousand points of light leaped out- . . . " †

6.1 Summary

This dissertation explored the design, fabrication, and characterization of visible ("red") vertical cavity surface emitting lasers (VCSELs). In Chapter 2, the general design principles for VCSELs and related resonant cavity structures were reviewed, with particular emphasis on materials and structures for visible VCSELs. The range of possible emission wavelengths from AlGaInP strained quantum well, optical cavity active regions was investigated theoretically and supported by experimental results. It was found that uncoupled quantum wells with thicknesses of ~3 to 10 nm and compressive strains of 0 to 0.6% could access the wavelength range of 620 to 690 nm. Further supporting data on AlGaInP and AlGaAs materials (lattice-matched to GaAs) for photonics applications, such as the subtle affects of ordering, were presented in Appendix A. Chapter 2 included a detailed discussion of distributed Bragg reflectors (DBRs) and Fabry-Perot etalons for visible photonic applications. Both measured and calculated DBR data was presented. Finally, a comparison of conventional GaInAs infrared (IR) VCSELs with the new AlGaInP visible VCSELs was accomplished. It was concluded that visible VCSELs would have lower differential gain and efficiency, and be more sensitive to heating effects. Also, that AlGaAs DBRs, rather than AlGaInP DBRs, would be the better design choice for visible VCSELs emitting at $\lambda_0 \geq 630$ nm.

† C. S. Lewis, *The Magician's Nephew* (1955).

The initial studies on optically pumped visible VCSEL structures concentrated on the emission range of 650 to 660 nm. For the development of visible VCSEL diodes, however, attention shifted to the longer wavelength range of 670 to 680 nm, where it is well known that threshold currents are lowest for AlGaInP edge-emitting lasers due largely to quantum well confinement (leakage) issues. Chapter 3 presented data on undoped, optically pumped visible VCSELs with both AlGaAs and AlGaInP DBRs. The structures were grown by metalorganic vapor phase epitaxy (MOVPE) on GaAs substrates, as described in Appendix B. The quantum well active regions were designed for emission near ~675 nm by employing 10 nm thick $\text{Ga}_{0.44}\text{In}_{0.56}\text{P}$ quantum wells, surrounded by 10 nm thick $(\text{Al}_{0.4}\text{Ga}_{0.6})_{0.5}\text{In}_{0.5}\text{P}$ barrier layers. Optically pumped lasing (using conservative designs with about four 9's (i.e. $R_b \geq 0.9999$) for the reflectance of the bottom DBR, and about three 9's (i.e. $R_t \geq 0.999$) for the reflectance of the top output coupling DBR) was only achieved with significant gain contributions from the $n=2$ quantum well state. In contrast, the previous optically pumped lasing results were achieved with primarily $n=1$ gain contributions for structures with thinner wells and barriers (i.e. 6 nm thick wells and 7 nm thick barriers).

In order to cover both the possibility of " $n=2$ and/or $n=1$ lasing", the important research technique of not rotating the wafers during MOVPE growth was employed. This also allowed an investigation of the effects of relative mismatches between the Fabry-Perot mode and the $n=1$ and $n=2$ quantum well gain peaks. The $n=2$ optically pumped lasing results were attributed to inefficient utilization of the quantum well gain, due most likely to the thick (10 nm) quantum well separation layers (and to a lesser extent due to the 10 nm thick quantum well layers). The thick barrier layers reduced the overlap of the quantum wells with the high intensity portion of the standing wave, resulting in less efficient gain. The calculations of the standing wave on resonance were performed with a

novel numerical model, based on the conventional matrix method, as outlined in Appendix C.

The design and spectral characteristics of resonant cavity light emitting diodes (RCLEDs) were presented in Chapter 4, including the first visible RCLEDs. These devices served as an important bridge between the undoped optically pumped visible VCSELs and the electrically injected visible VCSELs. The RCLEDs were useful as optical calibration structures for the subsequent MOVPE growth of VCSELs, and for the determination of optical cavity doping parameters to achieve efficient electroluminescence. (Also note that RCLEDs could serve as "test beds" for the investigation of microcavity physics, and, they are viable for a very large, commercial visible (~560 to 690 nm) LED market). A Classical Wave Interference Model was developed, and shown to provide a good, semi-quantitative estimate of the expected emission spectrum from an arbitrary RCLED structure. The spectral characteristics at several points across unrotated wafers showed clearly the enhanced spectral intensity for on-resonance wavelengths. The narrowed linewidth of the emission spectra (compared to the natural emission without the resonant cavity) was correlated to the design of the given RCLED, such as to the number of top coupling DBR pairs.

The studies of electrically injected visible VCSELs were presented in Chapter 5. These studies concentrated on the use of AlGaAs DBRs because of the compatibility with existing fabrication schemes, and because of other advantages over AlGaInP DBRs such as a reduced number of periods, ease of p-doping, potentially reduced absorptive losses, ability to be isolated with proton implantation, and reduced thermal resistivity. A Quick VCSEL fabrication process was developed for the rapid characterization of visible VCSEL material. As before, the wafers were not rotated during MOVPE growth to maximize the range of possible emission wavelengths. The first round of prototype Quick visible VCSELs operated with pulsed current excitation at room temperature over the

range of 639.1 to 660.9 nm, with a maximum output power of 3.38 mW at 650 nm with $J_{th} \sim 4.2 \text{ kA/cm}^2$ ($I_{th} = 30 \text{ mA}$) and $V_{th} \sim 2.7 \text{ V}$. Due to absorptive cavity losses and the unoptimized gain layer design (as identified by the optical pumping experiments), lasing could only be achieved with significant gain contributions from the $n=2$ quantum well state. This was the first demonstration of " $n=2$ " lasing in VCSEL diodes of any wavelength.

The subsequent second round of Quick visible VCSEL diodes included several design improvements such as reduced p-doping in the DBRs (decreasing absorptive losses), graded DBR interfaces (reducing series resistance), and reduced thickness of the quantum well and barrier layers in the active region (increasing the gain efficiency). These devices were shown to operate pulsed at room temperature over the very broad range of 629.6 to 691.4 nm, with gain contributions primarily from the $n=1$ quantum well state, and with threshold currents $\sim 1/3$ of those for the first round of Quick VCSELs. The gain characteristics, such as the dependence of emission wavelength on threshold current, were qualitatively analyzed by employing the standard quantum well gain models described in Appendix D. The second round of visible VCSEL material was also fabricated into conventional top emitting, ion implanted devices. These devices operated continuous wave (CW) at room temperature over the range 656.6 to 684.9 nm, with threshold currents of $\sim 2 \text{ mA}$ ($J_{th} \sim 2 \text{ kA/cm}^2$), threshold voltages of $V_{th} \sim 2$ to 3 V , and differential quantum efficiencies of $\sim 5\%$. The output powers ranged from $\sim 0.2 \text{ mW}$ for devices with $10 \text{ }\mu\text{m}$ diameter apertures, to over $\sim 0.5 \text{ mW}$ for devices with $20 \text{ }\mu\text{m}$ diameter apertures.

6.2 Suggestions for Future Work

This work has proven that AlGaInP visible VCSELs are practical devices, with tremendous potential. Indeed, the device performance reported in this dissertation

approaches that of conventional GaAs IR VCSELs circa 1988. Continued "pushing of the envelope" toward lower thresholds, higher powers, and shorter wavelengths, is a logical extension of this work. The following is a brief list of suggestions for future work on the visible VCSEL, motivated by interesting device physics, manufacturing issues, and by emerging technological applications. In addition to the suggestions, continued advances in the epitaxial growth of AlGaInP are essential (i.e. improved doping and compositional control, development of regrowth techniques), as are advances in the manufacturing technology (i.e. dry etching of AlGaInP).

Specific suggestions are as follows:

- 1) Fabricate and characterize 1D and 2D arrays. Investigate the wavelength variation of devices fabricated from wafers that are rotated during growth.
- 2) Develop a standard red ($\lambda_0 \approx 660$ to 690 nm) VCSEL technology. Further investigate the structured cavity mode to gain misalignment for maximum output power (also reduce the number of DBRs), or for minimum threshold current. Investigate and model heating effects, and methods to stabilize device operation. Investigate the polarization and modal characteristics of the lasing emission.
- 3) Investigate shorter wavelength operation (≤ 650 nm). Develop devices for efficient emission at $\lambda_0 \approx 632.8$ nm to replace HeNe lasers in barcode scanning or other applications.
- 4) Develop VCSELs for operation at $\lambda_0 \approx 650$ nm for use in plastic fiber communication systems. Develop RCLEDs for efficient emission at 650 nm and 575 nm.

- 5) Developed and characterize an all-AlGaInP visible VCSEL diode for comparison to the hybrid AlGaInP/AlGaAs visible VCSEL diode.
- 6) Decrease the thickness of the optical cavity active region to 1 or 2λ . Explore other means of reducing cavity losses such as pulse doping at the standing wave nodes.
- 7) Investigate the role of the AlGaInP-AlGaAs heterointerfaces on the performance of hybrid visible VCSELs. Investigate hybrid AlGaInP/AlGaAs DBR schemes. (For example, surround the optical cavity with a few AlGaInP DBRs, then switch to AlGaAs, or, explore a (p)DBR composed of C-doped AlAs and Mg or Zn-doped $(\text{Al}_y\text{Ga}_{1-y})_{0.5}\text{In}_{0.5}\text{P}$ $y \sim 0.2$ $\lambda/4$ layers for minimal valence band offset and improved doping control).
- 8) Explore novel device geometries, such as those that employ dielectric top DBR stacks, those that place the p-doped DBR on the bottom next to the substrate, or those that employ hybrid wafer fusion techniques.
- 9) Explore optoelectronic integrated circuits that combine red VCSELs with other devices such as heterojunction transistors and detectors. Demonstrate smart red pixels.
- 10) Continue the investigations of the optimal thicknesses of the quantum well and barrier layers, optimization of quantum well gain, and the overlap of the standing wave with the gain layers.

Appendix A Material Parameters

This Appendix reviews some selected material parameters of AlGaInP and AlGaAs relevant to the design of visible photonic devices. Some specific data on bulk and quantum well AlGaInP material grown at Sandia National Laboratories by metalorganic vapor phase epitaxy (MOVPE) is also presented.

A.1 Energy Bandgap and Lattice Constant

Plots of energy bandgap (lowest energy transition) and photon wavelength against lattice constant are given in Fig. A.1(a) and (b). The photon wavelength (λ) is calculated from $\lambda(\mu\text{m}) = 1.2398/E_g$ (eV). The data correspond to the equations in Table A.1.

A.2 Refractive Indices

This section reviews the refractive indices for $(\text{Al}_y\text{Ga}_{1-y})_{0.5}\text{In}_{0.5}\text{P}$ ($0.0 \leq y \leq 1.0$) and $\text{Al}_x\text{Ga}_{1-x}\text{As}$ ($0.0 \leq x \leq 1.0$) over the approximate energy range 1.0 to 2.3 eV, corresponding to the photon wavelength range 1239.8 to 539.0 nm. This data is used in the matrix calculations described in Appendix C. The complex refractive index (N) is given as $N = n - i\kappa$, where n is the real part and κ , the extinction coefficient, represents the imaginary part. The absorption coefficient α is related to κ by

$$\alpha = 4\pi\kappa/\lambda_0 \quad (\text{cm}^{-1}) \quad (\text{A.1})$$

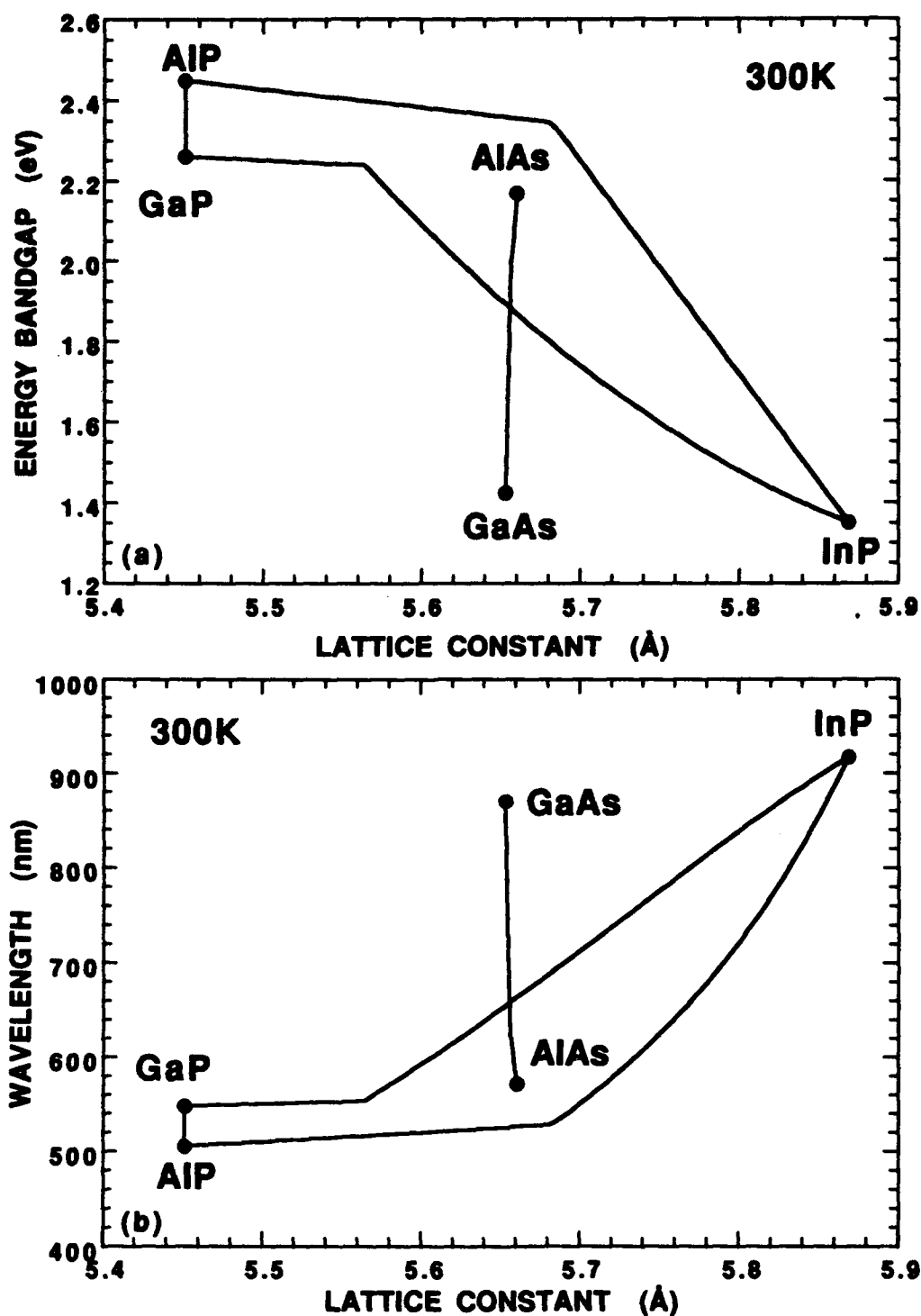


Fig. A.1 (a) Bandgap energy and (b) photon wavelength, both versus lattice constant for AlGaAs and AlGaInP III-V compound semiconductors.

Table A.1 Equations for Energy Bandgap and Lattice Constant

material	Equation	composition at direct indirect crossover
$\text{Al}_x\text{Ga}_{1-x}\text{As}$:	$E_g^\Gamma = 1.424 + 1.087x + 0.438x^2$ $E_g^X = 1.905 + 0.10x + 0.16x^2$ $a_0 = 5.6605x + 5.6533(1-x)$	$x_{\Gamma-X} \approx 0.43$
$\text{Ga}_{1-x}\text{In}_x\text{P}$:	$E_g^\Gamma = 2.78 - 2.215x + 0.786x^2$ $E_g^X = 2.26 - 0.0815x$ $a_0 = 5.8688x + 5.4512(1-x)$	$(1-x)_{\Gamma-X} \approx 0.27$
$\text{Al}_x\text{Ga}_{1-x}\text{P}$:	$E_g^X = 2.43x + 2.26(1-x)$ $a_0 = 5.451x + 5.4512(1-x)$	no crossover
$\text{Al}_x\text{In}_{1-x}\text{P}$:	$E_g^\Gamma = 1.351 + 2.23x$ $E_g^X = 2.43x + 2.26(1-x)$ $a_0 = 5.451x + 5.8688(1-x)$	$0.0 \leq x \leq 0.44$ $0.44 \leq x < 1.0$
$(\text{Al}_y\text{Ga}_{1-y})_{0.5}\text{In}_{0.5}\text{P}$	$E_g^\Gamma = 1.91 + 0.61y$	$x_{\Gamma-X} \approx 0.7$
(lattice matched at ~700 °C to GaAs)	$E_g^X = 2.25 + 0.1y$ $a_0 = 5.6533$	

where λ_0 is the free space wavelength. Note that $\kappa = 0$ near and below bandgap, except in cases of high doping. A plot of the real refractive index dispersion of unintentionally doped $(\text{Al}_y\text{Ga}_{1-y})_{0.5}\text{In}_{0.5}\text{P}$, in $\Delta y = 0.2$ steps, is given in Fig. A.2. Each curve stops at the energy corresponding to the lowest bulk direct bandgap energy transition for the given composition. This data was obtained from reflectance measurements at IR wavelengths and a fit to a single effective oscillator model [Tanaka *et al.* 1986]. Thus the values at visible wavelengths are extrapolated. Accurate absorption data near and above bandgap are not available for AlGaInP and values must be estimated. This is not true of $\text{Al}_x\text{Ga}_{1-x}\text{As}$. A plot of the real refractive index dispersion for unintentionally doped

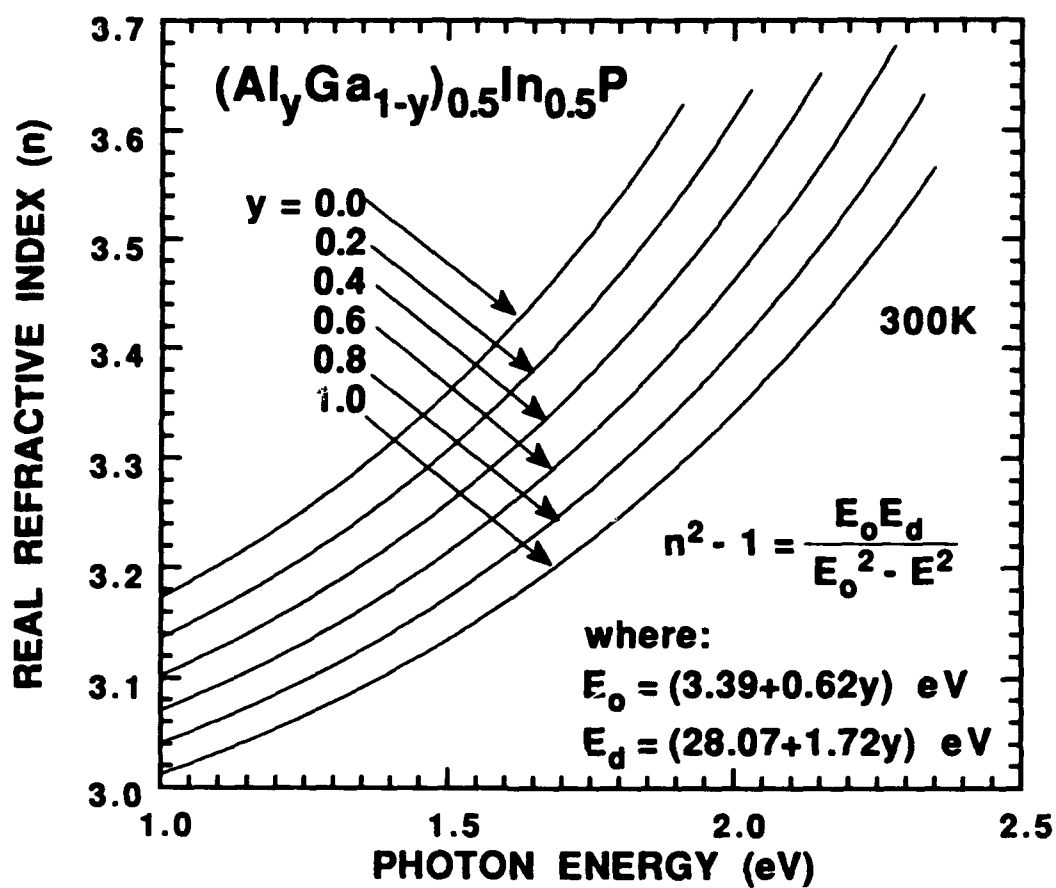


Fig. A.2 Real refractive index dispersion data for AlGaInP lattice-matched to GaAs [from Tanaka *et al.* 1986].

$\text{Al}_x\text{Ga}_{1-x}\text{As}$ below the lowest energy bandgap at a given composition is given in Fig. A.3. This data is from a model that neglects absorption but with parameters fit to measurements over the indicated range of wavelengths [Adachi 1985]. Accurate data for n and κ for $\text{Al}_x\text{Ga}_{1-x}\text{As}$, for specific values of x , from 1.5 to 2.5 eV is available [Aspnes *et al.* 1986]. A plot of n and κ for $x = 0.0$ and 0.5 is given in Fig. A.4. The values for $x = 0.5$ were interpolated from measured data at $x = 0.491$ and 0.590.

A.3 General Parameters

Tables A.2 and A.3 list several material parameters for $(\text{Al}_y\text{Ga}_{1-y})_{0.5}\text{In}_{0.5}\text{P}$ and $\text{Al}_x\text{Ga}_{1-x}\text{As}$ binary, ternary, and quaternary compounds.

Table A.2 Binary Material Parameters.

Parameter	unit	AlP	GaP	InP	AlAs	GaAs
a_0	Å	5.4510	5.4512	5.8688	5.6605	5.6533
E_g^Γ	eV	3.62	2.78	1.35	2.95	1.42
E_g^X	eV	2.43	2.26	2.26	2.17	1.91
Δ_0	eV	0.1	0.1	0.1	0.30	0.34
C_{11}	$\times 10^{12}$ dyn/cm ²	1.32	1.412	1.022	1.202	1.188
C_{12}	$\times 10^{12}$ dyn/cm ²	0.63	0.63	0.576	0.57	0.538
m_e^*/m_0	-	0.39	0.17	0.08	0.15	0.067
m_{hh}^*/m_0	-	0.67	0.67	0.60	0.76	0.62
m_{lh}^*/m_0	-	0.20	0.17	0.12	0.15	0.087

[Adachi 1985, Wang *et al.* 1990, Madelung 1991]

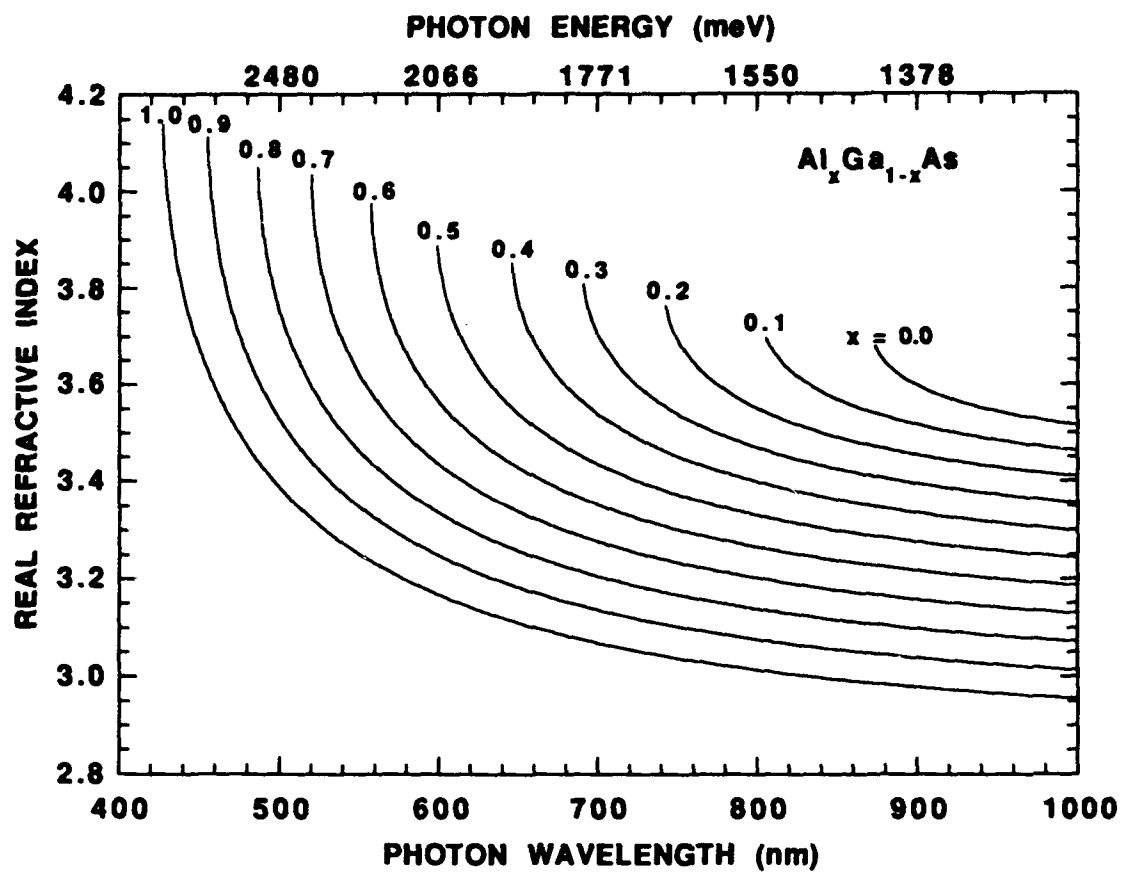


Fig. A.3 Real refractive index dispersion data for AlGaAs below the energy bandgap [from Adachi 1985].

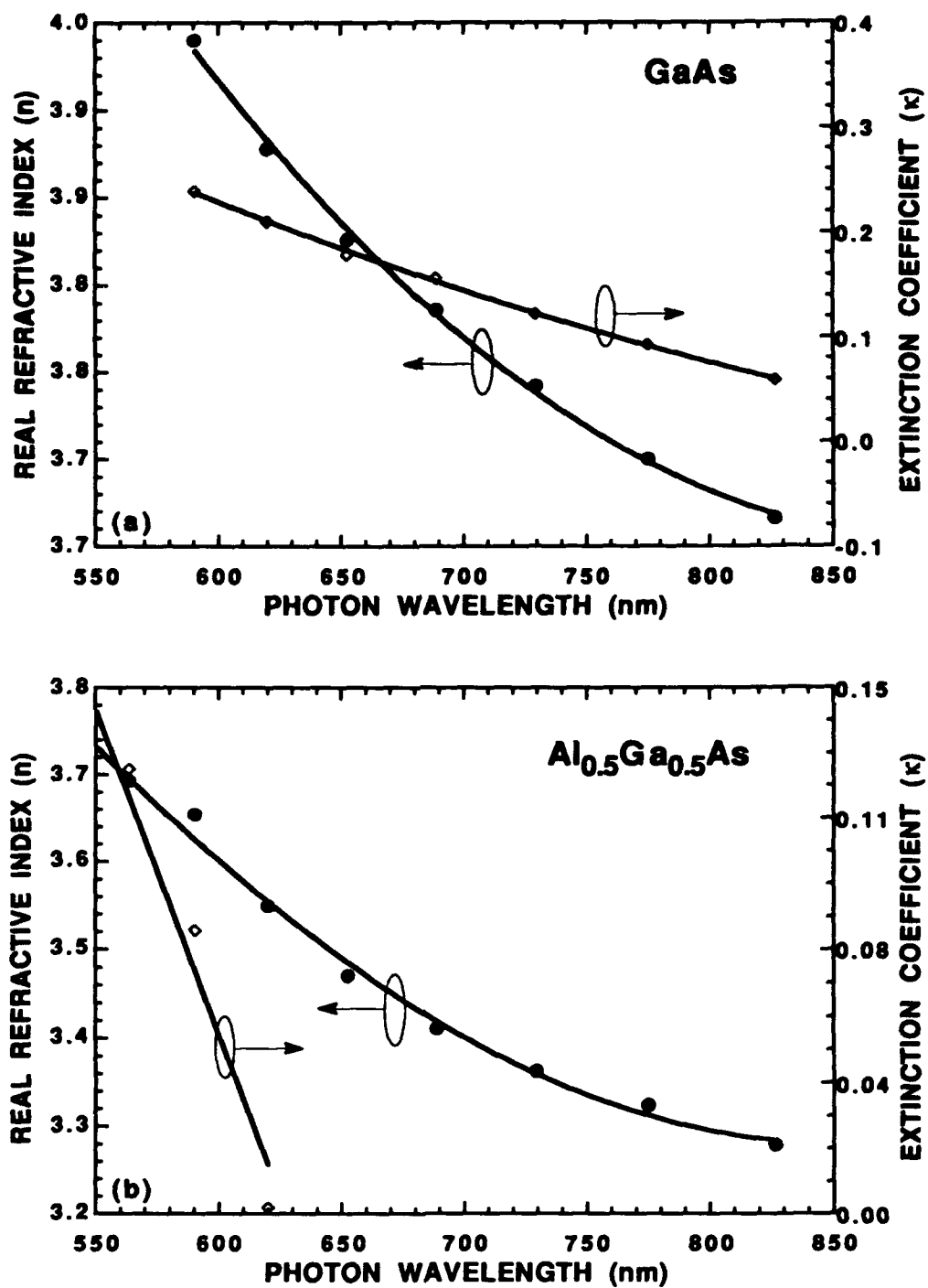


Fig. A.4 Complex refractive index dispersion data for (a) GaAs and (b) Al_{0.5}Ga_{0.5}As from photon wavelengths of 550 to 850 nm [from Aspnes *et al.* 1986].

Table A.3 Ternary and Quaternary Material Parameters.

Parameter	unit	Ga _{0.5} In _{0.5} P	Al _{0.5} In _{0.5} P	(Al _y Ga _{1-y}) _{0.5} In _{0.5} P
a_0	Å	5.6533	5.6533	5.6533
E_g^Γ	eV	1.91	2.52	1.91 + 0.61y (random)
		1.84	2.52	(ordered)
E_g^X	eV	2.25	2.35	2.25 + 0.10y
Δ_0	eV	0.1	0.1	0.1 + 0.035y
m_e^*/m_0	-	0.11	0.35	0.11 (y ≤ 0.7) 0.35 (x > 0.7)
m_{hh}^*/m_0	-	0.64	0.67	0.62 + 0.05y
m_{lh}^*/m_0	-	0.11	0.14	0.11 + 0.03y
C_{11}	$\times 10^{12}$ dyn/cm ²	1.22	1.17	1.22 - 0.05y
C_{12}	$\times 10^{12}$ dyn/cm ²	0.60	0.60	0.60

[Bour 1993, linear interpolation]

A.4 Epitaxial Growth and Ordering of AlGaInP

The optical properties of GaInP (and AlGaInP) are influenced by an ordered phase that occurs naturally, under certain crystal growth conditions, on the group III sublattice [Suzuki *et al.* 1988, Valster *et al.* 1991, Schneider *et al.* 1992]. As shown in Fig. A.5, the ordered alloy of GaInP consists of alternating monolayers of GaP and InP on {111} planes. This ordering occurs along two variants of the four {111} planes, ($\bar{1}11$) and ($1\bar{1}1$). In normal ternary alloys, the group III atoms would randomly occupy group III sublattice sites. Long range ordering is directly related to a reduction in the GaInP energy bandgap of up to ~135 meV as compared to fully disordered (random) epitaxial layers [Valster *et al.* 1991, Schneider *et al.* 1992]. Figure A.6 is the low temperature (12K) photoluminescence (PL) data from a study of Ga_{0.5}In_{0.5}P ordering. Bulk layers (~0.5 μ m thick) were grown by MOVPE over a range of substrate temperatures (600 to 800°C) on (100) GaAs substrates misoriented 0° and 2° toward the nearest <110>, and 5° and 6° (not

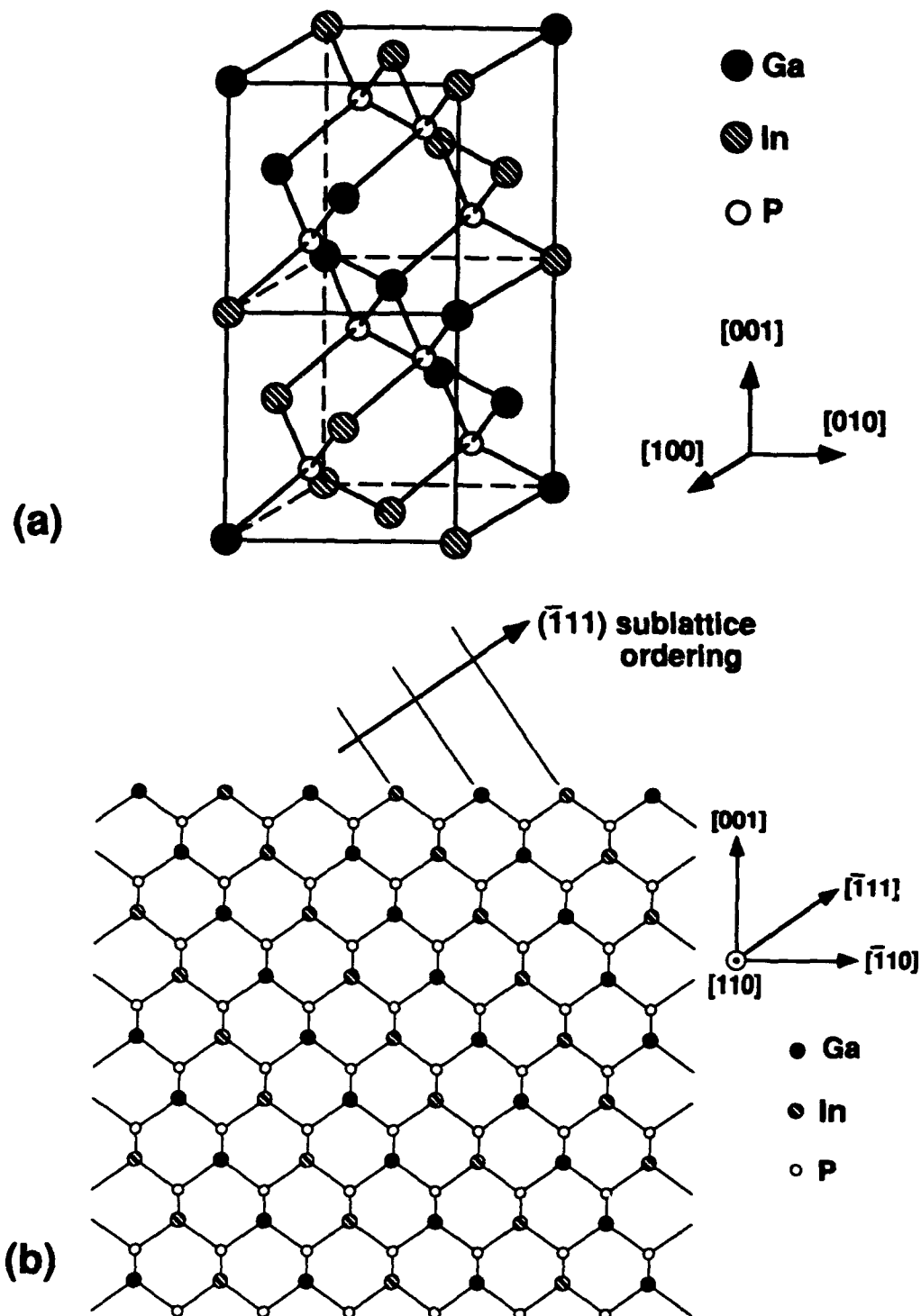


Fig. A.5 (a) Unit cell of ordered $\text{Ga}_{0.5}\text{In}_{0.5}\text{P}$ [Bour 1993], and (b) schematic diagram of a $\text{Ga}_{1-x}\text{In}_x\text{P}$ ordered crystal grown on (001) oriented GaAs [Ueno 1993].

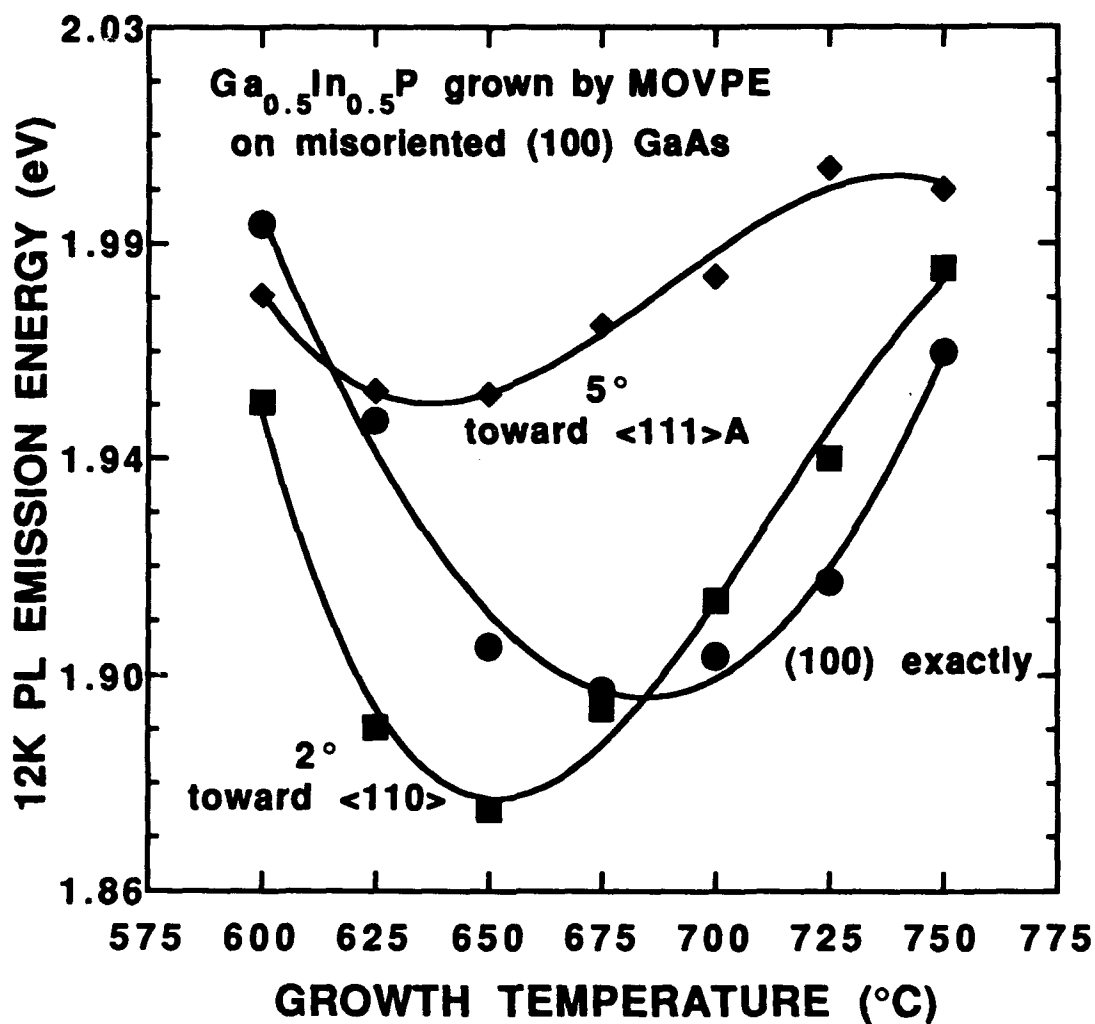


Fig. A.6 Low temperature photoluminescence peak emission energy of Ga_{0.5}In_{0.5}P epitaxial layers grown on (100) GaAs substrates misoriented 0° and 2° toward the nearest <110>, and 5° toward the nearest <111>A, against growth temperature [Schneider *et al.* 1992].

shown) toward the nearest $\langle 111 \rangle A$. The degree of disorder generally increases, corresponding to increased PL emission energy, as the substrate misorientation is increased. For a given misorientation, the PL energy is higher below 625 °C and above 725 °C, corresponding to increased disorder. Additionally, the PL linewidth generally decreases with increased disorder.

A.5 Photoluminescence of AlGaInP Structures

The low temperature (12K) normalized PL for disordered, undoped $(Al_yGa_{1-y})_{0.5}In_{0.5}P$ bulk epitaxial layers with $y = 0.0$ to 0.5 in 0.1 steps (except $y = 0.1$) is shown in Fig. A.7 [Schneider and Lott 1991]. These layers were grown on (100) GaAs substrates misoriented 6° toward the nearest $\langle 111 \rangle A$. The observed emission color is noted, along with the peak emission wavelength. At room temperature, the emission shifts about 30 nm to longer wavelengths for each composition.

The 12K PL spectra from $Ga_{1-x}In_xP/(Al_{0.7}Ga_{0.3})_{0.5}In_{0.5}P$ multiple single quantum well (MSQW) test structures with well thicknesses of 9, 6, 4, 2, and 1 nm and barrier thicknesses of 60 nm are shown in Fig. A.8 [Schneider 1993]. The upper curve (a) is from a sample grown at 750 °C on a 6° misoriented (100) wafer with $x = 0.56$ ($\epsilon \approx 0.55\%$ compressive strain). The sample represented by curve (b) is identical, except it was grown at 675 °C on a 2° misoriented (100) wafer. The PL peaks in curve (b) are broadened and shifted toward longer wavelengths, indicating increased ordering. The lower two curves in Fig. A.8, (c) and (d), are from samples identical to those represented by curves (a) and (b), respectively, except that $y = 0.5$ (i.e. lattice matched). Compared to curves (a) and (b), these curves are shifted toward shorter wavelengths due primarily to the increased energy bandgap of the quantum wells. The results in Fig. A.8 are qualitatively similar to those of a previous study by Valster *et al.* [1991].

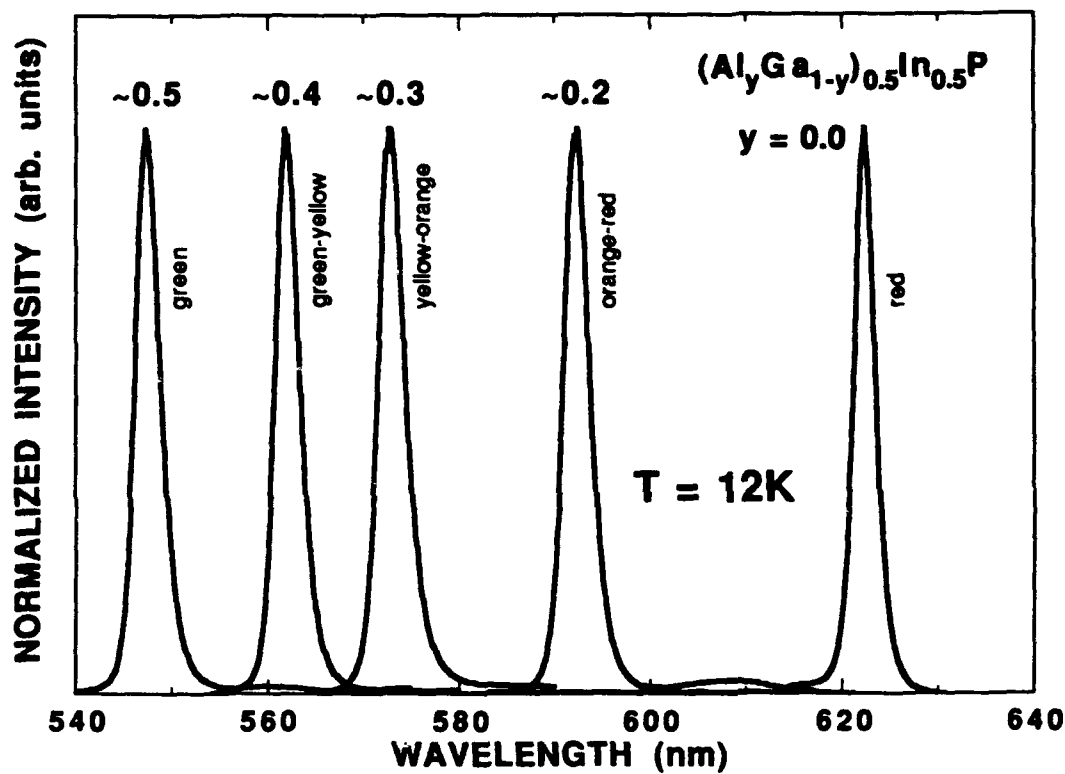


Fig. A.7 Low temperature photoluminescence of disordered $(Al_yGa_{1-y})_{0.5}In_{0.5}P$ epitaxial layers grown on (100) GaAs substrates misoriented 5° toward the nearest $\langle 111 \rangle_A$, with $y = 0.0, 0.2, 0.3, 0.4$, and 0.5 [Schneider and Lott 1991].

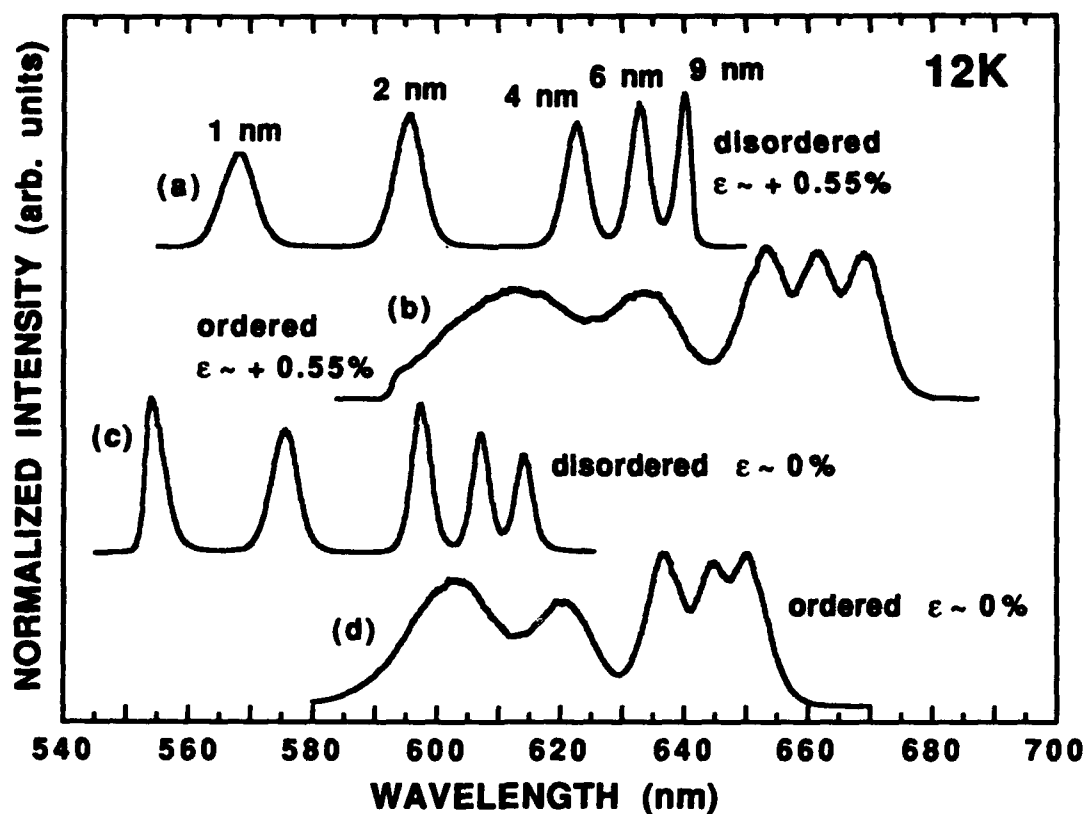


Fig. A.8 Low temperature photoluminescence spectra of ordered and disordered, strained and unstrained, AlGaInP quantum well heterostructures. Each structure contains five $\text{Ga}_{1-x}\text{In}_x\text{P}$ quantum wells that are 9, 6, 4, 2, and 1 nm thick, separated by 60 nm thick $(\text{Al}_{0.7}\text{Ga}_{0.3})_{0.5}\text{In}_{0.5}\text{P}$ barrier layers. Curve (a): $x \approx 0.56$, $T_g = 750^\circ\text{C}$, 6° off (100) substrate. Curve (b): $x \approx 0.56$, $T_g = 675^\circ\text{C}$, 2° off (100) substrate. Curve (c): $x \approx 0.50$, $T_g = 750^\circ\text{C}$, 6° off (100) substrate. Curve (d): $x \approx 0.50$, $T_g = 675^\circ\text{C}$, 2° off (100) substrate. The strain (ϵ) for spectra (a) and (b) is $\sim -0.55\%$ [Schneider 1993].

A.6 Heterojunction Band Offsets

The band offsets for the $(\text{Al}_y\text{Ga}_{1-y})_{0.5}\text{In}_{0.5}\text{P}$ system are not accurately known. The conduction band offset has been given as $\Delta E_c = Q_c \Delta E_g$, with $0.39 < Q_c < 0.75$ [Liedenbaum *et al.* 1990, Valster *et al.* 1991, Bour 1993, Schneider *et al.* 1993]. It is generally agreed that the direct/indirect crossover point occurs at about $y \sim 0.6$ to 0.7 , and that this composition gives the largest conduction band offset to $\text{Ga}_{1-x}\text{In}_x\text{P}$. For this dissertation, Q_c is estimated to be 0.6 . The value of Q_c for $\text{Al}_x\text{Ga}_{1-x}\text{As}$ is also believed to be ~ 0.6 . Using these values for Q_c , the data in Tables A.1 to A.3, and a $Q_c = 0.4$ for the $\text{GaAs}/\text{Ga}_{0.5}\text{In}_{0.5}\text{P}$ heterointerface [Gunapala *et al.* 1990, Hatakoshi *et al.* 1991, Masselink *et al.* 1992], Fig. A.9 was constructed. The relative energy differences in this plot can be used to estimate the energy band offsets for any given $\text{Al}_x\text{Ga}_{1-x}\text{As}$ and/or $(\text{Al}_y\text{Ga}_{1-y})_{0.5}\text{In}_{0.5}\text{P}$ heterojunction.

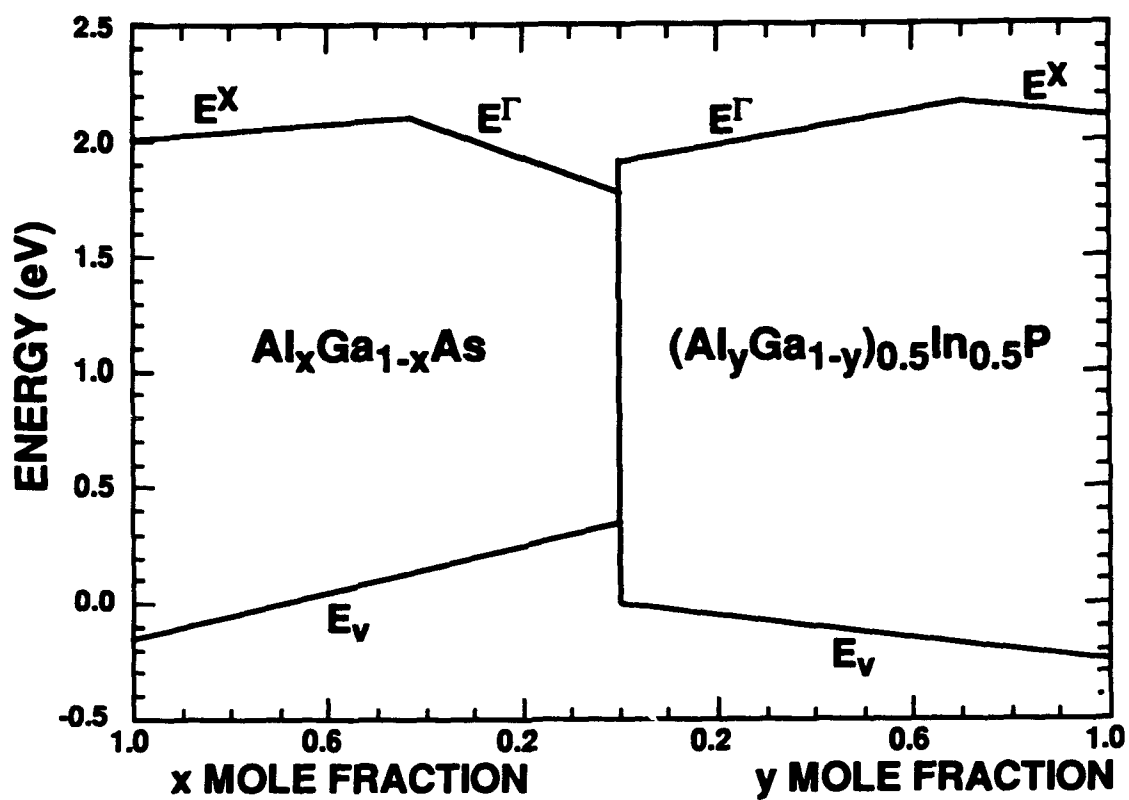


Fig. A.9 Compositional dependence of band offsets for Al_xGa_{1-x}As and (Al_yGa_{1-y})_{0.5}In_{0.5}P heterostructures [after Bour 1993].

References for Appendix A

Adachi, S., "GaAs, AlAs, and $\text{Al}_x\text{Ga}_{1-x}\text{As}$: Material Parameters for Use in Research and Device Applications", *Journal of Applied Physics*, 58(3), p. R1-R29 (1 August 1985).

Aspnes, D. E., S. M. Kelso, R. A. Logan, and R. Bhat, "Optical Properties of $\text{Al}_x\text{Ga}_{1-x}\text{As}$ ", *Journal of Applied Physics*, 60(2), p. 754-767 (15 July 1986).

Bour, D. P., "AlGaInP Quantum Well Lasers", Ch. 9, in *Quantum Well Lasers*, P. S. Zory, Jr., ed. (Academic Press:New York 1993).

Gunapala, S. D., B. F. Levine, R. A. Logan, T. Tanbun-Ek, and D. A. Humphrey, "GaAs/GaInP Multiquantum Well Long-Wavelength Infrared Detector Using Bound-to-Continuum State Absorption", *Applied Physics Letters*, 57(17), p. 1802-1804 (22 October 1990).

Hatakoshi, G., K. Itaya, M. Ishikawa, M. Okajima, and Y. Uematsu, "Short-Wavelength InGaAlP Visible Laser Diodes", *IEEE Journal of Quantum Electronics*, 27(6), p. 1476-1482 (June 1991).

Krijn, M. P. C. M., "Heterojunction Band Offsets and Effective Masses in III-V Quarternary Alloys", *Semiconductor Science Technology*, 6, p. 27-31 (1991).

Liedenbaum, C. T. H. F., A. Valster, A. L. G. J. Severens, and G. W. t' Hooft, "Determination of the GaInP/AlGaInP Band Offset", *Applied Physics Letters*, 57(25), p. 2698-2700 (17 December 1990).

Madelung, O., ed., *Semiconductors: Group IV Elements and III-V Compounds*, (Springer-Verlag:New York, 1991).

Masselink, W. T., M. Zachau, T. W. Hickmott, and K. Hendrickson, "Electronic and Optical Characterization of InGaP Grown by Gas-Source Molecular Beam Epitaxy", *Journal of Vacuum Science Technology B*, 10(2), p. 966-968 (March/April 1992).

Schneider, Jr., R. P., and J. A. Lott, unpublished (1991).

Schneider, Jr., R. P., E. D. Jones, J. A. Lott, and R. P. Bryan, "Photoluminescence Linewidths in Metalorganic Vapor Phase Epitaxially Grown Ordered and Disordered InAlGaP Alloys", *Journal of Applied Physics*, 72(11), p. 5397-5400 (1 December 1992).

Schneider, Jr., R. P., unpublished (1993).

Schneider, Jr., R. P., R. P. Bryan, E. D. Jones, and J. A. Lott, "Excitonic Transitions in InGaP/InAlGaP Strained Quantum Wells", *Applied Physics Letters*, 63(9), p. 1240-1242 (30 August 1993).

Suzuki, T., A. Gomyo, and S. Iijima, "Strong Ordering in GaInP Alloy Semiconductors: Formation Mechanism for the Ordered Phase", *Journal of Crystal Growth* 93, p. 396-405 (1998).

Tanaka, H., Y. Kawamura, and H. Asahi, "Refractive Indices of $\text{In}_{0.49}\text{Ga}_{0.51-x}\text{Al}_x\text{P}$ Lattice Matched to GaAs", *Journal of Applied Physics*, 59(3), p. 985-986 (1 February 1986).

Ueno, Y., "Oscillator Strength Enhancement for [110]-Polarized Light in Compressively Strained GaInP Ordered Crystals Used in AlGaInP Lasers", *Applied Physics Letters*, 62(6), p. 553-555 (8 February 1993).

Valster, A., C. T. H. F. Liedenbaum, M. N. Finke, A. L. G. Severens, M. J. B. Boermans, D. E. W. Vandenhoudt, and C. W. T. Bulle-Lieuwma, "High Quality AlGaInP Alloys Grown by MOVPE on (311)B GaAs Substrates", *Journal of Crystal Growth*, 107, p. 403-409 (1991).

Wang, T. Y., A. W. Kimball, G. S. Chen, D. Birkedal, and G. B. Stringfellow, "Atmospheric Pressure Organometallic Vapor-Phase Epitaxial Growth and Characterization of $\text{Ga}_{0.4}\text{In}_{0.6}\text{P}/(\text{Al}_{0.4}\text{Ga}_{0.6})_{0.5}\text{In}_{0.5}\text{P}$ Strained Quantum Wells", *Journal of Applied Physics*, 68(7), p. 3356-3363 (1 October 1990).

Appendix B Metalorganic Vapor Phase Epitaxy System

This Appendix contains a brief overview of the Aixtron 200 low pressure metalorganic vapor phase epitaxy (MOVPE) system. This system was used to grow the structures described in this dissertation [Schneider 1993]. A simplified schematic is shown in Fig. B.1, and a summary of precursors is given in Table B.1. The system consists of a low-pressure horizontal quartz reaction chamber with infrared lamp heating and a very fast vent-run switching manifold. Growth is on one 2-inch wafer per run, with or without rotation. As in most MOVPE systems, Pd-purified hydrogen is used as a carrier and dilution gas. The metalorganic (alkyl) bubbler sources are adduct purified and kept in temperature controlled baths at 13°C (trimethylindium) or 17°C (all others). Two each trimethylaluminum (TMAI) and trimethylgallium (TMGa) sources are used. This minimizes flow-rate changes in the bubblers that could lead to non uniform delivery. This is important for precise thickness and compositional growth control of $\text{Ga}_{1-x}\text{In}_x\text{P}/(\text{Al}_y\text{Ga}_{1-y})_{0.5}\text{In}_{0.5}\text{P}$ strained quantum well active regions. The multiple sources are also important for the precise growth of AlInP/AlGaInP and AlAs/AlGaAs distributed Bragg reflectors. For AlGaAs, the p-type dopant is C from the CCl_4 bubbler, while for AlGaInP the p-type dopant is either Zn or Mg. Both materials are doped n-type with Si. The gas handling system includes several electronic mass flow controllers (MFCs) and pressure controllers (PCs) that deliver precisely metered amounts of reactants at very high flow rates. This feature allows the accurate growth of very thin layers such as quantum wells.

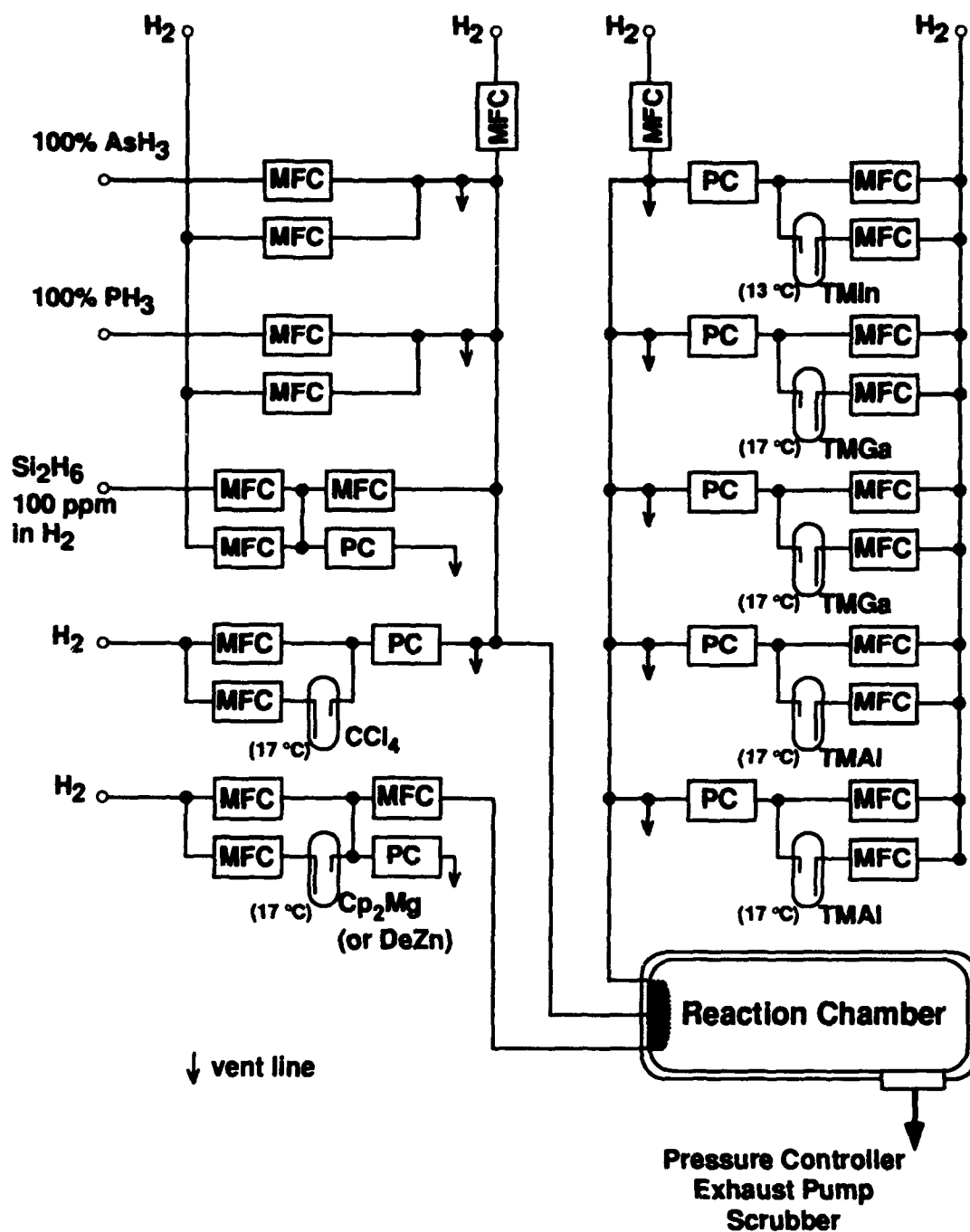


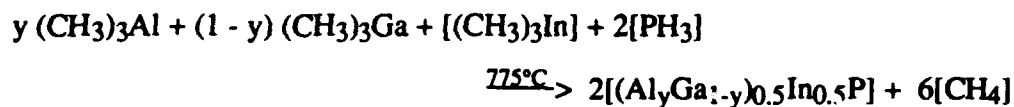
Fig. B.1 Simplified schematic diagram of the Aixtron MOVPE system.

Table B.1 Summary of Precursors for the Aixtron MOVPE System

Source	abbreviation	formula	delivery	type	comment
100% hydrogen	-	H ₂	bottled gas	-	carrier/dilution gas
100% phosphine	-	PH ₃	bottled gas	hydride	P (group V)
100% arsine	-	AsH ₃	bottled gas	hydride	As (group V)
diethylzinc	DEZn	(C ₂ H ₅) ₂ Zn	bottle or bubbler	metalorganic	Zn (p-type dopant)
carbon tetrachloride	-	CCl ₄	liquid in bubbler	chloride	C (p-type dopant)
100 ppm disilane	-	Si ₂ H ₆ in H ₂	bottled gas	hydride	Si (n-type dopant)
trimethylaluminum	TMAI	(CH ₃) ₃ Al	liquid in bubbler	metalorganic	Al (group III)
trimethylgallium	TMGa	(CH ₃) ₃ Ga	liquid in bubbler	metalorganic	Ga (group III)
trimethylindium	TMIIn	(CH ₃) ₃ In	solid in bubbler	metalorganic	In (group III)
bis(cyclopentadienyl)-magnesium	Cp ₂ Mg	(C ₅ H ₅)Mg	solid in bubbler	metalorganic	Mg (p-type dopant)

Also, a complex set of pressure actuated valves are used to control the gas flow at key points in the system. The valves, for example, start and stop the flow of the precursors. They also independently direct the precursors into the reaction chamber or into the vent line. The diluted precursors are mixed in a common manifold at the entrance to the reaction chamber and flow quickly through the susceptor hot zone where pyrolysis occurs, resulting in epitaxial growth. The excess gas flows into the exhaust and is fed to a scrubber which cracks the constituents into nontoxic end products for atmospheric release. The entire system is under computer control and follows a sequential program. Typical growth pressures of 80 to 110 mbar are used for the growth of AlGaAs and

AlGaInP compounds, respectively. The growth temperature is nominally 725 to 775 °C, and the growth rates are ~5 to 9 Å/s for AlGaAs and ~6 to 7 Å/s for AlGaInP. Although the exact growth mechanisms are not known, the following simplified reactions describe the MOVPE growth process for AlGaAs and AlGaInP:



where $0.0 \leq x, y \leq 1.0$. Detailed information on crystal growth by MOVPE is found in the review article by Ludowise [1985], and in the book by Stringfellow [1989].

References for Appendix B

Ludowise, M. J., "Metalorganic Chemical Vapor Deposition of III-V Semiconductors", *Journal of Applied Physics*, 58(8), p. R31-R55 (15 October 1985).

Schneider, Jr., R. P., Senior Member of Technical Staff, Sandia National Laboratories, Albuquerque, NM, private communication (1993).

Stringfellow, G. B., *Organometallic Vapor-Phase Epitaxy: Theory and Practice*, (Academic Press:New York, 1989).

Appendix C Matrix Calculations

This Appendix briefly reviews the 2x2 matrix calculation that is used to model the electric field intensity on resonance for visible vertical cavity surface emitting lasers (VCSELs). Similar methods are used throughout this dissertation to model the reflectance, reflectivity phase, transmittance, and absorptance of VCSEL and related structures such as distributed Bragg reflectors (DBRs). Computer programs (written in Pascal) that incorporate these methods have been developed and serve as useful design tools. The computer programs allow for very general layered structures, defined by an input file, where the refractive index $N(\omega) = n(\omega) - i\kappa(\omega)$ is complex in each layer in order to adequately model absorption. Also, the angle of incidence (with s- or p-polarized fields) is arbitrary. In general, however, the field parameters at normal incidence are of the most interest. The 2x2 matrix equations used to design multilayer optical interference coatings are well established and covered in varying detail in standard textbooks [Born and Wolf 1975, Yeh 1988, MacLeod 1989, Thelen 1989, and others]. Two types of matrix approaches are commonly used, based on 2x2 "characteristic" or "transfer" matrices with complex number entries. Both methods rely on the following assumptions:

- 1) nonmagnetic films
- 2) isotropic and homogeneous materials
- 3) smooth interfaces without scatter
- 4) plane parallel films of infinite lateral extent
- 5) semi-infinite incident and substrate media
- 6) linear wave equation

The characteristic matrix approach relates the complex amplitude of the sum total of both the electric and magnetic field vectors (tangential components) at a given boundary (interface) to these same fields at the adjacent boundary. Each 2x2 matrix includes the parameters of the individual layers such as the refractive index, thickness, and angle of incidence. In contrast, the transfer matrix approach uses 2x2 "dynamical" and "propagation" matrices to relate the incident (E^+) and reflected (E^-) electric field vectors to the same quantities at either side of a given interface or an adjacent interface. The matrices are multiplied together, in proper order, to find an overall transfer matrix for the multitude of layers. Both approaches were computer coded and found to run at nearly identical speeds, with and without the use of Chebyshev polynomials to calculate the powers of the complex 2x2 matrices for blocks of repetitive layers. The transfer matrix approach [Yeh 1988] was implemented to calculate the electric field intensity (standing wave pattern) on resonance as described below.

A general VCSEL structure for modeling purposes is shown in Fig. C.1. The amplitudes of the incident (E_o^+) and reflected (E_o^-) electric field plane waves at $x = 0$ are related to those at $x = N$ (E_s^+ and E_s^-) by

$$\begin{pmatrix} E_o^+ \\ E_o^- \end{pmatrix} = \begin{pmatrix} M_{11} & M_{12} \\ M_{21} & M_{22} \end{pmatrix} \begin{pmatrix} E_s^+ \\ E_s^- \end{pmatrix} \quad (C.1)$$

where the transfer matrix M is

$$\begin{pmatrix} M_{11} & M_{12} \\ M_{21} & M_{22} \end{pmatrix} = D_o^{-1} \left[\prod_{t=1}^N D_t P_t D_t^{-1} \right] D_s \quad (C.2)$$

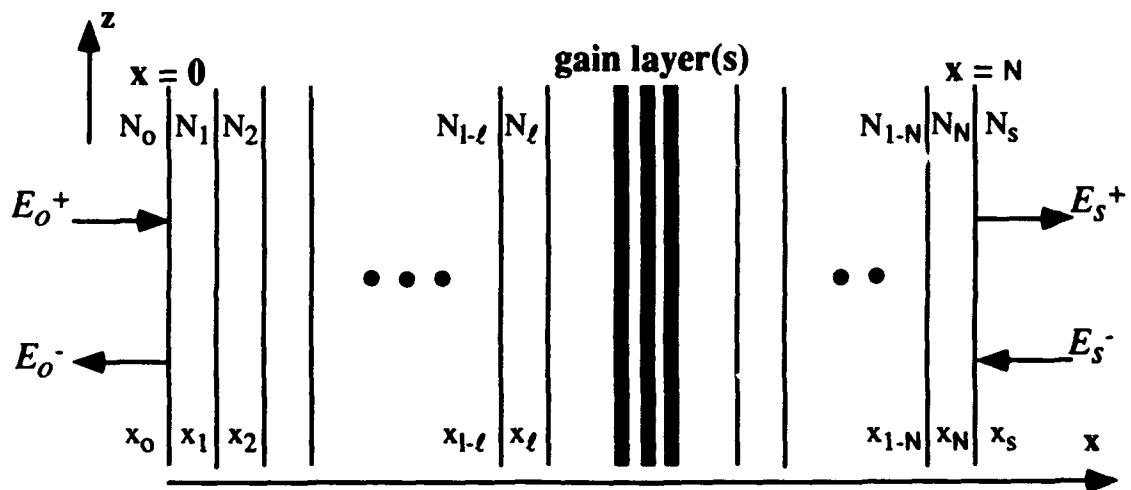


Fig. C.1 A multilayer VCSEL structure used to model the electric field intensity on resonance.

and $\ell = 0, 1, 2, \dots, N, s$. At normal incidence, the dynamical matrices for arbitrary layer ℓ are given by

$$D_\ell = \begin{pmatrix} 1 & 1 \\ N_\ell & -N_\ell \end{pmatrix} \quad \text{and} \quad D_\ell^{-1} = \frac{1}{2} \begin{pmatrix} 1 & 1/N_\ell \\ 1 & -1/N_\ell \end{pmatrix} \quad (\text{C.3})$$

where N_ℓ is the complex index of refraction for layer ℓ . The propagation matrix for layer P_ℓ is given by

$$P_\ell = \begin{pmatrix} e^{i\varphi_\ell} & 0 \\ 0 & e^{-i\varphi_\ell} \end{pmatrix} \quad (\text{C.4})$$

where

$$\varphi_\ell = k_{\ell x} d_\ell \quad \text{and} \quad k_{\ell x} = N_\ell \frac{\omega}{c_0} = N_\ell \frac{2\pi}{\lambda_0} \quad (\text{C.5})$$

and where d_ℓ is the thickness of layer ℓ and $k_{\ell x}$ is the x component of the wave vector.

The complex electric field amplitude throughout the structure is given by

$$E(x) = \begin{cases} E_o^+ e^{-ik_{ox}(x-x_o)} + E_o^- e^{ik_{ox}(x-x_o)} & x < x_o \\ E_\ell^+ e^{-ik_{\ell x}(x-x_\ell)} + E_\ell^- e^{ik_{\ell x}(x-x_\ell)} & x_{\ell-1} < x < x_\ell \\ E_s^+ e^{-ik_{sx}(x-x_N)} + E_s^- e^{ik_{sx}(x-x_N)} & x_N < x \end{cases} \quad (\text{C.6})$$

From Eq. (C.1), the reflectivity coefficient (ρ) with $E_s^- = 0$ is given by

$$\rho = \frac{M_{21}}{M_{11}} \quad (\text{C.7})$$

The reflectivity magnitude for typical VCSEL structures is > 0.999 . To solve for the electric field intensity on resonance, the complex part of the refractive index (κ) for the quantum well layer(s) is phenomenologically made negative (providing uniform gain) to cause the reflectivity to reach exactly 1.0 over a range of wavelengths slightly above and below the Bragg design wavelength (λ_0), so that $E_o^+ = E_o^-$. The gain per well goes through a minimum as a function of wavelength, quickly found numerically, and this wavelength is taken as the resonance wavelength. Once $p = 1.0$ is found, the values of the complex electric field amplitudes at the interfaces are known and Eq. (C.6) is used to calculate the electric field intensity throughout the entire VCSEL structure. The assumptions in the calculation are that the reflectance of the bottom DBR is 1.0, as seen from the optical cavity, and that the quantum well(s) provide uniform and equal gain. This calculation method is useful for modeling various constructions of the VCSEL such as designs with hybrid dielectric/semiconductor DBR mirror stacks. It is also useful for examining the overlap of the electric field intensity with the quantum well(s) in gain calculations, and for modeling the phase penetration depth of the standing wave into the DBR mirrors.

References for Appendix C

Born, M., and E. Wolf, *Principles of Optics*, 5th ed. (Pergamon Press:New York, 1975).

MacLeod, H. A., *Thin-Film Optical Coatings*, 2nd ed., (McGraw-Hill:New York, 1989).

Thelen, A., *Design of Optical Interference Coatings*, (McGraw-Hill:New York, 1989).

Yeh, P., *Optical Waves in Layered Media*, (Wiley:New York, 1988).

Appendix D Quantum Well Gain Calculations

This Appendix overviews two optical gain models for AlGaInP quantum well or similar structures, including a first order conventional model, and a semi-quantitative model. The models are useful for the analysis of the optically pumped and electrically injected visible vertical cavity surface emitting lasers (VCSELs) presented in Chapters 3 and 5.

Optical gain in semiconductors is commonly calculated using perturbation theory (i.e. Fermi's Golden Rule) [Holonyak *et al.* 1980, Arakawa and Yariv 1985, Yariv 1989, Zory 1993]. The end result is a spectrally dependent gain coefficient that is a parametric function of carrier density, or radiative current density. Several key factors determine the gain spectrum such as the carrier distribution in the energy bands, the transition (matrix element) probabilities, and the intraband relaxation of carriers due to scattering processes [Zory 1993]. The latter effect is usually included by convolving the expression for gain with a spectral lineshape function over all transition energies, effectively smoothing the gain spectrum. Other effects add further complexity, including for example carrier leakage out of a quantum well, nonradiative (Auger) recombination, bandgap renormalization (many-body interactions), and quantum well strain [Corzine *et al.* 1993, Kamiyama *et al.* 1993]. Compressive strain splits the heavy- and light-hole valence band degeneracy and results in a reduced in-plane heavy-hole mass. This reduces the density of carriers needed to reach transparency and also the threshold current density.

For the first order conventional model, assuming parabolic bands, the gain of a quantum well is [Chinn *et al.* 1988]

$$g(E) = \frac{q^2 |M|^2}{E \epsilon_0 m_0^2 c_0 \hbar n L_z} \sum_{i,j} m_{r,ij} C_{ij} A_{ij} [f_c - f_v] H(E - E_{ij}) \quad (\text{cm}^{-1}) \quad (\text{D.1})$$

where E is the energy, $|M|^2$ is the transition matrix element, $m_{r,ij}$ is the reduced mass for transition i to j (i and j are integers, 1, 2, 3, . . . , referring to the quantized electron, heavy hole, and light hole states), C_{ij} is the strength of the transition or degree of wavefunction overlap, A_{ij} accounts for the polarization dependence of the i to j transition, f_c and f_v are the Fermi-Dirac distribution functions, E_{ij} is the transition energy, H is the Heavyside function, L_z is the quantum well thickness, and n is a effective group refractive index of the quantum well material. The transition matrix element is given by [Agrawal and Dutta 1986]

$$|M|^2 \approx \frac{m_0^2 E_g (E_g + \Delta_0)}{12 m_e (E_g + 2\Delta_0/3)} \quad (\text{kg-J}) \quad (\text{D.2})$$

where E_g is the quantum well energy bandgap, m_e is the effective conduction band electron mass, and Δ_0 is the split-off band energy. The reduced mass, for the transition from the i^{th} quantized electron state to the j^{th} quantized hole state, is

$$m_{r,ij}^{-1} = m_i^{-1} + m_j^{-1} \quad (\text{kg}^{-1}) \quad (\text{D.3})$$

Assuming rigorous k -selection rules, C_{ij} becomes

$$C_{ij} = \begin{cases} 0 & \text{if } i \neq j \\ 1 & \text{if } i = j \end{cases} \quad (\text{unitless}) \quad (\text{D.4})$$

Considering only the amplification of transverse electromagnetic (TE) radiation, A_{ij} is given by [Chinn *et al.* 1988]

$$A_{ij} = \begin{cases} \frac{3}{4}(1 + E/E_{ij}) & \text{for heavy holes} \\ \frac{1}{4}(5 - 3E/E_{ij}) & \text{for light holes} \end{cases} \quad (\text{unitless}) \quad (\text{D.5})$$

The Fermi-Dirac distribution functions are given by

$$f_c = \frac{1}{\exp[(E_e - E_{fc})/kT] + 1} \quad (\text{unitless}) \quad (\text{D.6})$$

$$f_v = \frac{1}{\exp[(E_h - E_{fv})/kT] + 1} \quad (\text{unitless}) \quad (\text{D.7})$$

where for parabolic bands [Corzine *et al.* 1993]

$$E_e = E_c + (E - E_{ij}) \frac{m_r}{m_e} \quad (\text{eV}) \quad (\text{D.8})$$

$$E_h = E_v - (E - E_{ij}) \frac{m_r}{m_v} \quad (\text{eV}) \quad (\text{D.9})$$

where E_c and E_v are the relative energies of the conduction and valence band, respectively. Finally, the Heavyside function H is

$$H(y) = \begin{cases} 0 & \text{if } y < 1.0 \\ 1 & \text{if } y \geq 1.0 \end{cases} \quad (\text{unitless}) \quad (\text{D.10})$$

Once $g(E)$ is found, this gain is convolved with a spectral lineshape function to account for spectral broadening due to intraband scattering. The convolved "smoothed" gain is given by [Corzine *et al.* 1993]

$$G(\hbar\omega) = \int_{E_g}^{\infty} g(E) L(E) dE \quad (\text{cm}^{-1}) \quad (\text{D.11})$$

where $G(\hbar\omega)$ is the gain at photon energy $\hbar\omega$, and the integral is taken over all possible transition energies (E). A common phenomenological lineshape function $L(E)$ is the Lorentzian, given by [Asada 1993]

$$L(E) \equiv \frac{1}{\pi} \frac{\hbar/\tau_c}{(E - \hbar\omega)^2 + (\hbar/\tau_c)^2} \quad (\text{J}^{-1}) \quad (\text{D.12})$$

where τ_c ($\sim 1 \times 10^{-13}$ seconds) is the intraband scattering time.

The gain calculation proceeds, using Eqs (D.1) to (D.12), once the density of carriers in the quantum well is known or defined, assuming charge neutrality such that $N_e = P_h$ for an undoped quantum well, where N_e and P_h ($= P_{hh} + P_{lh}$) are the density of free electrons and holes, respectively. The relationship between the electron carrier density and the energy difference between the i^{th} quantized electron state and the quasi-Fermi level in the conduction band ($E_{ci} - E_{fc}$), assuming parabolic subbands, is

$$N_e = \frac{4\pi k_B T}{h^2 L_z} \sum_{i=1}^2 m_{ei} \ln \left\{ 1 + \exp[-(E_{ci} - E_{fc})/k_B T] \right\} \quad (\text{cm}^{-3}) \quad (\text{D.13})$$

where m_{ei} is the in-plane conduction band effective mass. The equivalent expression for P_h is

$$P_h = \sum_{k=hh, lh} \frac{4 \pi k_B T}{h^2 L_z} \sum_{i=1}^2 m_{k,i} \ln \{1 + \exp[-(E_{vi} - E_{fv})/k_B T]\} \quad (\text{cm}^{-3}) \quad (\text{D.14})$$

Thus given N_e and P_h , Eqs (D.13) and (D.14) are solved for $E_{ci} - E_{fc}$ and $E_{vi} - E_{fv}$, and then Eqs (D.1) to (D.12) are solved to determine $G(\hbar\omega)$.

The reduction in energy bandgap due to many-body interactions is taken as [Chinn *et al.* 1988]

$$\Delta E_g \approx -(3 \times 10^{-8}) N_{QW}^{1/3} \quad (\text{eV}) \quad (\text{D.15})$$

where ΔE_g is the shift in Γ -point bandgap energy due to the volumetric quantum well carrier density N_{QW} (in units of cm^{-3}).

In a similar manner, the rate of spontaneous emission is [Zory 1993]

$$R(E) = \frac{q^2 n E |M|^2}{\epsilon_0 m_0^2 c_0^3 \hbar^4 L_z} \sum_{i,j} m_{\tau,ij} C_{ij} [f_c (1 - f_v)] H(E - E_{ij}) \quad (1/\text{J-cm}^2\text{-s}) \quad (\text{D.16})$$

and the radiative volume current is given by

$$J_{Rad} = q \int_{E_g}^{\infty} R(E) dE \quad (\text{kA}/\mu\text{m-cm}^2) \quad (\text{D.17})$$

Multiplying J_{Rad} by the quantum well thickness gives the radiative current density.

As an alternative to the conventional gain model, a useful semi-quantitative optical gain model was developed that is far less difficult to implement [Mittlestein *et al.*

1986]. The model only considers the $n=1$ and $n=2$ quantum well states, and no distinction is made between valence and conduction band states. The modal gain (Γg) is given by

$$\Gamma g(E) = C \sum_{n=1}^2 \frac{1}{\exp([E_n - E]/\Delta E) + 1} [2f_c(E) - 1] \quad (\text{cm}^{-1}) \quad (\text{D.18})$$

where E is the photon energy, the constant C is the maximum available modal gain per quantized state ($C \approx 45 \text{ cm}^{-1}$ for a $\text{Ga}_{0.5}\text{In}_{0.5}\text{P}$ quantum well surrounded by $(\text{Al}_y\text{Ga}_{1-y})_{0.5}\text{In}_{0.5}\text{P}$ $y \sim 0.5$ barrier layers), E_n is the quantized state energy ($n = 1, 2$), and $\Delta E \approx \hbar/\tau_c$ is a phenomenological intraband scattering term. As before, charge neutrality is assumed. The inputs to the model are the desired carrier density, the quantum well transition energies, and the lattice temperature. The transition energies are calculated separately beforehand by using a standard finite rectangular well model that accounts for strain [Bastard 1990, Krijn 1991, Weisbuch and Vinter 1991]. Given a value for N_e , Eq. (D.13) is used to iterate to a solution for $E_{ci} - E_{fc}$. Then, f_c is found from Eq. (D.6), and Eq. (D.18) is used to calculate the modal gain as a function of photon energy $E = \hbar\omega$.

References for Appendix D

- Agrawal, G. P., and N. K. Dutta, *Long-Wavelength Semiconductor Lasers*, (Van Nostrand Reinhold:New York, 1986).
- Arakawa Y., and A. Yariv, "Theory of Gain, Modulation Response, and Spectral Linewidth in AlGaAs Quantum Well Lasers", *IEEE Journal of Quantum Electronics*, 21(10), p. 1666-1674 (1985).
- Asada, M., "Intraband Relaxation Effect on Optical Spectra", Chapter 2 in, *Quantum Well Lasers*, P. S. Zory Jr., ed., (Academic Press:San Diego, 1993).
- Bastard, G., *Wave Mechanics Applied to Semiconductor Heterostructures*, (Les Éditions de Physiques:Paris, 1990)
- Chinn, S. R., P. S. Zory, and A. R. Reisinger, "A Model for GRIN-SCH-SQW Diode Lasers", *IEEE Journal of Quantum Electronics*, 24(11), p. 2191-2214 (1988).
- Corzine, S. W., R. H. Yan, and L. A. Coldren, "Optical Gain in III-V Bulk and Quantum Well Semiconductors", Chapter 1 in, *Quantum Well Lasers*, P. S. Zory Jr., ed., (Academic Press:San Diego, 1993).
- Holonyak, Jr., N., R. M. Kolbas, R. D. Dupuis, and P. D. Dapkus, "Quantum-Well Heterostructure Lasers", *IEEE Journal of Quantum Electronics*, 16(2), p. 170-186 (1980).
- Kamiyama, S., T. Uenoyama, M. Mannoh, Y. Ban, and K. Ohnaka, "Theoretical Analysis of Valence Subband Structures and Optical Gain of GaInP/AlGaInP Compressive Strained-Quantum Wells", *IEEE Photonics Technology Letters*, 4(4), p. 439-441 (April 1993).
- Krijn, M. P. C. M., "Heterojunction Band Offsets and Effective Masses in III-V Quarternary Alloys", *Semiconductor Science Technology*, 6, p. 27-31 (1991).
- Mittelstein, M., Y. Arakawa, A. Larsson, and A. Yariv, "Second Quantized State Lasing of a Current Pumped Single Quantum Well Laser", *Applied Physics Letters*, 49 (25), p. 1689-1691 (1986).
- Weisbuch, C., and B. Vinter, *Quantum Semiconductor Structures*, (Academic Press: San Diego, 1991).
- Yariv, A., *Quantum Electronics*, 3rd ed., (Wiley:New York, 1989).
- Zory, Jr., P. S., ed., *Quantum Well Lasers*, (Academic Press:San Diego, 1993).